Title

Understanding the Structure, Electronic, Phononic, Optical, and Mechanical Properties of Low-Dimensional Materials

Author

Karkee, Rijan

Publication Date

2023

Peer reviewed|Thesis/dissertation

UNIVERSITY OF CALIFORNIA, MERCED

Understanding the Structure, Electronic, Phononic, Optical, and Mechanical Properties of Low-Dimensional Materials

A dissertation submitted in partial satisfaction of the
requirements for the degree
Doctor of Philosophy

in

Physics

by

Rijan Karkee

Committee in charge:

Professor Sayantani Ghosh, Chair
Professor Sarah Kurtz
Professor Elizabeth Nowadnick
Professor David Strubbe

2023

The dissertation of Rijan Karkee is approved, and
it is acceptable in quality and form for publication
on microfilm and electronically:

(Professor Sarah Kurtz)

(Professor Elizabeth Nowadnick)

(Professor David Strubbe)

(Professor Sayantani Ghosh, Chair)

University of California, Merced

2023

DEDICATION

For my parents and my wife.

EPIGRAPH

Knowledge is power; information is liberating; education is the premise of progress, in every society, in every family.

—Kofi Annan

TABLE OF CONTENTS

LIST OF FIGURES

LIST OF TABLES

ACKNOWLEDGEMENTS

I extend my sincere gratitude to Prof. David Strubbe for his encouragement, support, and guidance that have accompanied me since the inception of my doctoral journey. My heartfelt appreciation also goes out to the entire SAIL research group, including Enrique Guerrero, Kuntal Talit, Md. Mehdi Masud, Arabi Seshappan, Uday Panta, Mojdeh Banafsheh, Remi Leano, Sameen Yunus, Elsa Vazquez, Bradford Barker, Tobias Zier, and Rafael Rodrigues Del Grande. Their invaluable contributions and enlightening discussions have been instrumental in my research and personal growth. I am deeply indebted to my esteemed PhD committee members, Prof. Sarah Kurtz, Prof. Sayantani Ghosh, and Prof. Elizabeth Nowadnick, for their insightful comments, suggestions, and guidance. My sincere appreciation also extends to Dr. Michael Pettes for affording me a valuable internship at Los Alamos National Laboratory, where I delved into the realm of experimental work. I extend my heartfelt gratitude to all the remarkable collaborators who have been an integral part of various projects. Special acknowledgments go to the Baykara and Martini groups on campus, the Ma group from Florida State University, and the Yu group at the University of California, Davis. These collaborations have been invaluable for my personal growth and experience in working within a group setting.

I am immensely grateful to the University of California, Merced, for welcoming me as a PhD student and granting me the opportunity to further my education. I would also like to thank the Merced nAnomaterials Center for Energy and Sensing (MACES) for their generous support through two summer fellowships.

My heartfelt thanks go to my wife, Srijana, whose unwavering support and encouragement have been a constant source of strength during challenging times. I am also profoundly thankful to my parents, Rajkumar and Mina, who, despite not having the opportunity to complete high school themselves, provided me with unwavering motivation and resources to pursue my education right through to my PhD. I also wish to express my gratitude to my brother, Niksan, and my sister-in-law, Pratima, for their continuous support, both emotionally and financially, whenever I was in need. I am also deeply thankful to the Nepalese community

in Merced, Diego, and De for their warmth and support, which has made me feel right at home.

I also extend my thanks to my previous teachers and supervisors at Missouri State University, Kathmandu University, Nobel Academy-Kathmandu, Budhanilakantha Secondary School in Biratnagar, and Shree Saraswoti Ni Ma Vi in Pokhare Bhojpur. I'm grateful to organizations like the United States Education Foundation Nepal, Wells Mountain Initiative, and Abi Kattel Memorial Foundation for their guidance and financial support.

VITA

2016	B. Sc. in Applied Physics, Kathmandu University, Nepal
2021	M. S. in Physics, University of California, Merced
2023	Ph. D. in Physics, University of California, Merced

FELLOWSHIPS AND AWARDS

NASA-funded Merced Nanomaterials Center for Energy and Sensing (MACES) Summer Research Fellowship (2019, 2021)

PUBLICATIONS

R. Karkee, D. A. Strubbe, "Low energy nine-layer rhombohedral stacking of transition metal dichalcogenides", 2023 (in preparation)

R. Karkee, R. Del Grande, A. Ben-Akacha, B. Ma, M. T. Pettes, D. A. Strubbe, "Anisotropy and exciton self-trapping in the 1D organic metal halide hybrids", 2023 (in preparation)

R. Karkee, J. Liu, L. Jauregui, D. A. Strubbe, M. T. Pettes, "Polarized Raman spectroscopy of $HfTe_5$ under strain from DFT and experiment", 2023 (in preparation)

J. B. Park, W. Wu, J. Y. Wu, R. Karkee, T. M. Kucinski, K. C. Bustillo, M. Schneider, D. A. Strubbe, C. Ophus, and M. T. Pettes , "Carrier type switching in bismith telluride nanoribbons through in-situ organic molecule coating", (accepted) Nano Lett., 2023

S. Lee, R. Karkee, A. Ben-Akacha, D. Luong, J. S R. V. Winfred, X. Lin, D. A. Strubbe, B. Ma, "One-dimensional Organic Metal Halide Nanoribbons with Dual Emission", Chem. Commun., 59, 3711-3714, 2023

L. M. McClintock, L. Yuan, Z. Song, M. T. Pettes, D. Yarotski, R. Karkee, D. A. Strubbe, L. Z. Tan, A. Ben-Akacha, B. Ma, Y. Shi, V. Taufour, and D. Yu, "Surface Effects on Anisotropic Photoluminescence in One-Dimensional Organic Metal Halide Hybrids", Small Struc., 4, 2200387, 2023

R. Karkee, D. A. Strubbe, "Panoply of doping-induced reconstructions and electronic phases in Ni-doped 1T-MoS_2", (arXiv:2107.07541, 2021)

R. Karkee, E. Guerrero, D. A. Strubbe, "Enhanced interlayer interactions in Ni-doped MoS_2, and structural and electronic signatures of doping site", Phys. Rev. Materials, 5, 7, 2021

E. Guerrero, R. Karkee, D. A. Strubbe, "Phase Stability and Raman/IR Signatures of Ni-Doped MoS_2 from Density Functional Theory Studies", J. Phys. Chem. C, 125, 24, 13401–13412, 2021

PRESENTATIONS

R. Karkee, D. A. Strubbe, "Anisotropy and exciton self-trapping in the 1D perovskite $C_4N_2H_{14}PbBr_4$ from first principles", March Meeting, American Physical Society, Las Vegas, USA, 2023, **contributed talk**

R. Karkee, D. A. Strubbe, "Panoply of doping-induced reconstructions and electronic phases in Ni-doped 1T-MoS_2", March Meeting, American Physical Society, Chicago, USA, 2022, **contributed talk**

R. Karkee, E. Guerrero and D. A. Strubbe, "Structural studies of Ni-doped MoS_2 monolayers and polytypes using density functional theory (DFT)", March Meeting, American Physical Society, virtual, 2021, **contributed talk**

R. Karkee, D. A. Strubbe, "Structural studies of Ni-doped MoS_2 monolayers and polytypes using density functional theory (DFT)", Lawrence Berkeley National Laboratory, Molecular Foundry User Meeting, 2020, **poster**

R. Karkee, D. A. Strubbe, "Structural studies of Ni-doped MoS2 monolayers and polytypes using density functional theory (DFT)",Virtual Electronic Structure Methods, University of California-Merced, 2020, **poster**

WORKSHOPS

Virtual school on many body calculations using EPW and BerkeleyGW, 2023.

MagLab Summer School, University of Florida, 2023.

Wannier 2022 Summer School, virtual, May 16- 20, 2022.

11^{th} Computational Materials Science Summer School, Texas A&M University, 2022.

8^{th} BerkeleyGW Tutorial Workshop and 3^{rd} Berkeley Excited State Conference, virtual, 2022.

7^{th} BerkeleyGW Tutorial Workshop and 2^{nd} Berkeley Excited State Conference, virtual, 2021.

ABSTRACT OF THE DISSERTATION

Understanding the Structure, Electronic, Phononic, Optical, and Mechanical Properties of Low-Dimensional Materials

by

Rijan Karkee
Doctor of Philosophy in Physics
University of California Merced, 2023
Professor Sayantani Ghosh, Chair

Low-dimensional materials have attracted significant attention in the field of materials science and technology. These materials, characterized by their limited dimensions in one, two or three directions, exhibit exceptional properties different from those of their bulk counterparts. This deviation results from the interaction of quantum effects, surface interactions, and unique electronic structures, creating a wide range of innovative applications in various fields such as electronics, photonics, energy storage and more. This study not only reveals the scientific complexities of their behavior but also paves the way for disruptive innovations that could transform industries and transform our interactions with the world around us. In this work, I have studied different classes of low-dimensional materials such as bulk and monolayer transition-metal dichalcogenides, one-dimensional organic-metal halide hybrids, organic metal halide nanoribbons, Bi_2Te_3 and $HfTe_5$.

In the opening chapter, I lay the groundwork by discussing fundamental theories crucial for our subsequent calculations. These theories encompass density functional theory, density functional perturbation theory, GW and Bethe-Salpeter equations and other fundamental concepts on Raman, and calculation methods for elastic tensors. Chapter 2 delves into a comprehensive analysis of the impact of introducing Ni into the bulk phases of MoS_2, with a particular focus on the mechanism supporting low wear for lubrication applications. This chapter also

presents systematic doping studies conducted through first-principles calculations. Chapter 3 narrows the focus to examine the consequences of Ni doping on the monolayer phases of MoS_2, revealing the induction of various known and novel distorted phases. These induced phases bring forth unique properties, including those of ferroelectric materials, multiferroic semimetals, ferromagnetic polar metals, and the presence of multiple gaps in conduction bands. These findings have promising implications for applications in spintronics, intermediate band solar cells, and nonlinear optics. In Chapter 4, the attention shifts to a low-energy nine-layer phase within transition-metal dichalcogenides, where we explore methods for characterizing this phase through Raman spectroscopy and powder diffraction. Additionally, we investigate its potential applications in piezoelectricity and valleytronics. Next Chapter 5 delves into understanding the anisotropic properties of one-dimensional organic-metal halide hybrids and the mechanism of broadband emission. This chapter introduces an innovative approach for determining exciton-phonon coupling and the self-trapped exciton structure using excited state forces within a GW/Bethe-Salpeter framework. Chapter 6 offers a concise overview of my contributions to other collaborative works on low-dimensional materials, encompassing organic-metal halide hybrids, organic metal halide nanoribbons, Bi_2Te_3 and $HfTe_5$. Finally, I conclude with reflections on the potential of low-dimensional materials, their current progress, and future prospects.

Chapter 1

Theoretical Methods

In this chapter, I will briefly discuss about the theoretical methods that are the backbone of the calculations used for my entire work. I will use both ground state and excited state calculations; density functional theory (DFT) for ground state calculations is implemented in the Quantum Espresso [68] code, and GW-BSE theory for excited state calculations is implemented in the Berkeley-GW [39] code. In addition to that, I will also discuss about how Raman and elastic tensors are calculated from Quantum ESPRESSO.

1.1 Density functional theory

To understand the materials atomistically, we use and solve the many body Schrodinger equation ($H\Psi(\{r_i\},\{R_I\}) = E\Psi(\{r_i\},\{R_I\})$). The many body Hamiltonian for collection of elections and nuclei is given as [69]

$$H = -\sum_i \frac{\hbar^2}{2m_e}\nabla^2_{r_i} - \sum_I \frac{\hbar^2}{2M_I}\nabla^2_{R_I} - \sum_{i,I}\frac{Z_I e^2}{|R_I - r_i|} + \frac{1}{2}\sum_{i\neq j}\frac{e^2}{|r_i - r_j|} + \frac{1}{2}\sum_{I\neq J}\frac{Z_I Z_J e^2}{|R_I - R_J|} \tag{1.1}$$

Here, M_I and R_I represent mass and positions of nucleus, m_e is the electron mass, and r_i represents position of electron i. First two terms in equation 1.1 are kinetic energy operator for electron and nuclei, third term is Coulomb attraction between electrons and nuclei, and, electron-electron repulsion and nuclei-nuclei repulsion is represented in last two terms. The many body wavefunction is the function

of position of all electrons and ions ($\Psi(\{r_i\},\{R_I\})$. This equation does not have analytical solution and therefore is solved numerically through the computers. To further reduce the complexity of this problem, numerous approximations are made.

According to the Born-Oppenheimer (B-O) approximation, the mass of nucleus is much heavier than electrons and therefore the electrons are much faster than nucleus which enables the electron to find its ground state. This decouples the wavefunction $\Psi(\{r_i\},\{R_I\})$ to $\Psi(\{r_i\}$, meaning the wavefunction only depends on the position of electrons. This simplifies the problem into $3N$ variable for N electrons. Then Hohenberg-Kohn proposed density as a basic variable. [84] So instead of dealing each electron's wavefunction, they simplified the problem with a single variable density $n(\vec{r})$, which reduces $3N$ dimensional problem into just 3-dimension. Hohenberg-Kohn theorems is the heart of DFT which states:

1 The external potential $V_{ext}(\vec{r})$ is a unique functional of electron density $n(\vec{r})$. As a consequence, the total ground state energy E is also a functional of electron density $n(\vec{r})$.

2 The density $n(\vec{r})$ which minimizes the total energy $E[n]$ is the ground-state density and the corresponding energy is the ground-state energy $E[n]$.

From these considerations, the total energy of the system is a functional of the density, given by:

$$H = -\sum_i \frac{\hbar^2}{2m_e}\nabla^2_{r_i} - \sum_I \frac{\hbar^2}{2M_I}\nabla^2_{R_I} - \sum_{i,I}\frac{Z_I e^2}{|R_I - r_i|} + \frac{1}{2}\sum_{i\neq j}\frac{e^2}{|r_i - r_j|} + \frac{1}{2}\sum_{I\neq J}\frac{Z_I Z_J e^2}{|R_I - R_J|} \tag{1.2}$$

With the principle of variations, the density which minimizes the energy E is the true ground state density. Thus applying the variational principle on (1.2) yields the Kohn-Sham equation given as:

$$\left[-\frac{\hbar^2}{2m_e}\nabla^2 + V_{ext}(\vec{r}) + V_H(\vec{r}) + V_{XC}(\vec{r})\right]\psi_i(\vec{r}) = \epsilon_i\psi_i(\vec{r}) \tag{1.3}$$

Here V_H is the Hartree potential and $V_{XC}(\vec{r})$ is the exchange-correlation potential which accounts for different quantum mechanical interaction such as Pauli exclusion. The exchange-correlation potential's exact form is unknown and needs some approximation to solve such as Local Density Approximation (LDA) or Generalized Gradient Approximation (GGA). In LDA, the electron density $n(\vec{r})$ is assumed to vary slowly in space allowing to treat $n(\vec{r})$ as constant locally. In GGA the local variation of density $\nabla n(\vec{r})$ is considered. I have considered both functional in my calculation. The Hartree potential and exchange-correlation potential is expressed as:

$$V_H(\vec{r}) = \int \frac{e^2}{4\pi\epsilon_0} \frac{n(\vec{r'})}{|\vec{r} - \vec{r'}|} d^3r' \tag{1.4}$$

$$V_{XC}(\vec{r}) = \frac{\delta E_{XC}[n]}{\delta n(\vec{r})} \tag{1.5}$$

In practice, usually only valence electrons are considered for the calculation because core-electrons usually do not participate in bonding or optical properties or chemical reaction. This allows us to exclude the need of core-electrons via pseudopotential that replaces entire core electrons with an approximate potential.

1.2 Density functional perturbation theory

The primary function of density functional perturbation theory (DFPT) is to address the computation of phonon eigenvalues and eigenmodes. The subsequent summary is grounded in an extensive assessment conducted by Baroni et al. [13]. These eigenmodes encompass the vibrational configurations occurring within the crystal lattice, with the associated eigenvalues signifying their respective frequencies. These vibrational patterns bear relevance to various phenomena, spanning from heat conduction to infrared and Raman spectroscopy. In order to compute these vibrations, DFPT employs perturbation theory, wherein either E or ρ can be regarded as cumulative responses to a perturbing parameter λ:

$$E(\lambda) = E^{(0)} + \lambda E^{(1)} + \lambda^2 E^{(2)} + ... \tag{1.6}$$

$$E^{(n)} = E^{(0)} + \frac{1}{n!} \left. \frac{\mathrm{d}^n E}{\mathrm{d}\lambda^n} \right|_{\lambda=0} \tag{1.7}$$

We then apply the harmonic approximation to the total energy with perturbing displacements of atom α in direction μ, $\mathbf{u}_{\alpha\mu}$:

$$E = E^{(0)} + \frac{1}{2} \sum_{\alpha,\beta,\mu,\nu} \frac{\partial^2 E}{\partial \mathbf{u}_{\alpha\mu} \partial \mathbf{u}_{\beta\nu}} \mathbf{u}_{\alpha\mu} \mathbf{u}_{\beta\nu} \tag{1.8}$$

The linear term $E^{(1)} = 0$ because we calculate phonons at equilibrium coordinates. Other terms higher than $E^{(2)}$ are neglected under this approximation. In theory, resolving this equation would require the computation of $(3N)^2$ derivatives, along with a minimum of an equivalent number of DFT self-consistent computations for total energy. However, from a practical standpoint, it is more effective to expand E in the second term of equation 1.8. This efficiency stems from the observation that second-order derivatives of the total Hamiltonian's eigen energy can be derived employing solely first-order derivatives of the eigenfunctions.

In practice, we solve DFPT also by self consistent method, similar to DFT. We replace external potential ($V_{ext}(\vec{r})$) by perturbed potential ($V'_{ext}(\vec{r})$) and obtain ground state density, and hence wavefunctions based on this perturbed external potential. So we will have similar equation as in equation 1.3. For simplicity, lets call $\Delta = \frac{\hbar^2}{2m_e}\nabla^2$ and $V_{SCF} = V_{ext}(\vec{r}) + V_H(\vec{r}) + V_{XC}(\vec{r})$.

$$(-\Delta + V_{SCF} - \epsilon)\psi'(\vec{r}) = -P_c V'_{SCF} \psi(\vec{r}) \tag{1.9}$$

where, P_c is projector over all empty states defined by $\sum_c |\phi_c >< \phi_c|$, $V'_{SCF} = V'_{ext}(\vec{r}) + V'_H(\vec{r}) + V'_{XC}(\vec{r})$, and ϵ and ψ are eigenvalues and eigenfunctions of unperturbed system similar to equation 1.3.

1.3 GW-BSE

The Kohn-Sham equation calculates the ground state density based on fictitious non-interacting electron system. Although this gives accurate ground state density and corresponding eigen-values and wavefunctions it fails to accurately predict

the excited state properties. DFT does feature qualitative description of excited states. The GW approximation fixes the discrepancies in the DFT calculation for excited state with appropriate shift in the eigenvalues. The GW approximation is based on perturbation theory where electron or hole is injected into the system and the quasiparticle interaction and response is evaluated at later time. [81, 39] This injection of electron/hole is done through the Greens's function (the G in GW represents Green's function). As hole is injected into the system, the hole is screened by electrons and forms a quasiparticle which interacts differently than bare Coulomb interaction. This effective interaction is called screened Coulomb interaction and is represented by W. The GW in conjunction with Bethe-Salpeter equation (BSE) is used to calculate the absorption spectra.

The GW calculation requires the Kohn-Sham eigenfunctions as input. So DFT calculations must be computed prior to GW calculation. The GW portion of the calculation solves the Dyson equation which yeilds quasi-particle energies and wavefunctions. The Dyson equation in Hartree unit ($\hbar = 1$, $m = 1$) is given by [88]:

$$\left[-\frac{1}{2}\nabla^2 + V_{ext} + V_H + \Sigma(E^{QP}_{n\mathbf{k}})\right]\psi^{QP}_{n\mathbf{k}} = E^{QP}_{n\mathbf{k}}\psi^{QP}_{n\mathbf{k}} \tag{1.10}$$

The new $E^{QP}_{n\mathbf{k}}$ and $\psi^{QP}_{n\mathbf{k}}$ are eigenenergies and eigenfunctions of the quasiparticles at the point $\mathbf{k}$ in reciprocal space. The self-energy operator, $\Sigma(E^{QP}_{n\mathbf{k}})$, is the non-local, frequency dependent energy caused by the particle's change to its environment by its own excited state. The GW approximation makes the approximation that $\Sigma = iGW$, where i is the imaginary unit, G is the Green's function operator which describes particle propagation in an interacting system, and W is the screened Coulomb interaction.

Solution to Eq. 1.10 yields $\psi^{QP}_{n\mathbf{k}}$ and $E^{QP}_{n\mathbf{k}}$ which are used for solving BSE equation that helps to study the excitonic, bound electron hole states' contributions to the absorption spectra.

$$(E^{QP}_{c\mathbf{k}} - E^{QP}_{v\mathbf{k}})A^S_{vc\mathbf{k}} + \sum_{v'c'\mathbf{k}'} \langle vc\mathbf{k}| K^{eh} |v'c'\mathbf{k}'\rangle = \Omega^S A^S_{vc\mathbf{k}} \tag{1.11}$$

The Eqn. 1.11 allow us to find $A^S_{vc\mathbf{k}}$ and Ω^S, eigenfunctions and eigenenergies

respectively that describe the S exciton state given an electron-hole excitations in valence and conduction states v and c. K^{eh} is the interaction kernel for possible electron-hole excitations. $A^S_{vc\mathbf{k}}$ and Ω^S then can be used to calculate absorption spectra $\epsilon(\omega)$:

$$\epsilon_2(\omega) = \frac{16\pi^2 e^2}{\omega^2} \sum_S |\mathbf{e} \cdot \langle 0| \mathbf{v} |S\rangle|^2 \delta(\omega - \Omega^S) \tag{1.12}$$

Here, $\mathbf{e}$ is the incident polarization, and $\mathbf{v}$ is the velocity operator. The absorption spectra obtained are more accurate, especially in materials where excitonic effects are prevalent, such as in semiconductors. Therefore, this method is a useful tool for studying excited states and excitons in 1D DMEDAPbBr$_4$.

1.4 Excited state forces

The scientific community has extensively developed theoretical approaches for calculating optical absorption [88, 115, 158, 176, 39, 201, 29]. However, there is a limited body of work focused on computing excited state forces in materials. In theory, these excited state forces could be determined by obtaining the excitation energy's dependency on atomic displacements through finite difference methods [29]. Nonetheless, this methodology would demand significant computational resources, particularly for systems with a high atom count. In 2003, Ismail-Beigi and Louie [90] introduced a theory for calculating excited state forces, which integrates findings from GW calculations [88], solutions from the Bethe-Salpeter Equation (BSE) [176, 39], and Density Functional Perturbation Theory (DFPT) [13]. Subsequently, this theory was adapted for application within Time-Dependent Density Functional Theory (TDDFT) [187]. Other than these instances, over the past two decades, only the authors of the initial paper have employed this methodology to investigate exciton self-trapping in SiO_2 [91]. Notably, in 2012, Professor David Strubbe, within his Ph.D. thesis [195], revisited the approach and introduced new approximations for utilization in the theory of excited state forces. Regarding the approach proposed by Ismail-Beigi and Louie [91], the calculation of total energy

in an excited state is formulated as follows:

$$E(R) = E_0(R) + \Omega(R) \tag{1.13}$$

where $E_0(R)$ is the ground state energy (for example from a DFT calculation) for a given atomic configuration R and Ω is the excitation energy that is a solution to the BSE. The BSE is given by

$$H^{\mathrm{BSE}}|A\rangle = \Omega|A\rangle \tag{1.14}$$

where $|A\rangle$ is the exciton wavefunction that we can express in the basis of the direct product of the conduction c and valence v states ($|A\rangle = \sum_{cv}\langle cv|A\rangle|cv\rangle = \sum_{cv} A_{cv}|cv\rangle$) and each one of the BSE matrix elements is given by

$$H^{\mathrm{BSE}}_{cv,c'v'} = \langle cv|H^{\mathrm{BSE}}|c'v'\rangle = (E^{qp}_c - E^{qp}_v)\delta_{cc'}\delta_{vv'} + K_{cv,c'v'} \tag{1.15}$$

where $E^{qp}_{c(v)}$ are the quasiparticle energies for the conduction (valence) bands calculated in the GW approximation [88] and K is the electron-hole interaction kernel [39].

The differentiation of equation (1.13) concerning a specific atomic displacement δR can be performed. The initial component involves the derivative $\partial_R E_0$, which can be efficiently computed using the Hellman-Feynman theorem and is a commonly employed technique in density functional theory (DFT) codes [68, 67]. Meanwhile, the secondary term $\partial_R\Omega$ represents the derivative of the excitation energy, as outlined in the work of Ismail-Beigi and Louie [90].

$$\partial_R\Omega = \sum_{cv,c'v'} A^*_{cv}A_{c'v'}\partial_R H^{\mathrm{BSE}}_{cv,c'v'} = \sum_{cv,c'v'} A^*_{cv}A_{c'v'}\partial_R\left((E^{qp}_c - E^{qp}_v)\delta_{cc'}\delta_{vv'} + K_{cv,c'v'}\right) \tag{1.16}$$

In the reference [90], the derivatives of quasiparticle levels are approximated as being equivalent to the derivatives of DFT energy levels. These energy levels involve electron-phonon matrix elements, which are determined through density functional perturbation theory (DFPT) calculations [13] ($\partial_R E^{qp} = \partial_R E^{dft}$). Despite this approximation, it overlooks variations in the self-energy concerning atomic displacements, which has been demonstrated to hold significance and should

not be disregarded [120, 50]. In the reference [120], the authors introduced the GWPT method. In broad terms, this method can be considered an advancement of the DFPT approach where the GW Hamiltonian is utilized in place of the DFT Hamiltonian. However, it's worth noting that such calculations continue to be computationally intensive. Professor Strubbe in his thesis undertook a reassessment of this approach, taking into account the relatively minor variations in kernel energies and recognizing that the basis itself (comprising conduction and valence states) also undergoes changes. Consequently, he derived the subsequent expression:

$$\partial_R \Omega = \sum_{cv,c'v'} A^*_{cv} A_{c'v'} (\langle c|\partial_R H^{qp}|c'\rangle \delta_{vv'} - \langle v|\partial_R H^{qp}|v'\rangle \delta_{cc'}) \tag{1.17}$$

where $\langle i|\partial_R H^{qp}|j\rangle$ is the electron-phonon coefficient calculated at GW level. In the above expression, we are taking in account the effect of mixing of conduction (valence) bands due to atomic displacements. The approximation we use is that those electron-phonon coefficients are renormalized as

$$\langle i|\partial_R H^{qp}|j\rangle = \begin{cases} \langle i|\partial_R H^{dft}|j\rangle & \text{if } E_i^{dft} = E_j^{dft} \\ \langle i|\partial_R H^{dft}|j\rangle \left(\frac{E_i^{qp} - E_j^{qp}}{E_i^{dft} - E_j^{dft}}\right) & \text{else} \end{cases} \tag{1.18}$$

Differing from the more intricate GWPT method outlined in [120], this approximation offers a practical and computationally efficient alternative. Notably, it's worth highlighting that performing calculations for a system with N atoms per unit cell would necessitate approximately $3N$ GW/BSE calculations, corresponding to the need for displacing each atom along three distinct directions. Conversely, the excited state force calculations presented in this context demand only one GW/BSE calculation and one DFPT calculation.

1.5 Raman spectroscopy

Raman spectroscopy is an effective analytical technology that is widely used in the field of molecular vibration and interaction research. When light interacts with

the sample, a small portion of the scattering light changes energy due to molecular vibration. This phenomenon is known as the Raman shift, which generates a unique "fingerprint" spectrum that reveals information about the chemical composition and molecular structure. Raman spectroscopy measures the frequency shifts of scattered light relative to incident light and gives insights into bond strengths and crystal phase. It is widely applied in materials, chemistry, biology and other fields and offers non-destructive and label-free analysis of a wide range of materials, from solids to liquids to gases.

Raman effect depends on the change of polarizability of the system with respect to atomic vibration. If we consider the polarizability to be a function of nuclear coordinates, then the variation of the component in polarizability tensor with vibrational coordinates can be written as a Taylor series

$$\alpha_{ij} = (\alpha_{ij})_0 + \sum_k \left(\frac{\partial \alpha_{ij}}{\partial Q_k}\right)_0 Q_k + \frac{1}{2}\sum_{k,l}\left(\frac{\partial^2 \alpha_{ij}}{\partial Q_k \partial Q_l}\right) Q_k Q_l + \cdots \tag{1.19}$$

where $(\alpha_{ij})_0$ denotes the value of α_{ij} at equilibrium configuration. Q_k and Q_l are normal vibration coordinates at frequencies ω_k and ω_l. To get the first-order Raman spectra we can ignore the 2^{nd} order term in Taylor expansion. Considering a harmonic vibration for some K^{th} mode as $Q_k = Q_{k0}\cos(\omega_k t + \delta k)$ and the incident radiation as $E_0 \cos \omega t$ then the induced electric dipole moment can be written as

$$\begin{aligned}\mu^{(1)} = \alpha_0 E_0 \cos \omega t + \frac{1}{2}\left(\frac{\partial \alpha_k}{\partial Q_k}\right)_0 E_0 Q_{k0} \cos(\omega t + \omega_k t + \delta k) + \\ \frac{1}{2}\left(\frac{\partial \alpha_k}{\partial Q_k}\right)_0 E_0 Q_{k0} \cos(\omega t - \omega_k t - \delta k)\end{aligned} \tag{1.20}$$

Here we can see that the linear induced dipole moment $\mu^{(1)}$ has three components with different frequencies. The first term with same frequency ω as the incident radiation is for Rayleigh scattering. The second term with frequency $\omega + \omega_k$ represents anti-Stokes line and third term with frequency $\omega - \omega_k$ represents the Stokes line.

Quantum ESPRESSO calculates the normal modes through DFPT as discussed earlier and then it make use of group theory to find out which modes will be Raman active based on the symmetry. As we know that, if the irreducible representation

of a certain vibrational mode have a basis in x^2, y^2, z^2, xy, yz, xz or any linear combination of them then those modes are Raman active. To calculate the Raman intensity, it uses the Plackzek approximation [24, 112].

$$I^{\nu} \propto \left| e_i \cdot \overleftrightarrow{A^{\nu}} \cdot e_s \right|^2 \frac{1}{\omega_{\nu}} (n_{\nu} + 1) \tag{1.21}$$

where e_i and e_s are the polarization of the incident and scattered radiation. $n_{\nu} = [exp(\hbar\omega_{\nu}/k_B T) - 1]^{-1}$, T is the temperature.

$$A^{\nu}_{lm} = \sum_{k\gamma} \frac{\partial^3 \epsilon^{el}}{\partial E_l \partial E_m \partial u_{k\gamma}} \frac{W^{\nu}_{k\gamma}}{\sqrt{M_{\gamma}}} \tag{1.22}$$

Here ϵ^{el} is the total electronic energy of the system. E_l and E_m are the l^{th} and m^{th} Cartesian components of the uniform electric field, $u_{k\gamma}$ is the displacement of the γ^{th} atom in the k^{th} direction, M_{γ} is the atomic mass and $W^{\nu}_{k\gamma}$ is the orthonormal vibrational eigenmode ν. The third order derivative [112] is calculated by taking the second order derivative of the DFT density matrix with respect to electric field and then by using Hellmann-Feynman theorem

$$\frac{\partial^3 \epsilon^{el}}{\partial E_l \partial E_m \partial u_{k\gamma}} = 2Tr \left\{ \left(\frac{\partial^2 \rho}{\partial E_l \partial E_m} \right) \frac{\partial v^{ext}}{\partial u_{k\gamma}} \right\} \tag{1.23}$$

Here v^{ext} is the external ionic potential and ρ is the DFT density matrix.

1.6 Calculation of elastic tensor

When an external force is applied to a material, it undergoes deformation and reverts to its original shape once the force is removed. This intrinsic property of materials is known as elasticity. Stress, which is the force applied per unit area, and strain, the change in length per unit length, are the key parameters in describing this behavior. Within the elastic limit, stress and strain exhibit a linear relationship, a fundamental principle known as Hooke's law. Stress and strain are tensor quantities, encompassing various directional components. In the case of anisotropic materials, where the crystal orientations differ from one lattice vector to another, applying force results in different amounts of strain along each direction. This variation in strain levels leads to strain inhomogeneity or stress inhomogeneity

across different lattice directions. In certain situations, these stress-strain non-uniformities can lead to material damage. Therefore, a thorough comprehension of strain and elasticity is essential, particularly in low-dimensional materials, where anisotropy is commonly observed.

If we represent the stress tensor as σ_{ij} and the strain tensor as ϵ_{kl}, in accordance with Hooke's law, we can express this relationship as follows:

$$\sigma_{ij} = C_{ijkl}\epsilon_{kl} \tag{1.24}$$

where C_{ijkl} is known as the stiffness tensor. It is a 4^{th} rank tensor. The indices i, j, k, l can take values from 1-3 or x,y,z which makes 81 components for C_{ijkl}. Due to symmetry in stress ($C_{ijkl} = C_{jikl}$) and in strain ($C_{ijkl} = C_{ijlk}$) these 81 components drop down to 36 independent components. In contracted notation we can write the stress-strain equation as

$$\begin{pmatrix} \sigma_1 \\ \sigma_2 \\ \sigma_3 \\ \sigma_4 \\ \sigma_5 \\ \sigma_6 \end{pmatrix} = \begin{pmatrix} C_{11} & C_{12} & C_{13} & C_{14} & C_{15} & C_{16} \\ C_{21} & C_{22} & C_{23} & C_{24} & C_{25} & C_{26} \\ C_{31} & C_{32} & C_{33} & C_{34} & C_{35} & C_{36} \\ C_{41} & C_{42} & C_{43} & C_{44} & C_{45} & C_{46} \\ C_{51} & C_{52} & C_{53} & C_{54} & C_{55} & C_{56} \\ C_{61} & C_{62} & C_{63} & C_{64} & C_{65} & C_{66} \end{pmatrix} \begin{pmatrix} \epsilon_1 \\ \epsilon_2 \\ \epsilon_3 \\ \epsilon_4 \\ \epsilon_5 \\ \epsilon_6 \end{pmatrix} \tag{1.25}$$

Here, ϵ_i for i=1 to 6 is used where $1 = xx$, $2 = yy$, $3 = zz$, $4 = yz$, $5 = xz$ and $6 = xy$, and corresponding strain tensor are represented by Fig. 1.1 (a) through (f), respectively. Since, $C_{ij} = C_{ji}$, it drops this 36 independent component down to 21 components. So, the stiffness matrix is symmetric around the diagonals. Based on the crystal symmetry, these 21 independent components can further be reduced. For example, cubic structure has 4 three-fold rotational symmetry, which brings it down to 3 independent stiffness constants C_{11}, C_{12} and C_{44}. For a crystal structure which does not have much symmetry, we need to calculate all 21 stiffness constants.

We know that elastic strain energy is the energy spent by the external force in deforming an elastic body. This energy divided by the volume is called energy density. It can be shown that the energy density is related to strain and stiffness

constants through the equation [106]

$$U = \frac{1}{2}\sum_{\lambda=1}^{6}\sum_{\mu=1}^{6} C_{\lambda\mu}\epsilon_{\lambda}\epsilon_{\mu} \tag{1.26}$$

Using equation (1.26) we will be able to calculate all the C_{ij}. Using any of the two equations (eqn-1.24 and eqn-1.26) the full stiffness tensor can be calculated.

$$\begin{pmatrix} 1+\eta & 0 & 0 \\ 0 & 1 & 0 \\ 0 & 0 & 1 \end{pmatrix} \quad \begin{pmatrix} 1 & 0 & 0 \\ 0 & 1+\eta & 0 \\ 0 & 0 & 1 \end{pmatrix} \quad \begin{pmatrix} 1 & 0 & 0 \\ 0 & 1 & 0 \\ 0 & 0 & 1+\eta \end{pmatrix}$$

(a) (b) (c)

$$\begin{pmatrix} 1 & 0 & 0 \\ 0 & 1 & \eta/2 \\ 0 & \eta/2 & 1 \end{pmatrix} \quad \begin{pmatrix} 1 & 0 & \eta/2 \\ 0 & 1 & \\ \eta/2 & 0 & 1 \end{pmatrix} \quad \begin{pmatrix} 1 & \eta/2 & 0 \\ \eta/2 & 1 & 0 \\ 0 & 0 & 1 \end{pmatrix}$$

(e) (f) (g)

$$\begin{pmatrix} 1+\eta & 0 & 0 \\ 0 & 1-\eta & 0 \\ 0 & 0 & 1 \end{pmatrix} \quad \begin{pmatrix} 1+\eta & 0 & 0 \\ 0 & 1 & 0 \\ 0 & 0 & 1-\eta \end{pmatrix} \quad \begin{pmatrix} 1 & 0 & 0 \\ 0 & 1+\eta & 0 \\ 0 & 0 & 1-\eta \end{pmatrix}$$

(h) (i) (j)

Figure 1.1: Different strain tensors used to calculate the full stiffness tensor and other mechanical properties. Out of these nine strain tensors a,b and c represent uniaxial strain, e, f, and g represent shear strain and h, i, and j represent biaxial strain.

Calculation of different elastic parameters

To calculate the elastic parameters, we first strain the lattice vectors as given in Equation 1.27, where $\vec{a} = a_x\hat{i}+a_y\hat{j}+a_z\hat{k}$, $\vec{b} = b_x\hat{i}+b_y\hat{j}+b_z\hat{k}$, and $\vec{c} = c_x\hat{i}+c_y\hat{j}+c_z\hat{k}$) are lattice vectors and all the atoms in the unit cell can be expressed with respect to lattice vectors, also known as crystal coordinates. Here, ϵ_{ij} are the strain matrix along $i, j = x, y, z$ directions.

$$\begin{pmatrix} \epsilon_{xx} & \epsilon_{xy} & \epsilon_{xz} \\ \epsilon_{yx} & \epsilon_{yy} & \epsilon_{yz} \\ \epsilon_{zx} & \epsilon_{zy} & \epsilon_{zz} \end{pmatrix} \begin{pmatrix} a_x & b_x & c_x \\ a_y & b_y & c_y \\ a_z & b_z & c_z \end{pmatrix} = \begin{pmatrix} a'_x & b'_x & c'_x \\ a'_y & b'_y & c'_y \\ a'_z & b'_z & c'_z \end{pmatrix} \tag{1.27}$$

Following the application of strain tensors, each deformed structure requires ion relaxation while keeping the lattice parameters fixed. This relaxation process is conducted using Quantum ESPRESSO. Subsequently, the total energy of the system is calculated for each deformed and relaxed structure. Once these total energies are determined, we can proceed to compute the change in energy density (U). This calculation is carried out using equation (1.26).

Using the nine distinct strain tensors as illustrated in Figure (1.1), we can compute nine independent stiffness constants denoted as C_{ij} in accordance with equation (1.26). To determine C_{11}, C_{22}, and C_{33}, uniaxial strains as depicted in Figure 1.1(a, b, c) can be applied, and a straightforward quadratic fitting to the equation is employed. To calculate C_{44}, C_{55}, and C_{66}, shear strains as shown in Figure 1.1(e, f, g) are utilized. It's important to note that we intentionally use $\frac{\eta}{2}$ instead of η for the cross terms of ϵ because this leads to four terms in the summation, simplifying the final equation to $U = \frac{1}{2}C_{ii}\eta^2$. For the determination of C_{12}, C_{13}, and C_{23}, biaxial strains as presented in Figure 1.1(h, i, j) are applied. These strains result in an energy density equation in the form of $U = \frac{1}{2}(C_{ii} + C_{jj} - 2C_{ij})\eta^2$, with values of i and j taking on the values 1, 2, and 3. By applying these strains and using quadratic fitting in conjunction with the previously computed results of C_{ii} and C_{jj}, we can accurately determine the values of C_{ij}.

Chapter 2

Enhanced interlayer interactions in Ni-doped MoS_2, and structural and electronic signatures of doping site

2.1 Abstract

The crystal structure of MoS_2 with strong covalent bonds in plane and weak Van der Waals interactions out of plane gives rise to interesting properties for applications such as solid lubrication, optoelectronics, and catalysis, which can be enhanced by transition-metal doping. However, the mechanisms for improvement and even the structure of the doped material can be unclear, which we address with theoretical calculations. Building on our previous work on Ni-doping of the bulk 2H phase, now we compare to polytypes (1H monolayer and 3R bulk), to determine favorable sites for Ni and the doping effect on structure, electronic properties, and the layer dissociation energy. The most favorable intercalation/adatom sites are tetrahedral intercalation for 3R (like 2H) and Mo-atop for 1H. The relative energies indicate a possibility of phase change from 2H to 3R with substitution of Mo or S. We find structural and electronic properties that can be used to identify

the doping sites, including metallic behavior in Mo-substituted 3R and 2H, and in-gap states for Mo- and S-substituted 1H, which could have interesting optoelectronic applications. We observe a large enhancement in the interlayer interactions of Ni-doped MoS_2, opposite to the effect of other transition metals. For lubrication applications, this increased layer dissociation energy could be the mechanism of low wear. Our systematic study shows the effect of doping concentration and we extrapolate to the low-doping limit. This work gives insight into the previously unclear structure of Ni-doped MoS_2 and how it can be detected experimentally, the relation of energy and structures of doped monolayers and bulk systems, the electronic properties under doping, and the effect of doping on interlayer interactions.

2.2 Introduction

There has been great interest in transition metal dichalcogenides, particularly in MoS_2 which has been used in a wide variety of applications because of its unique physical, optical and electrical properties [192, 144, 119]. Tunability of the band gap from direct to indirect [192, 144], good electron mobility [101], the possibility of defect engineering including creating quantum emitters [124], and high current-carrying capabilities [114] open great potential in optics and electronics. MoS_2 has already shown promising applications in lubrication, hydrodesulfurization, and optoelectronics [148, 173, 131, 110]. Theoretical and experimental work has shown that transition-metal-doping in MoS_2 can improve catalytic reactivity [95, 77, 142], lubrication [100] and gas sensing [141, 206]. However, the detailed mechanism is still unclear for improved catalysis and lubrication with doping, and in general the exact location of dopants in MoS_2 is also uncertain. Our previous work addressed the most favorable sites for Ni in 2H-MoS_2 as a function of chemical potential and investigated signatures in Raman and IR spectroscopy [72]. We now extend this study to a systematic exploration of other polytypes, with consideration of the relation between monolayer and bulk structure and energetics, and study of doping concentration-dependence. This work will look specifically at implications

for solid lubrication, but also give insight into optoelectronic and other fundamental properties.

MoS_2 is a layered structure with weak Van der Waals forces between layers and strong covalent forces within the layers giving rise to interesting applications in solid lubricants because the weakly bound layers can slide against each other easily. Graphite is a commonly used solid lubricant, which also has a layered Van der Waals structure, but it needs to adsorb oxygen and moisture to develop the low shear strength necessary for lubrication [177]. MoS_2, on the other hand, works well under vacuum but shows degradation in lubrication under humidity and high temperature, for unclear reasons [105]. Therefore MoS_2 is preferred for solid lubrication in space applications such as NASA's James Webb Space Telescope [110] where the wide range of temperatures precludes the use of oils or greases for lubrication of moving parts.

A clear understanding of the mechanisms by which Ni-doped MoS_2 enhances lubrication performance of pristine MoS_2 is still lacking. A recent review [125] discusses low friction mechanisms based on ordering of crystallites in adjacent platelets. The early experimental work of Stupp [197] studied the friction properties in MoS_2 doped with various transition metals. MoS_2 doped with Ni or Ta showed the best results in terms of stable friction, excellent endurance, easy control, good effect on aging, and lower coefficient of friction than pristine MoS_2. Later, other researchers also confirmed the lower coefficient of friction for Ni-doping [170]. Ni is more abundant and less expensive than Ta [217, 181], making it more attractive. Most of the literature on doped MoS_2 is focused on electronic, optical, and catalytic applications and there have been only a small number of studies on tribology. There are already some studies on Ni-doped MoS_2 monolayers and nanosheets, for catalysis in solar hydrogen production [142], adsorption of CO or NO for potential gas sensors [141], or adsorption of O_2 molecules [240], but tribological applications have not been investigated. Different dopants such as Ni, Cr, Ti, Au, Zr and Sb_2O_3 have been studied for the improvement of tribological properties [211]. One popular proposed mechanism is increase in hardness as a result of distortion of the MoS_2 crystal structure, and the resultant hardness reduces

wear which is crucial to coating life (endurance) [174, 207]. A recent experiment specifically on Ni showed that wear is reduced by doping, extending the lifetime of MoS_2 films [212]. This work aims to understand mechanisms of wear reduction in those experimental results through theoretical and atomistic study of Ni-doped MoS_2.

We investigated Ni-doped MoS_2 structures and properties by Density Functional Theory (DFT). MoS_2 can exist in different phases [211]: 2H and 3R bulk, and 1T and 1H monolayers. Friction in MoS_2 involves sliding of layers, and 2H and 3R phases only differ by stacking, *i.e.* sliding followed by rotation. While 2H is the most studied bulk polytype and the predominant naturally occurring one, 3R is also found naturally and has a very similar energy to 2H [211]. Also, it is found that doping may alter the phase: for example, Li intercalation in MoS_2 causes a change from 2H to 1T phase [18] and Nb substitution on Mo favors 3R over 2H [198]. The possibility of alteration in phase due to doping, layer sliding, or the effect of mechanical load in tribology application is a motivation for considering other phases in MoS_2, as well as to assess whether deliberate production of different polytypes could improve performance.

In this paper, we will consider the effect of Ni-doping in MoS_2 polytypes, and investigate changes in local structure, the energetics of dopants at different sites, the possibility of phase changes, and the effect on interlayer interactions. Section 2.3 details our computational approach. Section 2.4 discusses the choice of dopant structures of different polytypes in MoS_2. Section 2.5 presents results on: (a) doping formation energy, (b) effect of doping on crystal structure and local structure, (c) effect on electronic properties (including oxidation states) and (d) effect on the layer dissociation energy. Finally, Section 2.6 concludes to discuss the impact of Ni-doping, experimentally measurable signatures of different doped structures, and a possible explanation for low wear in MoS_2 lubrication.

2.3 Methods

Our calculations use plane-wave density functional theory (DFT) implemented in the code Quantum ESPRESSO, version 6.1 [68, 67]. We used the Perdew-Burke-Ernzerhof (PBE) generalized gradient approximation [164] for all of our analysis except for the doping formation energy which is calculated with Perdew-Wang [165] local density approximation (LDA) functional. With PBE, we used the semi-empirical Grimme-D2 (GD2) [71] Van der Waals correction to the total energy, which gives lattice parameters and other properties considerably closer to experimental results for MoS_2 [163, 72]. Calculation with LDA has also been shown to give accurate lattice parameters [72]. The doping formation energy requires the energies of metal solids such as Ni and Mo which are not well described by PBE+GD2 [8], and therefore we used LDA for these calculations to obtain accurate energies for both metals and doped MoS_2 as in our previous work on 2H-MoS_2 [72]. We used Optimized Norm-Conserving Vanderbilt pseudopotentials [79] parametrized by Schlipf and Gygi [178] from the SG15 set [3] generally, except we used the Pseudodojo set [2] for partial density of states (PDOS), to have available pseudo-wavefunctions; and for LDA, to be consistent with our previous calculations [72]. Kinetic energy cutoffs of 816 eV (60 Ry) for PBE and 1088 eV (80 Ry) for LDA were used. Half-shifted k-point grids of $6 \times 6 \times 2$ for bulk and $12 \times 12 \times 1$ for monolayers (in the pristine case) were chosen to converge the total energies within 0.001 eV/atom. Atomic coordinates were relaxed using a force threshold of 1.0×10^{-4} Ry/bohr and the stresses were relaxed below 0.1 kbar. We used a Gaussian smearing of 0.05 eV for the bulk metals or whenever metallic cases arose. For doped structures, we decreased the k-grid in x- , y- or z-directions in proportion to the supercell size, to maintain consistent Brillouin zone sampling. For density of states calculations, a broadening of 0.02 eV and k-grid sampling of $20 \times 20 \times 1$ for $4 \times 4 \times 1$ monolayers and $20 \times 20 \times 10$ for $2 \times 2 \times 1$ bulk was used.

The doping concentration is varied by putting a single Ni atom in increasing supercells such as $2 \times 2 \times 1$, $3 \times 3 \times 1$, $3 \times 3 \times 2$, etc. All supercells are taken as neutral, as appropriate for neutral impurities or high concentration, though charged impurities are also possible [107]. In the 2H structure, we also considered

tetrahedrally intercalated structures with two Ni atoms per cell, one between each pair of layers, vertically above one another. Our supercells represent not only approximations to a disordered low-doping limit, but also possible ordered phases, as are found for Li intercalation [18]. The Ni atom fraction ranges from a minimum of 0.5% to maximum of 17%. The monolayers contain vacuum of 15 Å between layers to reduce the effect of spurious periodicity. We have tested the monolayers with dipole corrections [19] in case there would be an out-of-plane dipole moment in the doped phases, but the change in total energy was negligible ($\sim 10^{-4}$ eV) and structural parameters were unaffected. Our calculations in general are non-spin-polarized, as use of spin polarization did not significantly change the energy (less than 0.1 meV per atom). However, we used spin-polarized calculations for ferromagnetic bulk Ni, and also for test calculations on each doping case to check for magnetic moments.

Before calculations on doped systems, the structure of 2H-MoS_2 was benchmarked with PBE+GD2 and lattice parameters were calculated as $a = b = 3.19 \pm 0.02$ Å and $c = 12.4 \pm 0.2$ Å. The uncertainties come from a cubic fit to the total energy as a function of the lattice parameters. These results are in good agreement with previous theoretical [107] and experimental work [150]. For the energies of reference elemental phases, bulk Mo and Ni are calculated in body-centered and face-centered cubic lattice of 3.19 Å and 3.52 Å, respectively, with a $12 \times 12 \times 12$ half-shifted k-grid. For bulk S, a unit cell containing 48 atoms [1] is calculated with a $3 \times 3 \times 3$ k-grid. The energies of these reference phases, as in our previous work [72], are used to calculate the doping formation energy.

2.4 Structure and doping site selection

MoS_2 can exist in different possible structures in bulk and monolayer phases (Fig. 2.1) [211]. The known phases of MoS_2 are 1H (hexagonal monolayer), 1T (trigonal monolayer), 2H (hexagonal bulk) and 3R (rhombohedral bulk). For our interest in lubrication applications, we will not consider the 1T phase further due to its metastability and likelihood of converting to 1H. The 1H, 2H and 3R phases

contain 3, 6, and 9 atoms in a conventional unit cell respectively, and they differ by stacking. In 1H, each layer of MoS_2 is stacked exactly above each other (AA stacking). In 2H, the Mo atom in one layer is above an S atom of the preceding one, forming AB stacking, and 3R has ABC stacking with 3 layers per conventional unit cell. In 3R, all layers have the same orientation, but 2H has inversion symmetry between layers. Our DFT calculation (Table 2.1) shows only a small difference in total energy of the 2H and 3R phases in agreement with previous literature [23].

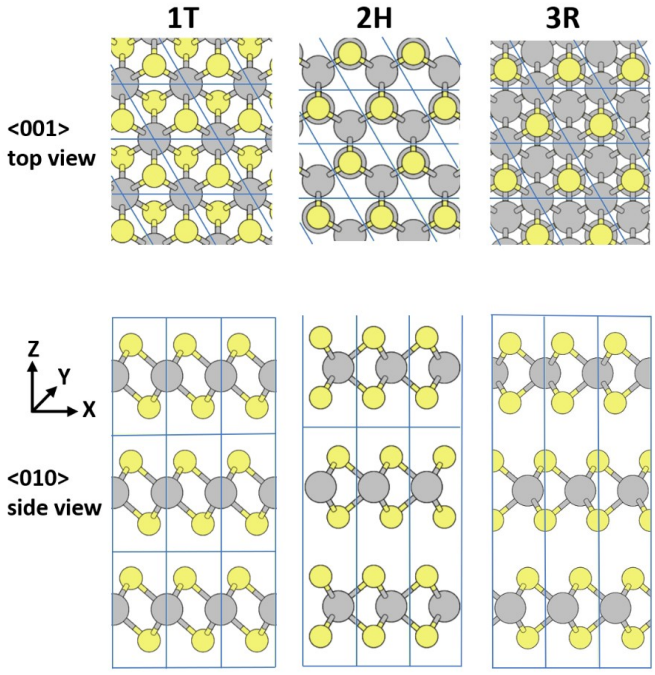

Figure 2.1: Structure of MoS_2 polytypes with conventional unit cell marked by blue lines. Mo is gray and S is yellow. 1H is a single monolayer of MoS_2 containing 3 atoms per unit cell, as in each layer of 2H or 3R. This work studies 1H, 2H, and 3R.

The most probable sites for dopants [72] in MoS_2 include substitutions and intercalations for bulk or adatoms for monolayers, and are shown in Fig. 2.2. We have also considered the bridge site along the Mo-S bond but found that intercalation/adatom in this site was unstable and relaxed to tetrahedral intercalation in 2H and 3R, and Mo-atop in 1H. Therefore the bridge site was not considered in further calculations. We will use these sites to study the various structural and

$E_f - E_{f,2H}$ (eV)	LDA	PBE+GD2
2H	0.00	0.00
1H	0.11	0.15
3R	1.3×10^{-3}	1.2×10^{-4}

Table 2.1: DFT calculation of formation energy per unit of MoS_2 in MoS_2 polytypes, with respect to 2H-MoS_2. The formation energy of 2H with respect to bulk Mo and S is-3.05 eV with LDA (expected to be more accurate) and -2.59 eV with PBE+GD2.

electronic properties of Ni-doped MoS_2.

2.5 Results and discussion

2.5.1 Doping Formation Energy

We begin by establishing which doped structures are energetically accessible, via the doping formation energy, which tells us the energy needed to incorporate the dopant (Ni) into the host system (MoS_2). As noted in our previous work [72], the doping formation energy depends on the chemical potentials during the growth process, and so the relative favorability between different stoichiometries (*e.g.* substitution *vs.* intercalation) depends on the conditions, which can be depicted in a phase diagram (Fig. 2.11). The doping formation energy is calculated as:

$$E_{\text{formation}} = E_{\text{system}} - NE_{\text{pristine}} - \mu_{\text{Ni}} + \mu_{\text{removed}} \tag{2.1}$$

for substitution cases, and

$$E_{\text{formation}} = E_{\text{system}} - NE_{\text{pristine}} - \mu_{\text{Ni}} \tag{2.2}$$

for intercalation cases, where E_{system} is the energy of the doped system, N is the number of cells in the supercell, E_{pristine} is the energy per unit cell of the corresponding phase of MoS_2, and μ_{Ni} and μ_{removed} are the chemical potential of the dopant (Ni) and removed atom, respectively. We consider μ_{Ni} equal to the energy

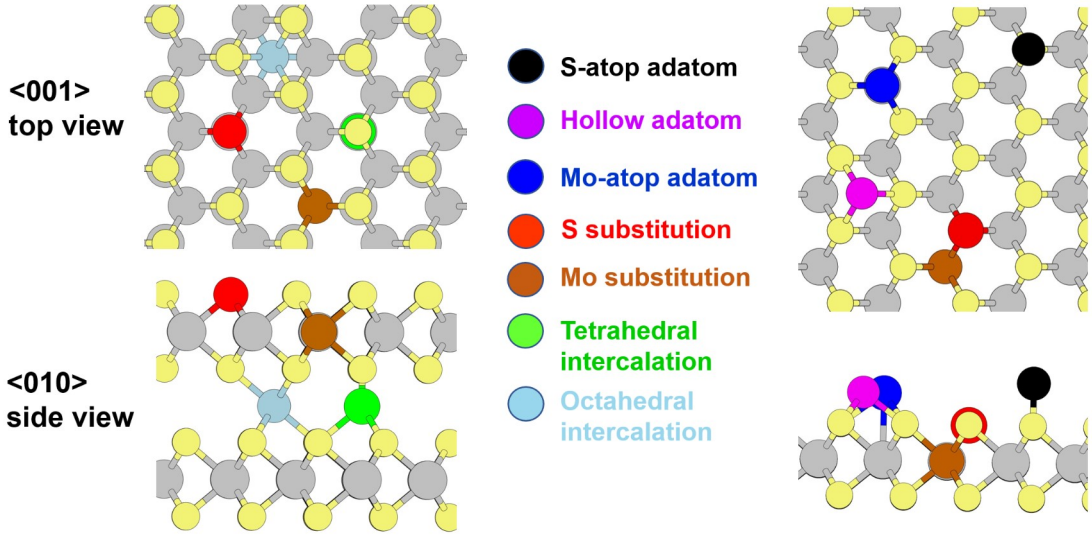

Figure 2.2: Different dopant sites for Ni in 2H (left) and 1H (right) MoS_2 with top view (upper) and side view (lower). Sites include substitution in the Mo site or S site, tetrahedral or octahedral intercalation for bulk phases (2H and 3R), and Mo-atop, S-atop and hollow adatoms for 1H (monolayer). 3R sites are similar to 2H (see detail in Fig. 2.4).

per atom of bulk Ni ("Ni-rich" conditions). For substitution cases, we consider equilibrium conditions for the given phase where $\mu_{\mathrm{Mo}} + 2\mu_{\mathrm{S}} = E_{\mathrm{pristine}}/N_{\mathrm{f.u.}}$ and $N_{\mathrm{f.u.}}$ is the number of MoS_2 units per pristine cell; then we look at conditions where either $\mu_{\mathrm{Mo}} = E_{\mathrm{Mo}}$ ("Mo-rich," which favors S substitution) or $\mu_{\mathrm{S}} = E_{\mathrm{S}}$ ("S-rich", which favors Mo substitution). These energies of Mo and S are calculated from their bulk phases, as in previous literature [92, 43, 72]. For example, in $2 \times 2 \times 1$ Mo substitution by Ni in 2H, E_{system} is the energy of $NiMo_7S_{16}$, N is 4, μ_{removed} is the chemical potential of bulk Mo, and E_{pristine} is the energy of Mo_2S_4. Similarly in $4 \times 4 \times 1$ Ni intercalation in 2H, E_{system} is the energy of $NiMo_{32}S_{64}$ and N is 16.

Monolayer: 1H

The doping formation energies for Ni-doped MoS_2 in the 1H phase with Mo or S substitution and different adatom sites (Fig. 2.2) were computed with supercells from $2 \times 2 \times 1$ to $4 \times 4 \times 1$. Fig. 2.3(a) shows results for adatoms in $4 \times 4 \times 1$

supercell. The Mo-atop adatom is the energetically favored adatom site and this result, along with the bond lengths, agrees with previous literature [241]. Fig. 2.3(b) shows the substitutional doping formation energy under Mo-rich and S-rich conditions. The doping formation energy for substitutional doping remains positive even in the most favorable conditions, indicating that substitutional doping may not be achieved at equilibrium conditions. At higher doping concentrations, the doping formation energy is reduced slightly but remains positive (Fig. 2.10 (b-c)).

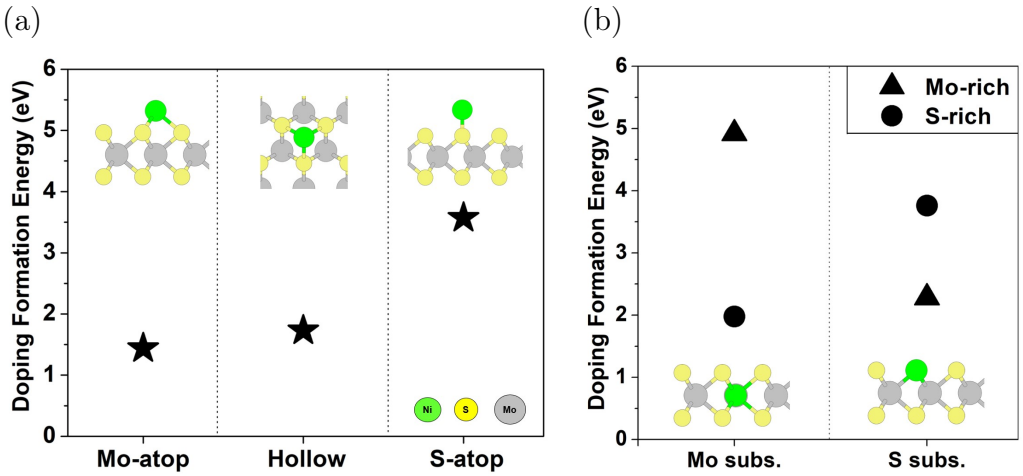

Figure 2.3: Doping formation energies from LDA for a $4 \times 4 \times 1$ supercell of monolayer 1H: a) adatoms, and b) substitution, under Mo-rich and S-rich conditions (which do not affect the value for adatoms). Insets show corresponding structures (side or top view).

Bulk

Bulk systems have intercalation rather than adatoms. In 2H, tetrahedral intercalation is energetically favored over octahedral intercalation at all concentrations. The tetrahedral intercalation site is Mo-atop and S-atop with respect to the layers on the either side as shown in Fig. 2.4, whereas octahedral intercalation consists of hollow sites on each layer. In 3R, we find three metastable intercalation cases. There are two sites with tetrahedral geometry: in one, the Ni atom is Mo-atop for one layer and S atop for the other ("Mo/S-atop"); in the second, the Ni atom is at

the hollow site for one layer and Mo-atop for the other ("hollow/Mo-atop"). The third intercalation site has trigonal pyramidal geometry and is Mo-atop for one layer and bridge site for the other; this site is only stable for supercells larger than $1 \times 1 \times 1$. Octahedral intercalation is unstable in 3R and generally relaxes to the trigonal pyramidal structure. The Mo/S-atop tetrahedral intercalation (similar to 2H tetrahedral intercalation) is the most favored intercalation site (Fig. 2.4 and Table 2.8). These most favorable sites in bulk phases are clearly related to energetics in the 1H phase. As discussed in Section 2.5.1, adatom on Mo is the most favorable site in 1H and all the most favored sites in bulk (2H and 3R) involve Mo-atop. The intercalant acts as an adatom for the neighboring layers and lower doping formation energy is achieved if the intercalant site resembles the monolayers' lowest-energy adatom sites. Doping formation energies for substitutions in 2H and 3R are similar to 1H, except that Mo substitution can be favorable under S-rich conditions for 2H and 3R in some cases (Table 2.5), such as $1 \times 1 \times 1$ (which would mean NiS_2 for 1H) or other $1 \times 1 \times N$ supercells of 1H.

Concentration Dependence of Doping Formation Energy

We can extrapolate defect energies to the low concentration limit as a function of inverse volume ($1/V$) according to the scheme of Makov and Payne (based on behavior of both local strain and electrostatics) [146]. We use this method for the doping formation energy and show results for the 2H phase in Fig. 2.5. The doping formation energies for each polytype and concentration are tabulated in Tables 2.5-2.9. Variation in doping formation energy is small along the z-axis ($1 \times 1 \times N$ and $2 \times 2 \times N$) in all cases, expected due to weak interaction between layers. This finding indicates the energetics of doped bilayers are similar to bulk. The doping formation energy for in-plane supercells depends significantly on the size for small supercells ($N \times N \times 1$ and $N \times N \times 2$), but converges at high supercell size. The limit of low doping concentration can be estimated by extrapolation to $1/V = 0$ from the last two points (red line in Fig. 2.5) as tabulated in Table 2.10. Low doping concentration calculations involve increasingly large number of atoms and it is more efficient to extrapolate.

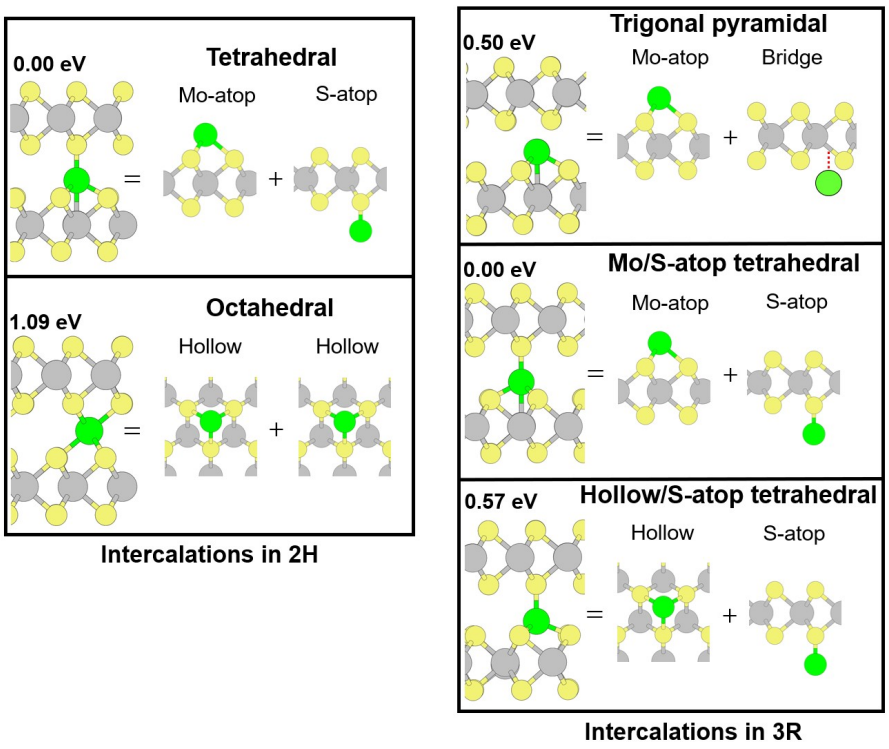

Figure 2.4: Intercalation structures in 2H and 3R $4 \times 4 \times 1$ supercells, classified by bonding geometry and compared to adatom sites with respect to each layer. Mo/S-atop tetrahedral sites are the most favorable for both 2H and 3R, consistent with Mo-atop as the lowest-energy adatom site on 1H. Doping formation energies from LDA are shown relative to the most stable structure.

The energy changes with concentration are due to interaction between dopants, and so the results demonstrate that that in both 2H (Fig. 2.5) and 3R (Fig. 2.9), Mo substitution has the most interaction, S substitution less, and intercalations very little. The negligible Ni-Ni interaction in intercalations is also seen by the fact that doubly intercalated 2H structures (one Ni between each pair of layers) have almost the same doping formation energy as the ones with one Ni per cell (Table 2.7). In the monolayer, the difference in doping formation energy with increase in supercell sizes is considerably smaller (a few tenths of an eV) than in bulk, except for the case of the S-atop adatom (Fig. 2.10 and Table 2.9).

When we compared the total energy with different supercell sizes but the same number of MoS_2 units, we found a significant difference ($\sim$1 eV) for smaller super-

cells ($1\times1\times4$ vs $2\times2\times1$) but much less ($\sim$0.2 eV) with larger supercells ($4\times4\times1$ vs $2\times2\times4$). This variation arises from the spatial arrangement of dopant atoms and can be thought as micro-clustering of dopants or the effect of local ordering of dopants. The reduction in differences at low doping can be clearly observed in the extrapolated lines in Fig. 2.5 where the doping formation energies are closer for different supercells of the same volume.

Next, we compared the energy difference between doped 2H and 3R to look for the possibility of phase changes. To compare directly the energy of doped 2H and 3R structures, we compared $2\times2\times2$ for 3R and $2\times2\times3$ for 2H, supercells with 24 units of MoS_2. We also compared supercells from the primitive cell of 3R that contains only one MoS_2 unit, $1\times1\times2$ and $2\times2\times2$ *vs.* $1\times1\times1$ and $2\times2\times1$ of 2H. Energy differences are shown in Fig. 2.5(d). Recall that pristine 3R is slightly higher in energy than 2H. We find Mo-substituted and S-substituted 3R are lower in energy than 2H at all considered doping concentrations, suggesting a possibility of phase change from 2H to 3R with substitutional doping. In experiment, Mo substitution by Ni was reported to modify the stacking sequence of MoS_2 layers forming 3R [152], consistent with our finding. Similarly, a phase change from 2H to 3R was reported for Nb substitution of Mo in MoS_2 [198]. By contrast, for tetrahedral intercalation, doped 2H is lower than doped 3R (Mo/S-atop) at all considered doping concentrations, further strengthening the stability of 2H over 3R.

We additionally constructed phase diagrams of the stable doping site as a function of chemical potentials μ_{Mo} and μ_{S}, for each polytype, as we did previously for 2H-MoS_2 [72]. These phase diagrams (Fig. 2.11) allow us to identify which doped structures can form in equilibrium and which are compatible with stability of the corresponding pristine structure. The 1H diagram is similar to 2H, with a shift to higher chemical potentials, and the Mo-atop adatom site is favored in the pristine stability region. The 3R phase diagram also closely resembles the 2H one [72], and only the Mo/S-atop intercalation is compatible with pristine stability, except at the highest doping levels. The other doping sites are predicted to be accessible only out of equilibrium.

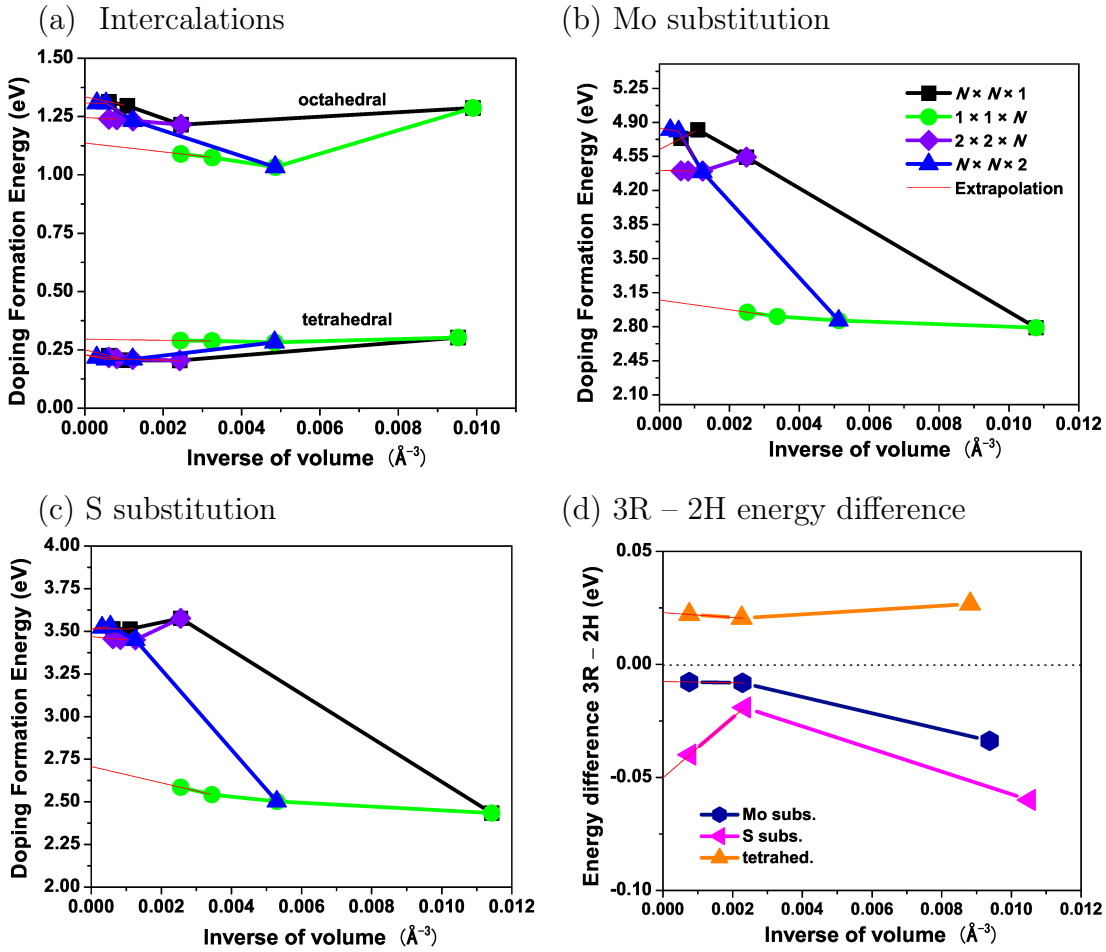

Figure 2.5: Doping formation energy from LDA in Ni-doped 2H-MoS_2 with respect to volume per Ni atom, in a) intercalations, b) Mo substitution (under Mo-rich conditions) and c) S substitution (under S-rich conditions). For S-rich conditions, (b) is shifted down by 3.06 eV; for Mo-rich conditions, (c) is shifted down by 1.53 eV. N is the parameter for the supercell size. Tetrahedral intercalation is favored over octahedral by a fairly constant amount. Red lines show extrapolation from the last two points (not always well converged yet) to the low-doping limit, achieved much more rapidly for the z-varying supercell series. d) Energy difference per Ni atom between Ni-doped 2H and 3R structures.

2.5.2 Structural parameters

Incorporating Ni into MoS_2 not only changes the energy, but also can cause local changes in structure (bond lengths and lattice parameters), which can be useful for experimental identification of the structure. Studying bonding also helps understand interlayer interactions and sliding. The maximum difference in Ni-S and Ni-Mo bond lengths with respect to the pristine Mo-S bond length is around 8% for the highest doping concentration in substitution sites. Mo-S bond lengths away from the doping site were very close to the pristine Mo-S bond (differing by less than 0.04 Å), showing only a local effect on the structure. For the $1 \times 1 \times 1$ supercell of 2H, the Ni-S bond length decreased *vs.* the pristine Mo-S bond length, and the Ni-Mo bond in S substitution increased, as shown in Table 2.2. The bond lengths for substitutional doping in all 2H and 3R structures are consistent with a covalent bond, judging by the covalent radii (Mo = 1.54 Å, Ni = 1.24 Å, S = 1.05 Å) [34]. Tetrahedral intercalation also shows covalent bonds, in agreement with our previous results based on electron density [72]: the Ni-S, and even Ni-Mo, bond lengths are far lower than the sum of Van der Waals radii (S = 1.81 Å [9], Ni = 1.97 Å [14] and Mo = 2.16Å [14]). For comparison, the S-S distance between pristine MoS_2 layers is 3.59 Å which is close to the sum of the Van der Waals radii of two S atoms. For a concentration less than 1% of Mo substitution in both 2H and 3R, we found only 4 Ni-S bonds instead of 6, breaking the symmetry in a pseudo-Jahn-Teller distortion. A similar five-fold coordination was calculated [77] for Ni substituting Mo at a 2H basal plane surface, attributed to population of anti-bonding *d*-orbitals by extra charge from Ni. Four-fold coordination like our result was reported in a previous theoretical calculation for Mo-substituted 2H-MoS_2 in few-layer nanosheets [38].

The 1H monolayer showed structural effects similar to the 2H phase. In Mo substitution, the Ni-S bond is decreased and in S substitution the Ni-Mo bond is increased, for all supercells considered. The bond lengths are close to the sums of covalent radii except for the S-atop case (1.96 Å), which is considerably shorter, presumably due to the fact that Ni is forming only one bond.

Results on lattice parameters are summarized in Table 2.3 for $2\times2\times1$ supercells.

Pristine **Mo-S=2.41** Å	**2H** (1 × 1 × 1)	**2H** (4 × 4 × 1)	**3R** (1 × 1 × 1)	**3R** (4 × 4 × 1)	**1H** (4 × 4 × 1)	**Covalent radii sum**
Ni-S (Mo subs.)	2.23 Å	2.23 Å	2.25 Å	2.24 Å	2.34 Å	2.29 Å
Ni-Mo (S subs.)	2.67 Å	2.55 Å	2.58 Å	2.55 Å	2.51 Å	2.78 Å
Ni-S (Intercal./adatom)	2.15 (2.17) Å	2.16 (2.10) Å	2.18 (2.16) Å	2.16 (2.10) Å	2.12 Å	2.29 Å

Table 2.2: Comparison of Ni bond lengths in Ni-doped MoS_2 polytypes, from PBE+GD2. The lowest-energy intercalation and adatom structures are considered. For 2H/3R tetrahedral intercalation, the 3 equivalent Ni-S bonds' length is listed first, followed by the 4th one (see Fig. 2.4).

The change in plane (a and b) was small (less than 2%) for all doping sites and polytypes. However, the c-parameter out of plane decreases slightly in the 2H and 3R phases in substitutional cases. In intercalations, the c-parameter was reduced slightly, though perhaps not significantly (within error bars). This is notable because intercalations are usually expected to increase the c-parameter due to Van der Waals interaction with the intercalant [223, 18]. However, as we previously showed, intercalated Ni forms covalent bonds [72], resulting in little or no change in interlayer spacing on intercalation. We present an error bar in c-parameters in Table 2.3 due to the insensitivity in total energy change in the c-direction with weak Van der Waals interactions (not observed along the stronger-bonded a- and b-directions). This error bar is calculated by parabolic fitting of the total energy per MoS_2 vs c and finding the range where the energy is within 0.01 eV of the minimum. As we lower the doping concentration, lattice parameters necessarily converge towards the pristine value, as the effect of a single Ni atom is diluted among pristine surroundings.

We have also analyzed the vertical displacement of atoms in an Mo or S plane. We find rough planes in Mo substitution that could reduce the effective contact area, resulting in a lower coefficient of friction. Fig. 2.6 shows the planes of Mo atoms under Mo substitution by Ni in the 2H phase. The Mo plane containing Ni has an uneven surface where the maximum displacement of an Ni atom is 0.24 Å and the maximum displacement of an Mo atom is 0.10 Å with respect to the pristine plane, occurring mostly for nearest neighbors of Ni. The two S planes sandwiching the substituted Mo plane also have uneven surfaces: S atoms near to

Ni were displaced up to 0.22 Å towards the Mo plane. In S substitution, only the Ni atom was significantly displaced, while the shift was negligible for all atoms in their respective planes. For all substituted structures, the planes of Mo and S in the unsubstituted layer are smooth and have negligible displacements. Intercalations also showed negligible displacements in Mo or S planes.

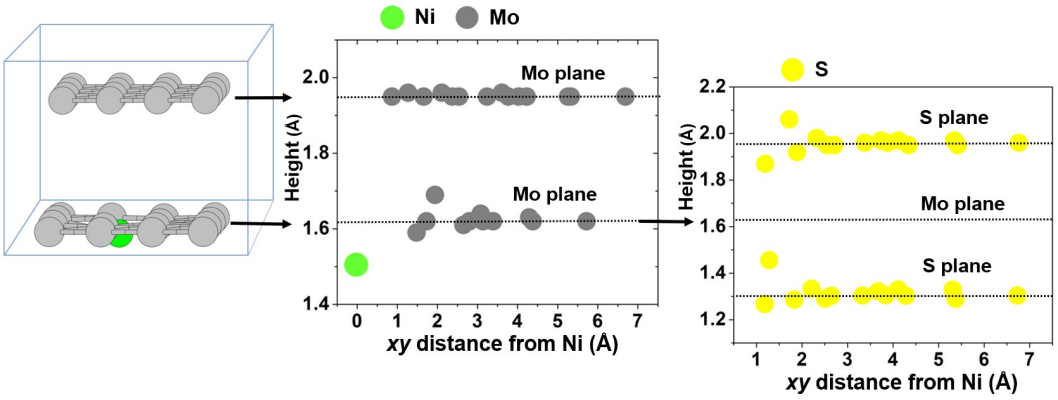

Figure 2.6: Vertical atomic displacements (from PBE+GD2) in a $4\times4\times1$ supercell of Mo-substituted 2H-MoS_2, with planes shifted vertically to show changes clearly. Blue arrows point to the plotted heights of the Mo planes. Center: height of atoms with respect to pristine, indicated by green and purple dotted lines. Right: the two S-planes sandwiching the Mo-plane containing Ni. Most changes in height are observed close to the Ni-atom.

These structural results can be a guide to identifying the doping site in Ni-doped MoS_2. Small expansion or unaltered interlayer spacing, which can be detected by X-ray diffraction [152] or atomic force microscopy measurements [121], indicates the presence of intercalants. The contraction of interlayer spacing indicates substitutional doping, consistent with recent experimental work on Ni-doped MoS_2: Mosconi *et al.* [152] found layer contraction in a sample believed to have Mo substitution. Thin films made under an excess of sulfur [66], which favors Mo substitution [72], were found to have a layer contraction increasing with Ni concentration, and also an increasing nanoscale roughness, consistent with our results. Lieber and Kim [121] interpreted lack of change in the in-plane lattice in atomic force microscopy (AFM) measurements of Ni-doped MoS_2 as indicative of Mo sub-

System	c **(2H)**	a **(2H)**	c **(3R)**	a **(3R)**	a **(1H)**
Pristine	12.4 ± 0.1	3.19	18.5 ± 0.1	3.19	3.19
Mo subs.	12.3 ± 0.1	3.20	18.4 ± 0.1	3.20	3.21
S subs.	12.2 ± 0.1	3.17	18.3 ± 0.1	3.18	3.15
Intercal./ adatom	12.5 ± 0.2 (tetrahed.)	3.19	18.7 ± 0.2 (Mo/S-atop tetrahed.)	3.20	3.20 (Mo-atop)
Intercal./ adatom	12.4 ± 0.2 (octahed.)	3.19	18.5 ± 0.2 (trigon. pyram.)	3.19	3.19 (S-atop)

Table 2.3: The lattice parameters a and c (all in Å) from PBE+GD2 for different polytypes and doping cases, in a $2 \times 2 \times 1$ supercell. In all cases $a = b$. The lattice parameters are expressed in terms of the conventional unit cell of the pristine phases. See text for definition of c error bar. Only substitutional doping decreases the c-parameter whereas the intercalations lie mostly within the error bar of pristine and the mean values indicate little or no expansion along c. Monolayer 1H does not have a c-parameter.

stitution, but our results shows little change in a in any case. Instead, from our results, we propose that Mo or S substitution can be distinguished by observing contracted Ni-S bonds (Mo substitution) or elongated Mo-Ni bonds (S substitution) via transmission electron microscopy (TEM), scanning tunneling microscopy (STM), or extended X-ray absorption fine structure (EXAFS). Thus, these results may be useful to experimentalists to characterize the Ni location in MoS_2.

2.5.3 Electronic properties

We studied the electronic properties to find observable signatures of the doping site, as well as to identify effects of Ni-doping that may be useful for electronic applications. When undoped, 1H is a direct-gap semiconductor, and 2H and 3R are indirect-gap semiconductors [107, 35]. The density of states for pristine MoS_2 polytypes is shown in Fig. 2.14. We find that Mo substitution makes bulk phases (2H and 3R) metallic, as shown in Fig. 2.7 and Fig. 2.13. The partial density of states (PDOS) reveals that such metallic character arises due to contributions at the Fermi level from d orbitals of Mo and Ni and p orbitals from S – not from Ni alone as one might expect. S substitution and intercalations in 2H and 3R preserved the semiconducting gap. In the 1H monolayer, Mo substitution showed a single in-gap state whereas S substitution showed two in-gap states at the band edges as shown in Fig. 2.7(c)-(d). Adatom systems are semiconducting; S-atop has a deep in-gap state, and Mo-atop and hollow have an in-gap state close to the valence band (Fig. 2.12). These in-gap states are due to d-orbitals of Mo and Ni and p-orbitals from S, as in 2H substitution. Zhao *et al.* [240] similarly reported two in-gap states at the band edges for S-substituted 1H. All the adatom cases in 1H showed semiconducting behavior.

These results are relevant for possible applications: the in-gap states could be useful for optoelectronic applications such as quantum emitters [167, 180]. The metallic Mo-substituted 2H-MoS_2 could be used as an electrode for electrochemical energy storage devices, as semiconducting pristine 2H-MoS_2 is not an ideal electrode material [4] and attempts have been made to enhance electrical conductivity by forming hybrid electrodes [37, 87]. The metallic nature for 3R also

suggests suitability of Ni substituting Mo as an active site for catalysis, as is well established for 2H [76]. The conductivity of Mo-substituted 2H- or 3R-MoS_2 could be identified by transport measurements or STM as a way of determining the doping site, in conjunction with the characteristic structural parameters mentioned in the previous section. Indeed, a recent study [66] grew Ni-doped MoS_2 under S-rich conditions, which favors Mo substitution [72], and found decreasing resistivity with Ni concentration, consistent with our results.

The oxidation state of Ni, as measured by X-ray photoelectron spectroscopy (XPS), has been used to infer the location of doping by transition metals [206] in MoS_2. For example, XPS has found Ni^0 and Ni^{2+} in Ni-doped 2H-MoS_2 [109], which could be assumed to represent intercalation and Mo substitution. The relation between oxidation states and local charges in *ab initio* calculations is not simple, but to investigate this issue, we first computed local charges on each atom by Löwdin charges [139] (similar to an integration of the PDOS) and found only small changes in local electron numbers for Mo and S in doped MoS_2 compared to pristine. In 2H, Ni has the most partial positive charge in Mo substitution ($+0.75e$), followed by intercalations ($+0.52e$) and S substitution ($+0.38e$) as least positive. We find only a small dependence on supercell sizes, and similar results for 1H as for 2H, which does not suggest detectable differences in XPS. On the other hand, we also tried the more advanced method of Sit *et al.* [186] for assigning oxidation states based on d-orbital occupations from spin-polarized DFT+U calculations, using U values of 5.5 eV for Ni [244] and 4 eV for Mo [221]. We found an oxidation state of Ni^{4+} in Mo substitution at high Ni concentrations in 2H (>16%), 3R (>11%), and 1H (>8%); lower concentrations showed Ni^{2+} in 1H, 2H, and 3R. S substitution and intercalations/adatoms showed Ni^{2-} in all polytypes. By contrast, the oxidation state for Mo could not be unambiguously assigned in this approach for either pristine or doped systems. These results indicate XPS can help detect Ni-doping sites, and are consistent with the idea of Ni^{2+} for Mo substitution, though we find the unusual Ni^{2-} for intercalation and adatoms instead of Ni^0 which has been previously expected. We compared DFT+U results for the density of states and did not observe any significant differences with respect to

results without U.

We also checked the presence of magnetic moments. While bulk Ni is ferromagnetic, the magnetism is itinerant, not localized on Ni, and therefore adding Ni dopants does not typically cause magnetism. All Ni-doped 2H and 3R structures are non-magnetic. Total magnetic moments per cell in Mo-substituted 1H were 3.99 μ_B for a $4\times4\times1$ supercell, in accordance with a previous calculation [244], and 3.62 μ_B for a $3 \times 3 \times 1$ supercell. No other doped 1H cases showed magnetization.

(a) Mo substitution in 2H ($2 \times 2 \times 1$) (b) Partial density of states for (a)

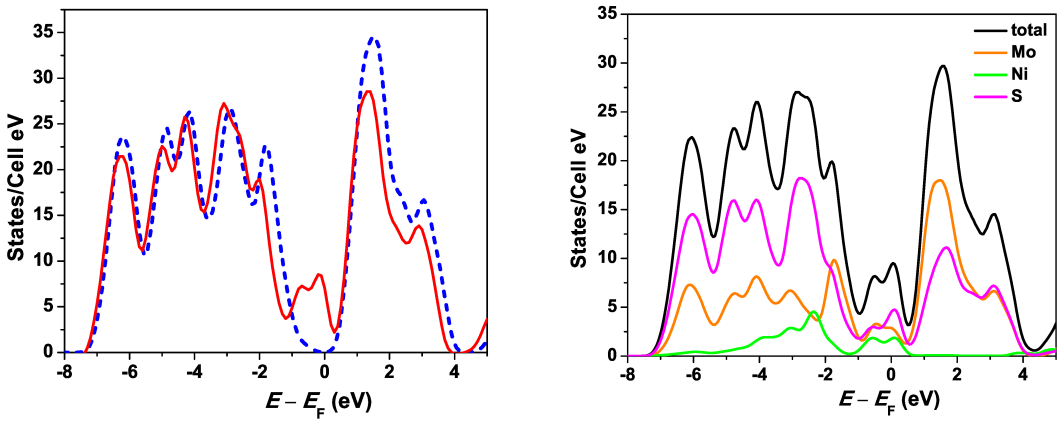

(c) Mo substitution in 1H ($4 \times 4 \times 1$) (d) S substitution in 1H ($4 \times 4 \times 1$)

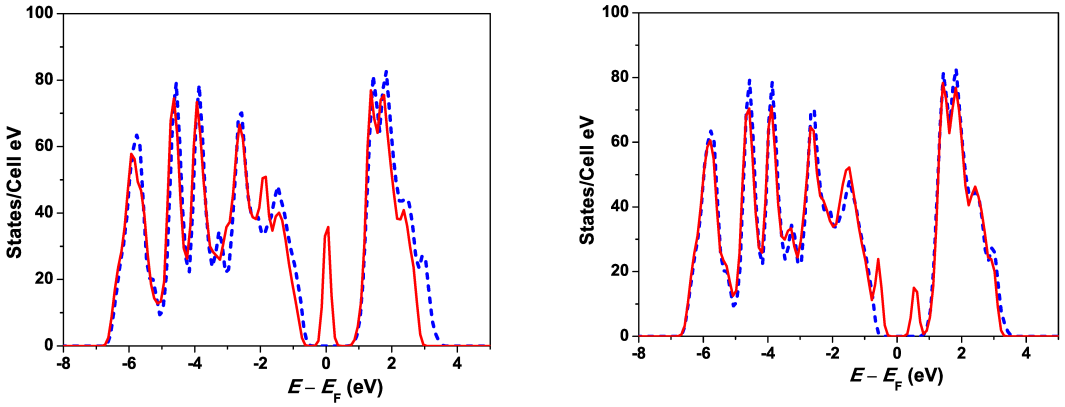

Figure 2.7: Density of states for doped 2H and 1H structures, from PBE+GD2. The blue dotted curves in (a), (c), (d) are the pristine density of states. (b) shows the partial density of states for 2H with Mo substitution. Around the Fermi level, we find (a) metallic behavior, (c) one in-gap state, and (d) two in-gap states.

2.5.4 Layer dissociation energy

The layer dissociation energy is defined as the energy required to dissociate MoS_2 into separate layers, as used in the work of Mounet *et al.* [155] to identify exfoliable compounds from a large database. We study the layer dissociation energy to assess how interlayer interactions change with doping and gain insight into the

likelihood of wear in solid lubrication. The layer dissociation energy for pristine 2H- and 3R-MoS_2 is calculated as

$$\Delta E_{\text{pristine}} = N E_{\text{1H-pristine}} - E_{\text{bulk-pristine}} \tag{2.3}$$

where $\Delta E_{\text{pristine}}$ is the layer dissociation energy for pristine, N is the number of layers in a bulk system, $E_{\text{1H-pristine}}$ is the energy of the monolayer of equivalent size used in $E_{\text{1H-doped}}$, and $E_{\text{bulk-pristine}}$ is the energy of the undoped bulk system. Similarly, the layer dissociation energy for the doped system is given by:

$$\Delta E_{\text{doped}} = E_{\text{1H-doped}} + (N-1)E_{\text{1H-pristine}} - E_{\text{bulk-doped}} \tag{2.4}$$

where $E_{\text{1H-doped}}$ is the energy of the doped monolayer of equivalent size and structure as used in $E_{\text{1H-pristine}}$, and $E_{\text{bulk-doped}}$ is the energy of the doped bulk system. To illustrate this, consider the $2 \times 2 \times 2$ supercell of 2H with Mo substitution by Ni. Here, $N = 4$, $E_{\text{bulk-pristine}}$ is the energy of $2 \times 2 \times 2$ undoped MoS_2 ($Mo_{16}S_{32}$), $E_{\text{1H-pristine}}$ is the energy of $2 \times 2 \times 1$ undoped 1H (Mo_4S_8), $E_{\text{1H-doped}}$ is the energy of Mo-substituted $2 \times 2 \times 1$ 1H ($NiMo_3S_8$), and $E_{\text{bulk-doped}}$ is the energy of Mo-substituted $2 \times 2 \times 2$ 2H ($NiMo_{15}S_{32}$). Given these quantities, we define a relative layer dissociation energy by $\Delta E_{\text{rel}} = \Delta E_{\text{doped}} - \Delta E_{\text{pristine}}$ which accounts for changes due to doping and is per Ni dopant atom since all our supercells contain just one Ni atom. The absolute value of the layer dissociation energy in a supercell can be much bigger than the pristine primitive cell's, and so it is more convenient to analyze this relative quantity.

In intercalation cases, we need to consider whether the dopant will remain in place or relax to a more favorable site, as shown in left side of Fig. 2.3. For example, 2H octahedral intercalation consists of two hollow sites with respect to the two layers, and when the layers are dissociated, the dopant may remain as before in the hollow of one layer (adiabatic case), or may relax to the most favorable site, Mo-atop, depending on the thermal energy available to overcome any barrier. ΔE_{rel} is always smaller with monolayer relaxation than in the adiabatic case. In tetrahedral intercalation of 2H, Ni remaining on the layer with S-atop has higher ΔE_{rel} than remaining on the layer with Mo-atop since Mo-atop in monolayer is

more strongly bound (Section 2.5.1): the energy difference between Mo-atop and S-atop in 1H is 1.68 eV and the average difference in ΔE_{rel} in tetrahedral intercalation for Mo-atop and S-atop is 1.70 eV. For comparison, our calculation shows the layer dissociation energy is 0.15 eV per MoS_2 unit in the layer (0.27 N m^{-1}), which is consistent with the result 0.22 N m^{-1} from experiment [202], and $\sim$0.32 N m^{-1} from a more accurate random-phase approximation calculation [21]. We have considered the different doping cases and found that nearly all increase the binding energy in both 2H and 3R, as shown in Fig. 2.8. We also considered higher Ni concentration, *i.e.* Ni between each layer, and found that ΔE_{rel} increased, even though doping formation energy per Ni is similar.

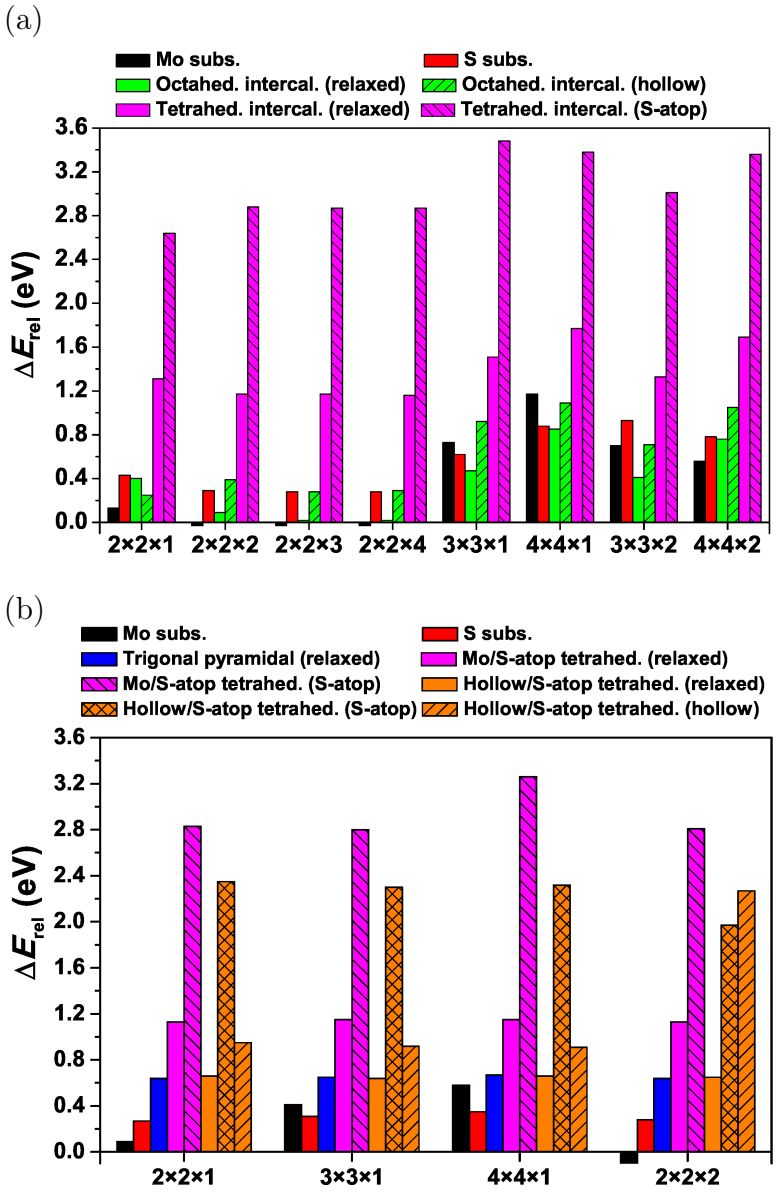

Figure 2.8: (a) Relative layer dissociation energy from PBE+GD2 in (a) 2H-MoS_2 and (b) 3R-MoS_2, for different doping sites and concentrations, showing a general increase in interlayer binding. We consider both adiabatic and relaxed structures of the doped monolayer.

The additional binding between layers is strongest with intercalation while substitution has a lesser effect, consistent with Ni forming covalent bonds between layers [72]. We note that by contrast intercalation with other metals is found

to *reduce* interaction between layers, as inferred from Raman spectroscopy for Li [182] and Ag [184]. In-plane supercell expansion generally increases ΔE_{rel}, suggesting bilayers will give similar results, whereas supercell expansion out of the plane has little effect. Ni-doping strengthens the binding between layers which can explain the experimental report of a reduced low wear rate in Ni-doped MoS_2 [212] compared to pristine. The lower wear rate is an important parameter leading to longer life of MoS_2 material for lubrication application [211]. We may expect a similar trend in a related quantity, the work of adhesion, which is defined as the energy needed to divide the material in two, whereas the layer dissociation energy involves splitting apart all the layers. Pastewka *et al.* [162] have argued that a larger work of adhesion increases contact area, which would be expected to increase the coefficient of friction, though this may be offset by the increase in atomistic roughness in doped layers.

Comparing tetrahedral intercalation (the most favorable structure for 2H and 3R), we see 3R has a higher layer dissociation energy in most cases, by 0.04 eV on average. The two structures have similar structural changes around Ni and a similar trend in doping formation energy. The doping formation energy and total energy have only a small difference between 2H and 3R tetrahedral intercalation: 2H is favored by 0.020 eV in doping formation energy and 0.022 eV in total energy. Insofar as the layer dissociation energy is determining the wear rate, we do not expect significant differences in wear between these two phases. Layer sliding simulations for bilayer MoS_2 in 2H and 3R-type configurations found that under load 3R has the less corrugated sliding path, both spatially and energetically, suggesting better lubricant properties [117]. Based on this, Ni-doped 3R may be an attractive target for further lubrication studies, with experimental tests of coefficient of friction and wear.

2.6 Conclusion

In this work, we studied MoS_2 and its different phases by doping with Ni. We found that the most thermodynamically favorable sites for Ni-doping are Mo-atop

Doping site	**Lattice in c–direction**	**Bond length**	**Band gap**	**Ni oxidation state**
Mo subs.	Decreases	Decreases (Ni-S)	Metallic	Ni^{2+}, Ni^{4+}
S subs.	Decreases	Increases (Ni-Mo)	Semiconductor	Ni^{2-}
Intercal.	No change/ small increase	New bonds	Semiconductor	Ni^{2-}

Table 2.4: Summary of experimentally observable structural and electronic signatures of different Ni doping sites in bulk 2H- and 3R-MoS_2. 1H is similar except: c-parameter does not apply, and all sites give semiconductors with in-gap states.

adatom in 1H monolayer, tetrahedral intercalation in 2H bulk, and 2H-like intercalation (Mo/S-atop) in 3R bulk. To help guide experimental identification of these sites and substitutional sites, we calculated structural and electronic signatures of the different sites, summarized in Table 2.4. In bulk phases, irrespective of doping concentration, we found Ni bond length contraction for Mo substitution and expansion in S substitution, *vs.* Mo-S bonds. The bulk lattice parameter out of plane contracted at high concentration of substitutional Ni but was unaltered or expanded for intercalation. The Mo-S bond lengths away from the dopant were close to pristine, and lattice parameters converged to pristine at lower doping concentration indicating that Ni-doping has only a local effect. On the other hand, we also found the possibility of a phase change from 2H to 3R with Mo or S substitution. Mo substitution also induced atomic roughening of the Mo and S planes. While most doped structures were semiconducting, we found that semiconducting 2H and 3R became metallic with Mo substitution by Ni, of interest for electrochemical or catalytic applications, whereas substitution and adatoms in 1H are semiconducting with in-gap states of potential interest for quantum emitters. We find oxidation states characteristic of doping site, which can be probed by XPS: Mo substitution has Ni^{4+} or Ni^{2+}, and S substitution, intercalations and adatoms have Ni^{2-}, for all polytypes. Lastly, we computed the layer dissociation energy where doped MoS_2 shows stronger binding between layers than pristine, particularly for intercalations – in contrast to findings for other transition metals. In conclusion we present local effects on bonding and structural changes, a possibility of phase change, interesting electronic properties upon Ni-doping and finally strongly increased interlayer interactions. This layer dissociation energy relates to improved

lubrication performance lifetime (wear) for doped MoS_2. Our results suggest that the Ni-doped 3R polytype may not have significant differences in wear rate than 2H and we propose further exploration of the friction properties of 3R, along with investigation of potential electronic and optical applications of Ni-doped MoS_2. Our structural and electronic results can be useful for identification of doping sites in Ni-doped samples.

2.7 Acknowledgments

We acknowledge useful discussions with Ashlie Martini and Mehmet Baykara. This work was supported by UC Merced start-up funds and the Merced nAnomaterials Center for Energy and Sensing (MACES), a NASA-funded research and education center, under award NNX15AQ01. This work used computational resources from the Multi-Environment Computer for Exploration and Discovery (MERCED) cluster at UC Merced, funded by National Science Foundation Grant No. ACI-1429783, and the National Energy Research Scientific Computing Center (NERSC), a U.S. Department of Energy Office of Science User Facility operated under Contract No. DE-AC02-05CH11231.

2.8 Supplementary Information

Table 2.5: Doping formation energy (eV) from LDA for Mo substitution under Mo-rich (S-rich) conditions.

Supercell	**2H**	**3R**	**1H**
1×1×1	2.76 (-0.30)	2.78 (-0.27)	-
2×2×1	4.52 (1.46)	4.52 (1.47)	4.65 (1.71)
3×3×1	4.80 (1.74)	4.64 (1.59)	4.91 (1.97)
4×4×1	4.71 (1.65)	4.71 (1.66)	4.92 (1.98)
1×1×2	2.84 (-0.22)	-	
1×1×3	2.88 (-0.18)	-	
1×1×4	2.92 (-0.14)	-	
2×2×2	4.37 (1.31)	-	
2×2×3	4.38 (1.32)	-	
2×2×4	4.38 (1.32)	-	
3×3×2	4.78 (1.72)	-	
4×4×2	4.80 (1.74)	-	

Table 2.6: Doping formation energy (eV) from LDA for S substitution under Mo-rich (S-rich) conditions.

Supercell	**2H**	**3R**	**1H**
1×1×1	0.88 (2.41)	1.32 (2.85)	1.89 (3.36)
2×2×1	2.02 (3.55)	1.99 (3.52)	2.35 (3.82)
3×3×1	1.96 (3.49)	1.93 (3.46)	2.27 (3.74)
4×4×1	1.96 (3.49)	2.04 (3.57)	2.27 (3.74)
1×1×2	0.95 (2.48)	-	
1×1×3	0.99 (2.52)	-	
1×1×4	1.03 (2.56)	-	
2×2×2	1.90 (3.43)	-	
2×2×3	1.90 (3.43)	-	
2×2×4	1.90 (3.43)	-	
3×3×2	1.97 (3.50)	-	
4×4×2	1.97 (3.50)	-	

Table 2.7: Doping formation energy (eV) from LDA per Ni for intercalations in 2H.

Supercell	**Tetrahedral**	**Octahedral**
1×1×1	0.28	1.26
2×2×1	0.18	1.19
3×3×1	0.18	1.27
4×4×1	0.20	1.29
1×1×2	0.26	1.01
1×1×3	0.26	1.05
1×1×4	0.26	1.07
2×2×2	0.19	1.21
2×2×3	0.19	1.21
2×2×4	0.19	1.22
3×3×2	0.18	1.28
4×4×2	0.19	1.28
1×1×1 (with 2 Ni)	0.25	-
2×2×1 (with 2 Ni)	0.17	-

Table 2.8: Doping formation energy (eV) from LDA in intercalations of 3R.

Supercell	**Mo/S-atop tetrahedral**	**Hollow/S-atop tetrahedral**	**Trigonal pyramidal**
1×1×1	0.34	0.85	-
2×2×1	0.22	0.80	0.75
3×3×1	0.23	0.81	0.75
4×4×1	0.25	0.82	0.75

Table 2.9: Doping formation energy (eV) from LDA for adatoms on 1H.

Supercell	**Mo–atop**	**S–atop**	**Hollow**
1×1×1	1.19	2.41	1.76
2×2×1	1.46	3.61	1.77
3×3×1	1.45	3.58	1.74
4×4×1	1.45	3.57	1.73

Table 2.10: Extrapolated doping formation energy (eV) from LDA, for the low-concentration limit as a function of doping site and phase. Linear extrapolations are from the smallest two calculated values of $1/V$ (Fig. 5), which may not be fully converged in all cases. 3R has less sensitivity along the z-direction (due to larger c-parameter) and convergence is achieved with flat slope (shown in Fig. S1). The $N \times N \times 1$ series is similar between 2H and 3R and hence we expect the same for rest of the series. For monolayer 1H, we only have $N \times N \times 1$ due to vacuum along z-direction. Doping formation for substitutions is reported for Mo-rich (S-rich) conditions.

a) 2H

Doping type	$N \times N \times 2$	$N \times N \times 1$	$2 \times 2 \times N$	$1 \times 1 \times N$
Mo subs.	4.82 (1.76)	4.60 (1.54)	4.39 (1.33)	3.08 (0.02)
S subs.	1.98 (3.51)	1.98 (3.51)	2.12 (3.65)	1.15 (2.68)
Tetrahed. intercal.	0.21	0.22	0.37	0.28
Octahed. intercal.	1.29	1.32	1.23	1.12

b) 3R and 1H, all $N \times N \times 1$

Doping type	3R	Doping type	1H
Mo subs.	4.78 (1.73)	**Mo subs.**	4.95 (2.01)
S subs.	2.16 (3.69)	**S subs.**	2.28 (3.75)
Trigonal pyramidal	0.75	**Mo-atop ad.**	1.42
Mo/S-atop tetrahed.	0.28	**S-atop ad.**	3.55
Hollow/S-atop tetrahed.	0.83	**Hollow ad.**	1.70

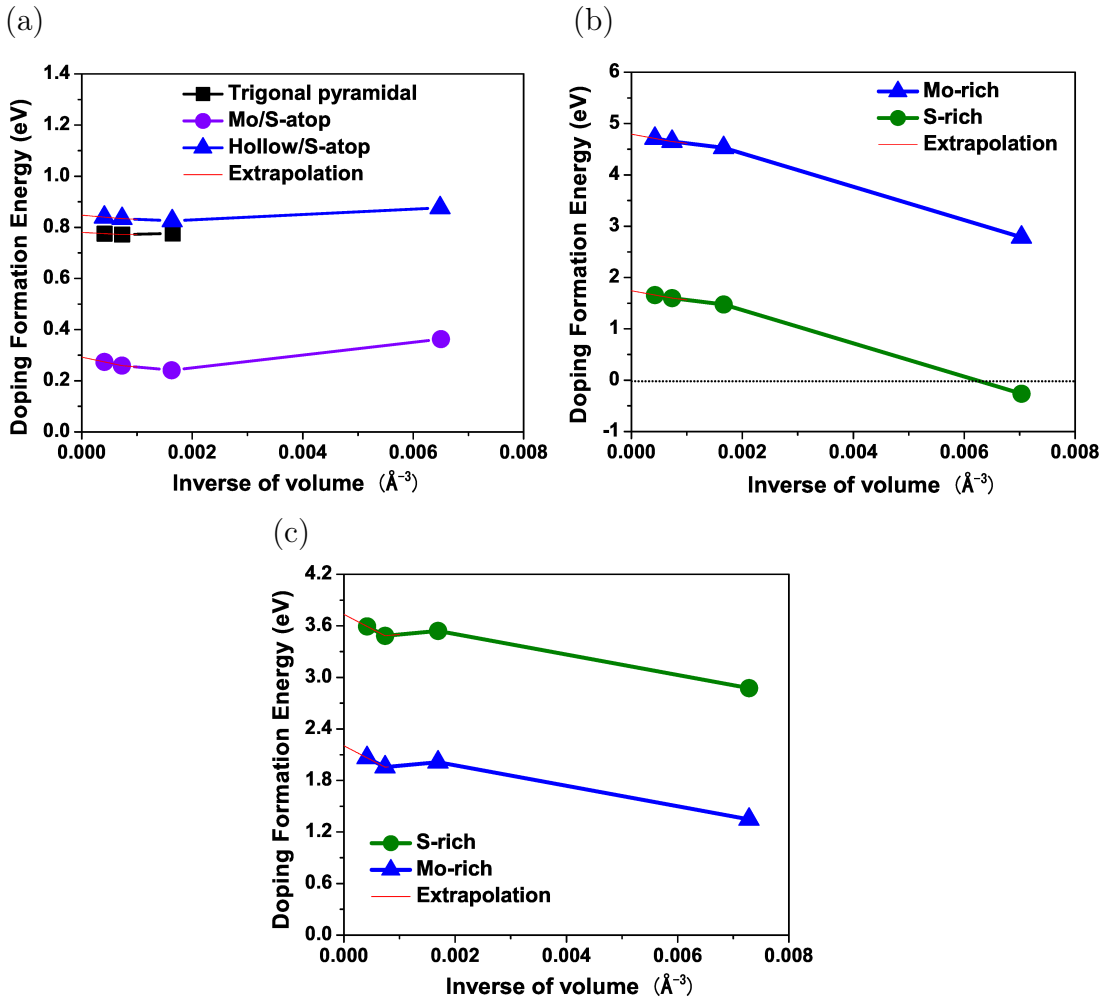

Figure 2.9: Doping formation energy from LDA of 3R-MoS_2: a) intercalations, b) Mo substitution under Mo-rich and S-rich conditions (where it can be negative), and c) S substitution under S-rich and Mo-rich conditions. Trigonal pyramidal for high concentration ($1 \times 1 \times 1$ supercell) is not shown because it is unstable.

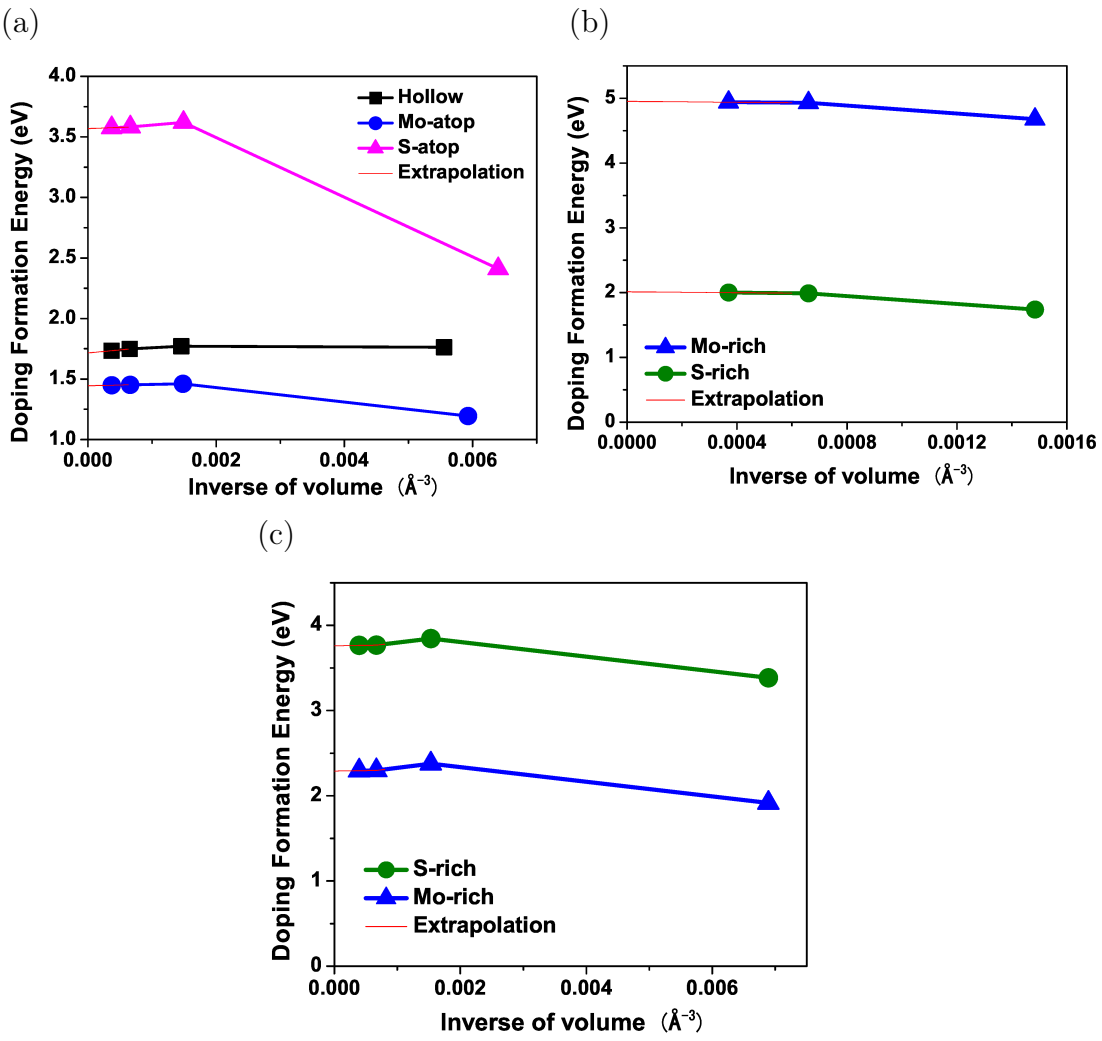

Figure 2.10: Doping formation energy from LDA of 1H-MoS_2: a) adatoms, b) Mo substitution under Mo-rich and S-rich conditions, and c) S substitution under S-rich and Mo-rich conditions.

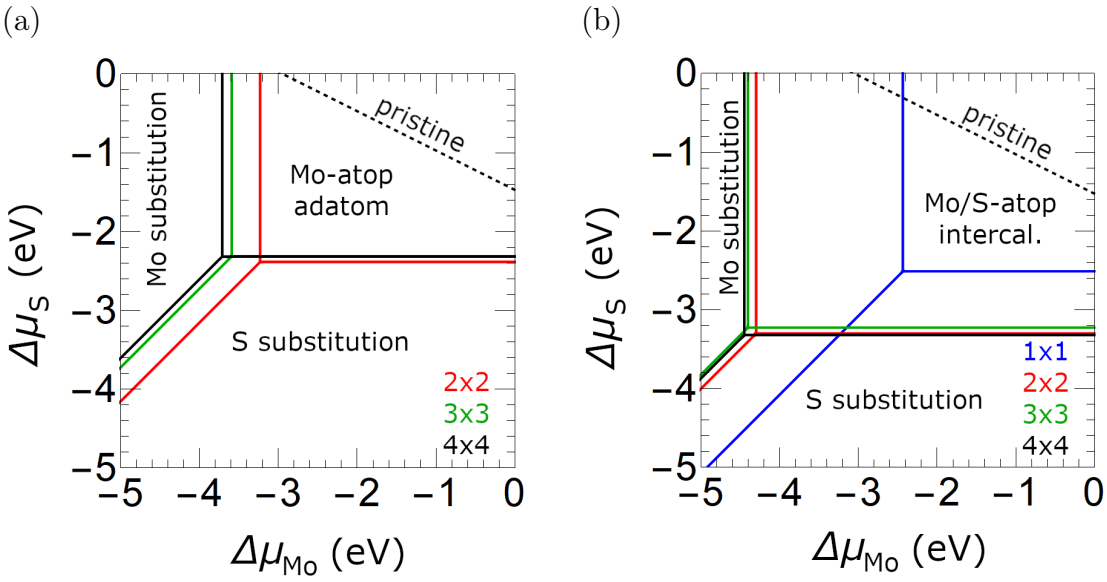

Figure 2.11: Phase diagrams from LDA for a) 1H and b) 3R polytypes, indicating the stable doping site as a function of Mo and S chemical potentials, as in Ref. 17. The pristine phase is stable in the triangle above and to the right of the dotted line.

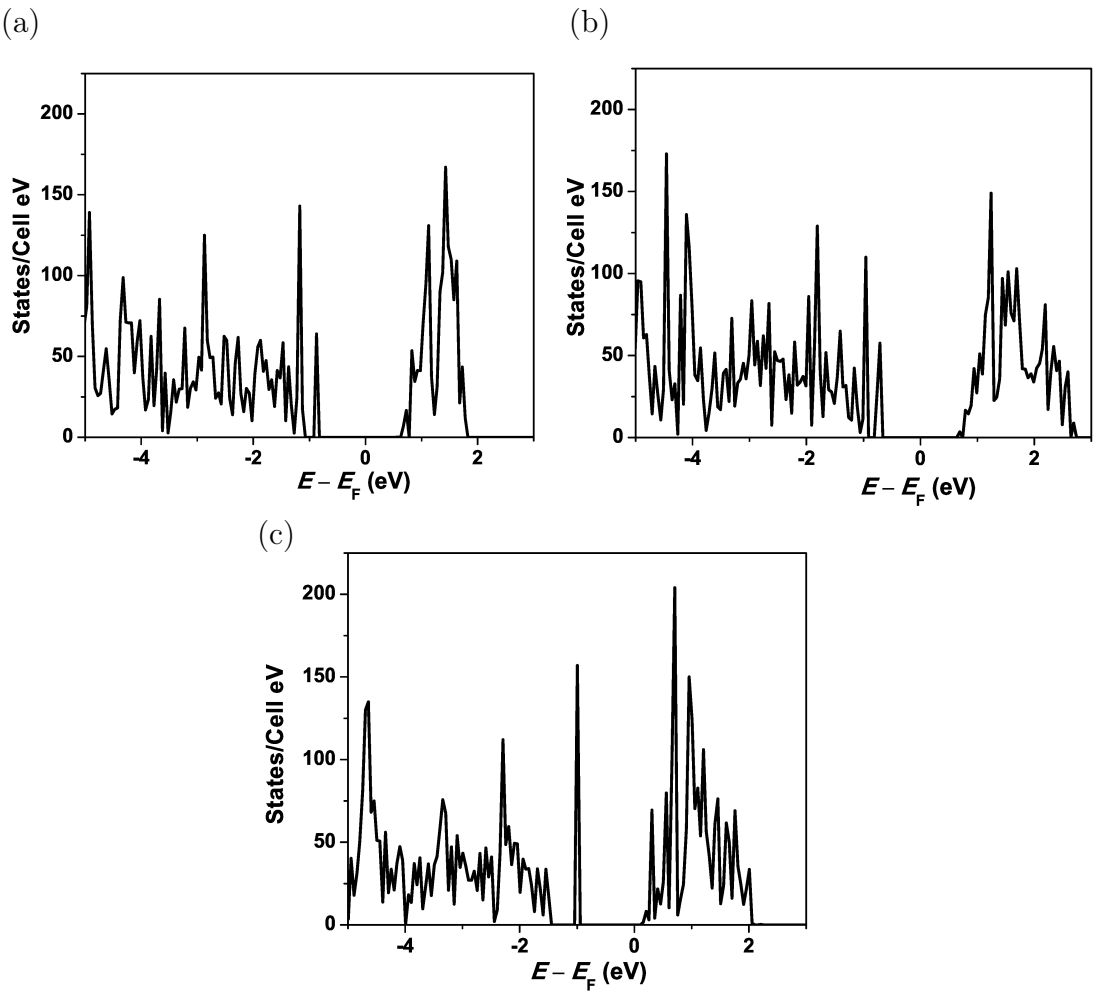

Figure 2.12: Electronic density of states from PBE+GD2 for 1H 4×4×1 structures for a) Mo–atop, b) hollow site, and c) S–atop. A broadening of 0.001 eV was used to show in-gap states.

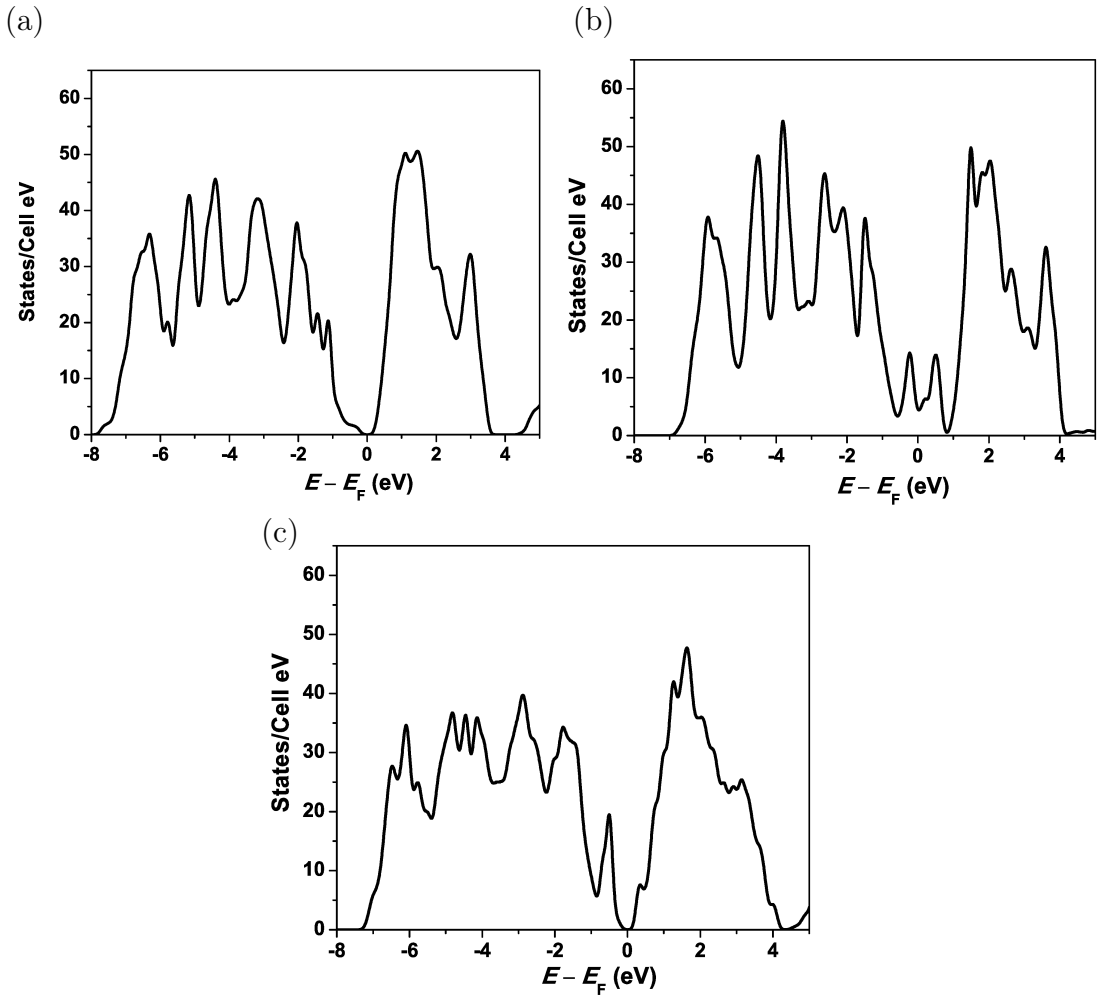

Figure 2.13: Electronic density of states from PBE+GD2 for 3R 2×2×1 structures: a) Mo/S-atop tetrahedral intercalation, b) Mo substitution, and c) S substitution.

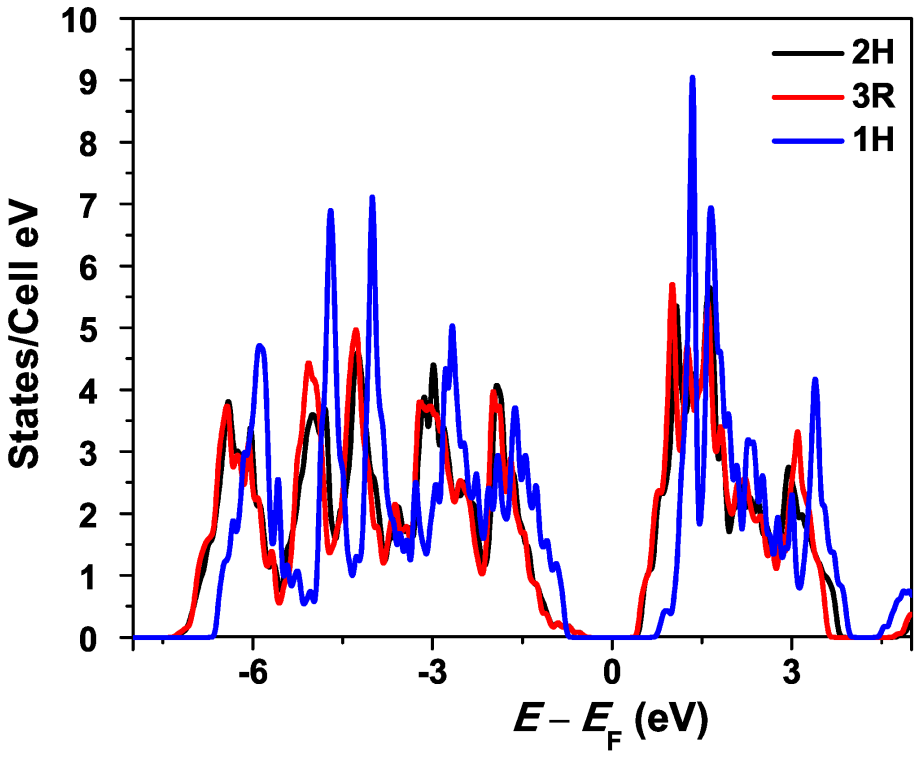

Figure 2.14: Electronic density of states from PBE+GD2 for pristine MoS_2 polytypes, per MoS_2 unit. E_F is taken as the mid-point of band gap in each case. A broadening of 0.002 eV was used to distinctly show gaps for each case.

Chapter 3

Panoply of Ni-doping-induced reconstructions, electronic phases, and ferroelectricity in 1T-MoS_2

This chapter has preprint version in arXiv:2107.07541v2.

3.1 Abstract

Monolayer 1T-MoS_2 has a variety of different distorted phases with distinct electronic properties, with potential applications in optoelectronics, catalysis, and batteries. In this work, we theoretically investigate the use of Ni-doping to generate distorted 1T phases, and find that it can generate the ones usually reported as well as two further phases (3×3 and 4×4), depending on the concentration and the substitutional or adatom doping site. Corresponding pristine phases are stable after dopant removal, offering a potential route to experimental synthesis. We find large ferroelectric polarizations in the pristine phases, associated with vertical corrugation of S atoms. The 3×3 phase is particularly interesting with 100 times greater ferroelectric polarization than the recently measured 1T$''$, a lower energy, and a larger bandgap. Doped phases include exotic multiferroic semimetals, ferromagnetic polar metals, and improper ferroelectrics with only in-plane polarization switchable. The pristine phases have unusual multiple gaps in

the conduction bands, with possible applications for intermediate band solar cells, transparent conductors, and nonlinear optics.

3.2 Introduction

The crystal structure of MoS_2 has several polymorphs – 2H and 3R in bulk, and in monolayers 1H and 1T – which differ by coordination around Mo: 1H has trigonal prismatic coordination in common with 2H and 3R, and 1T has octahedral bonding. 1T is higher in energy, and so most studies of monolayer MoS_2 have focused on the 1H phase. 2H-MoS_2 has shown promise in lubrication, hydrodesulfurization, and optoelectronics. [148, 173, 131, 110] Theoretical and experimental work has shown that doping with Ni and other transition metals in 1H- and 2H-MoS_2 can improve catalytic reactivity [95, 77, 142], lubrication and sliding [100, 211, 103, 73, 5] and gas sensing [141, 206]. 1T-MoS_2 and its well-known distortions to reconstructed phases [242] have recently been shown to have a variety of exciting properties such as topological bands, [171] high nonlinear optical susceptibility, [55] and ferroelectricity [126]. However, much less is known about transition-metal doping in 1T-MoS_2 (recently demonstrated experimentally with Ni [216, 134]) and its potential for modulating structural and electronic properties, in particular how it can interact with these distortions.

1T-MoS_2 shows metallic behavior, uniquely among the polytypes of MoS_2, which are otherwise semiconducting. Applications of 1T-MoS_2 have been explored such as catalysis of the hydrogen evolution reaction [7], supercapacitors and batteries [4, 63] and photocatalysis [44]. Theory [242, 62] and experiments show 1T is unstable and instead is found in more stable distorted phases such as 1T′ (2×1), 1T″ (2×2), 1T‴ $(\sqrt{3} \times \sqrt{3})$, $\sqrt{3} \times 1$, or $2\sqrt{3} \times 2\sqrt{3}$ [159, 188, 83]. (We will mostly use the reconstruction notation $N_a \times N_b$ for clarity.) These distorted 1T phases show interesting properties: 1T′ has been calculated to be a topological insulator [171], 1T‴ has been predicted to be a 2D ferroelectric material [185] and a recent experiment showed a superior hydrogen evolution reaction activity compared to 2H-MoS_2 [74], and 1T″ was recently demonstrated experimentally to be ferroelec-

tric. [126] Moreover, the different stackings of bulk 1T′ has been found to result in topological insulators or nodal-line semimetals, [75] indicating yet another degree of freedom to explore in this family of materials.

Reconstructed 1T phases have been synthesized typically via intercalated alkali metal ions in 2H-MoS_2: Li intercalation and exfoliation leads to formation of 1T′ [48] and 1T″ [47], and synthesis of $KMoS_2$ and deintercalation of K leads to 1T′ and 1T‴. [55] Calculations showed that adsorption of Li on 1H [102], Cu adsorption on 2H [86], and charge doping of 2H [246] or 1T [31] can also lead to 1T′. Other non-doping-related synthesis methods include laser writing on 2H to produce 1T′ regions [151], tensile strain on the corresponding 2H-$MoTe_2$ to produce 1T′-$MoTe_2$, [191] and direct synthesis methods for 1T-MoS_2 in vapor and liquid phases. [188] The variety of 1T-derived phases of MoS_2, the range of remarkable properties they show, and the use of intercalation, adsorption, and charge doping for their synthesis, together suggest the possibility of using other dopants to further explore the potential phase space for 1T reconstructions, searching for novel properties as well as ways to tune or optimize known properties of 1T phases.

In this paper, we perform systematic first-principles calculations to investigate the effect of Ni-doping on 1T-MoS_2 at various concentrations, including substitutions for Mo and S as well as adsorption on different sites. We discover a variety of different reconstructions induced by Ni-doping into 1T-MoS_2, which in many cases are retained even when the Ni atoms are removed or replaced, and include two phases not previously reported. This panoply of phases is found to have unique electronic, magnetic, and ferroelectric properties, thus showing that transition-metal doping can be a computational – and perhaps synthetic – approach to produce interesting new reconstructed phases of 1T transition-metal dichalcogenides.

3.3 Methods

Our calculations use density functional theory (DFT) in the plane-wave pseudopotential code Quantum ESPRESSO [67]. Further details are given in SI Sec. 1. We use the PBE exchange-correlation functional [164] and Grimme-D2 [71] van

der Waals correction for consistency with bulk calculations (SI Sec. 2), except for formation energies with respect to Mo and Ni, for which we use PBE alone. [72] Polarization is calculated with the dipole correction method [19] out of plane, and Berry-phase method [175] in plane. Phonon bandstructures to assess dynamical stability were calculated by density-functional perturbation theory. [13] We work with neutral systems, periodic in plane but separated by vacuum out of plane. We consider the most probable sites for dopants in monolayer MoS_2, including substitutions and adatoms (same as in 1H [103]), as shown in Fig. 3.1. (While adsorption may be considered a distinct process from doping, we classify it together with substitution here due to its connection with bulk intercalation and potential charge doping. [72]) The bridge adatom site relaxes to hollow and is not considered further. We study 2×2, 3×3, and 4×4 supercells, each with one Ni dopant, corresponding to different doping concentrations.

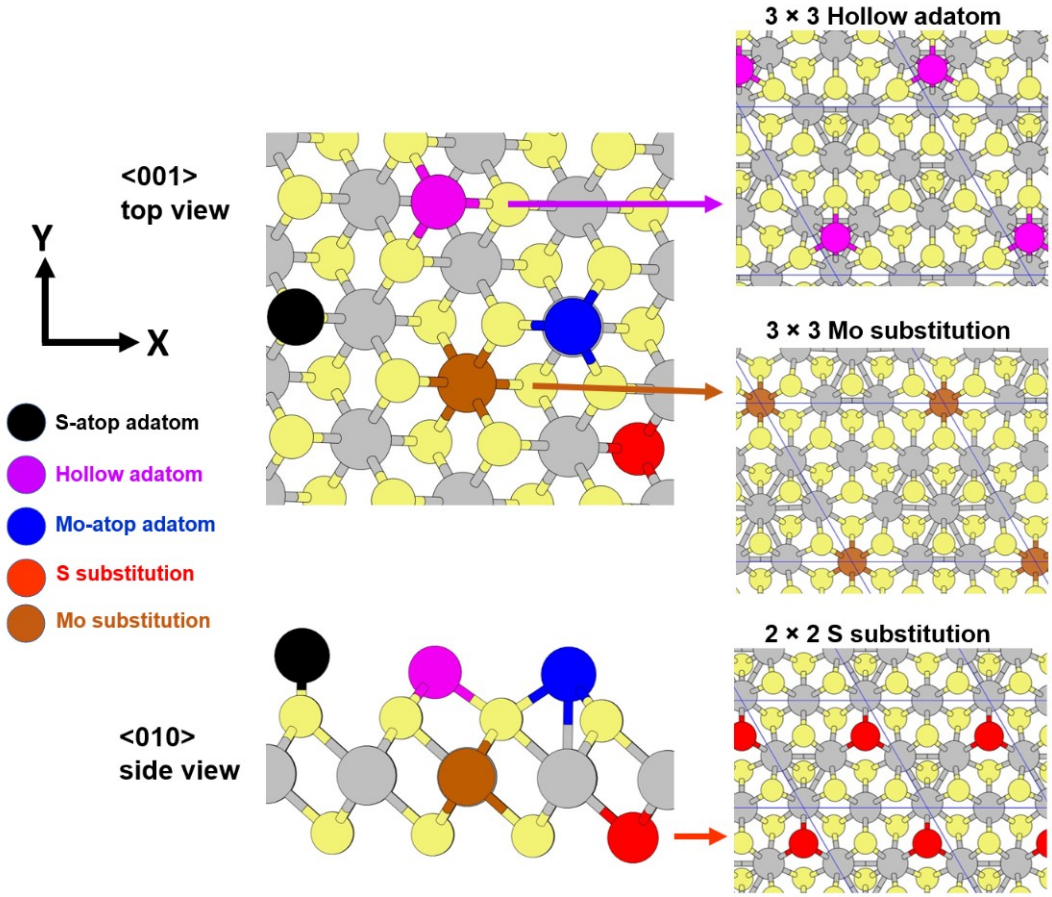

Figure 3.1: Left: Different doping sites for Ni in 1T-MoS_2, with definition of x and y axes. Right: Example reconstructions for different doping sites and concentrations.

3.4 Results and discussion

3.4.1 Doping formation energy and comparison with 1H

We compare the thermodynamic favorability via the doping formation energy, a function of the chemical potentials during growth [72] (SI Sec. 2). Our reference is the most stable distorted phase, 1T′ (2×1), which is 0.26 eV per MoS_2 unit lower in energy than 1T. The doping formation energies for Mo or S substitution and different adatom sites are shown in Fig. 3.2 and Figs. 3.7-3.8. Hollow is the most favorable adatom site, [80] though Mo-atop is favored for 1H [103]. Although these energies are positive, Ni doping is energetically favorable from undistorted

1T in nearly all cases due to lowering of energy by reconstructions. Substitutional doping formation energies are more favorable for 1T′ than 1H. [103] Doping lowers energy differences between 1H and 1T compared to the pristine $\Delta E = 0.85$ eV per MoS_2, but 1H remains favored (Fig. 3.9). Mo substitution at high concentration (8%) can bring the difference down to 0.23 eV per MoS_2 unit. The $T = 0$ phase diagram as a function of chemical potential [72] (Fig. 3.10(a)) shows that in equilibrium the hollow site is most compatible with stability of 1T or 1T′, but Mo and S substitution are also accessible under some conditions. We note that our previous work showed that Ni-doped MoS_2 is always above the convex hull at $T = 0$ compared to other compounds of Ni, Mo, and S. [72] Despite this thermodynamic unfavorability, abundant experimental evidence has been found of Ni incorporation into 2H-MoS_2 [109, 152], and more recently, 1T-MoS_2. [216, 134] Approaches can involve non-equilibrium conditions such as hydrothermal methods for Mo substitution, or creation of sulfur vacancies that can be filled by transition metals for S substitution. [127, 208]

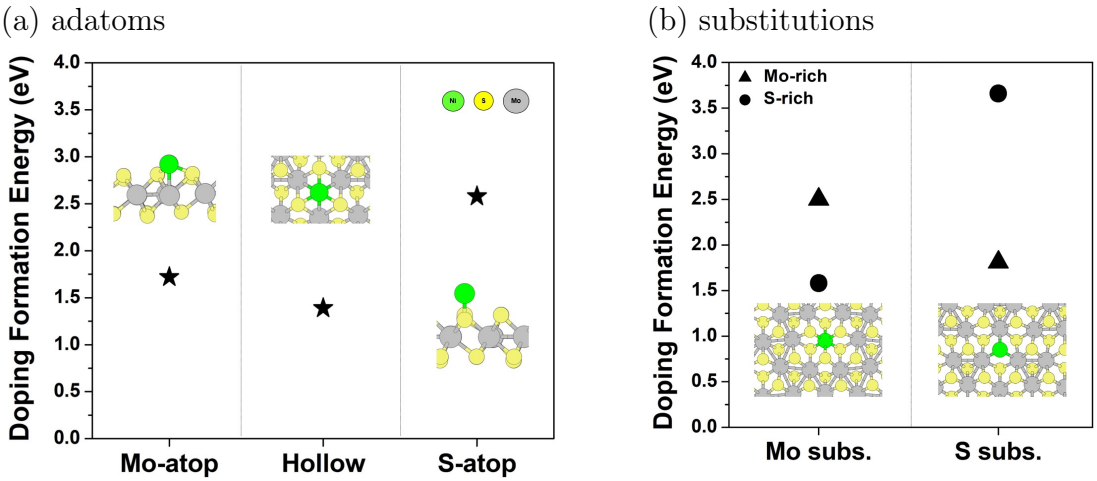

Figure 3.2: Doping formation energies in 4×4 supercells of 1T-MoS_2, with respect to 1T′ (2×1) [62]: a) adatoms, b) Mo and S substitution under Mo-rich and S-rich conditions.

3.4.2 Reconstructions

Doping is found to induce different reconstructions, with various patterns of Mo-atom clustering depending on supercell size and doping scheme (Fig. 3.1). The DFT relaxation trajectories show that the distortions are driven by bond length changes when Ni is introduced to the structure, which not only break the symmetry but also define the local geometry. Mo atoms whose bonds to S are stretched are induced to cluster, which can in turn stretch other Mo-S bonds and induce further clustering. As in 1H-MoS_2 [103], we find Ni-S bonds in Mo-substitution are shorter (2.25 Å) and Ni-Mo bonds in S-substitution are longer (2.51 Å), compared to Mo-S bonds. In Mo substitution, Ni pulls S closer, weakening neighboring Mo-S bonds and making the Mo atoms cluster. In S substitution, Ni pushes Mo farther away, causing now-closer Mo atoms to cluster. In S-atop, Ni weakens bonds from that S to Mo neighbors, causing clustering around Ni. In Mo-atop, Ni pulls S atoms closer, causing clustering away from Ni of Mo atoms with stretched bonds. In hollow, Ni pushes Mo away, causing clustering away from Ni.

Table 3.1: Different pristine reconstructions resulting after removal or replacement of Ni atom in different supercells of Ni-doped 1T.

Doping type	2×2	3×3	4×4
Mo subs.	2×2	3×3	4×4
S subs.	2×2	$\sqrt{3} \times \sqrt{3}$ 4B	2×2
Hollow	2×2	$\sqrt{3} \times \sqrt{3}$ 2B	2×2
Mo-atop	2×2	3×3	2×2
S-atop	2×2	$\sqrt{3} \times \sqrt{3}$ 2B	2×2

We found that the doped structures can give rise to reconstructions even of the pristine material: we reversed the doping by removing adatoms or restoring Mo or S atoms to Ni-substituted sites, and relaxed the resulting structures, finding stable distortions. This process of removal of adatoms is akin to the methods used to synthesize 1T phases via Li or K atoms [128], and undoing Ni substitution of Mo or S seems plausible via ion-exchange methods that have been used to

interconvert different TMDs [30]. Therefore the route used in our calculations may also constitute a viable method for experimental synthesis. Most of the structures relaxed to previously known phases (2×2 or $\sqrt{3} \times \sqrt{3}$) [246, 159, 62, 242] while a few reconstructions were not found in the literature (Table 3.1, Fig. 3.3). Note that the supercell size constrains the possible reconstructions: e.g. 2×2 can form only from 2×2 or 4×4, and $\sqrt{3} \times \sqrt{3}$ only from 3×3. We did not find 2×1 but include it in further analysis for comparison. The properties of the pristine reconstructions are shown in Table 3.2. Lattice parameters and Mo-Mo distances are consistent with [246] We find there are two different $\sqrt{3} \times \sqrt{3}$ structures, with the same C_{3v} symmetry (but different locations of the C_3 axis) and all 3 Mo atoms equivalent at the Wyckoff c positions. They have different numbers of bonds from Mo to other Mo atoms, so we will distinguish them as 2B and 4B. The distinction between these structures does not seem to have been appreciated previously: $\sqrt{3} \times \sqrt{3}$ in [246] is 2B whereas in [55] it is 4B. The phases not previously reported are obtained from 3×3 and 4×4 Mo substitution, and the energies are 0.24 eV and 0.15 eV per MoS_2 lower than 1T, respectively. Note that 3×3 is more stable than the experimentally established 2×2. [126] The most stable structure seen is $\sqrt{3} \times \sqrt{3}$ 4B, which has been synthesized experimentally [55] with lattice parameter $a = b = 5.58$ Å and Mo-Mo bond length 3.01 Å, close to our results of 5.61 Å and 3.02 Å. Space groups and point groups of the structures are given in Table 3.6. We confirmed that similar results are obtained for the relative energies and structural parameters using PBE+U [45] or the PBE0 hybrid functional [49, 6] (Table 3.7).

These structures are distorted out of plane as well: S atoms vary in their z-height (Fig. 3.4), a symmetry-breaking which allows out-of-plane polarization. There has been little attention in distorted 1T to this z-variation [246, 159, 242, 55, 185], and only recently has it been connected to polarization in the 2×2 structure. [126] The variations for 3×3 are largest, and as shown below, it has the largest ferroelectric polarization. While the maximum displacements are similar on the two sides, there is a net polarization because the patterns are different, and there can be significant variation in dynamical charges among S atoms in 1T-MoS_2 phases. [126, 33] In $\sqrt{3} \times \sqrt{3}$ 2B and 4B, the z-height of S atoms varies on one side

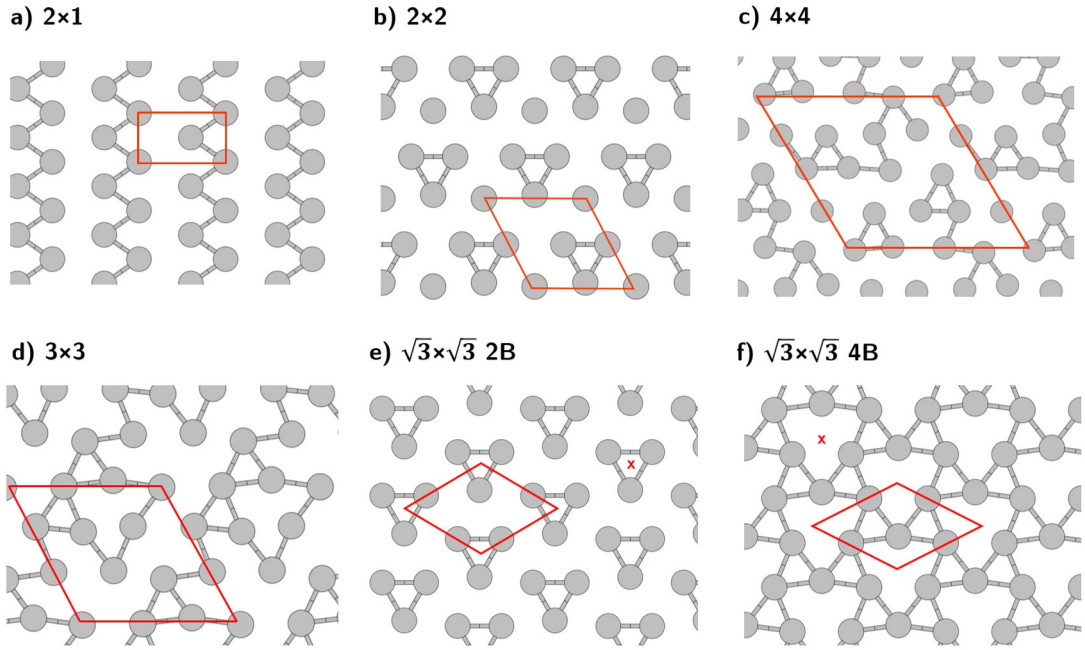

Figure 3.3: Mo clustering for different reconstructions. S atoms are not shown, for clarity. All Mo-Mo bonds shorter than 3.08 Å, twice the covalent radius of Mo, [34] are shown. There are several inequivalent bond lengths in 3×3 and 4×4. The red $\times$ in (e) and (f) denotes the location of the C_3 axis.

and is constant on the other, whereas in all other structures, we find variations on both sides. The pattern of z-variation in 2B and 4B is opposite: in 2B, lines of S atoms consist of pairs closer to the Mo plane separated by an atom farther; whereas in 4B there are pairs farther, separated by an atom closer. The variation on only one side in $\sqrt{3} \times \sqrt{3}$ is connected to the fact that these reconstructions only occur from an adatom or S substitution, which breaks the symmetry between the sides, but not from Mo substitution. We find Ni substituting S causes sites to move closer to the Mo plane, and Ni on S-atop and Mo-atop sites moves S farther from Mo. Ni on the hollow site moves some S atoms closer and some farther, on both sides. The S atoms centered in Mo triangular clusters are always farthest from the Mo plane. These vertical corrugations are consistent with previously calculated structures of $\sqrt{3} \times \sqrt{3}$ 4B in [55], 2×2 in [126], and $\sqrt{3} \times \sqrt{3}$ 2B (in plane [246] and out of plane [245]). This surface non-uniformity could be interesting for surface chemistry or

catalysis as it may tune reactivity: in 1T′ the reactivity for chemisorption is higher for S atoms closer to the Mo plane. [168]

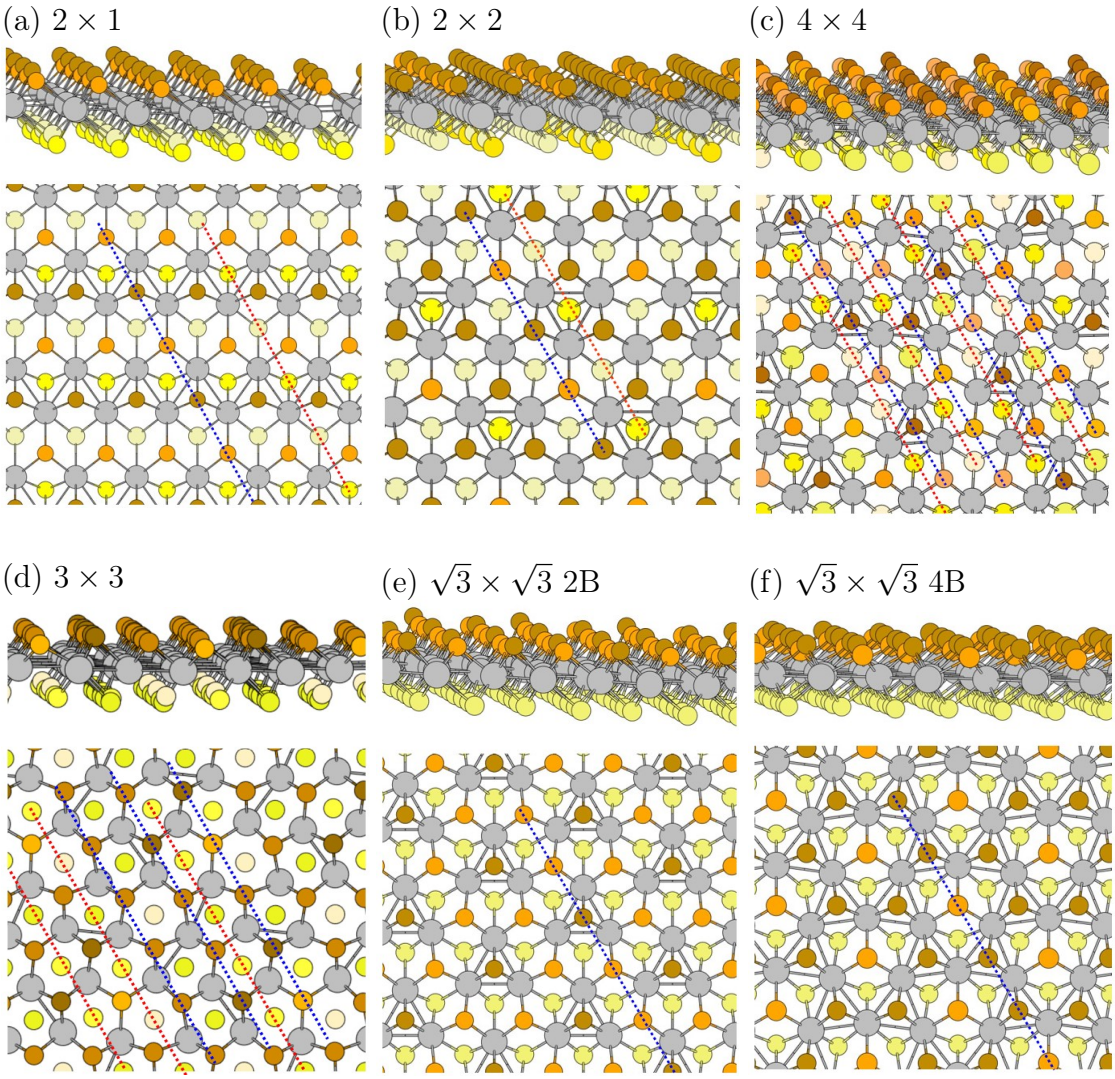

Figure 3.4: Structures in side and top views, showing vertical corrugation of S atoms. Orange and yellow colors are used to represent S atoms on the top and bottom of the Mo-plane, respectively. Darker color indicates greater distance from the Mo-plane. Blue and red dotted lines indicate directions along which S atoms heights vary for top and bottom S atoms, respectively.

a)

Structure	a, b (Å)	d (Å)	Δz (Å)	ΔE (eV)	E_g (eV)
1×1	3.18	3.18	0, 0	0	0
2×1	5.67, 3.18	2.78	0.39, 0.39	-0.26	0.02
2×2	6.43	2.78	0.27, 0.25	-0.21	0.08
3×3	9.70	2.93	0.47, 0.51	-0.24	0.71
$\sqrt{3} \times \sqrt{3}$ 2B	5.64	2.84	0, 0.17	-0.19	0.59
$\sqrt{3} \times \sqrt{3}$ 4B	5.61	3.02	0, 0.44	-0.26	0.83
4×4	13.01	2.78	0.32, 0.31	-0.15	0.25

b)

Structure	Bandgap (eV)	ΔE_{VBM} (eV)	N_{bands}
	0.46	1.63	2
1×1	0.58	3.98	2
2×1	0.30	4.81	8
	0.19	0.81	2
2×2	0.15	1.92	3
	0.52	4.52	11
	0.10	1.63	9
3×3	0.42	4.72	27
	0.83	1.20	3
$\sqrt{3} \times \sqrt{3}$ 2B	0.22	2.54	3
	0.73	4.40	6
	0.22	1.70	3
$\sqrt{3} \times \sqrt{3}$ 4B	0.38	4.89	9
4×4	0.11	1.84	17
	0.39	4.69	47

Table 3.2: Structure, energy, and DFT bandstructure properties of pristine reconstructions of 1T.*

* a) Structure, energy, and gap; a, b are the lattice parameters ($a = b$ in most cases); d is the shortest Mo-Mo distance, characterizing clustering; Δz gives the range of vertical positions of S atoms, for each of the two sides; ΔE is the energy difference per MoS_2 with respect to undistorted 1T. b) Conduction-band gaps: ΔE_{VBM} is the energy difference of the bottom of the gap from the valence band maximum (VBM); N_{bands} is the number of bands from the previous gap up to this gap.

3.4.3 Dynamical Stability

The pristine reconstructions result from relaxation of a structure whose symmetry was broken by the presence of the Ni dopants, which indicates a minimum level of stability. The dynamical stability of all reconstructions was further investigated by calculating phonon bandstructures, as shown in Fig. 3.5. We found structures 2×1, 3×3, and $\sqrt{3} \times \sqrt{3}$ 4B to be dynamically stable. However, in several cases instabilities were found – real in the case of $\sqrt{3} \times \sqrt{3}$ 2B and 3×3, but attributed to numerical issues [160] in the case of 2×1, 2×2 and 4×4. The instabilities were investigated by displacing the atomic coordinates in the direction of the imaginary-frequency displacement eigenvectors scaled by 0.01 Å, and then relaxing the atomic structure and lattice. [160] The higher-energy $\sqrt{3} \times \sqrt{3}$ structure (2B) [246] was found to be unstable, with imaginary frequencies at Γ, M and K. Relaxation after displacement by the imaginary mode at Γ yielded $\sqrt{3} \times \sqrt{3}$ 4B. We nonetheless retained $\sqrt{3} \times \sqrt{3}$ 2B structure in our data set due to interesting properties such as a higher ferroelectric polarization (see below), and the possibility that it might be stabilized by temperature, epitaxy, or other factors. Our originally obtained 3×3 structure (Fig. 3.18), which is 0.08 eV lower in energy than undistorted 1T, proved to be unstable, and relaxation after displacement led to the significantly more stable 3×3 structure analyzed in the text. In the case of 2×2, we found a small imaginary frequency at Γ which corresponds to a flexural mode (Fig. 3.19), notoriously difficult to calculate accurately in DFT. [36] Relaxation after displacement returned to the original structure, showing that the instability is a numerical artifact, which is consistent with the realization in experiment of this phase. [126] 2×1 shows a similar flexural instability at Γ, which we did not investigate further, since it is included here only for comparison to the phases resulting from Ni-doping, and the existence of this 1T′ phase is well established experimentally [48, 55, 151] and theoretically. [85, 246] For 4×4, relaxation in a 2×1 supercell after displacement by imaginary modes corresponding to the M point led back to the original structure, indicating no true instability. These modes also have flexural character (Fig. 3.19). We conclude that the 2×2 and 4×4 structures are indeed dynamically stable.

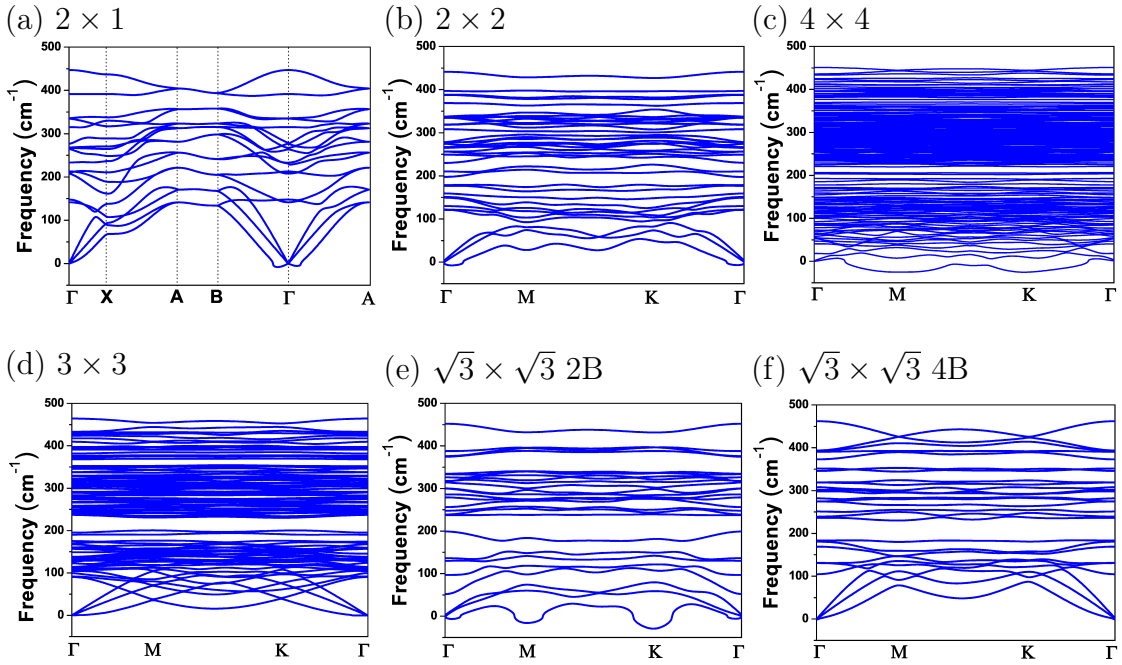

Figure 3.5: Phonon band structure of pristine reconstructed structures, in the Brillouin zone of each structure's primitive cell.

3.4.4 Electronic Structure

We found a variety of electronic structures in pristine and Ni-doped reconstructions. For pristine phases, band gaps are shown in Table 3.2, density of states (DOS) in Fig. 3.11, and band structures in Fig. 3.6. For Ni-doped phases, the band gaps are in Table 3.4, DOS in Fig. 3.12 and bandstructures in Fig. 3.14. The pristine 1T phase is metallic [107, 35], but becomes semiconducting with most distortions due to a Jahn-Teller mechanism. [242] This occurred with doping in most cases we considered; only Mo-substituted 2×2 and 3×3, S-substituted 4×4, and S-atop 2×2 and 4×4 remained metallic. All of the pristine reconstructions obtained from the doped ones are semiconducting, albeit with a very small gap in 2×1, as in [85] We calculated the Z_2 topological index of the pristine and doped reconstructions using Z2Pack, [70, 189] but found them to be topologically trivial, other than 2×1 [171]. We did however notice other unusual features in the

bandstructures of the pristine phases: there are multiple gaps in the conduction bands (Table 3.2(b), Fig. 3.6). Undistorted 1T has two conduction-band gaps even though it is metallic (Fig. 3.13), and these gaps are preserved or increase in number in distorted phases (except 2×1). DOS plots (Figs. 3.11-3.12) confirm the presence of these gaps. We note that while in general the fundamental gap is underestimated by PBE, other aspects of the bandstructure are typically well estimated. We verified that PBE+U and spin-orbit coupling do not significantly change the bandstructure (e.g. Fig. 3.16). In all calculated structures, a gap of 0.3–0.7 eV exists $\sim$ 5 eV above the VBM, between bands of mostly Mo d character below and Mo s character above. A similar gap $\sim$ 5 eV above the VBM is found in ReS_2 bilayers, between Re d and Re s bands, as probed by time–resolved second harmonic generation. [40] Similar second gaps are reported in other metal chalcogenides. [179, 118] However, the other gaps found in 1T are quite unusual, and there does not seem to be a standard explanation for such gaps.

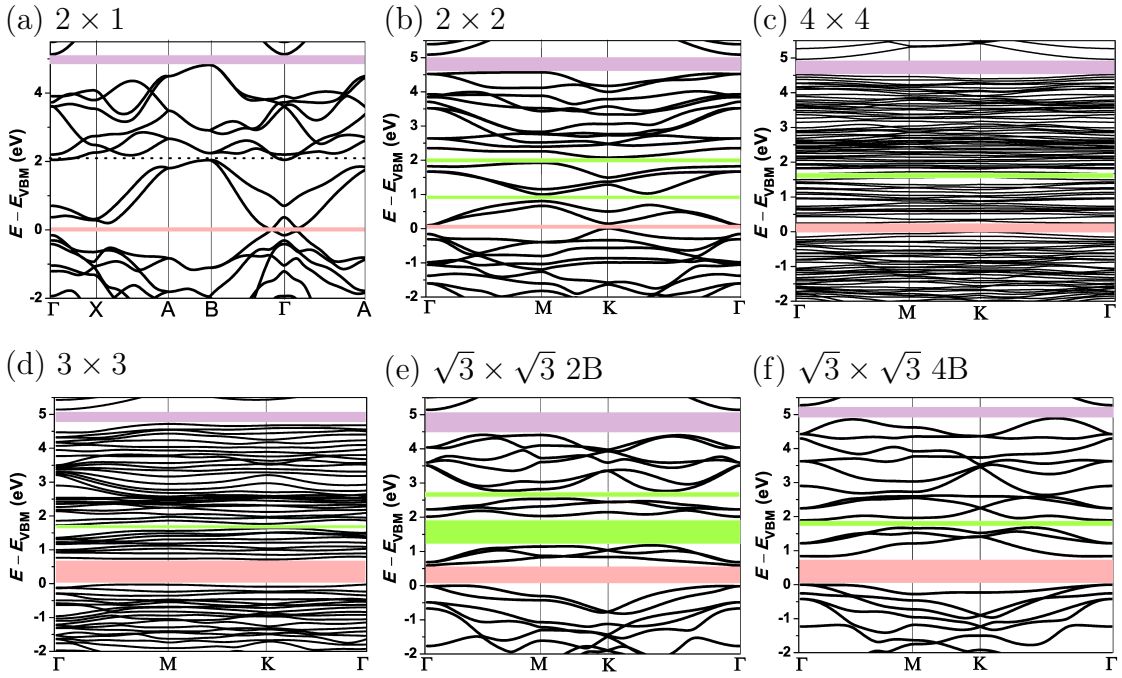

Figure 3.6: Band structure of pristine reconstructed structures, in the Brillouin zone of each structure's primitive cell. The colored stripes highlight the gaps, with pink as the fundamental band gap, purple as a gap common to all structures due to transition between Mo s and d-orbitals, and green for gaps in between those two. The dotted line in a) shows the small band overlap at this energy.

The origin of these gaps is complex. The gaps are induced by perturbations to the potential felt by the electrons at the reconstructed supercell periodicity, as for mini-bands in superlattices, [156] with the perturbation provided by Mo clustering. What explains the patterns in different structures? The gaps are not due to a transition between different types of orbitals as they are within bands all due to Mo d and S p-orbitals. We examined the wavefunctions of band complexes between gaps, and we find some common patterns. Some gaps are transitions between bands localized on clustered and non-clustered Mo orbitals. In $\sqrt{3} \times \sqrt{3}$ 2B and 4B, we see Hückel-type patterns of bonding, non-bonding, and anti-bonding among d-orbitals in a band complex. We examined local symmetries of Mo atoms for crystal field splitting (Table 3.6), and find mostly symmetry elements (C_1, C_{2v})

that break the degeneracy of d_{xz} and d_{yz}, and $d_{x^2-y^2}$ and d_{xy}. This breaking of degeneracy contributes to gap openings, and some of the gaps are found to be transitions between different crystal-field-split d-orbital shapes. We do not see any clear correlation between the multiple gap patterns and the overall symmetry, number of inequivalent Mo atoms, or symmetry of the Mo sublattice. In a tight-binding picture, loss of symmetry can increase the variation of on-site energies; for small hoppings (and bandwidths), this could open up gaps, but for large hoppings, it could overlap bands and close gaps. We investigated the Löwdin charges on Mo atoms and found significant variation (Fig. 3.17), which would correlate with on-site energies, but there is no clear correlation of the charges with number or magnitude of gaps. Ultimately we conclude that the gaps, and the number of bands between them, are due to a complex interplay of reconstructed periodicity, Mo cluster bonding, crystal-field splitting, and overall symmetry. Wannier-function-based analysis [161] may shed further light on the mechanisms.

These multiple gaps could possible be utilized in intermediate band solar cells (IBSCs) [136], a third-generation photovoltaic concept which can exceed the Shockley-Queisser limit by allowing the voltage to be increased without losing absorption. In IBSCs, electrons can be excited from the valence band across a first band gap to an intermediate band (from which recombination is slow), and then excited again across a second band gap. Whereas in a standard solar cell the single band gap controls both the voltage and the absorption, here the resulting voltage is related to the sum of the two band gaps. Such intermediate bands for solar cells are typically due to dopants, [231, 28] which can however cause undesired scattering and recombination. In our case, however, we have multiple gaps even in the pristine phases due to reconstruction. Ideally, an IBSC should have a partially filled intermediate band, to facilitate electronic transitions, [135], which could be obtained by electrostatic gating, or realized by some of the Ni-doped structures (Fig. 3.14 (b,d)) that have metallic intermediate bands. Multiple gaps, in particular in the metallic cases or with gating, could also be applied for transparent conducting materials (TCMs) [25] – in some successful TCMs, the bandstructure has a partially filled conduction band, providing conductivity, with a large second

gap above it, providing transparency. As with IBSCs, such bandstructures have typically been provided by doping, but here could be realized in an undoped system which may have better mobility. A final application is nonlinear optics, as studied for ReS_2, [40] since multiple gaps enable multiple simultaneous resonances for sum- or difference-frequency generation. Phases studied here are noncentrosymmetric and therefore have nonzero $\chi^{(2)}$, as has been in shown for $\sqrt{3} \times \sqrt{3}$ 4B [55] and 2×2 [126].

We find spontaneous polarization in the reconstructions. Pristine $\sqrt{3} \times \sqrt{3}$ 4B has been calculated to be ferroelectric with an equivalent bulk polarization of 0.18 μC/cm^2 (using the S-S distance as the height along the z-direction) [185]. Recently the out-of-plane polarization for a bulk 2×2 with layer height of 5.96 Å was calculated [126] to be 0.04 μC/cm^2 (we obtain 0.06 μC/cm^2). We will focus on the polarization per unit area as befitting a monolayer 2D material. We calculate polarization magnitudes of: 2×2, 4.06×10^{-4} e/Å; $\sqrt{3} \times \sqrt{3}$ 4B, 7.18×10^{-4} e/Å (consistent with [185]); $\sqrt{3} \times \sqrt{3}$ 2B, 2.19×10^{-3} e/Å (3× larger than 4B); 4×4, 1.34×10^{-2} e/Å; and 3×3, 5.37×10^{-2} e/Å. The polarizations are in the $-z$ direction for our $\sqrt{3} \times \sqrt{3}$ 2B and $\sqrt{3} \times \sqrt{3}$ 4B structures, as in-plane polarization is forbidden in C_{3v}. There is in-plane polarization for 2×2 (C_s), 3×3 (C_1) and 4×4 (C_1), with polarization vectors $(3.45, 0, 2.15) \times 10^{-4}$ e/Å, $(380, -380, -1.76) \times 10^{-4}$ e/Å, and $(126, -44.3, -3.07) \times 10^{-4}$ e/Å, respectively. These 3×3 and 4×4 structures' polarizations are 132 and 33 times larger than 2×2. Using the bulk 2×2 layer height, these correspond to bulk polarizations of $\sim$8 μC/cm^2 and $\sim$2 μC/cm^2 respectively, only one order of magnitude smaller than standard ferroelectrics $PbTiO_3$ (79 μC/cm^2) and $PbZrO_3$ (70 μC/cm^2). [17] For comparison, 2×1 has zero polarization due to C_{2h} symmetry. We can make a simple estimate of ferroelectric switching, considering coherent reversal via the (paraelectric) undistorted 1T structure [17], and using the energy differences in Table 3.2. We obtain barriers of 0.03–0.09 eV/atom, comparable to $PbTiO_3$ ($\sim$0.01 eV/atom) and $PbZrO_3$ ($\sim$0.04 eV/atom). [17] Moreover, there could be a lower-energy switching pathway. Out-of-plane polarization switching was recently observed in an experiment [126] for the 2×2 structure, for which we estimate a barrier of 0.21 eV. Since all of the

structures have similar or lower barriers, these results suggest the polarization is switchable in those cases too. The experimental results suggest that monolayer ferroelectric properties can be retained when stacked into a multilayers, for potential nanoelectronic devices.

To predict X-ray photoemission (XPS) on these structures, we characterize the oxidation state of Ni via d-orbital occupations from spin-polarized DFT+U calculations, [186] using U values of 5.5 eV for Ni [244] and 4 eV for Mo [221]. The results were similar to other polytypes [103]: we found an oxidation state of Ni^{4+} in Mo substitution for all concentrations in 1T (as for high concentration for 1H, 2H, 3R). This result agrees with a conclusion from XPS for Mo substitution by Ni in 1T-MoS_2 [216]. Our S-substitution and adatom calculations showed Ni^{2-} (as for all 1H, 2H, and 3R concentrations).

We investigated magnetism in doped structures, given its presence in some structures of doped 1H-MoS_2 [221, 103]. We found 3 ferromagnetic cases and 1 antiferromagnetic case, with moments on the Ni site (Table 3.3, Table 3.5). We estimated Curie temperatures with mean-field theory (SI Sec. 1), and find high T_C for the metals. Metals cannot have polarization in a periodic direction, but two of these cases have out-of-plane polarization, making them ferromagnetic polar metals. [243] Note that 2×2 was calculated and measured to be a polar metal as well [126] but only in the bulk, not monolayers. We also have unusual ferromagnetic and antiferromagnetic semimetals [238, 204], which have both out-of-plane and in-plane polarization, making them (anti)ferromagnetic-ferroelectric multiferroics, rarely reported in 2D. [61, 138] Polarization for all doped structures is in Table 3.4. The in-plane polarization is switchable via undistorted 1T where it is zero by symmetry, with switching energies per atom comparable to the pristine phases, and there could be other lower-barrier pathways. Doped structures (except for Mo substitution) have out-of-plane polarization due mainly to Ni (with oxidation state $2-$, described above) rather than distortion, which therefore cannot be feasibly switched. Mo substitution has switchable (though small) polarization since the undistorted 1T is centrosymmetric. The other cases are an unusual kind of improper ferroelectric controlled by in-plane distortion [157], where only the in-

plane polarization (up to $\sim 10^{-3}$ e/Å) is switchable. We note this type is distinct from recently reported ferroelectric doped 2D materials, which switch via interlayer sliding rather than intralayer distortions. [199]

Doping type	μ (μ_B)	ΔE_{mag} (meV)	T_C (K)	Type	Polarization (e/Å)
2×2 S subs.	0.05	-0.19	19.6	semimetal	$(-1.06, 1.18, -3.06) \times 10^{-3}$
4×4 S subs.	0.78	-27.91	493	metal	$(0, 0, -6.60) \times 10^{-4}$
2×2 S-atop	0.30	-17.32	485	metal	$(0, 0, -1.14) \times 10^{-2}$
3×3 S-atop	0 [0.07]	-0.09	-	semimetal	$(6.08, -6.08, -49.3) \times 10^{-4}$

Table 3.3: Magnetic doped structures.[a]

[a] Moment μ per Ni atom and energy difference ΔE_{mag} per Ni atom of spin-polarized state *vs.* the non-spin-polarized paramagnetic state. Moment in square brackets for 3×3 S-atop is the integrated absolute magnetization, indicating weak antiferromagnetism.

3.5 Conclusion

In conclusion, we found that Ni–doping 1T MoS_2 induces a panoply of different reconstructions with Mo clustering, due to the effect of Ni on neighboring bonds. Removing or replacing the dopant and relaxing (and adding a small perturbation in some cases) leads to pristine reconstructions are dynamically stable. These resulting phases include not only the typically reported ones but also 3×3 and 4×4. Two versions of $\sqrt{3} \times \sqrt{3}$ with two and four Mo-Mo bonds are present initially, but only the latter is dynamically stable. These structures show large ferroelectric polarizations and low switching barriers. Most notably, compared to the experimentally measured 2×2 [126], 3×3 has polarization higher by two orders of magnitude, is more stable, and has a significantly larger band gap, which reduces difficulties with charge leakage and conductivity. Most Ni-doped structures are semiconductors but they also include unusual ferromagnetic polar metals, multiferroic semimetals, and in-plane improper ferroelectrics. Pristine and doped phases showed multiple gaps in the conduction bands, a phenomenon which has potential application in intermediate band solar cells, transparent conducting materials, and nonlinear optics. Our calculations suggest that Ni-doping of 1T-MoS_2 (perhaps in-

cluding intercalation) could be a way to synthesize a range of distorted pristine phases, by removing or replacing dopants through methods such as dissolution or evaporation of adatoms, or ion exchange for Mo or S substitution; or perhaps epitaxy on a Ni-doped monolayer. Such structures, including the potential analogues involving other transition-metal dichalcogenides and transition-metal dopants, are interesting for applications in electronics, optics, energy storage, and catalysis, and may offer other intriguing properties.

Supplementary Information

Computational details, analysis of formation energies, full structural, electronic, polarization, and magnetic properties of Ni-doped 1T MoS_2, doping formation energies as a function of concentration, bandstructures of doped, density of states for doped and pristine, and further information on dynamical instabilities (PDF). PBE+Grimme-D2 relaxed coordinates for Ni-doped 1T MoS_2 and reconstructed pristine 1T structures, in XCrySDen format (TAR.GZ).

Acknowledgments

We acknowledge Enrique Guerrero for preparing the phase diagram. This work was supported by UC Merced start-up funds and the Merced nAnomaterials Center for Energy and Sensing (MACES), a NASA-funded research and education center, under awards NNX15AQ01 and NNH18ZHA008CMIROG6R. This work used computational resources from the Multi-Environment Computer for Exploration and Discovery (MERCED) cluster at UC Merced, funded by National Science Foundation Grant No. ACI-1429783, and the National Energy Research Scientific Computing Center (NERSC), a U.S. Department of Energy Office of Science User Facility operated under Contract No. DE-AC02-05CH11231.

3.6 Supplementary Information

3.6.1 Computational Details

We use the methods of our previous work on 2H, [72] 1H, and 3R [103]: plane-wave density functional theory (DFT) in Quantum ESPRESSO version 6.1 [68, 67]. We use the PBE exchange-correlation functional [164] with the semi-empirical Grimme-D2 (GD2) [71] van der Waals correction (for consistency with bulk calculations, though the effect is small for monolayers). However, for the doping formation energy we used PBE only, which gives a better energy for the bulk metals Ni and Mo which we need to compare to. [72] We used Optimized Norm-Conserving Vanderbilt (ONCV) pseudopotentials [79, 178] from the SG15 set [3]. Kinetic energy cutoffs were 60 Ry. Just as a point of comparison, we calculated formation energies also with the Perdew-Wang [165] local density approximation (LDA) functional, with ONCV pseudopotentials from Pseudodojo [2] and a kinetic energy cutoff of 80 Ry; the similarity of the results can be seen in Fig. 3.2(b). Half-shifted 12×12 k-point grids were used for pristine 1T, $6 \times 6 \times 4$ for bulk 1T, and sampling was decreased proportionately in each direction for supercells and other reconstructions. Relaxation was performed with a force threshold 1.0×10^{-4} Ry/bohr and stress threshold 0.1 kbar. Gaussian smearing of 0.05 eV was used for metallic cases, and for calculations of magnetization. Density of states (DOS) was calculated with broadening 0.02 eV and k-grids of 60×60 for 1×1, 45×45 for $\sqrt{3} \times \sqrt{3}$, 40×40 for 2×2, 30×30 for 3×3, and 20×20 for the 4×4 structures and supercells. Phonon calculations with density-functional perturbation theory [13] used a self-consistency threshold of 10^{-16}. We interpolated phonon bandstructures based on a 2×2 q-grid for all structures except 2×1 where we used 2×3.

We consider different doping concentrations via supercells with one Ni atom. All systems are treated as neutral, as appropriate for neutral impurities or high Ni concentration, and are ordered structures. A vacuum spacing of 15 Å between monolayers is used to reduce spurious periodicity.

We found no significant effect of dipole corrections [19] on energies or structures. However, for ferroelectric properties, we used the dipole correction in Quantum

ESPRESSO to compute out-of-plane dipole moments. We used the Berry-phase method for in-plane polarization, and found that it also gave a dipole moment in the z-direction consistent with the dipole correction method. For Berry-phase method, we used 20 k-points (`nppstr`=20) in the direction of k-point strings (`gdir`). The in-plane polarizations are all reduced by the quantum of polarization [175] to the value closest to zero.

We used non-spin-polarized calculations except for ferromagnetic bulk Ni, and for investigating magnetic properties of doped MoS_2. In that case, we checked variable-cell relaxations with spin-polarized calculations. For some structures, a spin-polarized calculation at the relaxed geometry from a non-spin-polarized calculation showed non-zero magnetic moments, but these moments went to zero after a spin-polarized variable-cell relaxation which lowered the energy. For the structures found to be magnetic, our reported out-of-plane polarization and band-structure are from spin-polarized calculations, but in-plane polarization is from a non-spin-polarized calculation since Berry's phase cannot work with smearing. For S substitution 2×2 and S atop 3×3 with very small gaps, we used a smaller smearing of 0.02 eV instead.

The $\sqrt{3} \times \sqrt{3}$ 2B and 4B pristine reconstructions obtained in the 3×3 supercell, and 2×2 obtained in 4×4 supercell, are obtained by finding the primitive cell from those supercells, with consistent results obtained from both Phonopy [209] and the Bilbao Crystallographic Server [11, 10]. We find space groups and point groups via Findsym [193].

We computed the oxidation state of Ni following the methodology suggested by Sit *et al.* [186] for assigning oxidation states based on d-orbital occupations from spin-polarized PBE+U calculations, using U values of 5.5 eV for Ni [244] and 4 eV for Mo [221]. The results were similar to other polytypes [103]: we found an oxidation state of Ni^{4+} in Mo substitution for all concentrations in 1T (as for high concentration for 1H, 2H, 3R). This result agrees with a conclusion from X-ray photoemission for Mo substitution by Ni in 1T-MoS_2 [134]. S-substitution and adatoms showed Ni^{2-} (as for all 1H, 2H, and 3R concentrations).

Curie temperatures are calculated from the data in Table 3.3 using mean-field

theory [106] as

$$T_C = \frac{2zJS(S+1)}{3k_B} \tag{3.1}$$

where $S = \mu/2$ based on $g \approx 2$ for purely spin magnetic moments, and the number of nearest neighbors $z = 6$ for hexagonal-based structures. From the Heisenberg model

$$U = -2J \sum_{<ij>} \vec{S}_i \cdot \vec{S}_j, \tag{3.2}$$

and the ferromagnetic/paramagnetic energy difference is

$$\Delta E = 2JzS^2 \tag{3.3}$$

so

$$J = \frac{\Delta E}{2zS^2} = \frac{1}{3}\frac{\Delta E}{\mu^2}. \tag{3.4}$$

The topological properties were analyzed using the Z2Pack [70, 189] software package. The Z_2 invariant is calculated for the planes at $k_z = 0$, with hybrid Wannier charge centers calculated along k_x and k_y acting as a pumping parameter. We used Wannier90 [153] as interface to Z2Pack. Our calculations confirmed $Z_2 = 1$ for 2×1 as in a previous report [171], but other pristine structures are topologically trivial ($Z_2 = 0$).

3.6.2 Formation energy

The doping formation energy is given by

$$E_{\text{formation}} = E_{\text{system}} - NE_{\text{pristine}} - \mu_{\text{Ni}} + \mu_{\text{removed}} \tag{3.5}$$

for substitution cases, and

$$E_{\text{formation}} = E_{\text{system}} - NE_{\text{pristine}} - \mu_{\text{Ni}} \tag{3.6}$$

for adatom cases, where E_{system} is the doped supercell energy, N is the number of units in the supercell, E_{pristine} is the pristine unit cell energy, and μ_{Ni} and μ_{removed}

are the chemical potential of Ni and the removed Mo or S atom, respectively. μ_{Ni} is taken equal to the bulk Ni energy per atom, and for substitution cases, we consider both the "Mo-rich" ($\mu_{\mathrm{Mo}} = E_{\mathrm{Mo}}$) and "S-rich" ($\mu_{\mathrm{S}} = E_{\mathrm{S}}$) conditions, where we use calculations of the bulk phases of Mo and S [72], and the other species' chemical potential is given by equilibrium with 1T-MoS_2.

We constructed the $T = 0$ phase diagram of the stable doping site as a function of chemical potentials μ_{Mo} and μ_{S}, for Ni-doped 1T, as we did previously for other MoS_2 polytypes [72, 103]. The phase diagram shown in Fig. 3.2 (a) allows us to identify which doped structures can form in equilibrium and which are compatible with stability of the corresponding pristine structure. The hollow adatom site occupies most of the pristine stability region for 2×2 and 4×4, but Mo substitution is also included. S substitution is not. For 3×3, hollow, Mo substitution, and S substitution are all accessible. The stability triangle for 1T$'$ is slightly larger due to its lower energy, but that does not change these conclusions. The phase stability can shift at high temperatures, and doping sites can also be accessible out of equilibrium.

Relative stability of different monolayer phases in MoS_2 is compared in Fig. 3.2(b). 1T is the highest-energy monolayer phase, and 1H is more favorable than 1T by 0.85 eV per MoS_2 unit, in agreement with previous literature [23]. For comparison, we look also at 1T bulk, which has been synthesized experimentally and showed superconductivity at 4 K [56]. Lattice parameters for 1T bulk are $a = b = 3.21$ Å and $c = 6.04$ Å, close to the experimental results [56] $a = b = 3.19$ Å and $c = 5.94$ Å. The layer dissociation energy for 1T bulk is 0.20 eV per MoS_2, which is 0.05 eV more than 2H-MoS_2 [103]. The most stable distorted phase is 1T$'$ (2×1), which is more stable than 1T bulk but less stable than 1H. For the purpose of doping formation energy calculations, in Equations 3.5 and 3.6, we use this most stable 1T$'$ for E_{pristine}.

Figure 3.7 shows doping formation energy as a function of dopant concentration expressed as inverse of area. Unlike Ni-doping in monolayer 1H [103], the graph looks non-linear and does not show any sign of convergence to a low-doping limit. This behavior is due to structural distortions and means that doping formation

energy depends on the initial structural configurations. For example, in adatom cases, more energy is required to dope Ni into 3×3 than others; likewise in S-substitution, less energy is required to dope into 3×3 than others. The doping formation energy for unrelaxed structures (Fig. 3.8) instead shows a more regular trend, and convergence at low-doping in comparison to undistorted 1T.

Table 3.4: Properties of doped 1T-MoS_2. Doping formation energy per MoS_2 unit is in reference to distorted 1T′, under Mo-rich (S-rich) conditions which give the same values for adatoms. Distortion energy per MoS_2 unit (PBE+Grimme D2) is the energy of relaxation from a doped undistorted 1T. Doped undistorted 1T has $P_x = P_y = 0$ due to C_{3v} symmetry mostly, and $P_z = 0$ also for Mo substitution with D_{3d}. Asterisks mark the magnetic structures (Table 3.3).

	Lattice $a = b$ (Å)	Doping Formation Energy (eV)	E_g (eV)	Mo–Mo bond (Å)	Polarization (P_x, P_y), P_z (e/Å)	$\Delta E_{\text{distort}}$ (eV)	Undistorted P_z (e/Å)
1 × 1							
Mo subs.	-	-	-	-	-	-	-
S subs.	2.92	0.36 (2.21)	0	2.92	0, -3.09×10^{-3}	0.45	-5.23×10^{-3}
Hollow	3.50	1.69	0.05	3.49	0, -4.28×10^{-3}	0.21	-3.46×10^{-3}
Mo atop	3.22	1.03	0.37	3.22	0, -3.11×10^{-3}	0.38	-2.63×10^{-3}
S atop	3.09	2.15	0	3.09	0, -6.24×10^{-3}	0.22	-9.06×10^{-3}
2 × 2							
Mo subs.	3.29	2.88 (1.95)	0	3.29	0, 0	0.19	0
S subs.*	3.20	1.19 (3.04)	0	2.79	0, -3.06×10^{-3}	0.26	-3.94×10^{-3}
Hollow	3.28	1.09	0.33	2.80	$(1.44, -1.45) \times 10^{-3}$, 0	0.47	-2.60×10^{-3}
Mo atop	3.24	1.15	0.07	2.82	0, -5.28×10^{-3}	0.26	-5.18×10^{-3}
S atop*	3.22	3.30	0	2.82	0, -1.14×10^{-2}	0.25	-6.41×10^{-3}
3 × 3							
Mo subs.	3.23	2.14 (1.22)	0	2.76, 2.99	0, -7.96×10^{-5}	0.29	0
S subs.	3.21	0.42 (2.27)	0.64	2.98, 3.01	0, -5.28×10^{-4}	0.29	-1.58×10^{-3}
Hollow	3.28	1.84	0.35	2.84, 2.89	0, -3.80×10^{-3}	0.28	-1.24×10^{-3}
Mo atop	3.27	2.61	0.28	2.94, 3.02	0, -2.43×10^{-3}	0.09	-2.57×10^{-3}
S atop*	3.25	3.72	0.06	2.83, 2.87	0, -4.93×10^{-3}	0.16	-5.63×10^{-3}
4 × 4							
Mo subs.	3.24	2.50 (1.58)	0.23	2.76	$(1.17, -1.17) \times 10^{-3}$, 0	0.25	0
S subs.*	3.22	1.81 (3.66)	0	2.78, 2.82	0, -6.60×10^{-4}	0.18	-8.05×10^{-4}
Hollow	3.23	1.39	0.06	2.78	$(-2.56, 2.58) \times 10^{-5}$, 0	0.37	-3.71×10^{-4}
Mo atop	3.22	1.72	0.06	2.82	$(1.47, -1.45) \times 10^{-5}$, 0	0.21	-1.31×10^{-3}
S atop	3.24	2.58	0	2.79	0, -4.40×10^{-4}	0.20	-4.08×10^{-4}

Table 3.5: Magnetism in Ni-doped 1T-MoS_2: net (and absolute) magnetization μ (in μ_B) for the ground state, and energy difference ΔE (meV) of spin-polarized state *vs.* the non-spin-polarized paramagnetic state. μ and ΔE are per supercell, each with one Ni atom. The magnetic moment of Ni, where nonzero, is given in square brackets.

Doping type	1×1		2×2	
	μ net (abs.) [Ni]	ΔE	μ net (abs.) [Ni]	ΔE
Mo subs.	-	-	0 (0)	-0.08
S subs.	0 (0)	-0.02	0.05 (0.10) [0.07]	-0.19
Hollow	0 (0)	-0.02	0 (0)	-0.08
Mo-atop	0 (0)	-0.02	0 (0)	-0.09
S-atop	0 (0)	-0.02	0.30 (0.42) [0.32]	-17.32

Doping type	3×3		4×4	
	μ net (abs.) [Ni]	ΔE	μ net (abs.) [Ni]	ΔE
Mo subs.	0 (0)	-0.17	0 (0)	-0.30
S subs.	0 (0)	-0.10	0.78 (1.03) [0.56]	-27.91
Hollow	0 (0)	-0.17	0 (0)	-0.30
Mo-atop	0 (0)	-0.19	0 (0)	-0.31
S-atop	0.00 (0.07) [0.03]	-0.09	0 (0)	-0.30

Table 3.6: Symmetry analysis for pristine structures: overall (space group and point group), local symmetry of each Mo with its nearest S (point group), overall symmetry of just the Mo atoms (space group and point group), and local symmetry of each Mo with its Mo neighbors. For local symmetry, the number of Mo atoms in the cell with each point group is indicated.

Structure	Overall	Mo and S neighbors	All Mo	Mo and Mo neighbors
2×1	$P2_1/m$, C_{2h}	$2\times C_s$	$P2_1/m$, C_{2h}	$2\times C_s$
2×2	Cm, C_s	$4\times C_s$	Cm, C_s	$3\times C_1$ $1\times C_s$
3×3	$P1$, C_1	$6\times C_1$ $3\times C_s$	Cm, C_s	$6\times C_1$ $3\times C_s$
$\sqrt{3} \times \sqrt{3}$ 2B	$P31m$, C_{3v}	$3\times C_s$	$P\bar{6}2m$, D_{3h}	$3\times C_{2v}$
$\sqrt{3} \times \sqrt{3}$ 4B	$P31m$, C_{3v}	$3\times C_s$	$P\bar{6}2m$, D_{3h}	$3\times C_{2v}$
4×4	$P1$, C_1	$16\times C_1$	$P1$, C_1	$16\times C_1$

Table 3.7: Comparison of energies between PBE (as in main text), PBE+U, and the hybrid functional PBE0. [49, 6] Here, a, b are the lattice parameters ($a = b$ in most cases); d is the shortest Mo-Mo distance, characterizing clustering, and ΔE is the energy difference per MoS_2 with undistorted 1T in each case. The a, b for PBE0 functional were fixed to those of PBE.

Structure	**PBE**			**PBE** $+U$			**PBE0**	
	ΔE	a, b (Å)	d	ΔE	a, b (Å)	d	ΔE	d
1×1	0	3.18	3.18	0	3.13	3.18	0	3.18
2×1	-0.26	5.67, 3.18	2.78	-0.27	5.59, 3.14	2.73	-0.25	2.79
2×2	-0.21	6.43	2.78	-0.19	6.32	2.78	-0.18	2.78
3×3	-0.24	9.70	2.93	-0.24	9.55	2.88	-0.22	2.95
$\sqrt{3} \times \sqrt{3}$ 2B	-0.19	5.64	2.84	-0.22	5.57	2.80	-0.20	2.83
$\sqrt{3} \times \sqrt{3}$ 4B	-0.26	5.61	3.02	-0.26	5.52	2.97	-0.24	3.05
4×4	-0.15	13.01	2.78	-0.18	12.81	2.74	-0.13	2.77

Table 3.8: Symmetry analysis for doped structures: (space group and point group).

Supercell	Mo subs.	S subs.	Hollow	Mo atop	S atop
1×1	-	$P3m1, C_{3v}$	$P3m1, C_{3v}$	$P3m1, C_{3v}$	$P3m1, C_{3v}$
2×2	Cm, C_s	$P3m1, C_{3v}$	Cm, C_s	$P3m1, C_{3v}$	$P3m1, C_{3v}$
3×3	$P3m1, C_{3v}$	$P3m1, C_{3v}$	$P3m1, C_{3v}$	$P3m1, C_{3v}$	$P3m1, C_{3v}$
4×4	Cm, C_s	$P3m1, C_{3v}$	Cm, C_s	Cm, C_s	$P3m1, C_{3v}$

(a) adatoms

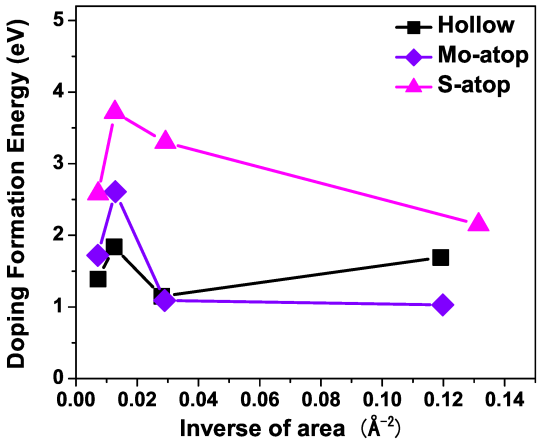

(b) Mo substitution

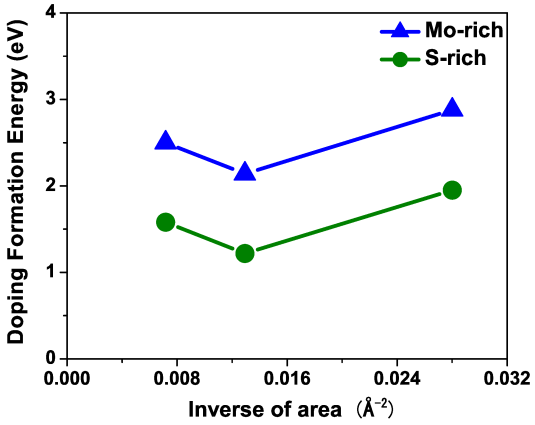

(c) S substitution

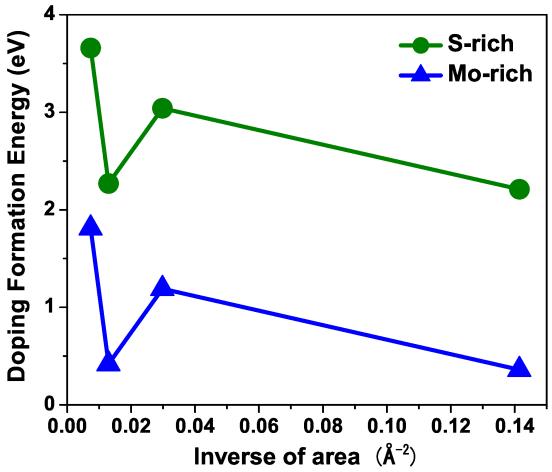

Figure 3.7: Doping formation energies of 1T-MoS_2, vs. concentration: a) adatoms, b) Mo substitution under Mo-rich and S-rich conditions, and c) S substitution under S-rich and Mo-rich conditions. Irregular trends are due to reconstructions, unlike in Fig. 3.8. There is no 1×1 Mo-substituted structure as it would be NiS_2 which adopts a different structure.

(a) adatoms

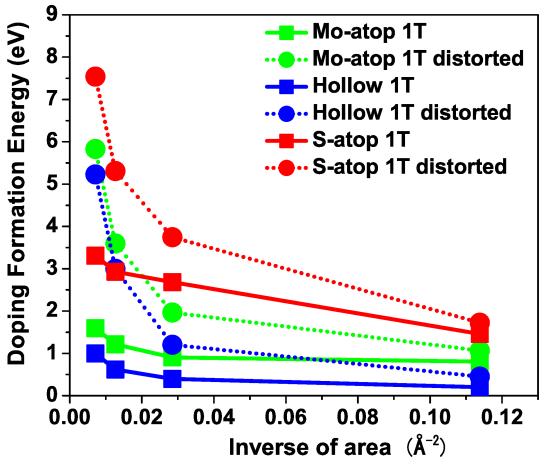

(b) Mo substitution

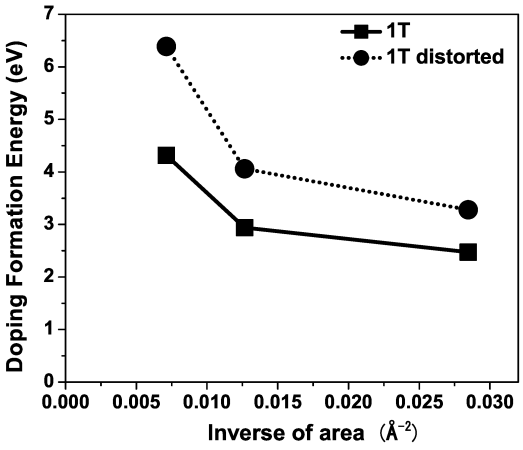

(c) S substitution

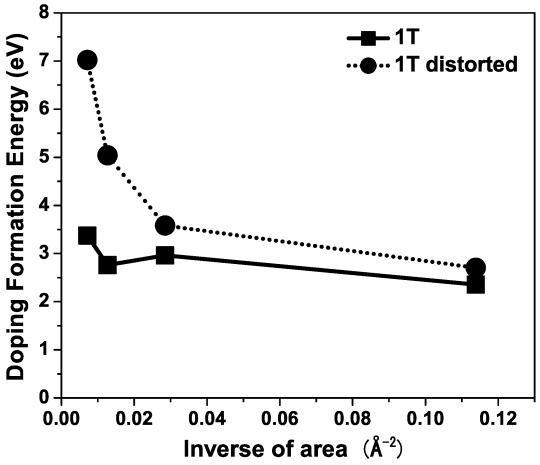

Figure 3.8: Unrelaxed doping formation energies of 1T-MoS_2, where the lattice and Mo and S coordinates are fixed as those of pristine 1T, with comparison to distorted 1T′ or undistorted pristine 1T: a) adatoms, b) Mo substitution under Mo-rich and S-rich conditions, and c) S substitution.

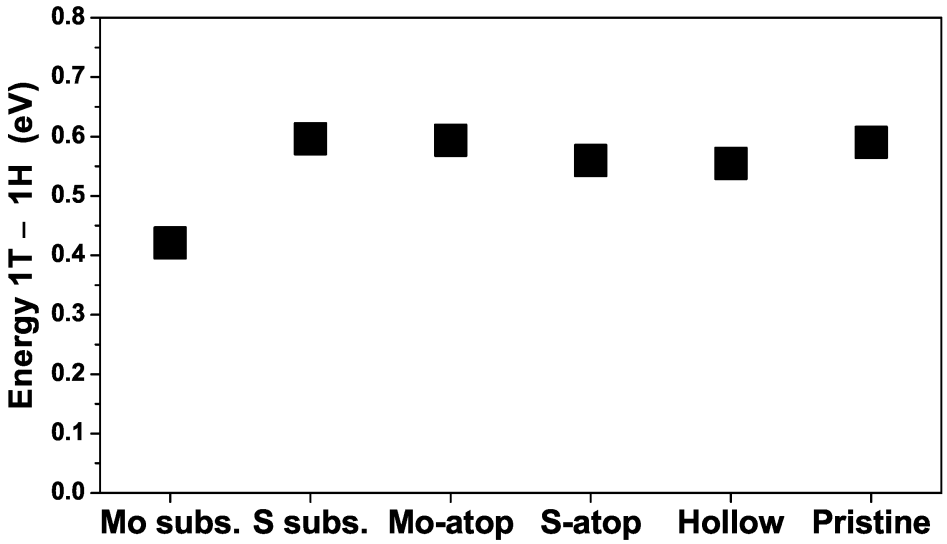

Figure 3.9: Energy difference (1T-1H) per MoS_2 for doped and undoped monolayers with $4 \times 4 \times 1$ supercell. Here, pristine is the most stable distorted 1T (1T′). The lower total energy for 1H indicates formation of 1H phase is more likely given isolated Mo, Ni and S atoms.

(a) phase diagram

(b) formation energy

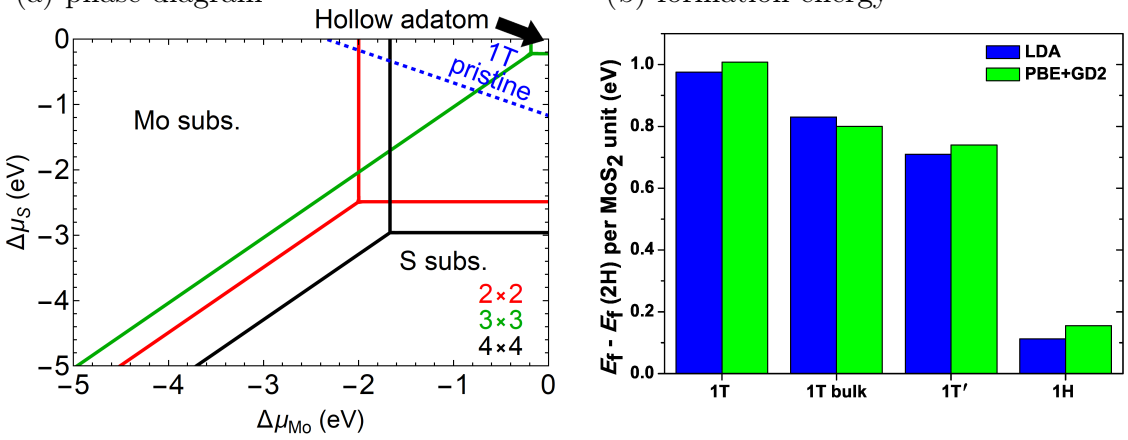

Figure 3.10: a) Phase diagrams for 1T indicating the stable doping site as a function of Mo and S chemical potentials, as in [72] The pristine phase is stable in the triangle above and to the right of the dotted line. b) Formation energy of MoS_2 polytypes, with respect to 2H. [103]

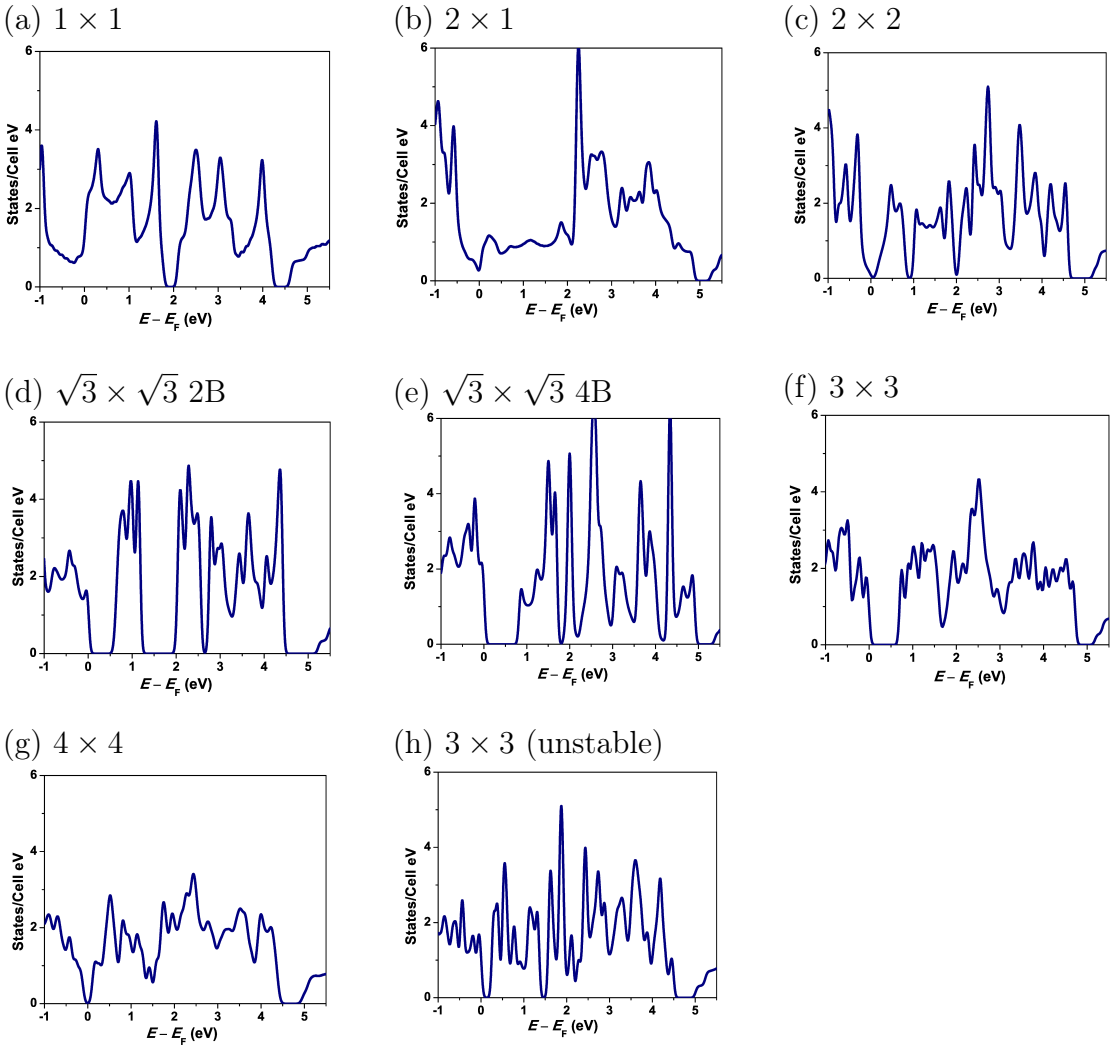

Figure 3.11: Density of states (DOS) showing gaps in higher conduction bands for pristine (a) 1×1, (b) 2×1, (c) 2×2, (d) $\sqrt{3} \times \sqrt{3}$ 2B, (e) $\sqrt{3} \times \sqrt{3}$ 4B, (f) 3×3, (g) 4×4, and (h) unstable 3×3 1T.

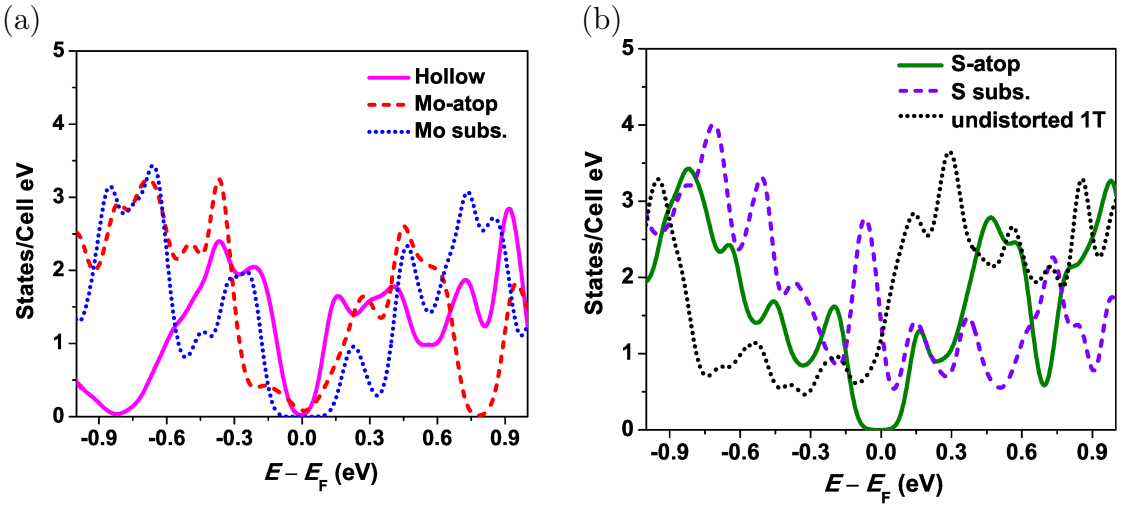

Figure 3.12: Density of states for 1T 4×4×1 structures, comparing doped structures with undistorted pristine 1T.

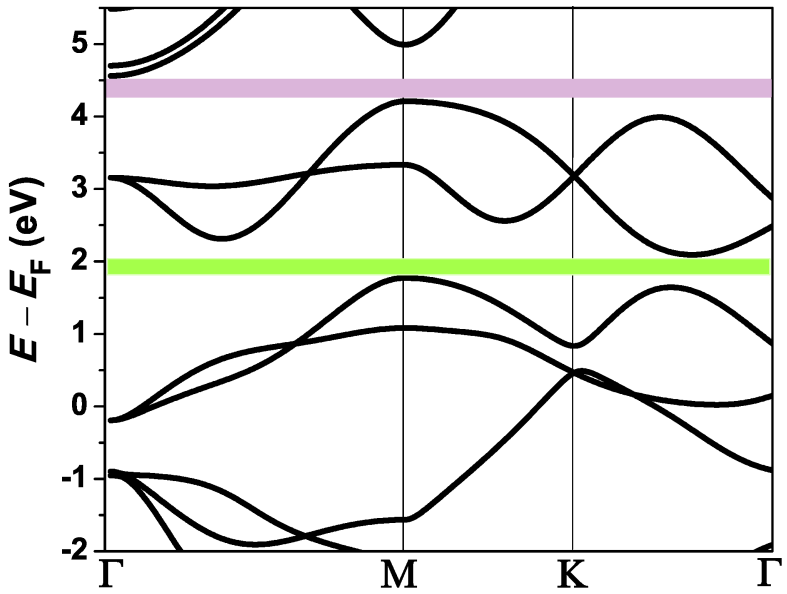

Figure 3.13: Band structure of metallic undistorted 1T (1×1) showing gaps among conduction bands: purple for a gap common to all structures due to transition between Mo *s* and *d*-orbitals, and green for other gaps above the fundamental gap.

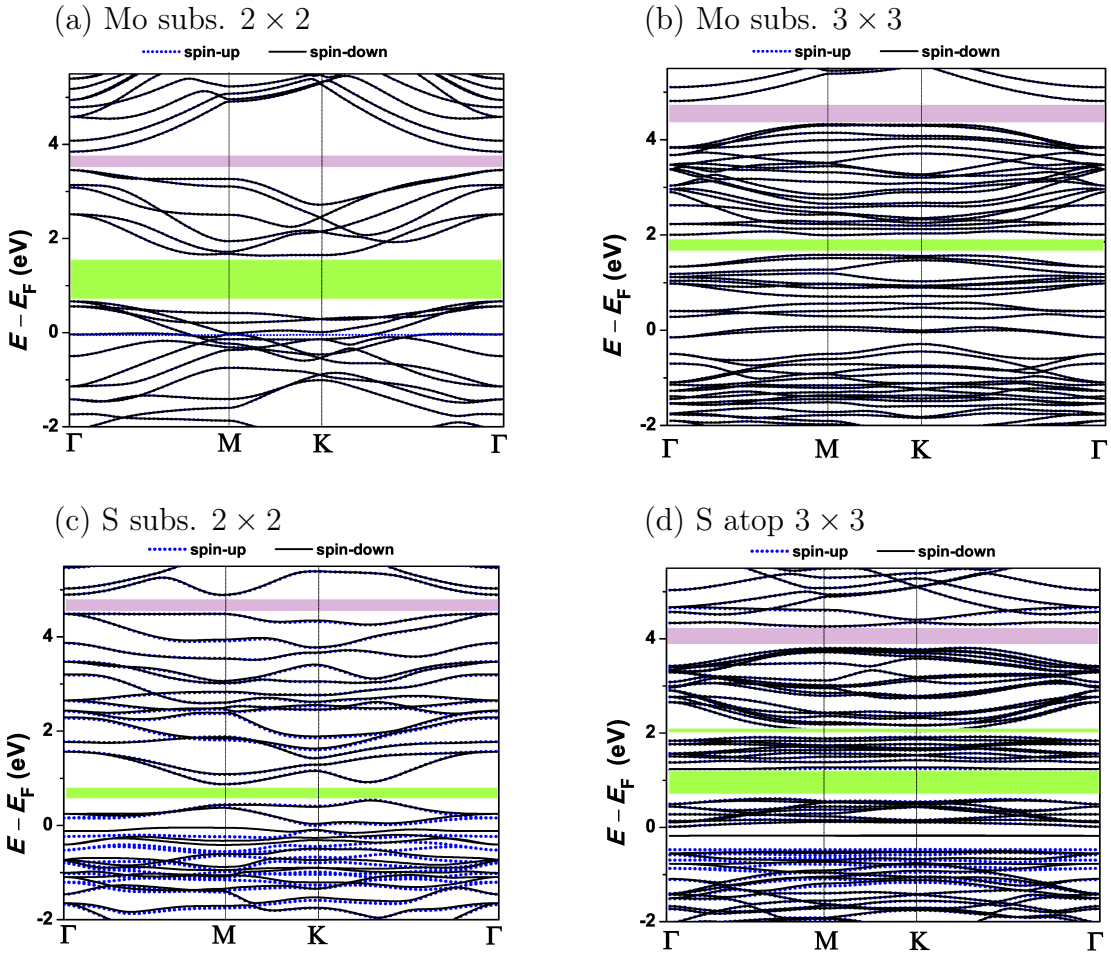

Figure 3.14: Bandstructures of Ni-doped 1T MoS_2 structures showing any magnetism. For metallic cases (Mo substitution 2×2 and 3×3, S substitution 2×2), energies are plotted with respect to the Fermi energy. As in pristine cases, we find multiple gaps even in case of metals. As in main text, colored stripes highlight the gaps, with pink as the fundamental band gap, purple as a gap common to all structures due to transition between Mo s and d-orbitals, and green for gaps in between those two. Detail of (c) in Fig. 3.15.

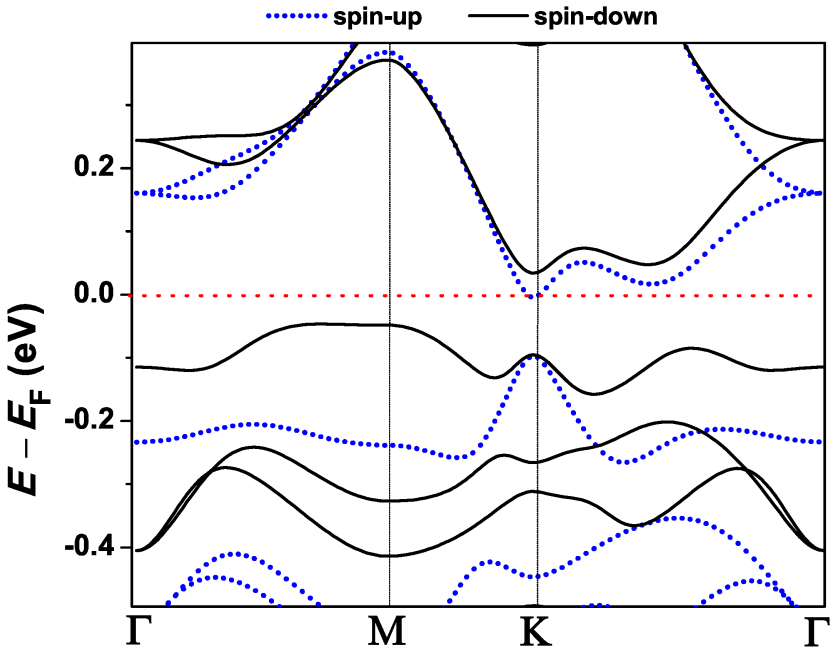

Figure 3.15: Detail of band structure of S substitution 2×2 (Fig. 3.14 (c)), showing a semimetallic nature with a very small gap and a small band crossing of one spin at the Fermi level.

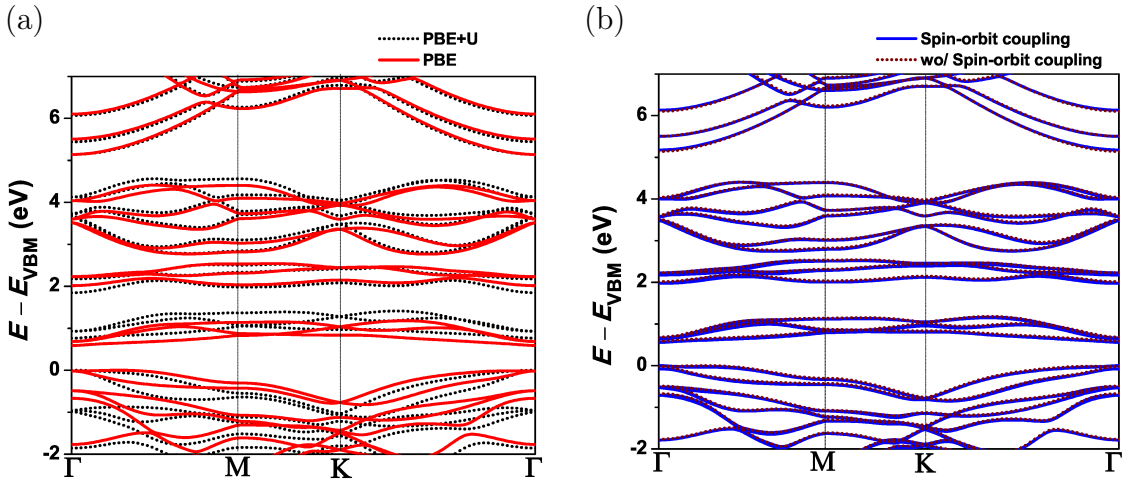

Figure 3.16: Bandstructure comparison for $\sqrt{3}\times\sqrt{3}$ 2B, with and without a) U [5.5 eV for Ni [244] and 4 eV for Mo [221]], and b) spin-orbit coupling. Bandstructure differences are small.

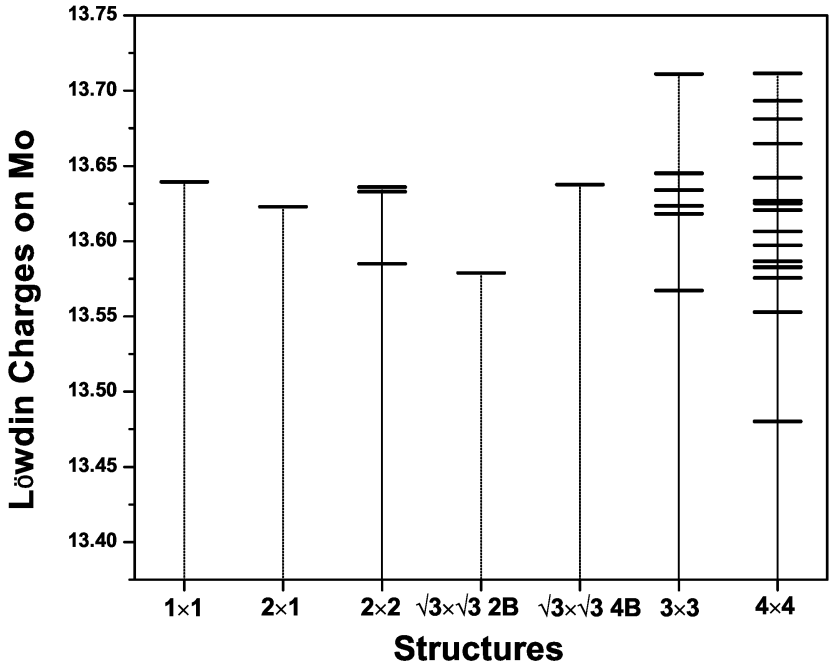

Figure 3.17: Distribution of Löwdin charges on each Mo in different pristine structures, showing partial charges of $+0.3e$ to $+0.6e$. The ionic charge is Z=14 for this pseudopotential.

(a) Mo clustering

(b) Phonon bandstructure

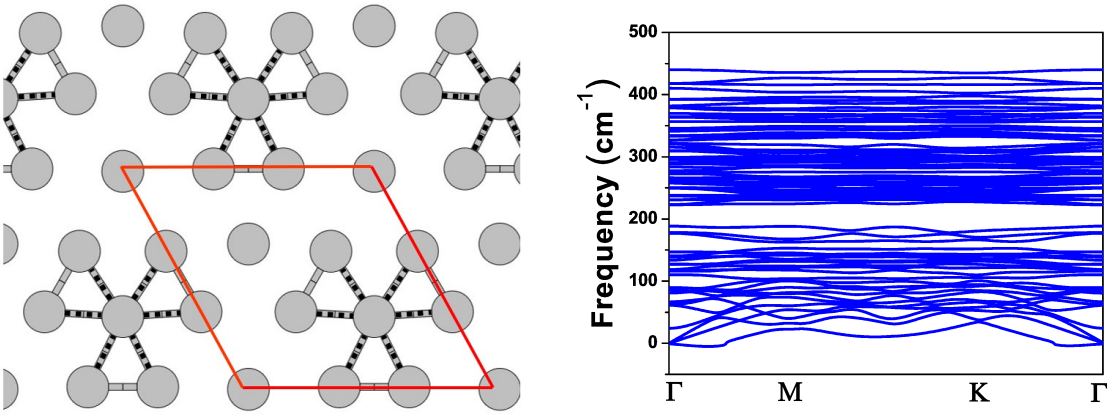

Figure 3.18: The pristine 3×3 unstable reconstruction: (a) Mo-clustering, and (b) phonon dispersion showing imaginary frequencies at Γ and nearby, in the Brillouin zone of its primitive cell.

(a)

(b)

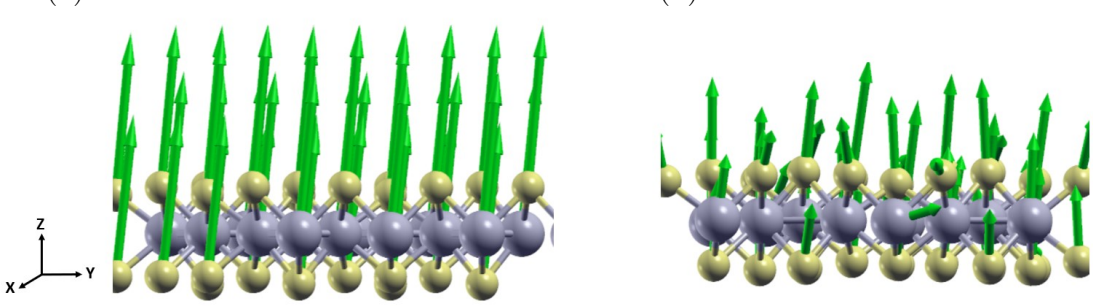

Figure 3.19: Displacement patterns of flexural modes for a) 2×2 structure at Γ point and b) 4×4 structure at M point.

Chapter 4

Low-energy nine-layer rhombohedral stacking of transition metal dichalcogenides

4.1 Abstract

Transition-metal dichalcogenides (TMDs) show unique physical, optical, and electronic properties. The known phases of TMDs are 2H and 3R in bulk form, 1T and associated reconstructions, and 1H in monolayer form. This paper reports a hypothetical phase, 9R, that may exist in TMDs meeting both dynamical stability and elastic stability criteria. 9R phase has a similar space group to 3R *i.e.* trigonal $R3m$ and has 9 layers in a conventional unit cell. Here, we calculate the electronic, elastic, piezoelectric, and Raman signatures of 9R and compare them with the 2H and 3R phases in TMDs. 9R has similar properties as 3R but shows distinctive Raman peaks in the low-frequency regime, improved piezoelectric properties, and unique band splitting arising from layer coupling at the conduction band minimum. These distinct properties make 9R an attractive candidate for applications in the fields of piezotronics and valleytronics devices.

4.2 Introduction

Transition-metal dichalcogenides (TMDs) have emerged as a class of attractive two-dimensional materials and have attracted significant attention in the fields of condensed matter physics and nanotechnology. TMDs exhibit a layer structure consisting of transition metal atoms, usually in groups 4 to 7, sandwiched between Chalcogen atoms such as Sulfur, Selenium, or Tellurium. The different atomic arrangements and reduced dimensions of TMDs produce a wealth of unique electronic [20], optical [145] and mechanical properties [229], attracting considerable interest in their fundamental research and potential technological applications. Due to their adjustable band gaps [144], strong spin-orbit couplings [52], and high carrier mobility [101], TMDs have proved promising capabilities in the fields of optical, electronics, catalysis, and energy storage. In recent years, significant progress has been made in synthesizing and characterizing TMD monolayers and heterostructures, revealing new phenomena and enabling the engineering of multifunctional devices [169, 15]. Research in this field is ongoing, and the characterization of complex TMD behaviors and their unique characteristics has a profound impact on the development of next-generation electronic and photonic technologies.

Furthermore, to add the prospect, TMDs come in different phases *i.e.* monolayer and bulk offering further interesting properties. For example, in MoS_2, monolayer 1T is metallic while monolayer 1H is semiconducting with a direct gap [104]; and 2H and 3R are bulk phases that differ by stacking (sliding followed by rotation) but are similar in energetics and electronic bandstructure with indirect band-gap from theoretical calculation [103], yet 2H is centrosymmetric while 3R is noncentrosymmetric offering different applications such as piezoelectricity and second harmonic generation [194]. Given the importance of other phases might bring new insight into the application, it is important to look for other polymorphs. In this paper, we report a nine-layer phase belonging to R3m space group and because of this, we call 9R, as per Ramsdell notation, hereafter as a potential new phase of TMDs. The 9R phase is a known phase for other compounds like SiC [224] but not reported for TMDs. A literature investigated hypothetical polytypes of MoS_2 based on a random searching method using density function theory reported

several stable and unstable polymorphs of MoS_2 but did not report the nine-layer phase. [27] In that paper, an unstable 6R phase is reported.

In this paper, we propose the stability of the nine-layer phase in 6 TMDs, namely MoS_2, $MoSe_2$, $MoTe_2$, WS_2, WSe_2, and WTe_2 meeting the criteria of dynamical stability and Elastic stability. We then discuss the unique signatures in Raman, SHG and diffraction patterns for the new phase and explore some properties, like piezoelectricity and spin-orbit splitting of bands. Finally, we suggest possible experiments that would allow us to synthesize the new phase.

4.3 Methodology

Our calculations use plane-wave density functional theory (DFT) implemented in the code Quantum ESPRESSO, version 7.1 [68, 67]. We used the Perdew-Burke-Ernzerhof (PBE) generalized gradient approximation [164] for structural analysis and electronic bandstructure, and local density approximation (LDA) functional [165] for Raman, elastic and peizoelectric properties. With PBE, we used the semi-empirical Grimme-D2 (GD2) [71] Van der Waals correction to the total energy, which gives lattice parameters and other properties considerably closer to experimental results [163, 72]. Calculation with LDA has also been shown to give accurate lattice parameters [72]. We used Optimized Norm-Conserving Vanderbilt pseudopotentials [79] and fully relativistic pseudopotential set for spin-orbit calculation from Pseudodojo set [2]. Kinetic energy cutoffs of 952 eV (70 Ry) for PBE and 1224 eV (90 Ry) for LDA were used. Half-shifted k-point grids of $6 \times 6 \times 2$ were chosen to converge the total energies within 0.001 eV/atom for 2H, 3R and 9R. Atomic coordinates were relaxed using a force threshold of 10^{-4} Ry/bohr and the stresses were relaxed below 0.1 kbar. For calculating the piezoelectricity, we used the Berry-phase method [175] for calculation of polarization, where we used 30 k-points (`nppstr`=30) in the direction of k-point strings (`gdir`).

4.4 Results

4.4.1 Structure, energetics, and stability

The structure of the 9R phase has the same space group of 3R *i.e.*$R3m$ containing nine layers with 27 atoms in a conventional unit cell. The stacking sequence of the structure is bAb cBc bAb aCa bAb aCa cBc aCa cBc, where small letter represents the transition metal and capital letter represents the chalcogens as shown in Figure 4.1. The details of the lattice parameters comparison are shown in Table 4.1. The conventional unit cell of 9R has $a = b \neq c$ and $\alpha = \beta = 90°$and $\gamma = 120°$. Also, note that there exists a primitive unit cell for 9R phase with 9 atoms per unit cell. In the primitive cell, $a = b = c$ and $\alpha = \beta = \gamma \neq 90°$.

TMDs	$a = b$			c			**Layer spacing**		
	2H	3R	9R	2H	3R	9R	2H	3R	9R
MoS_2	3.18	3.19	3.19	12.36	18.47	55.42	6.18	6.16	6.16
$MoSe_2$	3.24	3.25	3.25	12.18	18.06	54.20	6.09	6.02	6.02
$MoTe_2$	3.52	3.53	3.53	13.96	20.95	62.87	6.98	6.97	6.97
WS_2	3.18	3.18	3.18	12.14	18.14	54.43	6.08	6.04	6.05
WSe_2	3.24	3.26	3.26	12.04	17.86	53.61	6.02	5.95	5.95
WTe_2	3.56	3.56	3.56	13.78	20.68	62.07	6.89	6.89	6.90

Table 4.1: Lattice parameters comparison in 2H, 3R and 9R phase in a conventional unit cell for 3R and 9R using PBE+GD2. All units are in Å.

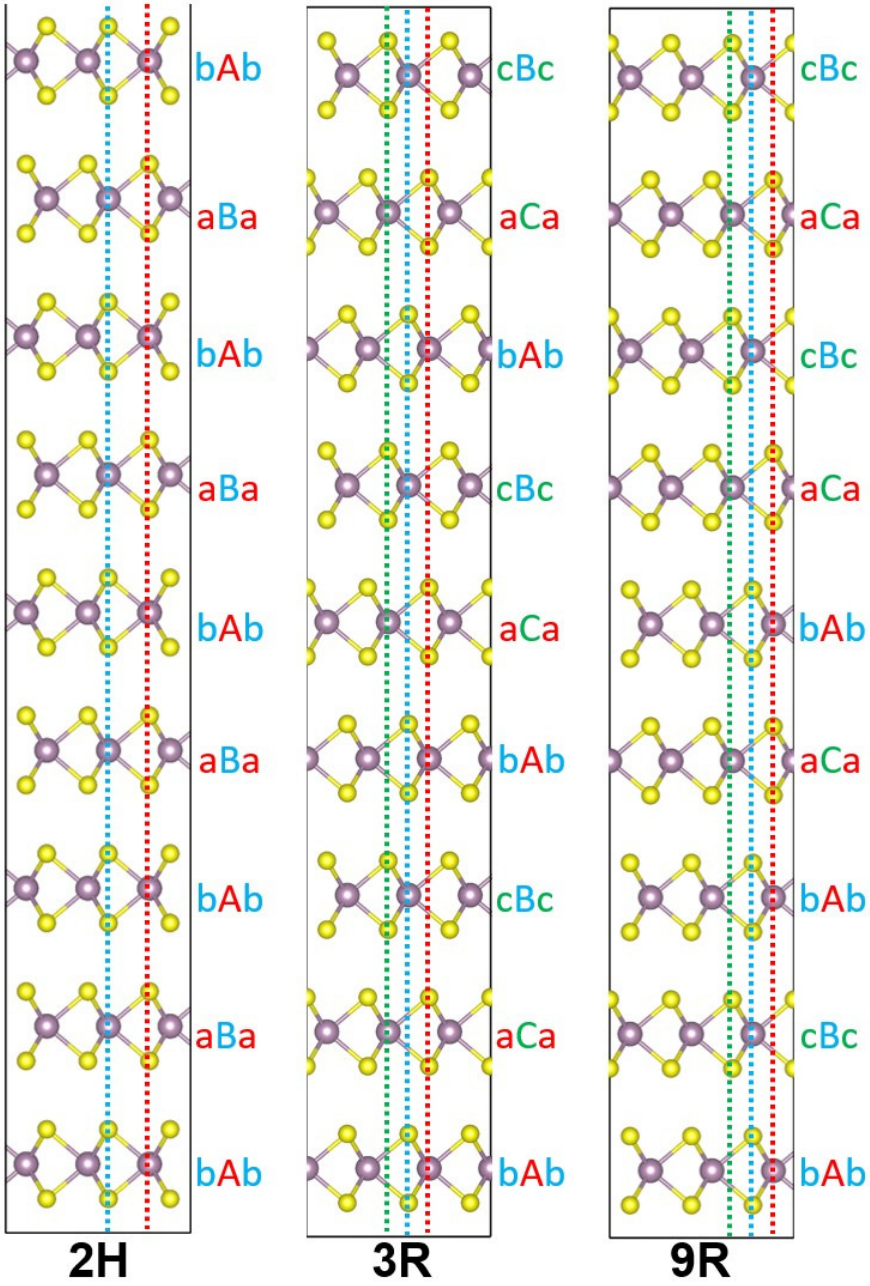

Figure 4.1: Structure comparison in 2H, 3R and 9R phase. The dotted red, blue and green lines corresponds to A, B and C alphabets and transition metal layer is represented by capital letters and sandwiching chalcogens are represented by small letters.

Table 4.2 shows the energy difference between the 2H, 3R, and 9R phases in 6 TMDs with PBE+ GD2 and LDA. We see that the energy difference between 3R

and 9R phase is very small.

Table 4.2: Energy difference between 2H, 3R and 9R phases (meV). Here the energy of 3R is set to zero, so more the negative value, the more the phase is favorable. 2H phase is most favorable and 9R is least favorable phase, except in LDA calculation in $MoTe_2$, where 9R has lower energy than 3R.

Structure	**PBE+GD2**		**LDA**	
	Δ_{2H-3R}	Δ_{3R-9R}	Δ_{2H-3R}	Δ_{3R-9R}
MoS_2	-0.11	0.11	-0.97	0.31
$MoSe_2$	-8.61	0.03	-4.72	0.34
$MoTe_2$	-12.4	0.45	-17.1	-1.11
WS_2	-0.83	0.21	-4.70	0.23
WSe_2	-5.57	0.33	-8.62	0.24
WTe_2	-15.6	0.60	-21.3	0.47

Dynamical stability

We tested the dynamical stability of the material by computing the phonon dispersion and found no imaginary frequencies in the dispersion for all TMDs. The presence of non-negative frequency modes corresponds to the structure being stable and at local minimum in the potential energy surface. So, under small perturbation, the structure can be retained after relaxation. Figure 4.2 shows the phonon bandstructure of 9R TMDs in the in-plane and out-plane of the hexagonal Brillouin zone. For comparison, we also calculated the phonon bandstructure of 3R TMDs and results are similar and is shown in Supplementary Information (Fig 4.9).

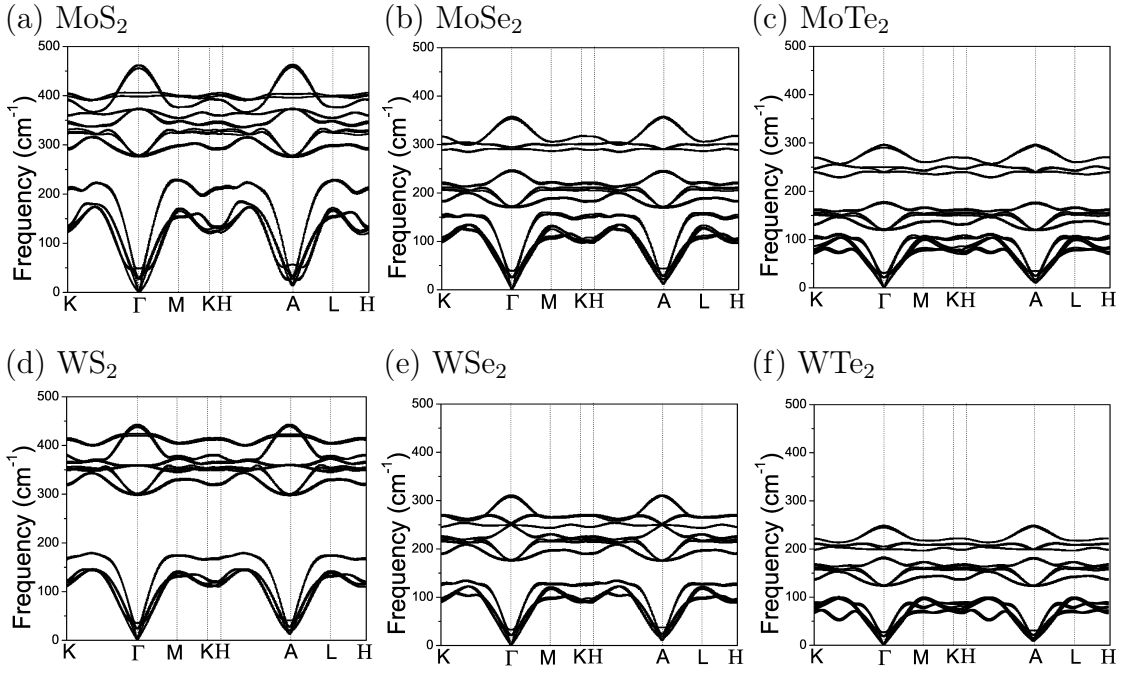

Figure 4.2: Calculated phonon bandstructure of 9R TMDs both in the in-plane and out-plane of the Brillouin zone.

Elastic stability

The crystal structure is stable in the presence of external loads within the harmonic approximation limit if and only if both the dynamical stability and elastic stability criteria are satisfied. In the previous section, we discussed the stability based on positive phonon frequencies across the Brillouin zone. The paper by [154] describes the necessary and sufficient elastic criteria based on different crystal system. Based on it, the necessary and sufficient elastic criteria for Rhombohedral class of crystals must satisfy:

$$\begin{aligned} &C_{11} > |C_{12}|, C_{44} > 0, \\ &C_{13}^2 < \tfrac{1}{2} C_{33}(C_{11} + C_{12}), \\ &C_{14}^2 < \tfrac{1}{2} C_{44}(C_{11} - C_{12}) \end{aligned} \tag{4.1}$$

Based on Table 4.3, we can see that all elastic criteria as shown in Equation 4.1 are satisfied for 9R. Many elastic constants of 2H- and 3R- in those TMDs are

Table 4.3: Elastic coefficients (in GPa).

Phase		C_{11}	C_{12}	C_{13}	C_{14}	C_{33}	C_{44}
MoS_2	2H	240	57	10	0	53	17
	3R	242	60	15	4	45	19
	9R	242	60	16	1	46	18
$MoSe_2$	2H	194	44	13	0	52	17
	3R	194	46	17	4	45	17
	9R	194	46	18	1	46	17
$MoTe_2$	2H	138	32	14	0	52	23
	3R	138	35	18	3	42	18
	9R	137	34	18	1	42	17
WS_2	2H	261	55	10	0	52	22
	3R	262	57	14	4	44	21
	9R	262	57	15	1	45	16
WSe_2	2H	210	40	12	0	52	25
	3R	209	42	16	4	44	17
	9R	208	40	16	1	44	15
WTe_2	2H	147	25	13	0	52	23
	3R	146	28	17	3	42	17
	9R	145	27	16	1	42	16

not reported. Some of them we found agree well with experimental or theoretical works. For example, 2H- MoS_2 agrees well with the experiment [57] and DFT works [232]. Similarly, the elastic tensor of 3R-MoS_2 agrees well with the theoretical work [194]. Furthermore, the elastic tensor of 2H-phase of $MoSe_2$ agrees well with the experiment [12].

4.4.2 Raman characterization of TMDs

We conducted a comprehensive characterization of the Raman spectra for all bulk phases across six different TMDs. Figure 4.4 presents the calculated Raman spectra for these TMDs in all bulk phases, and detailed information regarding peak positions and the corresponding mode characteristics can be found in Table 4.4. Notably, both the 2H and 9R phases exhibit a distinct peak in the low-frequency regime (below 50 cm^{-1}), which is notably absent in the 3R phase. Conversely, both the 3R and 9R phases feature a high-frequency peak, with the specific frequency varying depending on the type of TMD. This high-frequency peak is not observed in the 2H phase. Based on these observations, we propose that it is possible to distinguish between the 9R, 3R, and 2H phases in Raman experiments by comparing the Raman shifts at both the low- and high-frequency regimes. In the majority of cases, the Raman active modes in the 2H, 3R, and 9R phases exhibit similar vibration patterns. At the low-frequency regime, we observe layer vibrations in opposite directions in both the 2H and 9R phases as shown in 4.3. In the mid-frequency range, the Raman active modes are dominated by D (Dichalcogenides) vibrations, which occur either in-plane in parallel and anti-parallel directions or out-of-plane. The widest Raman active regime is characterized by TM (Transition Metal) and D atoms vibrating in opposite directions out-of-plane in 3R and 9R (see Fig. 4.3). These shared vibration patterns provide valuable insights into the structural and vibrational characteristics of these phases.

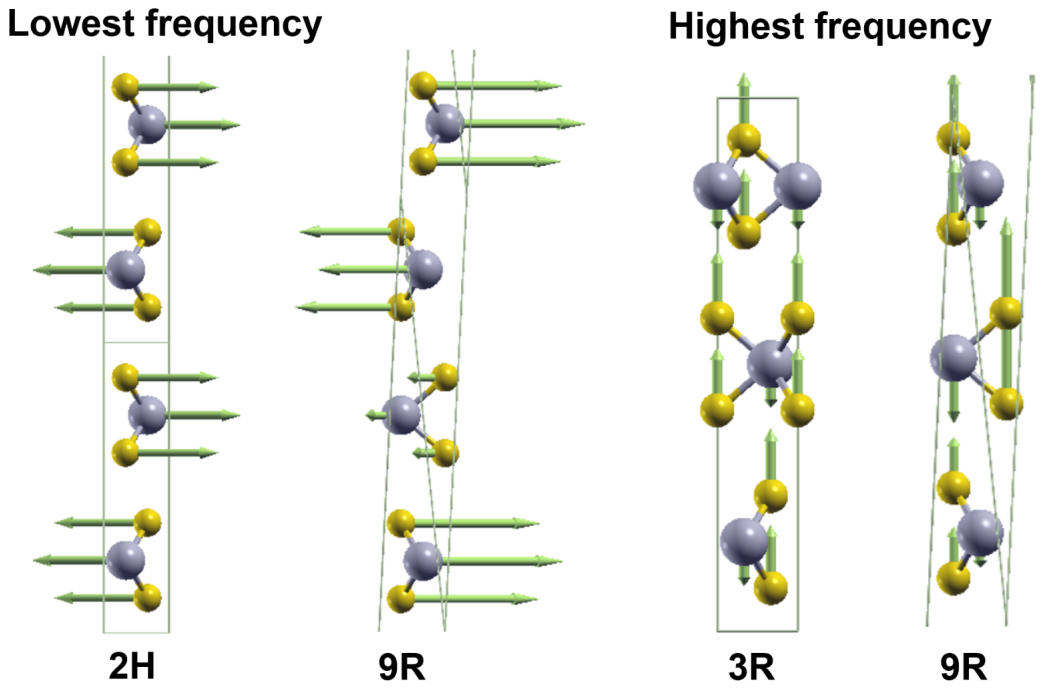

Figure 4.3: Modes of vibration in low and high Raman active modes. Here, transition metal is shown in grey and chalcogens are shown in yellow. The boxes represent primitive (2H and 9R) and a conventional cell (3R). Farthest Raman modes varies depending on material but this mode corresponds to the rightmost Raman active mode in Fig. 4.4.

Additionally, the 9R phase, which shares the lack of inversion symmetry with the 3R phase, should, in principle, exhibit second-harmonic generation (SHG). On the other hand, the 2H phase lacks this property. In experiments, researchers have often relied on SHG to differentiate between the 2H and 3R phases, as shown in [78]. However, we argue that SHG alone may not be sufficient to distinguish between 2H and 3R, especially given the existence of the 9R phase. Instead, we suggest that SHG can help rule out the 2H phase, while Raman spectroscopy can provide confirmation between the 3R and 9R phases, particularly by examining the low-frequency Raman peaks. To facilitate experimentalists working with SHG, we have provided two significant ratios for distinguishing between the 3R and 9R phases, as outlined in Table 4.5. Specifically, we have found that the $\chi^{(2)}_{zzz}$ ratio is approximately twice as large in the 3R phase compared to the 9R phase. However,

the ratio of $\chi^{(2)}_{yyy}$ varies, with the 3R phase exhibiting greater SHG intensity for the Mo family and the 9R phase displaying higher SHG intensity for the W family. This insight can guide SHG experiments in determining the intensity ratio between the 3R and 9R phases. The exact tensor of $\chi^{(2)}$ for C_{3v} point group is given by [94]:

$$\overleftrightarrow{\chi}^{(2)} = \begin{pmatrix} \begin{pmatrix} 0 & -\chi_{222} & \chi_{131} \\ -\chi_{222} & 0 & 0 \\ \chi_{113} & 0 & 0 \end{pmatrix} \\ \begin{pmatrix} -\chi_{222} & 0 & 0 \\ 0 & \chi_{222} & \chi_{131} \\ 0 & \chi_{113} & 0 \end{pmatrix} \\ \begin{pmatrix} \chi_{311} & 0 & 0 \\ 0 & \chi_{311} & 0 \\ 0 & 0 & \chi_{333} \end{pmatrix} \end{pmatrix} \tag{4.2}$$

TMDs	2H	3R	9R
MoS_2	36.58 (E_{2g}), 291.3 (E_{1g}), 389.4 (E_{2g}), 414.4 (E_{2g})	292.2 (E), 389.1 (E), 414.1 (A_1), 470.5 (A_1)	30.3 (E), 292.1 (E), 389.8 (E), 414.7 (A_1), 469.4 (A_1)
$MoSe_2$	49.6 (E_{2g}), 180.9 (E_{1g}), 264.6 (A_{1g}), 297.9 (E_{2g})	172.1 (E), 246.5 (A_1), 289.6 (E), 352.9 (A_1)	23.3 (E), 169.8 (E),172 (E), 246.7 (A_1), 289.7 (E), 352.3 (A_1)
$MoTe_2$	29.6 (E_{2g}), 121.8 (E_{1g}), 178.3 (A_{1g}), 239.5 (E_{2g})	122.5 (E), 178.9 (A_1), 240.1 (E), 290.7 (A_1)	20.5 (E), 120.6 (E), 177.9 (A_1), 239 (E), 289.2 (A_1)
WS_2	28.4 (E_{2g}), 300.4 (E_{1g}), 358.6 (E_{2g}), 423 (A_{1g})	301.5 (E), 358.5 (E), 423.6 (A_1), 438 (A_1)	24.1 (E), 298.7 (E), 301.4 (E), 358.5 (E), 424.2 (A_1), 436.8 (A_1)
WSe_2	43 (E_{2g}), 185.4 (E_{1g}), 255.1 (E_{2g}), 269.9 (A_{1g})	177.2 (E), 248.8 (E), 252.7 (A_1), 307.5 (A_1)	33.7 (A_1), 184.3 (E), 248.9 (E), 253.3 (A_1), 306.8 (A_1)
WTe_2	26.3 (E_{2g}), 125.4 (E_{1g}), 183 (A_{1g}), 198.9 (E_{2g})	125.6 (E), 182.7 (A_1), 199.2 (E), 244.6 (A_1)	18 (A_1), 127.3 (E),129.8 (E), 183.8 (A_1), 199.6 (E), 243.8 (A_1)

Table 4.4: Raman active modes (in cm^{-1}) and their corresponding character are given in parenthesis.

We also performed calculations of the powder diffraction patterns on the TMDs

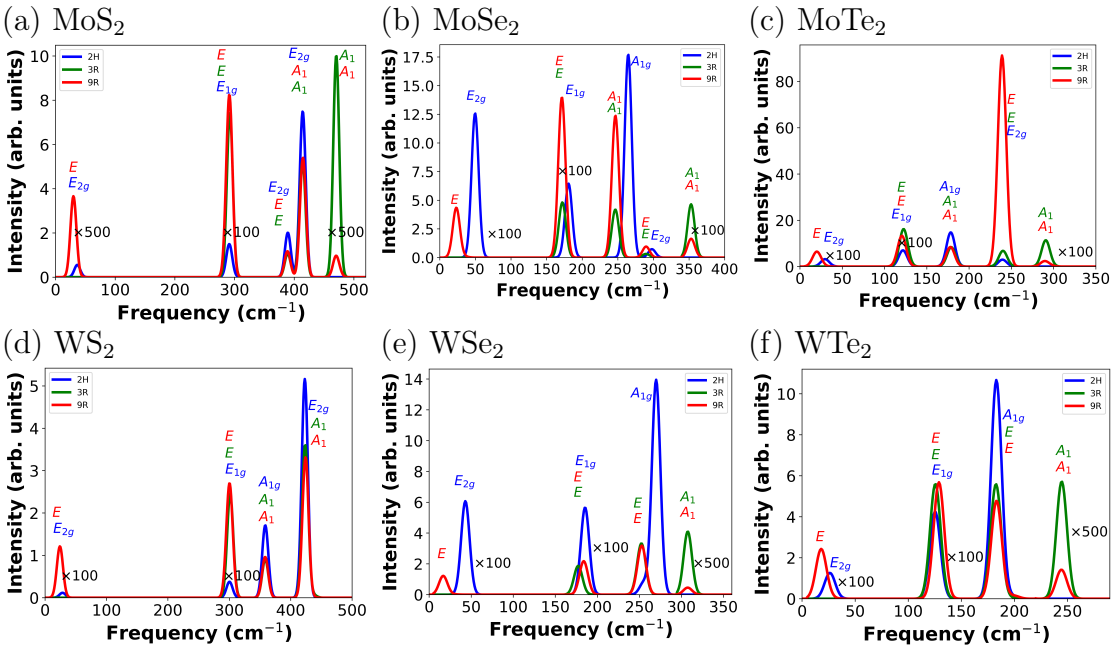

Figure 4.4: Calculated Raman spectra of different TMDs in 2H, 3R and 9R phases. The highest frequency modes in WS_2 do exist (see Table 4.4) but are mixed to larger nearby peaks. In a few frequency ranges, we scaled the intensities (shown by a multiplicative factor for all phases in that range) for visualization purposes.

TMDs	$\frac{^{9R}\chi^{(2)}_{yyy}}{^{3R}\chi^{(2)}_{yyy}}$	$\frac{^{9R}\chi^{(2)}_{zzz}}{^{3R}\chi^{(2)}_{zzz}}$
MoS_2	0.75	0.37
$MoSe_2$	0.06	0.40
$MoTe_2$	0.46	0.37
WS_2	3.70	0.37
WSe_2	7.14	0.43
WTe_2	8.33	0.45

Table 4.5: SHG ratios of 3R and 9R.

based on VESTA using methodology described by [93], with the aim of providing guidance to experimentalists for detecting the presence of the 9R phase. A crucial distinction becomes evident in the 2θ at 39° for 2H and 9R, and 38° and 40° for 3R, for all except WTe_2 which has similar feature at 35° for 2H and 9R, and 34° and 36° for 3R, as illustrated in Figure 4.5. The crystallographic planes hkl corresponding to these angles are (013) for 2H, (554) for 9R, and $(01\bar{4})$ and $(\bar{1}1\bar{5})$ for two adjacent peaks in 3R. These characteristic diffraction patterns could also help in the identification or differentiation of structural phases in TMDs.

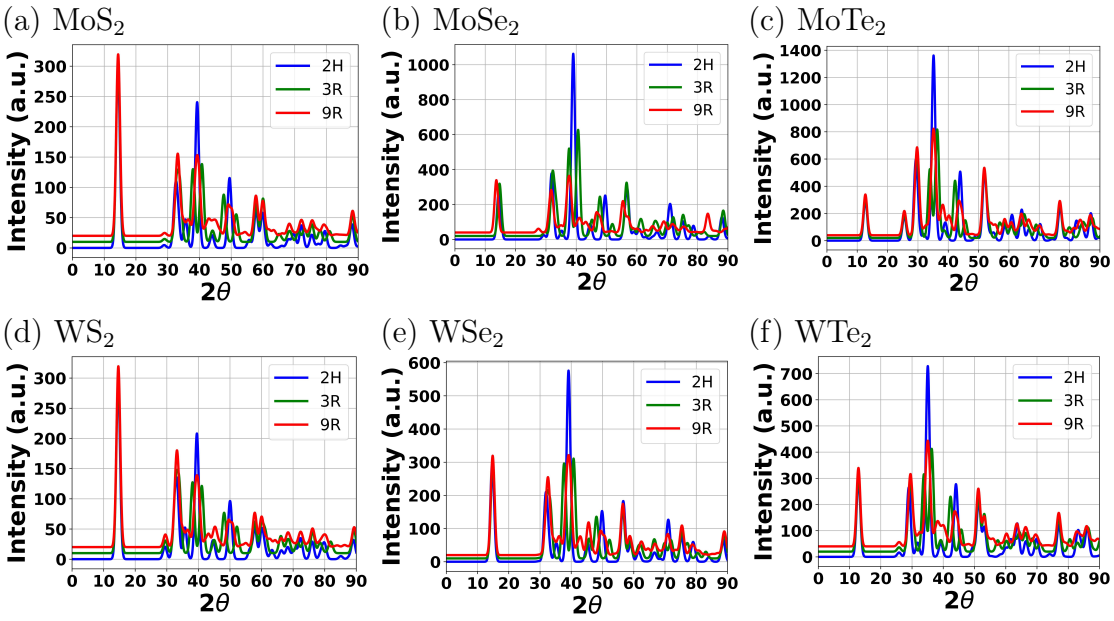

Figure 4.5: Calculated diffraction patterns of different TMDs in 2H, 3R and 9R phases. The peaks of 3R and 9R are shifted along y-axis for better view.

4.4.3 Important features

We explored some properties, such as electronic band structure, the optoelectric tensor for SHG but found it similar to the 3R phase. We found two properties that are better than the 3R phase and is discussed below.

Piezoelectricity

Piezoelectric substances find application in various significant devices, including microphones, medical imaging tools, and sensors. [236, 230] Notably, recent advancements have showcased the utility of piezopotentials generated by piezoelectricity as a gate voltage for manipulating the electronic band gap in piezoelectric semiconductors. This development has brought a novel research domain known as "piezotronics". [130] In this context, 2D semiconductors are particularly promising materials, given their ability to withstand the substantial deformations encountered in piezoelectric applications. The piezoelectric properties can be calculated by evaluating the change in the electrical polarization in response to the applied strain and can be expressed as:

$$e_{ijk} = \frac{dP_i}{d\epsilon_{jk}} \tag{4.3}$$

Here, P_i is the electrical polarization along i^{th} direction due to strain along j, k direction where $i, j, k \in$ 1,2,3, with 1,2,3 corresponding to x, y, and z directions, respectively. Likewise, piezoelectric strain coefficients d_{ij} can be obtained from the stress coefficients and elastic constants C_{ij} by:

$$e_{ik} = \sum_{j=1}^{6} d_{ij} C_{jk} \tag{4.4}$$

The d_{ij} matrix tensor for 3R or 9R belonging to $3m$ space group and C_{3v} point group has only 4 non-zero elements [108] (d_{15}, d_{22}, d_{31}, and d_{33}) resulting in:

$$\begin{pmatrix} 0 & 0 & 0 & 0 & d_{15} & -d_{22} \\ -d_{22} & d_{22} & 0 & d_{15} & 0 & 0 \\ d_{31} & d_{31} & d_{33} & 0 & 0 & 0 \end{pmatrix} \tag{4.5}$$

Considering the data presented in Table 4.7 and Fig. 4.6, it's evident that d_{15} and d_{22} tend to exhibit greater values in 9R compared to 3R structures. There are not many theoretical or experimental works on 3R phase of TMDs. One theoretical work [108] reports first principle calculation on e_{ij} and d_{ij} coefficients for MoS_2, $MoSe_2$, WS_2 and WSe_2. In comparison with [108], e_{ij} are similar in magnitudes but some of the d_{ij} coefficients are significantly smaller or larger than what we

calculated. For example, we calculated d_{33} for 3R MoS_2 as 3.65 pm/V and they reported 0.27 pm/V. Also, a recent experiment on 3R MoS_2 flakes with the thickness from 4 to 90 nm, or ≈ 6 to ≈ 128 layers showed d_{33} in a range 0.7 ± 0.2 to 1.5 ± 0.2 pm/V. [78] In [108], some of the elastic coefficients C_{14}, C_{33} and C_{44} are significantly higher than this work or other theoretical calculations. [194] This might have led to discrepency in some of the d_{ij} coefficients. The d_{15} and d_{22} are also significantly larger in magnitude than their monolayer counterparts computed from clamped ion method (d_{11} ranges from 1.88- 4.33 pm/V) and relaxed-ion method (d_{11} ranges from 2.19- 9.13 pm/V) among the discussed TMDs. [46] Also, d_{15} and d_{22} in 3R and 9R are greater than other known bulk piezoelectric materials such as α-quartz ($d_{11} = 2.3$ pm/V), [16] wurtzite GaN ($d_{33} = 3.1$ pm/V), and wurtzite AlN ($d_{33} = 5.1$ pm/V). [132] Depending on the specific application requirements, we can select the most suitable material by prioritizing the one with the highest piezoelectric coefficients.

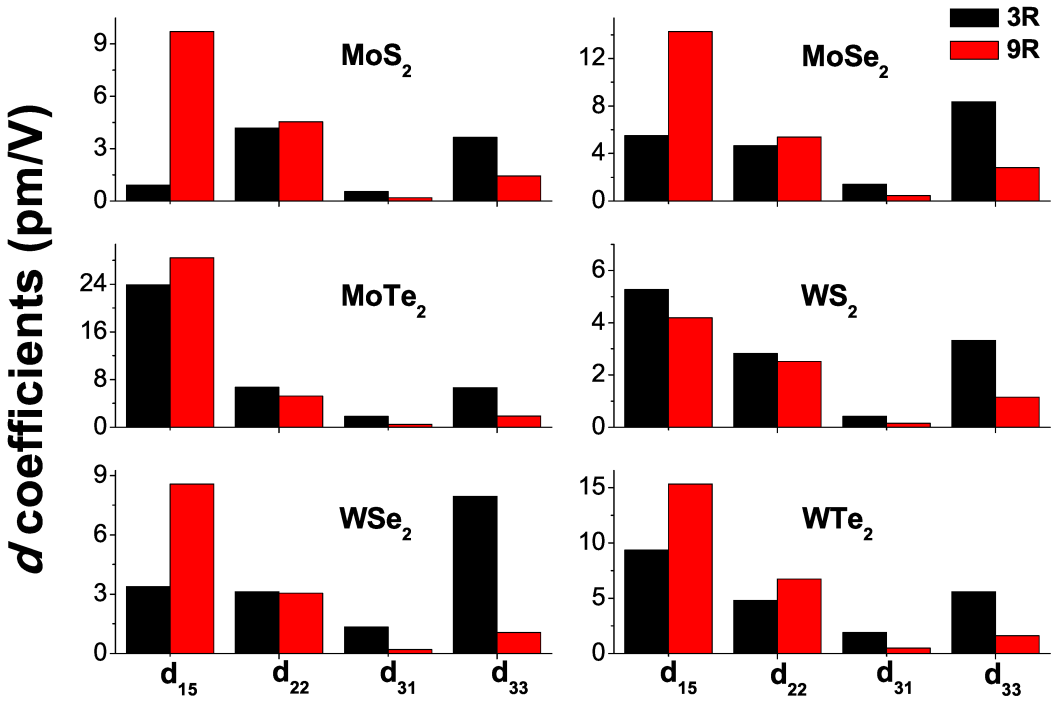

Figure 4.6: Piezoelectric coefficients on various TMDs.

Band-splitting

The monolayers TMDs lacks inversion symmetry and because of this symmetry breaking and stronger spin-orbit splittings, the two degenerate K and K' follows different optical selection rule due to opposite spin degenerate states. [222] Such spin-valley locking phenomenon has been studied for valleytronics devices such as qubits in quantum computing, low-power transisters, circularly polarized light emitters, polarization detectors, etc. [214, 227, 26] In bulk crystals, this band separation primarily arises from a combination of spin-orbit coupling and interlayer coupling effects. [52] Despite the relatively weaker interlayer interactions in TMDs, they can influence the states near the band edges, particularly affecting the valence band maximum and conduction band minimum, which are sensitive to interlayer coupling. [51] Previous literature has studied different multilayer MoS_2 with different stacking sequences [53]. In our calculations, we observed band splitting in 2H, 3R and 9R bulk structures within the conduction and valence bands. Prior research on few-layer 3R-MoS_2 has demonstrated that the band splitting at the conduction band minimum is primarily dominated by layer coupling, with spin-orbit coupling perturbing this behavior. [53] In our calculation in bulk structures, we find no splitting in the CBM of 2H, and slightly equal splitting due to spin orbit coupling in 3R and 9R. In the same paper [53], the valence band splitting at K is mainly contributed by spin-orbit but we find mix contribution in band splitting at valence band at K in bulk structures. The band splitting at K of 2H is mainly due to layer coupling and inclusion of spin-orbit has little contribution. In 3R at VB K point, the splitting is only due to spin-orbit coupling whereas at same point in 9R, we find the combined contribution of layer coupling and spin-orbit effect in band splitting. Similar is observed in CB- K point, with almost twice splitting in 9R than 3R. In the case of 9R stacking, which differs from 3R and 2H, we observed band splitting at VBM Γ in the range of 46 meV to 109 meV across various TMDS but not observed in both 2H and 3R. This splitting at VBM Γ in 9R is solely due to layer coupling as spin-orbit coupling has no contribution to it as shown in Fig. 4.7 and as detailed in Table 4.6. The bandstructure of MoS_2 with opposite spin channels at K and K' for 3R and 9R is shown in Supplementary Information Fig.

4.10 and 4.11.

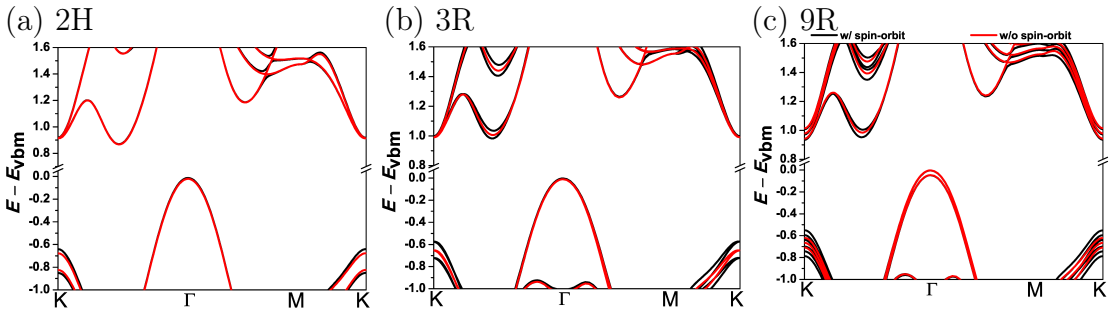

Figure 4.7: Electronic bandstructure with and without spin-orbit coupling in MoS_2.

TMDs	CBM			VB-K			VB-Γ			CB-K		
	2H	3R	9R	2H	3R	9R	2H	3R	9R	2H	3R	9R
MoS_2	0	51	54	200	150	240	0	0	46	2	40	70
$MoSe_2$	0	30	26	410	190	270	0	0	40	40	50	80
$MoTe_2$	0	20	16	310	220	337	0	0	46	15	40	100
WS_2	0	195	190	480	430	560	0	0	56	40	40	130
WSe_2	0	160	167	660	447	580	0	0	109	22	50	120
WTe_2	0	165	171	560	490	650	0	0	59	80	40	140

Table 4.6: Band splitting due to spin-orbit coupling in meV for different TMDs.

4.4.4 Possible experimental synthesis

In this section, we delve into the potential experimental synthesis of the 9R phase. There have been reports of successfully synthesizing the 3R phase by various means, such as restacking 2H monolayers, as discussed in [218]. Using similar methods, it is conceivable to create the 9R phase by directly stacking monolayers in the 2H phase configuration.

Furthermore, our previous research on Ni-doped MoS_2 [103] yielded the 9R phase as an outcome. In this case, the doping of 3R MoS_2 at the octahedral in-

tercalation site induced a phase transition from 3R to 9R. This transition resulted in the formation of trigonal pyramidal intercalation sites. It's worth noting that while the Mo/S-atop tetrahedral intercalation is energetically favored in 3R MoS_2 for Ni-doping, the trigonal pyramidal site represents a metastable state that offers the nearest minima for unstable octahedral intercalation in the 3R structure. Indeed, it appears that a precise approach to transition metal doping in the 3R phase has the potential to induce a phase transition to the 9R configuration. This method could serve as an alternative route for synthesizing the 9R phase, offering a controlled and potentially versatile means of achieving the desired crystal structure. It underscores the importance of doping strategies in tailoring the properties and phase transitions of two-dimensional materials like MoS_2.

Another approach that 9R may be synthesized is through shear strain on 3R. We found that under the strain S defined by the following matrix:

$$S = \begin{pmatrix} 1-\epsilon & 0 & 0 \\ 0 & 1+\epsilon & -\frac{\epsilon}{2} \\ 0 & -\frac{\epsilon}{2} & 1 \end{pmatrix} \tag{4.6}$$

The total energy difference between 3R and 9R reduces to a small number or 9R becomes more energetically favorable, as shown in Figure 4.8. This suggests, given the energy barrier between 3R and 9R being small, the perturbation in the structure due to external strain S could favor 9R. We obtain matrix S by minimizing the energy difference between two phases from equations 4.7 and 4.8.

$$U = \frac{V}{2} \sum_{ij=1}^{6} \epsilon_{ij} C_{ij} \tag{4.7}$$

$$U^{3R} - U^{9R} = \frac{1}{2} \sum_{ij=1}^{6} \epsilon_{ij} (V^{3R} C_{ij}^{3R} - V^{9R} C_{ij}^{9R}) \tag{4.8}$$

Here, V is the volume per unit and U is the energy. The difference $U^{3R} - U^{9R}$ is minimum when the eigenvalues of $V^{3R}C_{ij}^{3R} - V^{9R}C_{ij}^{9R}$ is minimum, and the corresponding eigenvectors defines the required strain for a given common factor ϵ.

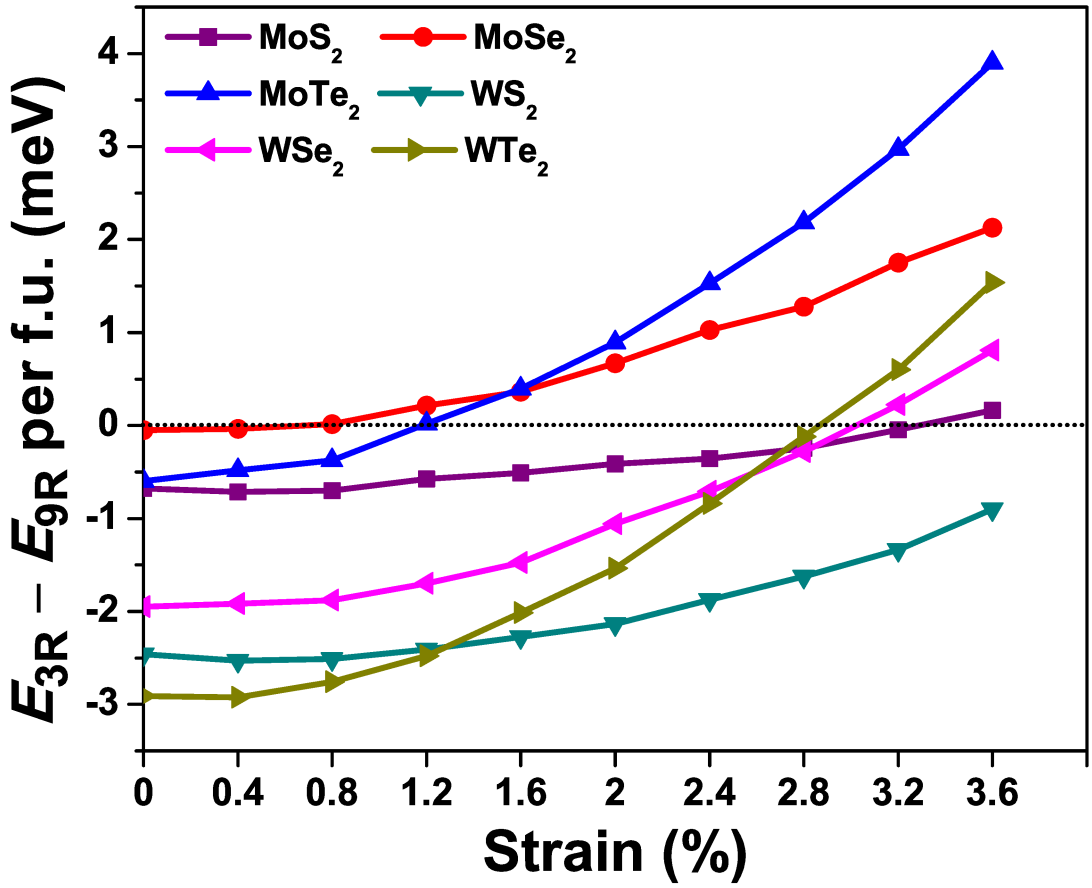

Figure 4.8: Relative energy of 3R compared to 9R with (as described in Equation 4.6). Dotted horizontal line at 0 represents the strain at which 9R becomes more energetically stable than 3R.

We also tested with non-shear strains such as compressive or tensile strains, hydrostatic and biaxial compression or elongation, but we found energy difference between 3R and 9R go up instead of down. We also tested the phase stability at higher temperature with harmonic approximation by calculating the lattice vibrations' contributions to the free energy $F = E - TS$, using the entropy as: [107]

$$S(T) = k_B \sum_{\lambda} n_B(\hbar\omega_\lambda) \ln n_B(\hbar\omega_\lambda) \tag{4.9}$$

where, n_B is Bose-Einstein, ω is phonon frequency, E is total energy (electronic and vibrational) and T is temperature. We found at higher temperature, energy

difference increases further making 2H more stable than 3R and 9R, and 3R is more stable than 9R, as shown in example case of MoS_2 in Supplementary Information Fig. 4.12.

4.5 Conclusion

In this research paper, we have introduced a novel nine-layer transition metal dichalcogenide (referred to as 9R) characterized by its dynamic and elastic stability. Notably, this phase exhibits Raman activity within the low-frequency range, a distinguishing feature not observed in the more established rhombohedral 3R phase. The 9R phase demonstrates superior piezoelectric properties, especially with regards to coefficients d_{15} and d_{22}, and also displays a greater band splitting at the conduction band minimum compared to the 3R phase. We have also proposed several potential methods for synthesizing this phase, including direct stacking of monolayer 1H, inducing phase changes through transition metal doping, and applying shear strain. The introduction of the novel stacking sequence in 9R brings forth opportunities for exploring various applications related to stacking sequences. For instance, a study by [137] has demonstrated the significance of stacking sequences in improving the hydrogen evolution reaction. Additionally, applications that arise from the breaking of inversion symmetry in this context demands further exploration.

Acknowledgments

This work was supported by the National Science Foundation under Grant No. DMR-2144317. This work used computational resources from the Multi-Environment Computer for Exploration and Discovery (MERCED) cluster at UC Merced, funded by National Science Foundation Grant No. ACI-1429783, and the National Energy Research Scientific Computing Center (NERSC), a U.S. Department of Energy Office of Science User Facility operated under Contract No. DE-AC02-05CH11231.

4.6 Supplementary Information

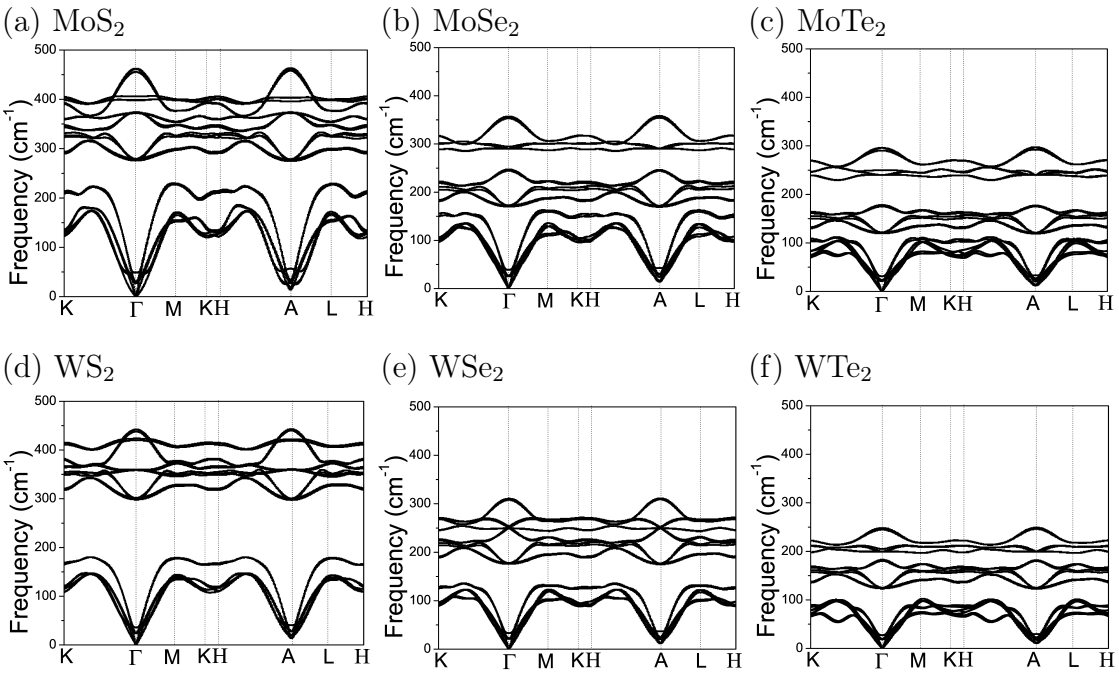

Figure 4.9: Calculated phonon bandstructure of 3R TMDs both in the in-plane and out-plane of the Brillouin zone.

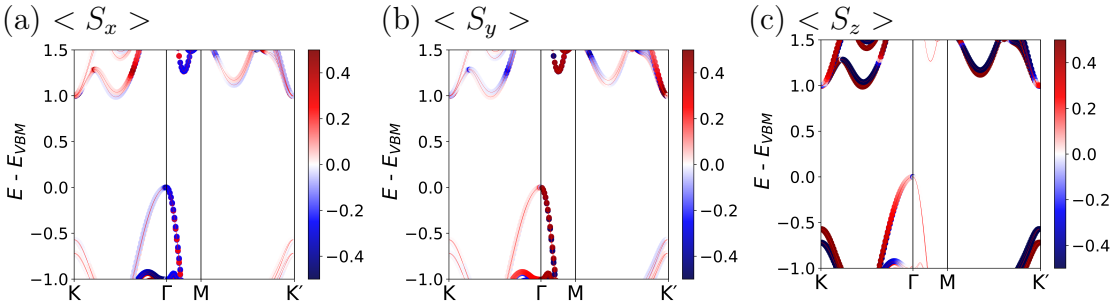

Figure 4.10: Electronic bandstructure of 3R MoS_2 showing spin projections.

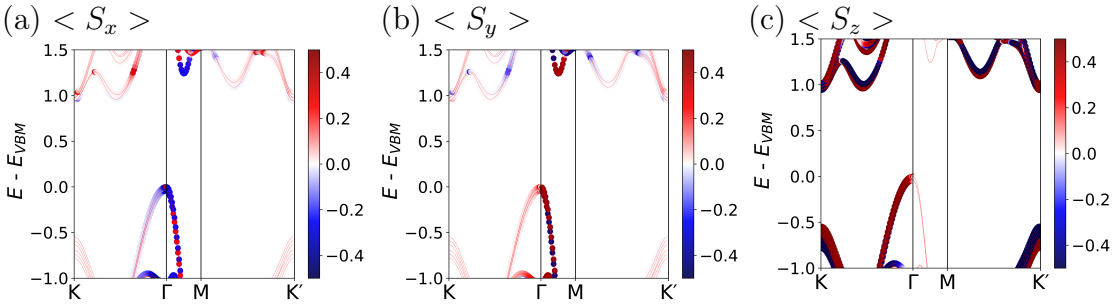

Figure 4.11: Electronic bandstructure of 9R MoS_2 showing spin projections.

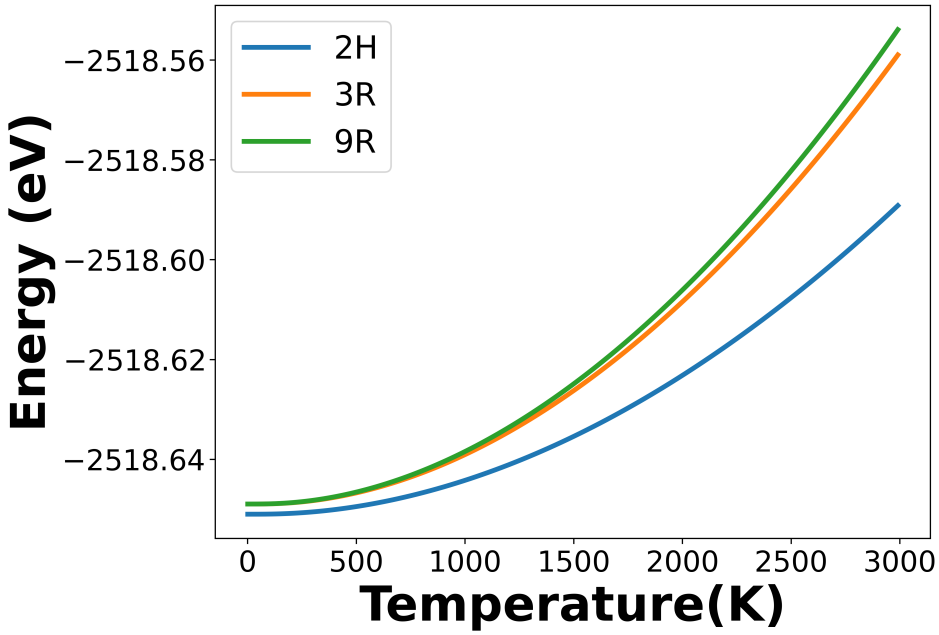

Figure 4.12: Free energy calculation of 2H, 3R and 9R MoS_2 as a function of temperature.

Table 4.7: Piezoelectric coefficients. The d coefficients are in units of pm/V and e coefficients are in units of C/m^2.

Phase		e_{15}	d_{15}	e_{22}	d_{22}	e_{31}	d_{31}	e_{33}	d_{33}
MoS_2	3R	-0.035	-0.909	0.771	4.201	-0.021	0.545	-0.172	-3.650
	9R	-0.182	-9.708	0.840	4.540	-0.008	0.194	-0.060	-1.431
$MoSe_2$	3R	-0.111	-5.510	0.713	4.660	-0.058	1.410	-0.328	-8.370
	9R	-0.242	-14.26	0.816	5.380	-0.021	0.465	-0.112	-2.830
$MoTe_2$	3R	-0.470	-23.92	0.774	6.701	-0.026	1.807	-0.210	-6.627
	9R	-0.476	-28.41	0.815	5.252	-0.005	0.464	-0.070	-1.910
WS_2	3R	-0.101	-5.280	0.560	2.836	-0.017	0.425	-0.135	-3.324
	9R	-0.071	-4.197	0.523	2.528	-0.006	0.150	-0.047	-1.162
WSe_2	3R	-0.040	-3.384	0.514	3.137	-0.051	1.346	-0.306	-7.945
	9R	-0.131	-8.575	0.523	3.060	-0.004	0.213	-0.041	-1.060
WTe_2	3R	-0.173	-9.376	0.601	4.824	-0.009	1.928	-0.171	-5.587
	9R	-0.257	-15.33	0.810	6.747	-0.004	-0.512	-0.050	-1.607

Chapter 5

Anisotropy and exciton self-trapping in one-dimensional organic metal halide hybrids ($C_4N_2H_{14}PbBr_4$) from first principles

5.1 Abstract

Low-dimensional organic-inorganic metal halide hybrids (OMHH) have remarkable optical and electronic properties and better stability against heat and moisture. We study a 1D metal halide hybrids of formula $C_4N_2H_{14}PbBr_4$, consisting of Pb-Br chains separated by organic cations. Experiments showed a large Stokes shift (0.83 eV) with broadband emission which hints at interesting photo-physics involving self-trapped excitons. We calculate the highly anisotropic optical, band-structure, and transport properties of this 1D OMHH, which could be used for polarized photodetectors and LEDs. The bands are highly dispersive along Pb-Br chains and nearly flat along other directions, leading to a significantly larger conductivity as calculated by Boltzmann transport. We find an indirect gap and a direct gap which is just slightly higher in energy. We investigate self-trapped excitons via our approach for excited state forces in the GW/Bethe Salpeter equa-

tion method with the BerkeleyGW code. We examine how excitons couple with phonon modes which we find to be consistent with the temperature dependent photoluminescence data. We relax the structure using the excited state forces to identify the self-trapped exciton structure. This simulation of the dynamics of the exciton self-trapping gives insight into the contribution to broadband emission.

5.2 Introduction

Lower dimensional perovskites [60] have recently received significant attention due to (i) an increase in stability against heat, light and moisture, [226] and (ii) strong quantum confinement giving rise to excitonic physics for optoelectronics applications. [234, 220] The detailed mechanism of these properties are not well understood. One argument for stronger resistance against moisture is due to replacement of unstable small hydroscopic organic cations with bulkier hydrophobic organic cations which could strain the surface B-X bonds (considering ABX_3 as perovskite structure) and repel the water molecules from reactive sites. [60, 225] Another thought is that there is a stronger van der Waals interaction between bulkier organic molecules with B-X sublattice leading to better stability than 3D perovskite. [172] This better stability could be interesting for solar photovoltaic application. The mixed composites of 3D/2D perovskite [210] and 3D/1D perovskites [140] have been reported with relatively longer stability than 3D. The low dimensional perovskite having larger band-gap could therefore be exciting absorber material in a perovskites tandem solar cell, to not only absorb high energy photons but also act as a shield against degradation.

Another aspect of lower dimensional perovskites is broadband white light emission as a result of exciton self-trapping. [42, 234] The excitons are the bound state of electron and hole held together by electrostatic Coulomb force. The self-trapped excitons are a type of exciton that generates a lattice distortion and becomes self-trapped by the distortion it induced. Self-trapped excitons can be considered as excited state defects, as they exist only upon excitation and the lattice distortion disappears following decay to the ground state. With large-amplitude structural

distortion, the resulting luminescence is often broad and has a large Stokes shift. The exciton self-trapping due to exciton-phonon interaction depends on dimensionality of the system. [64, 219] So, further lowering the dimensionality to 1D makes easier self-trapping, which has been observed in broadband luminescence with large Stokes shifts. [205] This could lead to an efficient white light emitter from a single material and has already been observed experimentally. [234] This could be huge as creating effectively a high-quality white light from a single source is a challenge. In commercial white-light sources, one or more light-emitting diodes, coated by one or more phosphors are combined to yield white light. This combined emitter system can become problematic due to unequal degradation rates of different emitters. A single material that emits white light is therefore desired.

Due to its strongly anisotropic structure, resembling a bundle of nanowires, there naturally exists anisotropy in the absorption and emission of light in this material. While absorption anisotropy is relatively weak, our previous work [149] and recent findings by others [32] have shown a pronounced anisotropy in emission. This observation raises intriguing questions because one would typically expect the polarization dependence to be similar in both absorption and emission if the same structures and states were involved. However, it's worth noting that the photoluminescence intensity is maximized for linear polarization parallel to the 1D chains, regardless of the linear polarization of the excitation and this has been found due to fast recombination caused by nonradiative recombination via surface defects or by the crystal structure distortion near the surface. [149] This experimental finding also hints at fascinating photophysics, most likely related to the self-trapped excitons that dominate the emission from these materials [190, 234]. It's established that the broadband emission in these crystals is a result of self-trapped excitons and is associated with a substantial Stokes shift. The intriguing aspect is that the polarization of absorption and emission differs, indicating that distinct structures and states are implicated in these two processes. To delve deeper into this phenomenon and gain insights into the properties of self-trapped excitons and the polarization of their emission, we are employing our unique GW/Bethe-Salpeter equation force formalism [39, 195]. Through this approach, we aim to elucidate

the contribution of self-trapped excitons to the experimental observations and better understand the underlying photophysics of these materials. Furthermore, it's worth noting that our approach to understanding the self-trapped structure differs from previous methods that rely on the Constrained DFT method, which does not take into account excitonic effects as discussed in [97]. By incorporating these excitonic effects, we gain a more comprehensive understanding of the self-trapping phenomenon in this material, which has the potential to significantly impact its optical properties and applications. This novel approach opens up new possibilities for exploring the exciton dynamics in OMHH and similar materials.

In this work, we discuss the crystal structure of OMHH and then validate the structure through Raman experiment and theory. We then discuss the anisotropic properties in electrical conductivity and quasi-direct bandstructure of this material. Finally, we delve into excited state forces, exciton-phonon coupling and discuss the methodology to obtain the self-trapped structures.

5.3 Methodology

We used plane-wave DFT calculations in the Quantum ESPRESSO code, [68, 67] with the Perdew-Burke-Ernzerhof (PBE) [164] exchange-correlation functional for all calculation except for Raman, where we used local density approximation (LDA) functional. [165] ONCV pseudopotentials [79] from PseudoDojo [2] were used. A wavefunction energy cutoff of 816 eV and a $3 \times 3 \times 3$ half-shifted k-grid were used for self-consistent field (SCF) calculations. Forces and stresses were relaxed below 10^{-4} Ry/bohr and 0.1 kbar, respectively. For BerkeleyGW [39] calculations, we found that 300 empty bands, a $4 \times 4 \times 4$ q-grid, and a 204 eV screened-Coulomb cutoff converged GW quasiparticle corrections near the gap to within 100 meV. Excited state forces are computed with the Bethe-Salpeter equation in BerkeleyGW using 8 occupied states and 12 unoccupied states and a $6 \times 6 \times 6$ fine k-grid, and are plotted with 0.1 eV Gaussian broadening. For technical reasons, to obtain electon-phonon coefficients, a Gaussian smearing of 0.001 eV was used. The electrical conductivity was calculated using the post-processing tool

BoltzTrap2 [143] that solves Onsager transport coefficients for extended systems in a linearized Boltzmann transport equation framework.

The Raman spectroscopic measurements were conducted at ambient conditions in reflection mode using 532.3 nm continuous wave excitation (∼1.6 mW, Oxxius LCX-532S-100, continuous wave (CW) single longitudinal mode diode pumped solid state laser), in a Horiba LabRAM HR Evolution high resolution confocal Raman microscope fitted with volume Bragg gratings. The experiment was configured using an 1800 mm^{-1} holographic grating blazed at 500 nm, a 100 mm confocal hole diameter, and a 20X, 0.9 N.A. cover glass-corrected objective. Spectral calibration was performed using the 1332.5 cm^{-1} band of a synthetic Type IIa diamond, and spectral intensity was calibrated using a VIS-halogen light source (NIST test no. 685/289682-17).

The temperature dependent Photoluminiscence spectra and OMHH sample preparation follows similar methodology as discussed in [234].

5.4 Results

5.4.1 Structure

The crystal structure of OMHH comprises a linear chain of Pb-Br atoms surrounded by organic molecules, making it a pseudo one-dimensional material. This structure is classified under the $Imma$ space group and exhibits D_{2h} point group symmetry. Through relaxation starting from the XRD structure [234] with initial lattice parameters (a = 14.62 Å, b = 6.10 Å, c = 14.40 Å, $\alpha = \beta = \gamma = 90°$), we obtained lattice parameters in close agreement (a = 14.70 Å, b = 6.06 Å, c = 14.56 Å, $\alpha = \beta = \gamma = 90°$). This alignment is consistent with studies on other hybrid perovskites and OMHHs [200, 113]. Our calculations utilize a primitive cell of this body-centered tetragonal structure, featuring lattice parameters $a = b = c$ = 10.80 Å, and angles α = 32.48°, β = 94.86°, γ = 85.88°, with the Pb-Br chain oriented along the z direction.

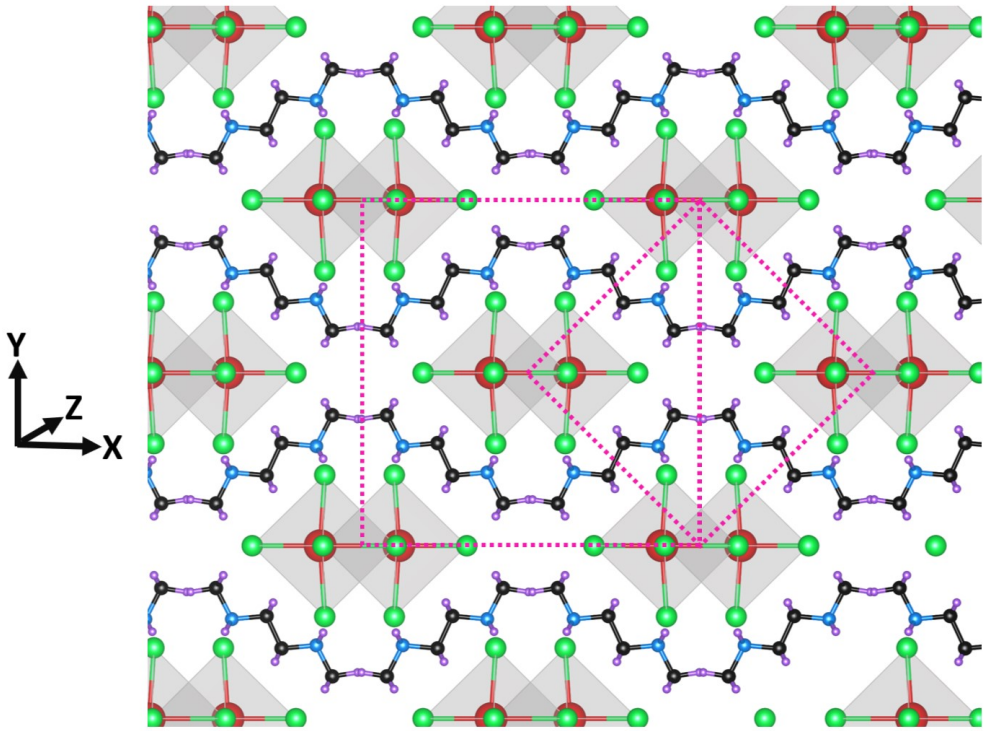

Figure 5.1: Structure of $DMEDAPbBr_4$ that has Pb-Br chain into the page wrapped by the organic cations (red spheres: lead atoms; green spheres: bromine atoms; blue spheres: nitrogen atoms; black spheres: carbon atoms; purple spheres: hydrogen atoms; grey polyhedra: $PbBr_6^{4-}$ octahedra). Dotted square and diamond represents the conventional and primitive unit cells.

5.4.2 Raman Spectroscopy

We conducted both calculations and measurements of the polarized Raman spectra of this material, aiming to validate the consistency between experimental and theoretical results. Our analysis revealed favorable agreement in the positions of most Raman peaks. To compensate the temperature effects, we reduced the experimental results by multiplication factor of $\omega(1-e^{-\frac{-\hbar\omega}{kT}})$ (where ω is the Raman shift and T= 300 K) which helps to compare to the calculated absolute Raman intensities as discussed by [196]. However, there was still disparity in the relative intensities of these peaks compared to the theoretical predictions. There are also variations in the Raman-active modes depending on whether the polarization is

parallel or perpendicular to the Pb-Br chain, which is due to the material's high anisotropy. The Raman peaks corresponding to directions parallel to the Pb-Br chain have A_g mode symmetry, while the peaks in the other two directions have B_{3g} symmetry (parallel to the y-direction) and B_{1g} symmetry (parallel to the x-direction). These symmetries align with the crystal symmetry in the D_{2h} point group. Notably, the two perpendicular directions to the Pb-Br chain are not equivalent. By examining the polarized Raman results presented in Figure 5.2 (b), it becomes evident that considering the analyzer parallel to the crystal's y-axis provides a closer match to the theoretical predictions than the analyzer along the x-axis. This shows that polarized Raman spectroscopy can aid in identifying the lattice orientation by comparison against theoretical calculations. The details of Figure 5.2 are further shown in Table 5.1. In $z(HH)\overline{z}$, we found two Raman peaks in experiment at low frequency regime having mode symmetry B_{1g} that do not appear in theoretical calculations. All the other Raman active modes have A_g symmetry suggesting those two Raman peaks could be due to imperfections in crystal. These findings highlight the importance of taking into account polarized Raman spectroscopy, especially in anisotropic materials. Surprisingly, this material does not have much anisotropy in dielectric permitivity, as they are fairly similar. The electronic dielectric permittivity (F/m) are $\varepsilon_{xx} = 3.55$, $\varepsilon_{yy} = 3.56$, and $\varepsilon_{zz} = 3.64$.

Exp. (HH)	Theory (HH) A_g	Exp. (HV)	Theory (HV ∥ y) B_{3g}	Theory (HV ∥ x) B_{1g}
27.0 (B_{1g})	-	41.5	42.8	28.1, 39.9
38.3 (B_{1g})	-	51.5	55.4	48.6, 64.3
44.6	44.8	103.2	106.9	118.0
59.7	59.3	132.7	131.4	144.2
95.0	107.7	197.6	227.9	321.8
132.5	140.9	280.1	276.7	383
176.2	161.3	-	-	-
335.5	333.8	-	-	-
387.2	385.6	-	-	-

Table 5.1: Raman shift (cm^{-1}) comparison from theory and experiment.

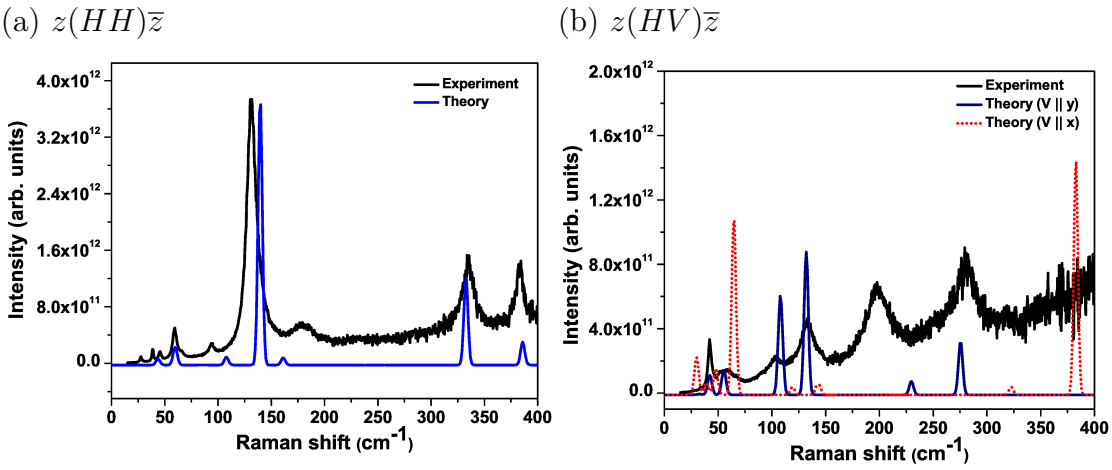

Figure 5.2: Polarized Raman intensity from theory and experiment. Polarization parallel to Pb-Br chain is termed as 'H' and perpendicular to the chain is termed as 'V'. The experimental Raman is measured at room temperature. 'V' ∥ x or y means analyzer is parallel to the crystal's x- or y-direction (two perpendicular directions of Pb-Br chain).

5.4.3 Conductivity

Our calculations of electrical conductivity have revealed significant anisotropy in this property. Notably, at the band edges, the electrical conductivity primarily occurs along the Pb-Br chain direction (σ_{zz}). This finding suggests that, for device applications, the optimal voltage bias direction should align with the Pb-Br chain. In Figure 5.3, we can observe the band structure and electrical conductivity along both the parallel (z) and perpendicular (x and y) directions with respect to the Pb-Br chain. The curvature of the band structure is closely related to the electrical conductivity, with stronger curvature indicating higher electrical conductivity. Figures 5.3(a) and (b) exhibit consistent behavior. They highlight the substantial anisotropy in electrical conductivity, both parallel and perpendicular to the Pb-Br chains. Furthermore, there are noticeable differences in electrical conductivity between the two perpendicular directions. Also, we have found anisotropy in Seebeck coefficients as shown in Fig. 5.8. The calculated Seebeck coefficients are about 5 times larger than usual thermoelectric materials such as Bi_2Te_3. [82] These distinctive properties, coupled with the anisotropy of optical absorption that we've previously observed, suggest the potential utility of this material in direct-polarization detector devices. [41] Such devices could take advantage of the material's anisotropic electrical and optical properties, offering new possibilities for practical applications.

(a) Electrical conductivity (b) Bandstructure

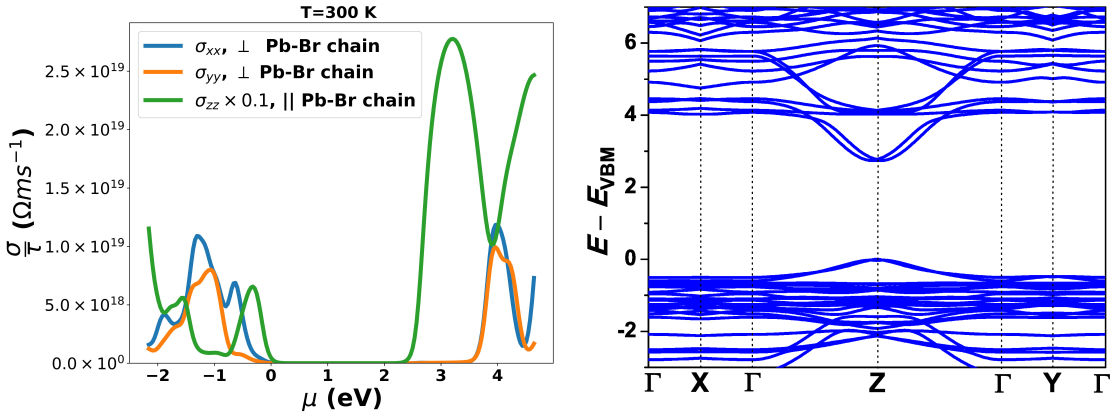

Figure 5.3: Bandstructure and electrical conductivity along different direction. a) Electrical conductivity along different directions. The much larger σ_{zz} has been reduced by a factor of 10 for easier comparison of curves. b) x and y are perpendicular directions to the Pb-Br chains, and z is parallel to the Pb-Br chains.

5.4.4 Indirect Bands

We also performed a detailed characterization of the electronic band structure at the DFT level. A notable aspect of this structure is the presence of strong spin-orbit coupling, primarily due to the heavy Pb atoms and Br atoms within the compound. The presence of spin-orbit coupling also has substantial consequences on the electronic structure. Unlike the typical scenario where band extrema occur at high-symmetry points, in this system, these extrema are slightly shifted away from such points. This deviation from high-symmetry points is reminiscent of what is observed in other spin-orbit semiconductors, such as Bi_2Te_3. [65] To understand these characteristics, we systematically explored the Brillouin zone to identify the band extremum, which allowed us to determine both the direct and indirect band gaps, as illustrated in Fig. 5.4. Notably, the indirect gap is only 16 meV smaller than the direct gap, which is less than kT at room temperature. We anticipate that the emission properties of this material will essentially resemble those of a direct-gap semiconductor, particularly at room temperature and above. The un-

derstanding of these features in the electronic structure is important for predicting the material's optical properties and its behavior under various conditions, and has been an interest for other optoelectronic applications. [237] Also note that a similar result as above is obtained with inclusion of spin-orbit coupling, and GW approximation (rigid shift of -0.5 eV from spin-orbit coupling and non-rigid shift +1.30 eV from GW correction). The direct-indirect gap from GW methods is 20 meV.

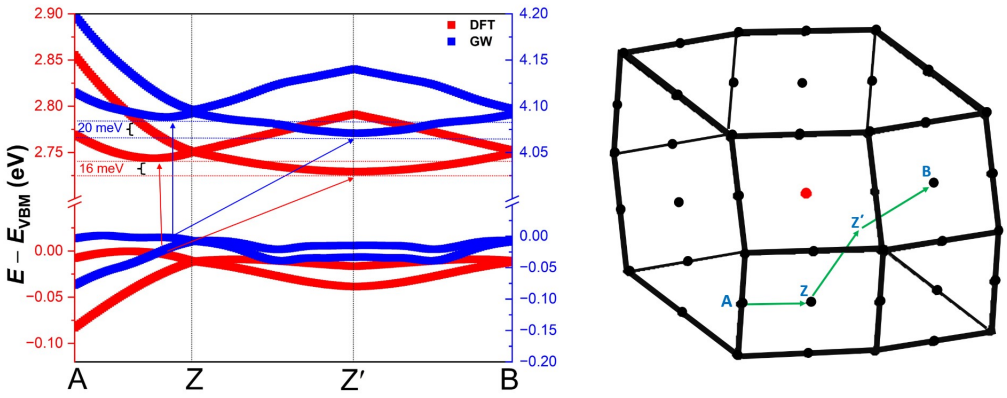

Figure 5.4: Left: DFT and GW bandstructures of 1D perovskite, zoomed in to show band extrema and direct and indirect gaps. Band extrema are not at high symmetry points, due to spin-orbit coupling. Right: k-point paths in Brillouin zone used for bandstructure. The $k-$ points used in this plot are: A (-0.4770000 0.2730000 0.7309500), Z (0.24890862 0.24890862 -0.24890862), Z′ (-0.1962821 -0.1898718 0.2939551), and B (0.0000000 -0.5000000 -0.0000000).

5.4.5 Excited State Structures

When a system absorbs a photon it goes from the ground state to an excited state, in doing so, it goes to a new potential energy surface, which is different from the ground state potential energy. Therefore, the ions experience forces toward the new minimum. The force experienced on this new potential energy surface is called excited state force. Those excited state forces may help explain several phenomena such as the DNA degradation after absorption of UV light [89], self-trapped excitons [190, 91] and the stability in solar cells materials [215, 99].

First, we calculate excited state forces and based on the total force ($F_{total} = F_{DFT} + F_{EX}$, where F_{DFT} is the force due to DFT and F_{EX} is the force due to excitation), we then estimate the displacements of the atoms according to the harmonic approximation given by $\vec{x} = k^{-1}\vec{F_{total}}$, where k is the force constant matrix and $\vec{x}$ is the displacements occurring in the new potential energy surface. This method relies on the approximation that the force constants are the same in both ground and excited state.

The displacements resulting from the excited state forces can also be determined by projecting these forces from a Cartesian basis to a phonon basis. This conversion reveals the contributions of significant phonon modes of vibration. In our specific case, we have identified vibration modes 23 and 27 as the most influential. Also, note that the low frequency vibration modes are mostly contributed due to Pb and Br atoms as shown in vibrational density of states in Fig. 5.9. When we combine the displacement patterns associated with these modes, we obtain the actual displacement patterns caused by the excited state forces, as illustrated in Figure 5.5. This analysis also provides insights into the coupling between excitons and phonons, indicating their interplay in the lattice deformation during excitation of light.

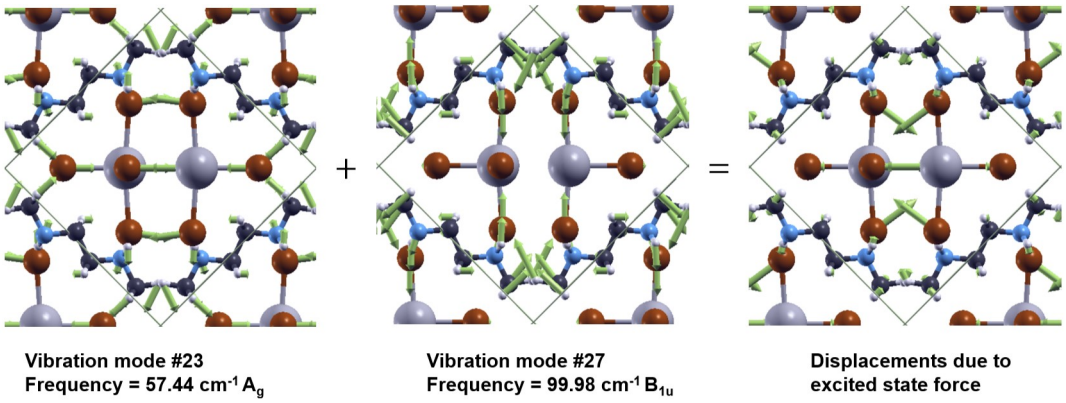

Figure 5.5: Displacement patterns in different vibration modes or due to excited state force. The green arrow shows displacement direction.

We have also generated a plot illustrating the excitation energy as a function of phonon frequency, which provides insights into the coupling between excitons

and phonons. This analysis indicates that most excitons couple with a phonon frequency of 99.98 cm^{-1}, which is equivalent to 12.39 meV, as demonstrated in Figure 5.6. Furthermore, we have plotted the temperature-dependent full-width at half-maxima (FWHM) of photoluminescence peaks and fitted the data using Equation 5.1, as done in other literature. [133] This fitting process has yielded two crucial parameters: the Huang-Rhys factor (S), which reflects the strength of the coupling between electrons and phonons, and the corresponding phonon frequency. [239] The fitted graph is presented in Figure 5.7, revealing a substantial Huang-Rhys factor of 137 ± 4. In double perovskite, also emitting white light has Huang-Rhys factor of 37. [133] This shows a strong exciton-phonon coupling, and the associated phonon energy is approximately 11 ± 1 meV. Notably, this value aligns well with the simulated phonon frequency of 99.98 cm^{-1}.

The current calculation based on a primitive unit cell may not incorporate localized displacements due to excitons because of the translation symmetry of the crystal. Previously shown calculations using constrained DFT method indicates that excitons can localize in specific regions of the Pb-Br chain. This localization suggests that employing a larger supercell may be necessary to accurately represent the localized electron-hole pairs and to estimate the structure based on exciton self-trapping. However, it's worth noting that the current approach we've utilized has provided valuable insights into the working mechanism to determine the self-trapped structure, serving as a benchmark for future studies that aim to capture exciton self-trapping in larger supercells.

$$FWHM = 2.36\sqrt{S}\hbar\omega_{\text{phonon}}\sqrt{\cot\frac{\hbar\omega_{\text{phonon}}}{2k_BT}} \tag{5.1}$$

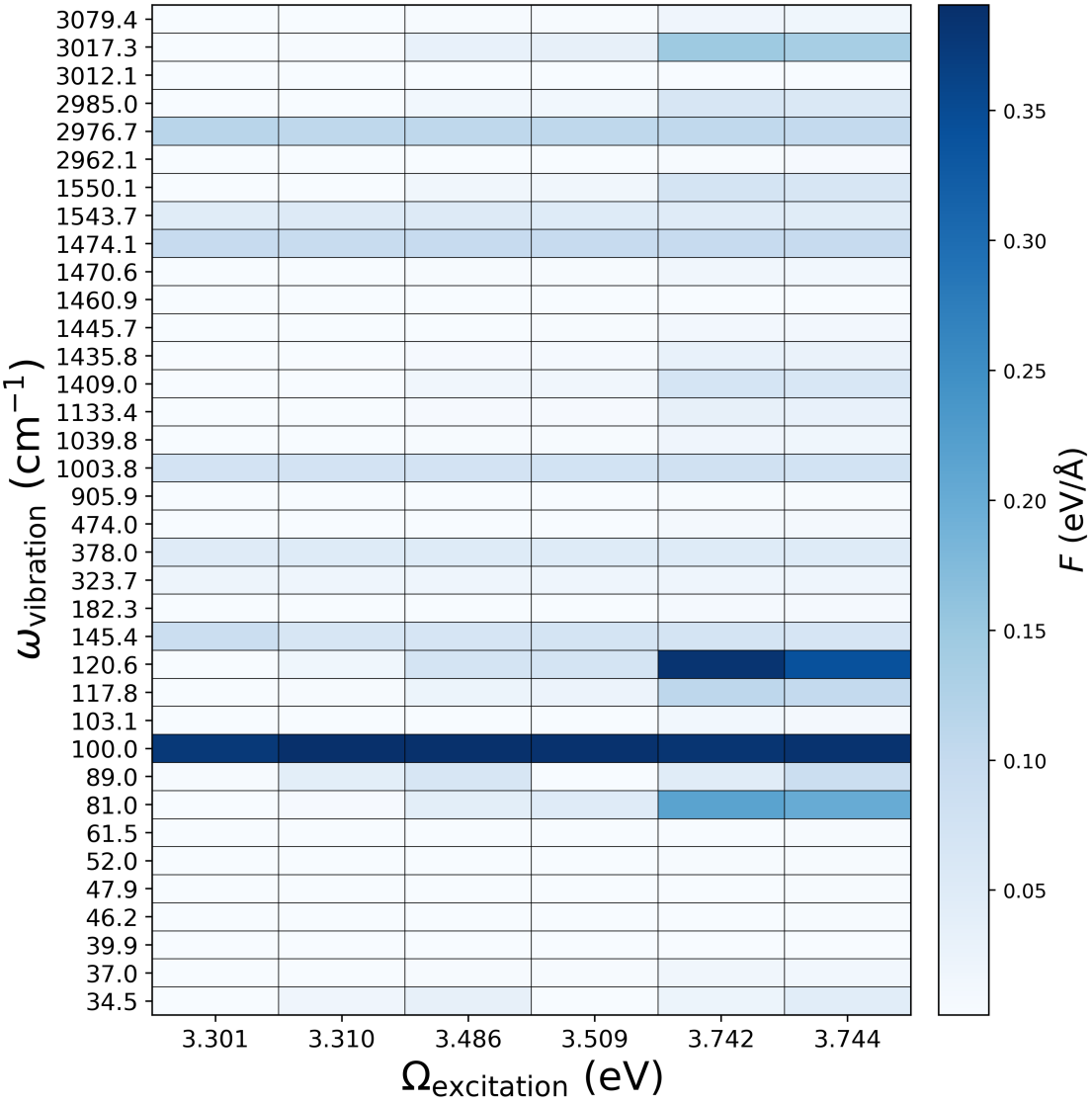

Figure 5.6: Exciton-phonon coupling coefficients for lowest 6 excitons.

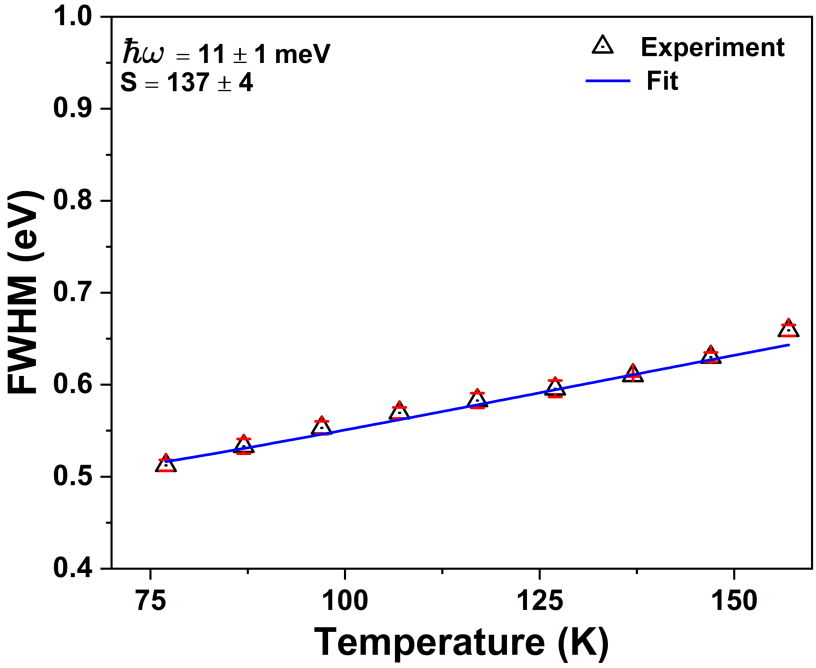

Figure 5.7: The fitting results of full width at half maximum (FWHM) as a function of temperature for OMHH. PL FWHM derived from 77 K to 300 K in a step of 10 K. Red lines on top and bottom of each data points shows the errorbar in the obtained point.

5.5 Conclusion

In summary, our results provide valuable insights into the crystal structure, Raman spectroscopy, electrical conductivity, and excited state dynamics of OMHH, a pseudo one-dimensional material with unique properties. Our investigation into Raman spectroscopy emphasizes the importance of polarized measurements to understand the anisotropic nature of this material. The electrical conductivity analysis reveals strong anisotropy, with conductivity predominantly occurring along the Pb-Br chain direction. This guides to properly apply the voltage bias for device applications, and anisotropic conduction could also potentially be useful in direct-polarization detector devices. We also delved into a new methodology to understand the excited-state dynamics and exciton-phonon coupling. We found significant Huang-Rhys factor of 137 $\pm$ 4, suggesting strong electron-phonon cou-

pling. Our simulated phonon frequency corresponding to coupling agrees well with experiments. Further exploration of the dynamics of the structure due to excited state forces in larger supercell will provide insights into exciton self-trapping structures, contributing to broadband emission and uniform polarization in emission, regardless of the polarization direction in absorption.

Acknowledgement

This work is supported by the Air Force Office of Scientific Research under award number FA9550-19-1-0236. This work is also partially supported by the National Science Foundation under Grant No. DMR-2144317. This work used computational resources from the Multi-Environment Computer for Exploration and Discovery (MERCED) cluster at UC Merced, funded by National Science Foundation Grant No. ACI-1429783, and the National Energy Research Scientific Computing Center (NERSC), a U.S. Department of Energy Office 17 of Science User Facility operated under Contract No. DE-AC02-05CH11231.

5.6 Supplementary Information

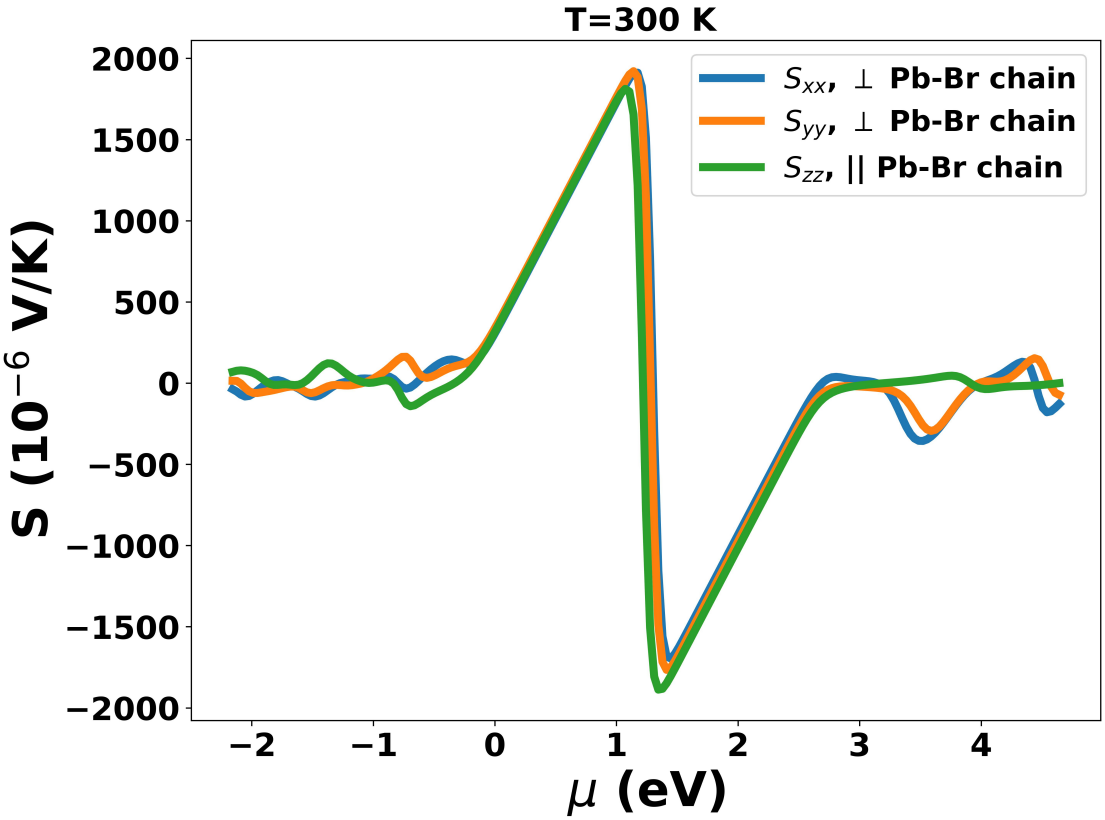

Figure 5.8: Seebeck coefficients at room temperature. Seebeck coefficients parallel to Pb-Br chain is slightly smaller than other two perpendicular directions.

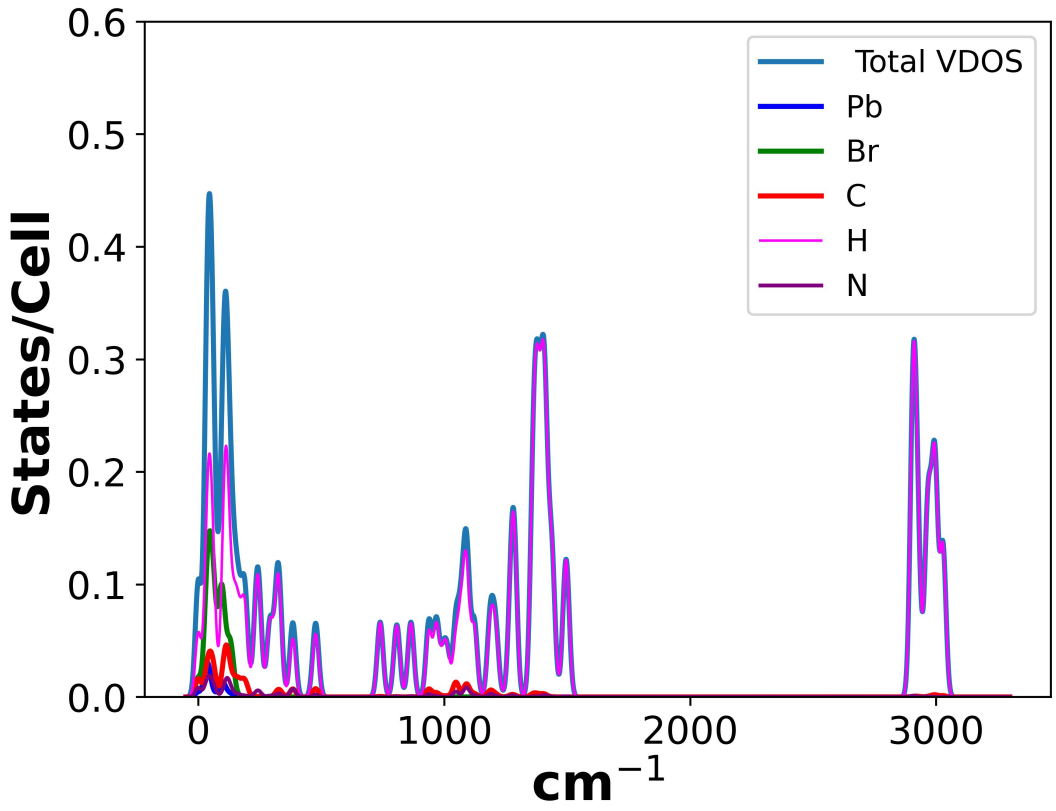

Figure 5.9: Vibrational density of states along with each atom contribution to total vibrational modes.

Chapter 6

Collaborative works

In this chapter, I will briefly go over some of my contributed works on other low-dimensional materials. In Sections 6.1 through 6.3, I will begin by providing an overview of the project, followed by my specific contributions to the work. Section 6.1 has been reprinted with permission from Small Structures, 4, 2200378, 2023. Copyright 2023, Small Structures published by Wiley-VCH GmbH. [149] Section 6.2 has been reproduced from Ref. [113] with permission from the Royal Society of Chemistry. Section 6.4 is accepted for publication in Nano Letters, titled "Enabling oxidation protection and carrier-type switching for bismuth telluride nanoribbons via in-situ organic molecule coating", Jun Beom Park, Wei Wu, Jason Yingzhi Wu, Rijan Karkee, Theresa Marie Kucinski, Karen C. Bustillo, Matthew Schneider, David A. Strubbe, Colin Ophus, and Michael Thompson Pettes, 2023.

6.1 Surface Effects on Anisotropic Photoluminescence in One-Dimensional Organic Metal Halide Hybrids

One-dimensional (1D) organic metal halide hybrids have emerged as intriguing materials with remarkable optical properties, characterized by strong anisotropy, highly efficient light emission, and significant Stokes shifts. These features hold great potential for innovative applications in photodetection and lighting. How-

ever, the underlying mechanisms governing these unique optical properties, particularly the influence of surface effects, have remained elusive. In this study, we investigate the material 1D $C_4N_2H_{14}PbBr_4$ using polarization-dependent time-averaged and time-resolved photoluminescence (TRPL) spectroscopy across various photoexcitation energy levels. Our findings reveal that the emission when photoexcited with polarization parallel to the 1D metal halide chains can either strengthen or weaken relative to perpendicular polarization, depending on the excitation energy. We attribute this excitation-energy-dependent anisotropic emission to rapid surface recombination, supported by first-principles calculations of optical absorption in the material. This fast surface recombination is directly confirmed through TRPL measurements when excitation is polarized parallel to the chains. My work contributes to a more comprehensive understanding of the optical anisotropy in 1D organic metal halide hybrids, employing GW-BSE methods to gain insights into electronic properties and absorption spectra.

To summarize the key findings of the experiment: (a) Photoluminescence (PL) emission exhibits varying intensity depending on the orientation of excitation polarization. Specifically, when excited at a wavelength of 400 nm (360 nm), PL emission is stronger when the excitation polarization is parallel (perpendicular) to the 1D chains. (b) Regardless of the excitation wavelength or polarization, PL emission consistently displays stronger polarization along the chain direction. (c) Time-resolved photoluminescence (TRPL) measurements reveal a rapid decay, occurring in less than 20 picoseconds (ps), exclusively when the excitation polarization aligns with the chain direction.

These observations are attributed to surface effects on photoluminescence, which can be explained as follows: the optical absorption characteristics of 1D halide perovskites are highly anisotropic and strongly influenced by the optical polarization. This behavior stems from the fact that the optical electric field parallel to the chain has a greater ability to polarize electrons along the 1D chain, which consists of inorganic octahedra. Due to the insulating organic structure surrounding the chain, electrons find it more challenging to be polarized by a transverse electric field. This inherent anisotropy in optical absorption contributes to the ob-

served optical polarization and emission characteristics in 1D organic metal halide hybrids.

We performed plane-wave DFT calculations in the Quantum ESPRESSO code, [68] with the Perdew-Burke-Ernzerhof (PBE) [164] exchange-correlation functional. Relaxation starting from the XRD structure (a = 14.62 Å, b = 6.10 Å, c = 14.40 Å, $\alpha = \beta = \gamma = 90°$) gave lattice parameters in close agreement (a = 14.70 Å, b = 6.06 Å, c = 14.56 Å, $\alpha = \beta = \gamma = 90°$), as seen in work on other hybrid perovskites and OMHHs. [200, 113]. Our calculations use a primitive cell of this body-centered tetragonal structure, with lattice parameters $a = b = c$ = 10.80 Å, and α = 32.48°, β = 94.86°, γ = 85.88° with the Pb-Br chain along the z direction. The calculated electronic band structure of the 1D metal halides in the GW approximation (with a simple spin-orbit correction) is shown in Figure 6.1A; the gap is indirect and computed to be 3.6 eV, though the difference between the direct and indirect bandgap is only 16 meV. The valence band maximum (VBM) has contributions mostly from the p-orbitals of Br, whereas at the conduction band minimum (CBM), p-orbitals of Pb dominate (Figure 6.1C). The electronic bands are dispersive along the Pb-Br chain direction but are nearly flat along the other two perpendicular directions.

Additionally, we calculated the absorption spectrum through the Bethe-Salpeter Equation (BSE) in the BerkeleyGW code [39], shown in Figure 6.1B. The lowest exciton energy is found at 2.9 eV. Results from the random phase approximation (RPA) are also provided for comparison, which do not include excitonic effects. By comparing the absorption peaks of BSE and RPA, we find a substantial exciton binding energy (830 meV), as is usual in low-dimensional structures [22]. The first absorption peak is strong along the Pb-Br chain (z-polarized), consistent with the Pb-Br chain mainly contributing to the electronic transition at the band edges. The peak is mainly due to transitions at $\vec{k} = Z$ from the VBM and the next band below the VBM to the CBM and the next band above the CBM (CBM+1). For x- and y-polarizations, the dominant transitions are at $\vec{k} = X$ and Y respectively, and in both cases are from VBM to CBM and CBM+1. Figure 6.1B shows large anisotropy in absorption in this material.

Though the overall absorption spectrum of a sample containing many randomly oriented needles has been measured, [233] the polarization dependent absorption spectrum of a single needle has not been obtained due to its small size. The above calculation clearly indicates strong anisotropic absorption for the lowest energy excitation, and hence in the excitation energy range used in our experiment (3.02-3.44 eV), which is just above the (perhaps slightly underestimated) calculated peak energy (2.9 eV) through BSE, after considering excitonic effects. Note the minimum absorption energy is determined by the excitonic energy instead of the single-particle gap. The calculated optical transition rates are much higher for the parallel electric field in the lowest energy peak shown in Figure 6.1B. The corresponding absorption depth reaches as shallow as 10 nm for polarization parallel to the Pb-Br chain, at least two orders of magnitude smaller than that under perpendicular polarization (Figure 6.1D).

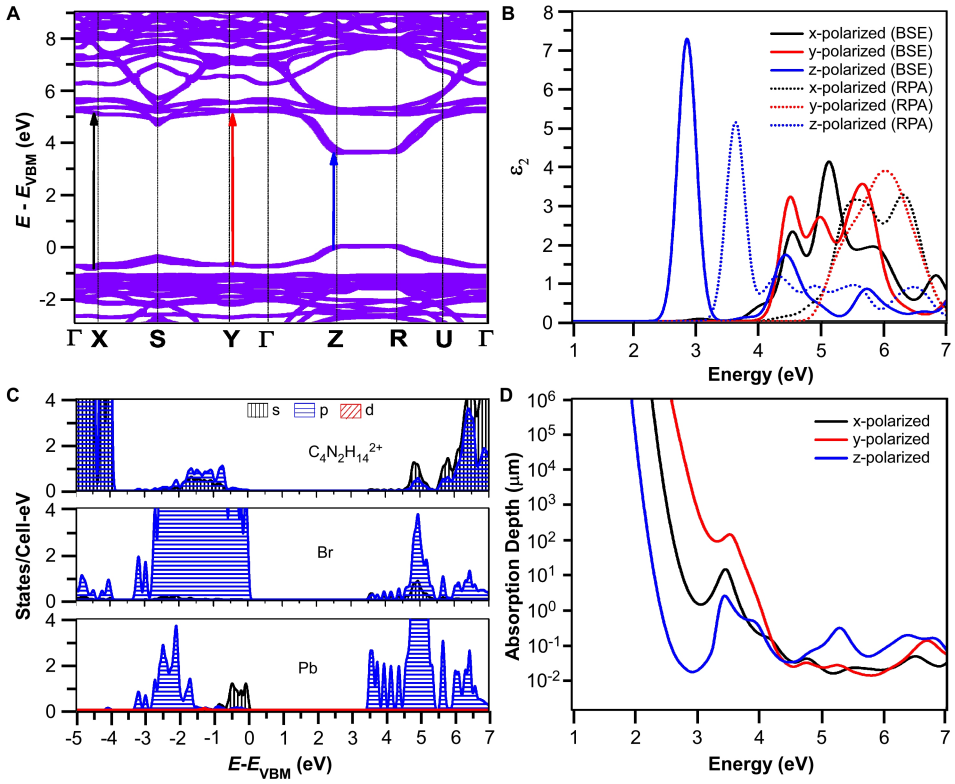

Figure 6.1: Electronic structure simulations. A) Electronic band structure, in the conventional Brillouin zone, in the GW approximation plus a spin-orbit correction to the gap. Arrows show the dominant transitions for the lowest-energy peaks for light polarized along x (black), y (red), and z (blue) directions, where z is the direction along the Pb-Br chains. B) Polarized absorption spectra with (BSE, solid) and without (RPA, dashed) electron-hole interactions, based on the GW bandstructure with spin-orbit correction to the gap. C) Partial density of states from DFT to show atomic orbital character of bands, with gap corrected by GW and spin-orbit coupling. D) Absorption depth for polarized light, from BSE as in B).

Our first-principles calculations demonstrates highly anisotropic optical absorption across the range of our excitation energies. Building upon our experimental and theoretical findings, we attribute the excitation energy-dependent anisotropic emission to a fundamentally distinct recombination process occurring at the surface of one-dimensional organic metal halide hybrids (1D OMHHs). This study

underscores the critical role of surface effects in elucidating the optical properties of 1D OMHHs, shedding light on their anisotropic and broadband emission characteristics. These insights have significant implications for harnessing these unique materials in innovative applications, particularly in the realms of lighting and photodetection, where their distinctive optical properties can be strategically employed.

6.2 One-dimensional organic metal halide nanoribbons with dual emission

In recent years, there has been a growing fascination with organic metal halide hybrids characterized by their low-dimensional molecular structures. These materials have garnered significant attention due to their exceptional versatility in terms of structural adjustments and their unique photophysical properties.This particular study introduces a pioneering achievement – the synthesis and thorough characterization of a one-dimensional (1D) organic metal halide hybrid. This remarkable material, denoted by the chemical formula $C_8H_{28}N_5Pb_3Cl_{11}$, boasts metal halide nanoribbons with a width spanning three octahedral units, making it a noteworthy addition to the family of organic metal halide hybrids. When subjected to photoluminescence studies, it exhibits not one, but two distinct emissions. The quantum efficiency of these emissions, often referred to as the photoluminescence quantum efficiency (PLQE), is found to be remarkably high, hovering around 25%. This exceptional PLQE is a testament to the material's efficiency in converting absorbed light into emitted photons, rendering it highly promising for various photonic applications.

To unravel the underlying mechanisms responsible for this dual emission phenomenon, our research combines experimental photophysical studies with theoretical density functional theory (DFT) calculations. These computational simulations and theoretical analyses offer crucial insights into the material's electronic structure and the dynamics of excitons – electron-hole pairs – within the metal halide nanoribbons.What emerges from this comprehensive investigation is the following:

the dual emission observed in this 1D organic metal halide hybrid is a consequence of the coexistence of two distinct types of excitons. On one hand, we have delocalized free excitons, which exhibit an extended spatial distribution across the material. On the other hand, there are localized self-trapped excitons, which are confined to specific regions within the metal halide nanoribbons. The interplay between these two types of excitons gives rise to the complex dual emission behavior, enriching our understanding of the photophysics of this material.

To gain a better understanding of the structure–property relationship for 1D $C_8H_{28}N_5Pb_3Cl_{11}$, we have performed planewave DFT calculations. Relaxation starting from the SCXRD structure (a = 11.35 Å, b = 15.85 Å,c = 32.12 Å, $\alpha = \beta = \gamma = 90°$) gave lattice parameters in close agreement (a = 11.32 Å, b = 15.85 Å, c = 32.15 Å, $a = b = c = 90°$), as in work on other materials. [200] The calculated electronic band structure of $C_8H_{28}N_5Pb_3Cl_{11}$ is shown in Fig. 6.2a; the gap is direct and computed to be 3.24 eV. This is close to, though slightly less than, the experimental result from Tauc fitting, in accordance with the common cancellation of errors between neglect of spin–orbit coupling and quasiparticle corrections in hybrid perovskites. [116] The valence band maximum (VBM) has contribution mostly from p-orbitals of Cl and C, whereas at the conduction band minimum (CBM), p-orbitals of Pb dominate (Fig. 6.2b and c). The electronic bands are dispersive along the Pb–Cl chain direction (x), with effective masses at the Γ point of $m^*_{\mathrm{VBM}} = 0.34\ m_0$ and $m^*_{\mathrm{CBM}} = 0.09\ m_0$,but are nearly flat along other two perpendicular directions (y: $m^*_{\mathrm{VBM}} = 2.25\ m_0$, $m^*_{\mathrm{CBM}} = 4.23\ m_0$; z: $m^*_{\mathrm{VBM}} = 18.5\ m_0$, $m^*_{\mathrm{CBM}} = 12.5\ m_0$) as shown in Fig. 6.2a. Additionally, we have calculated the absorption shown in Fig. 6.2d. The first absorption peak is strong along the Pb–Cl chain (x-polarized), suggesting that the electronic transition in the band edges is coming from the Pb–Cl chain. For x-polarization, the strong transition is due to VBM-8 and VBM-7 to CBM+4 bands (very close in energy to VBM to CBM transitions). This calculated direct absorption peak matches well with our experimental absorption results. [113] Similarly for y-polarization, a transition from VBM-17 to CBM+47 bands dominates; and for z-polarization, from VBM-21 to CBM+27 bands. Furthermore, Fig. 6.2d shows strong anisotropy in absorption. These cal-

culations indicate that the FE emission comes from the recombination of excitons on the Pb–Cl chain. The experimental emission energy for both emitting states should be lower than the bandgap due to the strong exciton binding as usual in low-dimensional structures, as well as Stokes shifts. Also note that the experiment [113] confirmed presence of a small quantity of water molecules, approximately 1.5%, within $C_8H_{28}N_5Pb_3Cl_{11}$ single crystals through thermogravimetric analysis and elemental analysis. Interestingly, computational studies indicate that these oxygen-containing impurities, specifically H_2O, have minimal to negligible impacts on the structural characteristics of the crystals. Furthermore, their influence on the optical properties is primarily characterized by an increased absorption of light at shorter wavelengths when the light polarization is in the x-direction. This suggests that, while the presence of water molecules is acknowledged, their effects on the overall structural and optical properties of the 1D $C_8H_{28}N_5Pb_3Cl_{11}$ crystals remain limited as shown in Fig 6.3. Additionally, we also constructed an analogous bulk structure containing 2D sheets of Pb–Cl atoms in plane (Fig. 6.4a and b), separated by organic molecules out of plane, and obtained a bandgap of 2.84 eV. The orbital nature of the band edges is similar to 1D $C_8H_{28}N_5Pb_3Cl_{11}$. This suggests a quantum confinement effect of 0.40 eV in this material as one goes from 2D to 1D.

In essence, this pioneering work not only introduces a novel 1D organic metal halide hybrid but also sheds light on the intricate interplay of excitons within its structure, leading to the dual emission phenomenon. These findings hold immense promise for a wide range of applications in the realm of photonics and materials science, further underscoring the significance of low-dimensional organic metal halide hybrids in modern materials research.

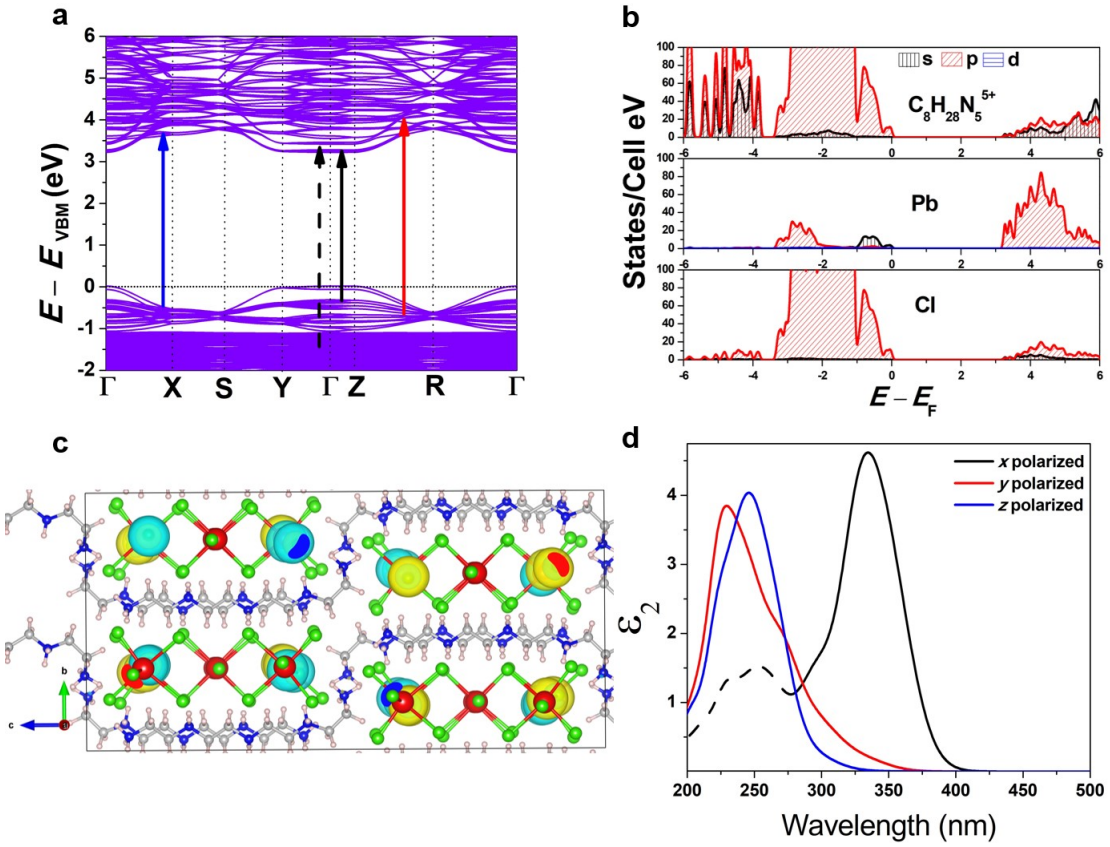

Figure 6.2: Density-functional theory simulations: (a) electronic band structure, with arrows showing optical transitions for peaks polarized along x (black), y (red), and z (blue) directions, where x is the direction along the Pb–Cl chains, and the solid and dotted black arrows indicate the lowest and second-lowest energy x-polarized peaks; (b) partial density of states; (c) wavefunction of the conduction band minimum at Γ, localized along the Pb–Cl chains; (d) polarized absorption spectra, where the x-polarized peaks are solid and dotted as in (a)

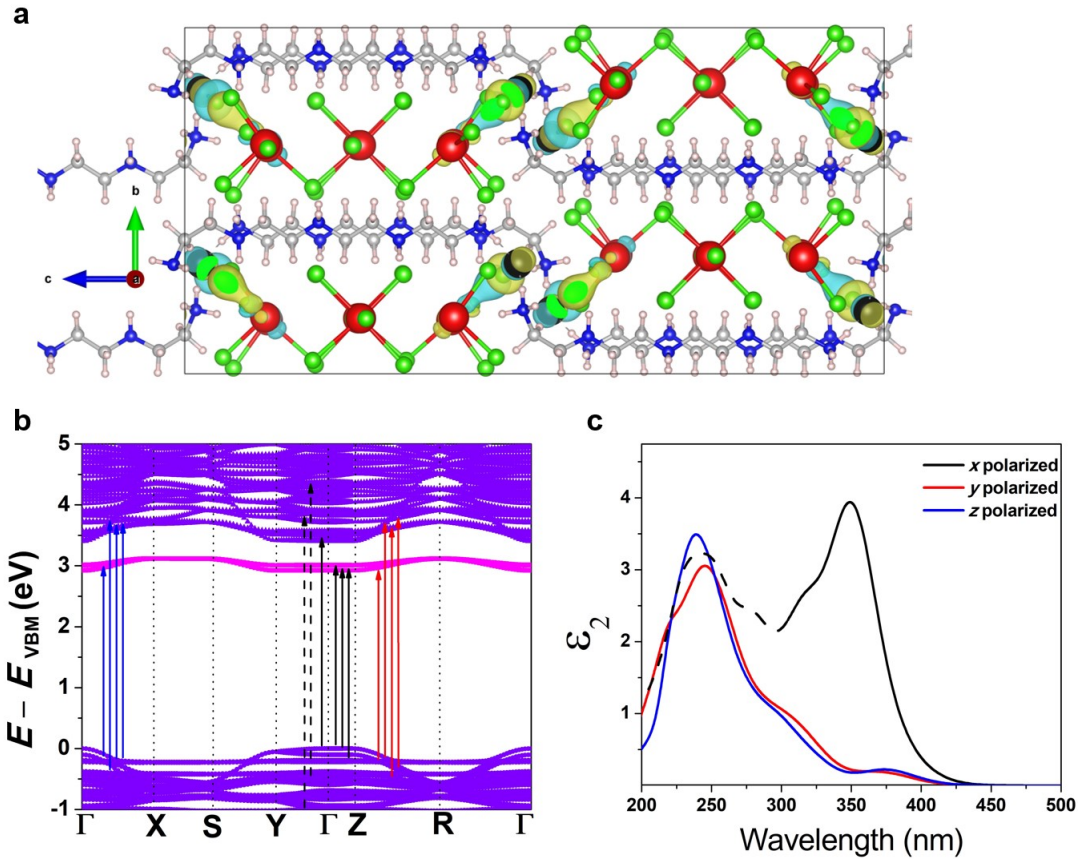

Figure 6.3: Calculations of structure from SCXRD containing an O atom, with formula unit $C_8H_{28}Cl_{11}N_5OPb_3$. (a) Relaxed structure with lattice parameters a = 11.32 Å, b = 15.92 Å, c = 32.15 Å, $\alpha = \beta = \gamma = 90°$; minimally different from structure without O atom. The O atom (black) makes a bond with Cl. (b) Bandstructure, showing a new flat conduction band in the gap, localized on the O-Cl bond. The next lowest conduction bands are on the Pb-Cl chain as in the structure without O, and they are pushed up slightly higher in energy. Arrows show optical transitions for peaks polarized along x (black), y (red), and z (blue) directions, where x is the direction along the Pb-Cl chains, and the solid and dotted black arrows indicate the lowest and second-lowest energy transitions. (c) Optical absorption spectrum, with x-polarized peaks are solid and dotted as in (a), showing similar features to that without O, but with somewhat modified intensities of higher peaks. Surprisingly, the transitions involved are quite different from those without O, apparently due to some small symmetry-breaking and the VBM to CBM transition becoming allowed. The O-Cl flat band makes a significant contribution despite its localization.

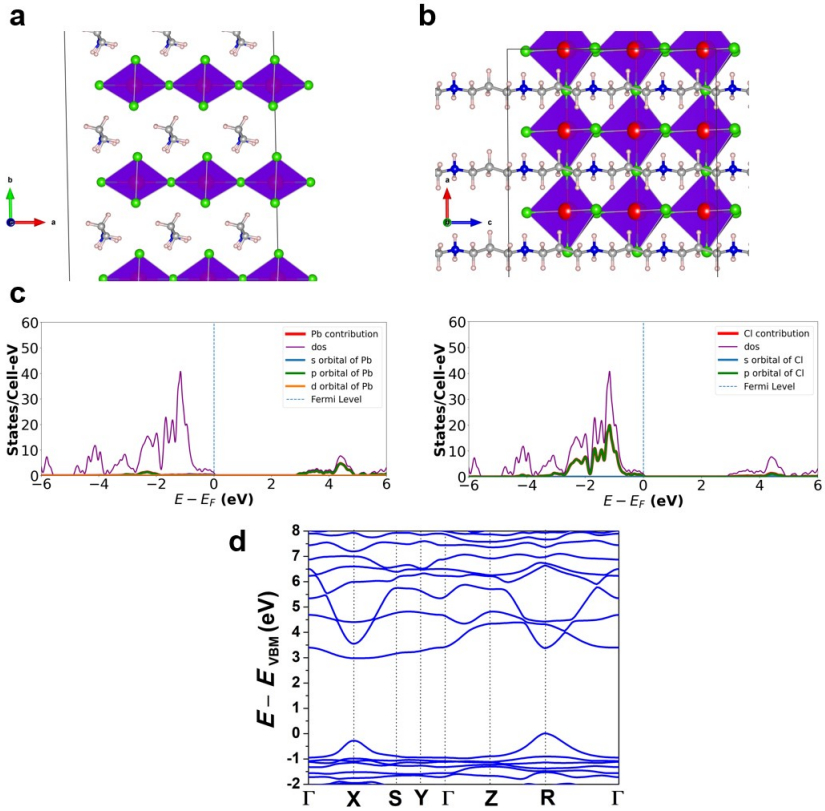

Figure 6.4: Calculations of hypothetical 2D sheet structure, corresponding to the 1D $C_8H_{28}N_5Pb_3Cl_{11}$, to show quantum confinement effects. The relaxed structure has lattice parameters $a = 5.67$ Å, $b = 7.92$ Å, $c = 4.92$ Å, $\alpha = 93.35°$, $\beta = 90.33°$, $\gamma = 91.15°$. The unit cell contains 16 atoms with chemical formula $C_3H_8NPbCl_3$. The Pb-Cl sheets are in the ac plane, separated by polymeric cations. SCF calculations used a $4 \times 2 \times 4$ half-shifted k-grid. (a) View showing separation between layers. (b) View showing a layer. (c) Partial density of states (using a $20 \times 2 \times 20$ half-shifted k-grid), showing that the VBM is primarily due to Cl p orbitals and CBM is primarily due to Pb p orbitals, as in 1D $C_8H_{28}N_5Pb_3Cl_{11}$ (Figure 6.2b). (d) Bandstructure, showing a smaller gap compared to the 1D structure, and an indirect gap with neither VBM nor CBM at Γ. Bands are fairly flat in the out-of-plane y-direction but generally dispersive in the in-plane x- and z-directions.

6.3 Enabling oxidation protection and carrier-type switching for bismuth telluride nanoribbons via in-situ organic molecule coating

In recent years, there has been a strong emphasis on developing thermoelectric materials with high electrical conductivity and low thermal conductivity to efficiently convert waste heat into electricity [235, 228], particularly at near-room temperatures. [147] One notable material, Bi_2Te_3, excels in this regard, effectively generating electrical energy from heat. [82, 203] The use of nanostructured Bi_2Te_3 has revealed unique properties, including enhanced thermoelectric characteristics and topologically protected electronic surface states. [166] Theoretical models suggest that reducing the thickness of these nanostructures can significantly improve their thermoelectric figure of merit (zT). [65] However, practical applications often fall short of this potential due to defects, impurities introduced during material growth, and surface oxidation after growth, all of which hinder precise chemical potential control and impact thermoelectric performance.

This project introduces an innovative synthesis method for producing core-shell nanoribbons composed of Bi_2Te_3 and F4-TCNQ. These nanoribbons exhibit the remarkable ability to restore the thermoelectric performance of bulk Bi_2Te_3. The key to this achievement is the in-situ application of an organic F4-TCNQ barrier to the Bi_2Te_3 nanoribbons. This process causes a significant shift in the major carrier type, transforming it from n-type to p-type. This shift has an impact on the Seebeck coefficient and the thermoelectric figure of merit (zT), enhancing their performance. Additionally, the F4-TCNQ barrier effectively shields the core material from oxidation. As a result, even after exposure to air for one month, no surface oxidation or loss of thermoelectric properties is observed.

In this project, we used the BoltzTrap2 post-processing tool [143] to calculate the Seebeck coefficients (as a function of temperature and concentration) and electrical conductivity (using the common electron relaxation time of 10^{-14} seconds), solving Onsager transport coefficients for extended systems in a linearized Boltzmann transport equation framework, in conjuction with DFT. For computa-

tional work in DFT, we use plane-wave pseudopotential code Quantum ESPRESSO [68, 67] with PBE [164] exchange-correlation functional and Grimme-D2 van der Waals correction [71] to quantitatively estimate the electronic band structure (potential shifts and carrier concentrations) of Bi_2Te_3. (Note: to match the band gap found with the GW approximation and spin-orbit coupling, the conduction bands are shifted down by 0.19 eV). We use scalar relativistic Optimized Norm-Conserving Vanderbilt pseudopotentials [79] obtained from Pseudodojo [2] to obtain the relaxed lattice parameters (a = b = 4.33 Å, and c = 31.46 Å; with $\alpha = \beta = 90°$ and $\gamma = 120°$) for a half-shifted 8×8×2 k-grid with a kinetic energy cutoff of 1224 eV.

These calculations help estimate the shift in effective potential and estimate the doping concentration in the experiment. We used our bulk Bi_2Te_3 results to approximate also the doped nanoribbons, assuming the rigid band approximation. With the electronic bandstructure calculated, we can now calculate the shift of the nanoribbon's surface potential by assuming the electronic structure of bulk Bi_2Te_3 and coating an external p-type carrier donor. In Figure 4e, we have plotted the points where the experimentally measured Seebeck coefficient and electrical conductivity at 250 K intersect with the theoretically obtained curves for both Bi_2Te_3 and Bi_2Te_3/F4-TCNQ samples. This analysis allowed us to estimate the effective range of surface potential shift achieved through extrinsic p-type dopant coating, falling within the range of 625–640 meV, as shown in Fig. 6.5

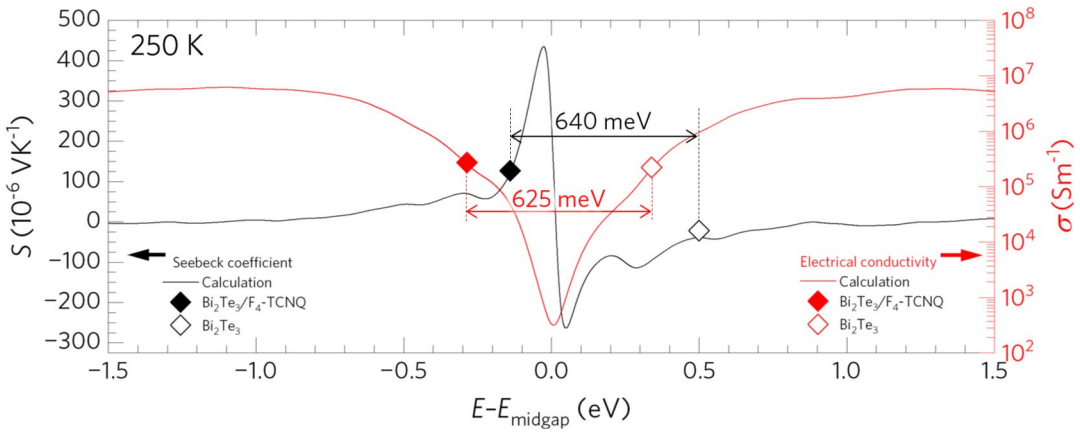

Figure 6.5: Intersections of the measured S (black diamonds) and σ (red diamonds) at 250 K with the calculated S (black line) and σ (red line) as a function of chemical potential with respect to the middle of the electronic band gap.

The Bi_2Te_3 nanoribbon displays a consistently negative Seebeck coefficient, ranging from -4 to -22 μV K^{-1}, with this effect diminishing as the temperature rises from 30 to 250 K. In contrast, the Bi_2Te_3/F4-TCNQ nanoribbon exhibits a strikingly positive Seebeck coefficient, spanning from 12 to 127 μV K^{-1} over the same temperature range. This observation strongly indicates a transformation of the primary carrier type, shifting from n-type to p-type. Our theoretical calculation (see Fig 6.6) confirms this transformation, as the Bi_2Te_3 nanoribbon demonstrates a high n-type carrier concentration of $\sim 10^{21}$ cm^{-3}, whereas the Bi_2Te_3/F4-TCNQ nanoribbon displays a substantial p-type carrier concentration of around 10^{20} cm^{-3}. Consequently, the Bi_2Te_3/F4-TCNQ nanoribbon consistently outperforms the Bi_2Te_3 nanoribbon, exhibiting performance improvements of at least 3 times across the entire temperature range of 30–250 K and about 6 times within the range of 150–250 K.

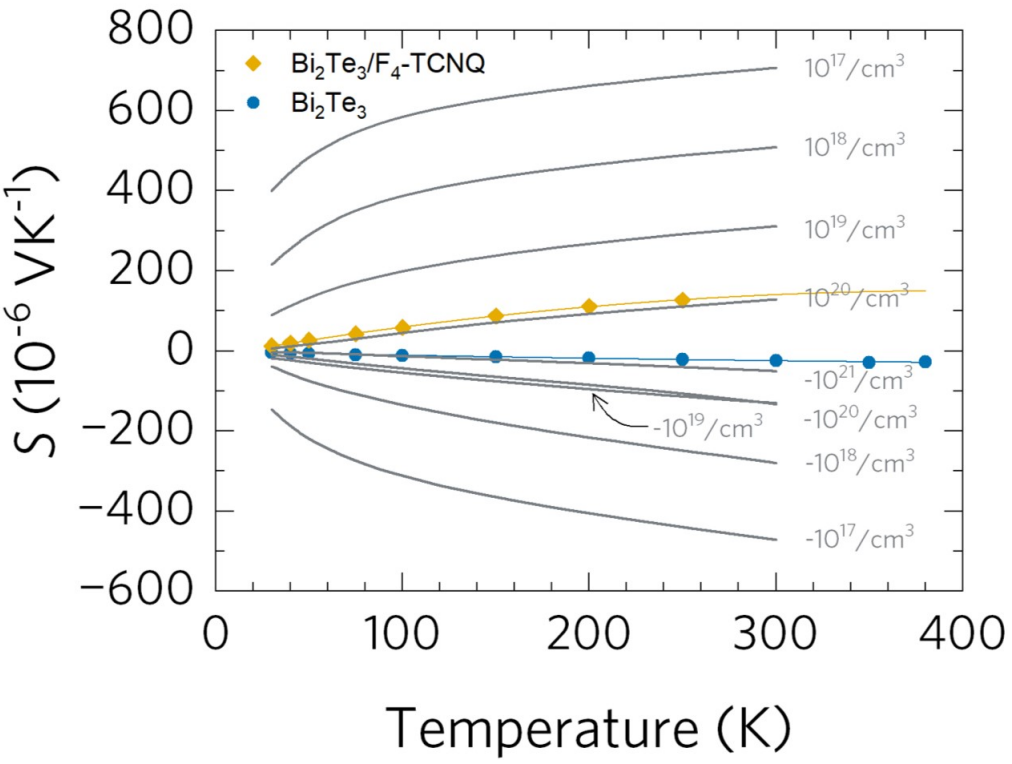

Figure 6.6: Plot for Seebeck coefficient versus temperature with different carrier concentrations for heavily doped cases, showing comparison between measured points and simulated curves.

6.4 Polarized Raman spectroscopy of $HfTe_5$ under strain from DFT and experiment

Hafnium Telluride ($HfTe_5$) is a compound that has recently gained significant attention in the fields of condensed matter physics due to topological and thermoelectric properties. As a topological insulator, $HfTe_5$ exhibits unique electronic behavior on its surface, characterized by protected Dirac fermions. These surface states enable efficient and low-energy dissipation conduction channels, holding great potential for applications in next-generation electronics and quantum computing. [129, 54] Additionally, $HfTe_5$ possesses excellent thermoelectric properties, making it a promising candidate for converting heat into electricity. [96] With a

high thermoelectric figure of merit (zT) [98] and low thermal conductivity, [183] it has the potential to revolutionize the field of thermoelectric materials, enabling more efficient energy harvesting and waste heat recovery. $HfTe_5$'s versatility, stability, and compatibility with existing technologies make it a standout material for advancing both topological physics and thermoelectric applications, paving the way for innovative solutions in energy conversion and quantum technologies.

The research interest in strained-tuned topological phase transitions is on the rise. This field of study presents significant challenges, and one widely accepted mechanism for inducing topological phase transitions is the application of strain to the material. [122] This phenomenon has been investigated in various materials, including Cd_3As_2 [213] and $ZrTe_5$ [59], where topological phase transitions have been calculated and explored. $HfTe_5$, similar to $ZrTe_5$ also could have topological phase transition under strain. Therefore, understanding the elastic and strain properties is crucial. This work mostly reports the polarized Raman under strain.

The Raman spectroscopic measurements were conducted at ambient conditions in reflection mode using 532.3 nm continuous wave excitation (∼1.6 mW, Oxxius LCX-532S-100, continuous wave (CW) single longitudinal mode diode pumped solid state laser), in a Horiba LabRAM HR Evolution high resolution confocal Raman microscope fitted with volume Bragg gratings. The experiment was configured using an 2400 mm^{-1} holographic grating blazed at 500 nm, a 100 mm confocal hole diameter, and a 50X, 0.9 N.A. cover glass-corrected objective. Spectral calibration was performed using the 1332.5 cm^{-1} band of a synthetic Type IIa diamond, and spectral intensity was calibrated using a VIS-halogen light source (NIST test no. 685/289682-17).

For our DFT calculations, we use plane-wave density functional theory (DFT) implemented in the code Quantum ESPRESSO, version 7.1 [67]. We used local density approximation (LDA) functional [165] from Pseudodojo set [2]. Kinetic energy cutoffs of 952 eV (70 Ry) was used. Half-shifted k-point grids of $4 \times 4 \times 2$ were chosen to converge the total energies within 0.001 eV/atom and the stresses were relaxed below 0.1 kbar.

The crystal structure of $HfTe_5$ has the D_{2h} point group with an orthorhombic

crystal structure in a conventional unit cell. The lattice parameters are $a = 3.92$ Å, $b = 14.27$ Å, and $c = 13.42$ Å, as shown in Fig. 6.7. Because of this crystal anisotropy, we expect different Raman spectra when strain is applied.

We initiated our study by comparing the polarized Raman spectra obtained from both theoretical calculations and experimental measurements. In the experimental setup, we aligned the long, needle-like shape of the material, believed to represent the a-axis, [58] with the horizontal polarization of incident light. As shown in Figure 6.8(a), we achieved a good agreement in the spectra, with incoming and outgoing polarizations aligned parallel to the a-axis. Note that in order to compensate the temperature effects, we reduced the experimental results by multiplication factor of $\omega(1 - e^{-\frac{-\hbar\omega}{kT}})$ (where ω is the Raman shift and T= 300 K) which helps to compare to the calculated absolute Raman intensities as discussed in [196]. In the (HV) polarization setup, there are two possible perpendicular axes to the known a-axis. The measured spectra in this configuration only partly agree with both polarizations, as demonstrated in Figure 6.8(b). This suggests that further measurements and analysis are necessary to confirm the exact lattice orientation. Additionally, calculated results shown in Figures 6.9, 6.10, and 6.11 depict the impact of tensile and compressive strain applied along the x-, y-, and z-axes of the crystal, respectively, under different polarizations of light. These results highlight the sensitivity of anisotropic $HfTe_5$ to strain-induced Raman shifts. This is a valuable asset in understanding and characterizing the effects of strain on $HfTe_5$, especially when applied in other studies, such as those related to topological phase transitions.

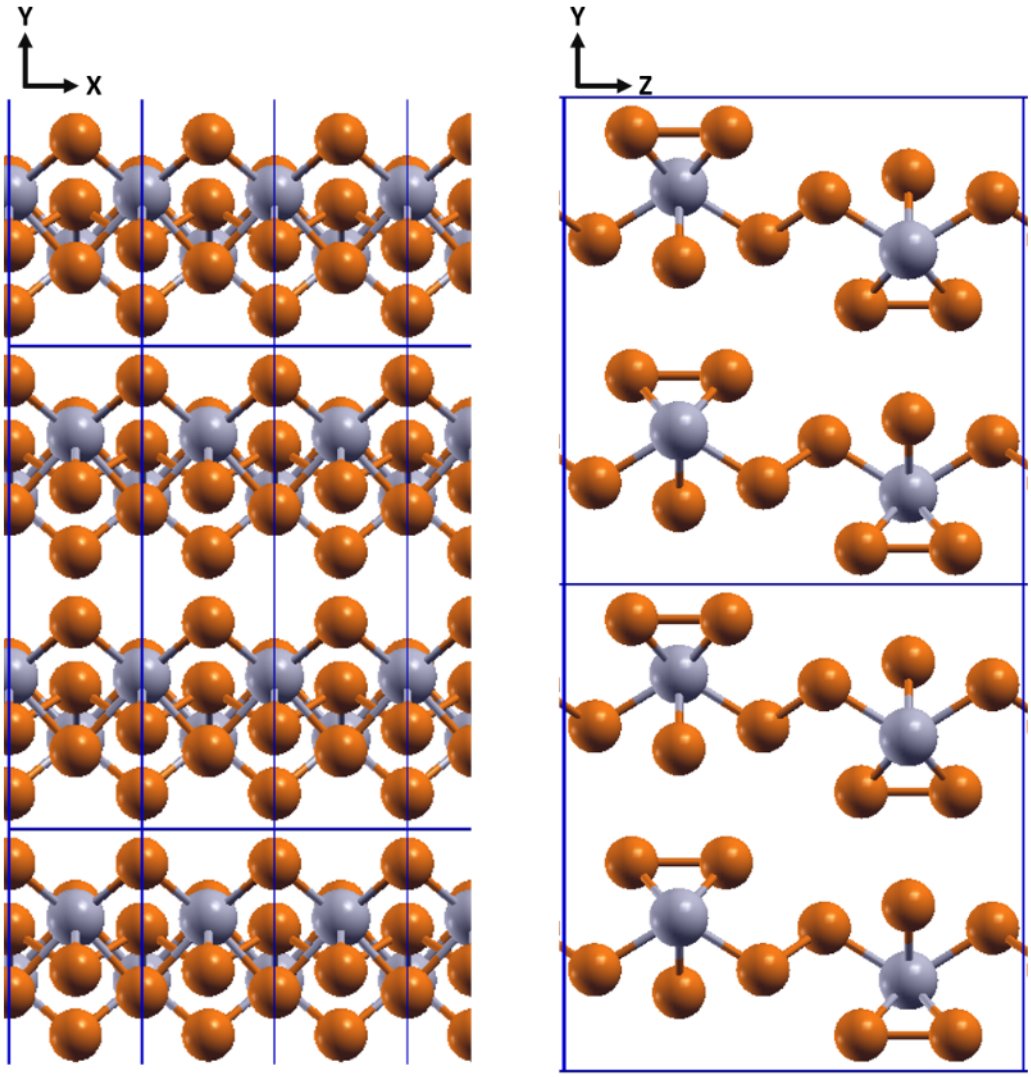

Figure 6.7: Crystal structure of $HfTe_5$ with two different views. Blue rectangular box represents conventional unit cell. Crystal is layered structure along y-axis.

(a) $z(HH)\overline{z}$ (b) $z(HV)\overline{z}$

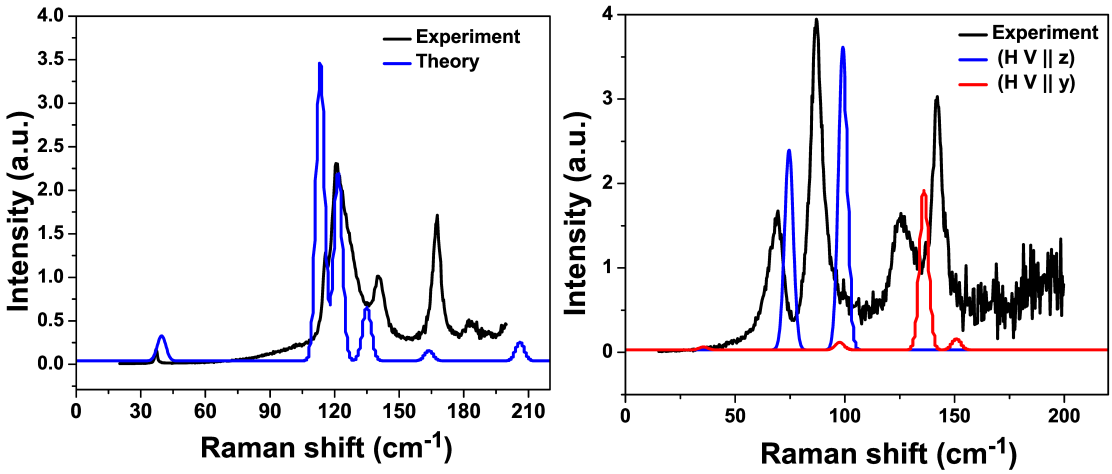

Figure 6.8: Polarized Raman intensity from theory and experiment. Polarization parallel to long needle is termed as 'H' and perpendicular to the chain is termed as 'V'. Usually, long needle like chain is x-axis [58]. The experimental Raman is measured at room temperature. 'V' $\parallel$ y or z means analyzer is parallel to the crystal's y- or z-direction.

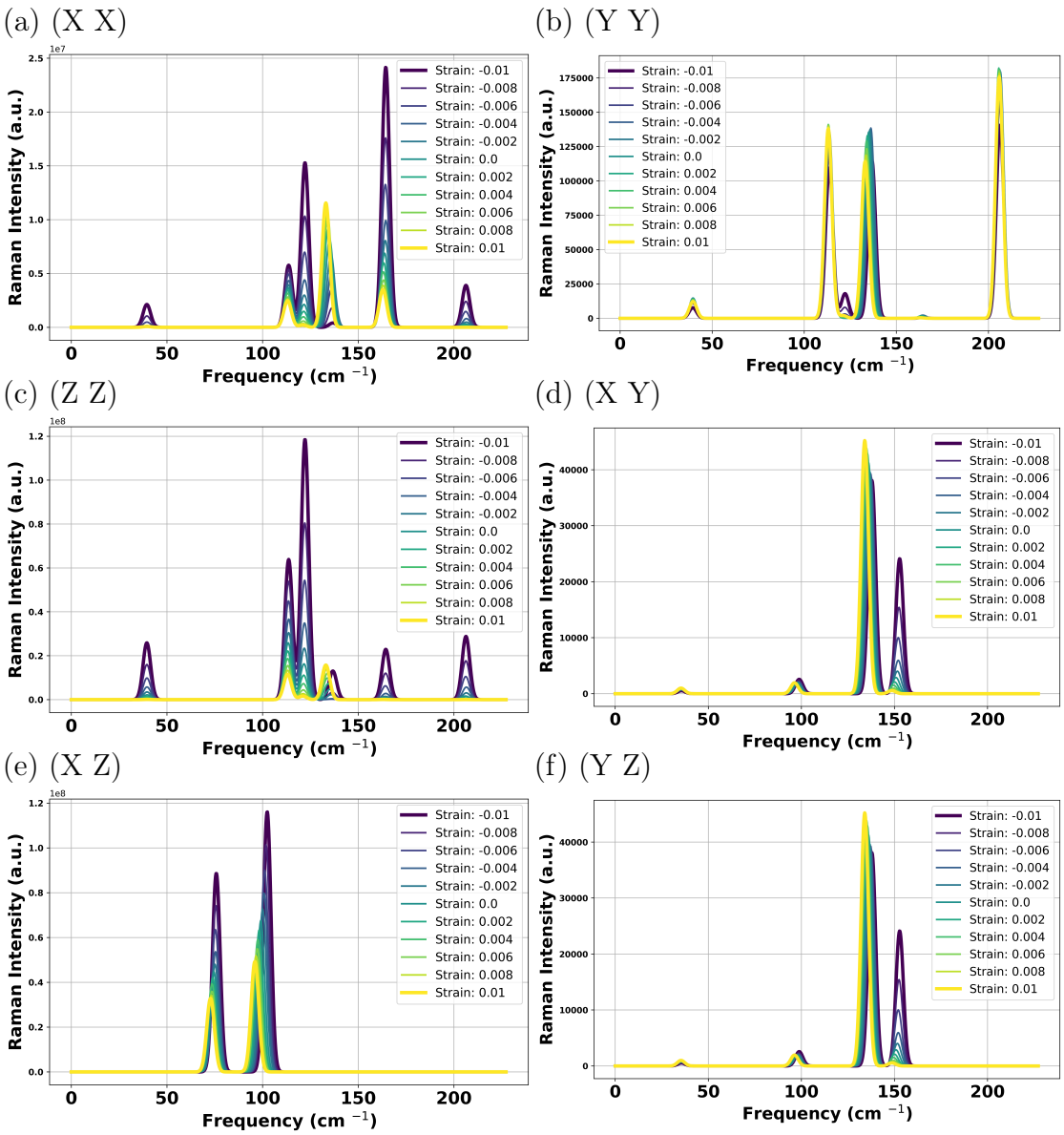

Figure 6.9: Calculated Raman spectra under strain. Strain is along x-axis of crystal. Symbols in parentheses represent the direction of polarization of light.

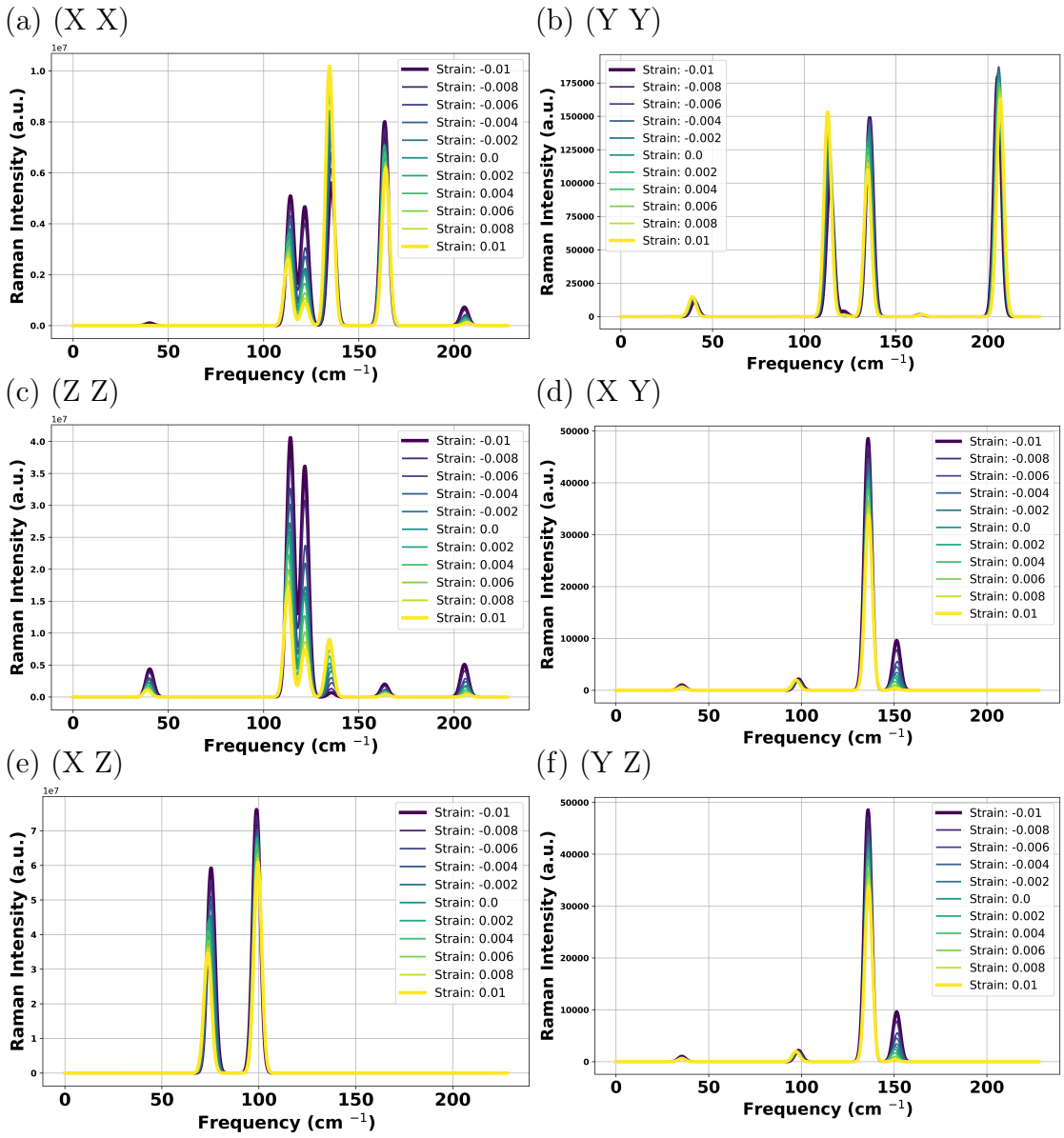

Figure 6.10: Calculated Raman spectra under strain. Strain is along y-axis of crystal. Symbols in parentheses represent the direction of polarization of light.

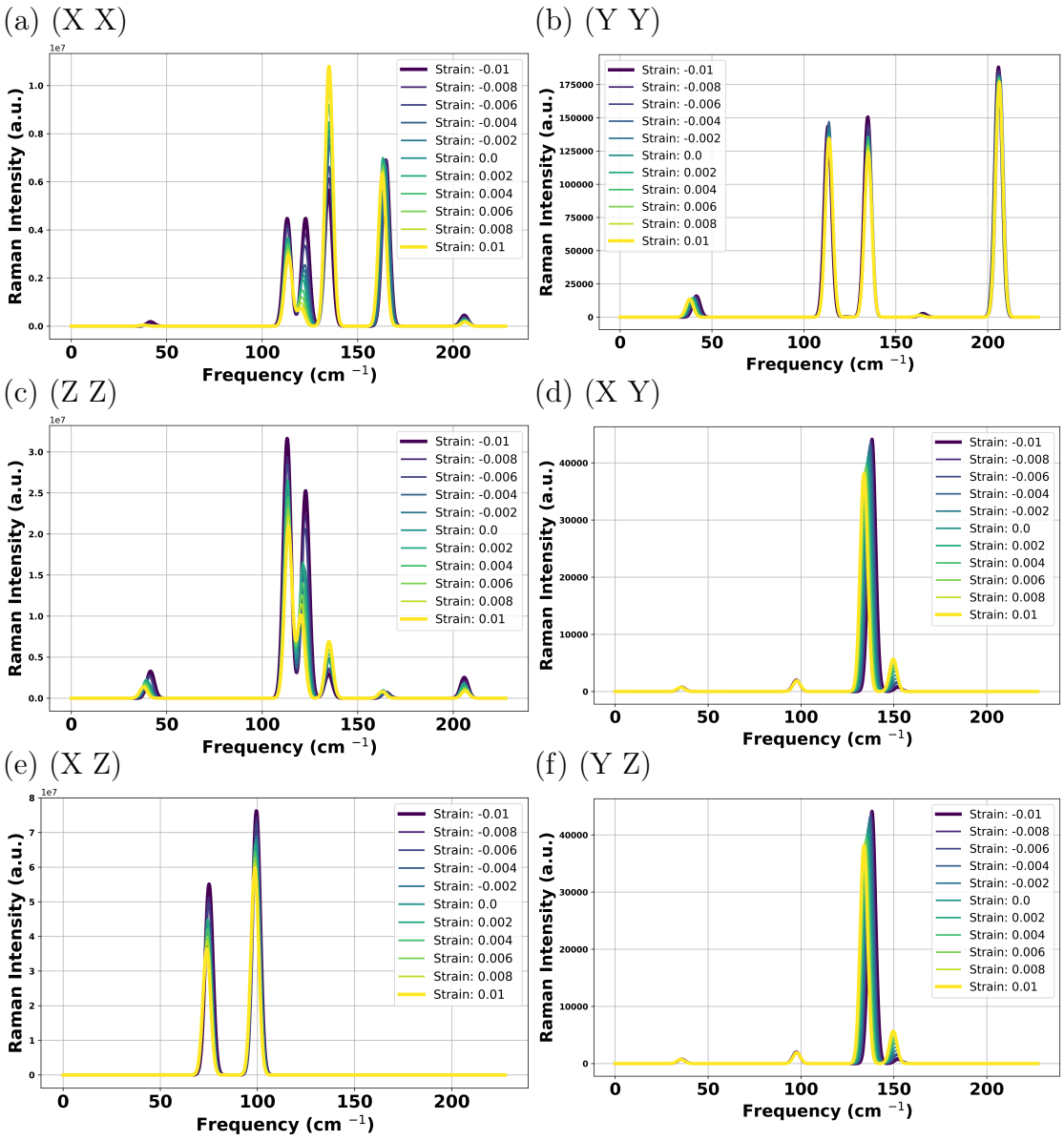

Figure 6.11: Calculated Raman spectra under strain. Strain is along z-axis of the crystal. Symbols in parentheses represent the direction of polarization of light.

Chapter 7

Conclusions

Low-dimensional materials, such as Transition Metal Dichalcogenides (TMDs) and perovskites, represent an intriguing frontier in materials science and nanotechnology. These materials have the potential to revolutionize device technology by making them faster, more efficient, cost-effective, and durable. However, despite their remarkable potential, the integration of low-dimensional materials into the real-world devices is hindered by several significant challenges.

One of the foremost challenges lies in the synthesis and scalability of these materials. While various synthesis methods exist [111], ensuring consistent and large-scale production with minimal defects remains an ongoing hurdle. [123] Each material often requires specific synthesis techniques, making it challenging to efficiently produce a diverse array of materials. Integrating low-dimensional materials into existing electronic and photonic devices is complex. These materials often necessitate the development of novel manufacturing processes and materials to ensure compatibility and optimal performance, adding complexity and cost to integration efforts.

On the flip side, the prospects for these materials are equally compelling. They offer great promise in the realm of optoelectronic devices, as they efficiently absorb and emit light, potentially enhancing the efficiency of solar cells, LEDs, and photodetectors. Furthermore, they are emerging as strong contenders in quantum technologies due to their unique quantum properties and tunability, opening exciting opportunities in quantum computing and communication. Perovskites,

in particular, have the potential to revolutionize the renewable energy sector and LEDs, thanks to their cost-effectiveness, high energy conversion efficiency in solar cells, and broadband emission. These materials are also well-suited for flexible and transparent electronics, heralding innovations in wearable technology, transparent displays, and portable devices. Their tunable properties enable customization to meet specific application requirements, making them versatile for a wide range of technological advancements. Moreover, the multifunctional properties often exhibited by TMDs and perovskites, combining electrical conductivity, optical response, and magnetism, hold the potential to revolutionize various industries through the development of multifunctional devices.

In this dissertation, I have explored a diverse array of low-dimensional materials, spanning transition metal dichalcogenides, perovskites/organic metal halide hybrids, Bi_2Te_3, and $HfTe_5$. Each class of material presents unique and intriguing features. For instance, the incorporation of Ni into MoS_2 enhances lubrication performance, offering low wear and extended lifetime, particularly beneficial for space applications. Metallic layered materials exhibit promise for battery applications, while Ni-doped 1H monolayer MoS_2 introduces in-gap states suitable for quantum emitters. The ferroelectric properties of 1T monolayer MoS_2 make it valuable for data storage devices, and its distinct electronic structure with higher gaps in the conduction band holds potential for transparent conductors, intermediate band solar cells, and photon down conversion. Bi_2Te_3 and $HfTe_5$ demonstrate enhanced thermoelectric and topological insulating properties, shaping the future of electronics with efficient electron transport in topological insulators. Moreover, organic metal halide hybrids offer broad-spectrum emission for LEDs and photon down-conversion applications. Furthermore, this work not only highlights the potential applications but also provides a methodology for studying these materials. The systematic exploration of doping effects, analysis of new crystal phases, and the examination of exciton dynamics during light absorption contribute to a comprehensive understanding of studying similar materials. These methodologies offer a guide for future researchers, enabling them to unravel the properties of other low-dimensional materials and further expand the scope of knowledge in this

field. Moreover, this thesis paves the way for further explorations. While we investigated Ni doping on MoS_2, there's an opportunity to explore on what happens when we dope other TMDs with Ni or other transition metals. The novel reconstructed structures observed in Ni-doped 1T phase MoS_2 raise questions about potential similar or distinct reconstructions in other 1T phase TMDs with diverse transition metal dopants. The exploration of doping in the 9R phase, which we introduced, is an open field for further investigation. Additionally, our novel approach to comprehend excited state dynamics raises further opportunity to extend the understanding of light-induced degradation. These unexplored aspects provide exciting opportunities for future research in the field of low-dimensional materials.

In conclusion, low-dimensional materials, while accompanied by challenges in synthesis, stability, and integration, hold remarkable prospects for transforming multiple industries. These materials are poised to reshape the landscape of optoelectronics, energy conversion, quantum technologies, and flexible electronics. Researchers and industry leaders are dedicated to overcoming these challenges, marking a new era where low-dimensional materials may influence the way we harness energy and interact with our environment. Their potential for sustainable and high-performance technologies is a driving force behind ongoing research and innovation in this field.

Bibliography

[1] *web*, https://materialsproject.org/materials/mp-557869/.

[2] *web*, http://www.pseudo-dojo.org.

[3] *web*, http://www.quantum-simulation.org/potentials.

[4] Muharrem Acerce, Damien Voiry, and Manish Chhowalla. Metallic 1T phase MoS_2 nanosheets as supercapacitor electrode materials. *Nat. Nanotech.*, 10:313–318, 2015.

[5] Ogulcan Acikgoz, Enrique Guerrero, Alper Yanilmaz, Omur E Dagdeviren, Cem Çelebi, David A Strubbe, and Mehmet Z Baykara. Intercalation leads to inverse layer dependence of friction on chemically doped MoS_2. *Nanotechnology*, 34(1):015706, 2022.

[6] Carlo Adamo and Vincenzo Barone. Toward reliable density functional methods without adjustable parameters: The PBE0 model. *J. Chem. Phys.*, 110(13):6158–6170, 1999.

[7] Adriano Ambrosi, Zdeněk Soferb, and Martin Pumera. 2H →1T phase transition and hydrogen evolution activity of MoS_2, $MoSe_2$, WS_2 and WSe_2 strongly depends on the MX_2 composition. *Chem. Commun.*, 51:8450–8453, 2015.

[8] M. P. Andersson. Density functional theory with modified dispersion correction for metals applied to self-assembled monolayers of thiols on Au(111). *J. Theor. Chem.*, 2013:2356–7686, 2013.

[9] Vincenzo Aquilanti, Daniela Ascenzi, Elisabetta Braca, David Cappelletti, and Fernando Pirani. Production, characterization and scattering of a sulfur atom beam : Interatomic potentials for the rare-gas sulfides, RS (R = Ne, Ar, Kr, Xe). *Phys. Chem. Chem. Phys.*, 2:4081–4088, 2000.

[10] M. I. Aroyo, J. M. Perez-Mato, C. Capillas, E. Kroumova, S. Ivantchev, G. Madariaga, A. Kirov, and H. Wondratsche. Bilbao Crystallographic Server

I: Databases and crystallographic computing programs. *Z. Krist.*, 221:15–27, 2006.

[11] M. I. Aroyo, J. M. Perez-Mato, D. Orobengoa, E. Tasci, G. de la Flor, and A. Kirov. Crystallography online: Bilbao Crystallographic Server. *Bulg. Chem. Commun.*, 43:183–197, 2011.

[12] Visnja Babacic, David Saleta Reig, Sebin Varghese, Thomas Vasileiadis, Emerson Coy, Klaas-Jan Tielrooij, and Bartlomiej Graczykowski. Thickness-dependent elastic softening of few-layer free-standing $MoSe_2$. *Adv. Mater.*, 33:2008614, 2021.

[13] Stefano Baroni, Stefano de Gironcoli, and Andrea Dal Corso. Phonons and related crystal properties from density-functional perturbation theory. *Rev. Mod. Phys.*, 73:515–562, 2001.

[14] S.S. Batsanov. Intramolecular contact radii close to the van der Waals radii. *Zh. Neorg. Khim.*, 45:992–996, 2000.

[15] Britton W. H. Baugher, Hugh O. H. Churchill, Yafang Yang, and Pablo Jarillo-Herrero. Optoelectronic devices based on electrically tunable p–n diodes in a monolayer dichalcogenide. *Nat. Nanotech.*, 9:262–267, 2014.

[16] R. Bechmann. Elastic and piezoelectric constants of alpha-quartz. *Phys. Rev.*, 110:1060–1061, 1958.

[17] S. P. Beckman, Xinjie Wang, Karin M. Rabe, and David Vanderbilt. Ideal barriers to polarization reversal and domain-wall motion in strained ferroelectric thin films. *Phys. Rev. B*, 79:144124, 2009.

[18] E Benavente, M.A. Santa-Ana, F Mendizábal, and G González. Intercalation chemistry of molybdenum disulfide. *Coord. Chem. Rev.*, 224:87 – 109, 2002.

[19] Lennart Bengtsson. Dipole correction for surface supercell calculations. *Phys. Rev. B*, 59:12301–12304, 1999.

[20] Daniel I. Bilc, Diana Benea, Viorel Pop, Philippe Ghosez, and Matthieu J. Verstraete. Electronic and thermoelectric properties of transition-metal dichalcogenides. *J. Phys. Chem. C*, 125(49):27084–27097, 2021.

[21] T. Björkman, A. Gulans, A. V. Krasheninnikov, and R. M. Nieminen. Van der Waals bonding in layered compounds from advanced density-functional first-principles calculations. *Phys. Rev. Lett.*, 108:235502, 2012.

[22] J.-C. Blancon, A. V. Stier, H. Tsai, W. Nie, C. C. Stoumpos, B. Traoré, L. Pedesseau, M. Kepenekian, F. Katsutani, et al. Scaling law for excitons in 2D perovskite quantum wells. *Nat. Commun.*, 9:2254, 2018.

[23] Chen Xiao Bo, Chen Zhen Lian, and Li Jun. Critical electronic structures controlling phase transitions induced by lithium ion intercalation in molybdenum disulphide. *Chin. Sci. Bull.*, 58:1632–1641, 2013.

[24] P Brüesch. Phonons: Theory and Experiments II, of springer series in solid-state sciences vol. 65, chap. 2, 1986.

[25] Guillaume Brunin, Francesco Ricci, Viet-Anh Ha, Gian-Marco Rignanese, and Geoffroy Hautier. Transparent conducting materials discovery using high-throughput computing. *npj Comput. Mater.*, 5:63, 2019.

[26] Ting Cao, Gang Wang, Wenpeng Han, Huiqi Ye, Chuanrui Zhu, Junren Shi, Qian Niu, Pingheng Tan, Enge Wang, Baoli Liu, and Ji Feng. Valley-selective circular dichroism of monolayer molybdenum disulphide. *Nat. Commun.*, 3:887, 2012.

[27] Riccarda Caputo. Polytypism of MoS_2. *J. J. Inorg. Chem.*, 1:1, 2016.

[28] Emily Ann Carter, Nima Alidoust, and Martina Lessio. Multiple band gap Co-Ni oxide compositions and applications thereof. pages patent number:10,256,361, 2019.

[29] Onur Çaylak and Björn Baumeier. Excited-state geometry optimization of small molecules with many-body green's functions theory. *Journal of Chem. Theory and Comp.*, 17(2):879–888, 2021.

[30] Huihui Chen, Zhuo Chen, Binghui Ge, Zhen Chi, Hailong Chen, Hanchun Wu, Chuanbao Cao, and Xiangfeng Duan. General strategy for two-dimensional transition metal dichalcogenides by ion exchange. *Chem. Mater.*, 29(23):10019–10026, 2017.

[31] Kaiyun Chen, Junkai Deng, Qian Shi, Xiangdong Ding, Jun Sun, Sen Yang, and Jefferson Zhe Liu. Charge doping induced reversible multistep structural phase transitions and electromechanical actuation in two-dimensional 1T′-MoS_2. *Nanoscale*, 12:12541–12550, 2020.

[32] Xue Cheng, Jiaqi Ma, Yunxi Zhou, Chen Fang, Jun Wang, Junze Li, Xinglin Wen, and Dehui Li. Optical anisotropy of one-dimensional perovskite $C_4N_2H_{14}PbI_4$ crystals. *J. Phys.: Photonics*, 2:014008, 2020.

[33] Ji-Hae Choi and Seung-Hoon Jhi. Origin of robust out-of-plane ferroelectricity in d1T-MoS_2 monolayer. *J. Phys.: Condens. Matter*, 32(4):045702, 2019.

[34] Beatriz Cordero, Verónica Gómez, Ana E. Platero-Prats, Marc Revés, Jorge Echeverría, Eduard Cremades, Flavia Barragán, and Santiago Alvarez. Covalent radii revisited. *Dalton Trans.*, 21:2832–2838, 2008.

[35] S.S. Coutinho, M.S. Tavares, C.A. Barboza, N.F. Frazão, E. Moreira, and David L. Azevedo. 3R and 2H polytypes of MoS_2: DFT and DFPT calculations of structural, optoelectronic, vibrational and thermodynamic properties. *J. Phys. Chem. Solids*, 111:25 – 33, 2017.

[36] Alexander Croy. Bending rigidities and universality of flexural modes in 2D crystals. *J. Phys. Mater.*, 3(2):02LT03, 2020.

[37] Edney Geraldo da Silveira Firmiano, Adriano C. Rabelo, Cleocir J. Dalmaschio, Antonio N. Pinheiro, Ernesto C. Pereira, Wido H. Schreiner, and Edson Robeto Leite. Supercapacitor electrodes obtained by directly bonding 2D MoS_2 on reduced graphene oxide. *Adv. Energy Mater.*, 4:1301380, 2014.

[38] Jiao Deng, Haobo Li, Jianping Xiao, Yunchuan Tu, Dehui Deng, Huaixin Yang, Huanfang Tian, Jianqi Li, Pengju Rena, and Xinhe Bao. Triggering the electrocatalytic hydrogen evolution activity of the inert two-dimensional MoS_2 surface via single-atom metal doping. *Energy Environ. Sci.*, 8:1594, 2015.

[39] Jack Deslippe, Georgy Samsonidze, David A. Strubbe, Manish Jain, Marvin L. Cohen, and Steven G. Louie. BerkeleyGW: A massively parallel computer package for the calculation of the quasiparticle and optical properties of materials and nanostructures. *Comput. Phys. Commun.*, 183:1269–1289, 2012.

[40] Krishna P. Dhakal, Hyunmin Kim, Seonwoo Lee, Youngjae Kim, JaeDong Lee, and Jong-Hyun Ahn. Probing the upper band gap of atomic rhenium disulfide layers. *Light Sci. Appl.*, 7:98, 2018.

[41] Qingfeng Ding, Yifan Zhu, Lanyong Xiang, Jiandong Sun, Yang Shangguan, Jinfeng Zhang, Xinxing Li, Lin Jin, and Hua Qin. Terahertz direct polarization detector based on integrated antenna-coupled algan/gan high-electron-mobility transistors. *Opt. Express*, 30(24):42956–42966, 2022.

[42] Emma R. Dohner, Eric T. Hoke, and Hemamala I. Karunadasa. Self-assembly of broadband white-light emitters. *J. Am. Chem. Soc.*, 136:1718–1721, 2014.

[43] Kapildeb Dolui, Ivan Rungger, Chaitanya Das Pemmaraju, and Stefano Sanvito. Possible doping strategies for MoS_2 monolayers: An ab initio study. *Phys. Rev. B*, 88:075420, 2013.

[44] Ping Du, Yuanzhi Zhu, Junyang Zhang, Danyun Xu, Wenchao Peng, Guoliang Zhang, Fengbao Zhang, and Xiaobin Fan. Metallic 1T phase MoS_2 nanosheets as a highly efficient co-catalyst for the photocatalytic hydrogen evolution of CdS nanorods. *RSC Adv.*, 6:74394–74399, 2016.

[45] S. L. Dudarev, G. A. Botton, S. Y. Savrasov, C. J. Humphreys, and A. P. Sutton. Electron-energy-loss spectra and the structural stability of nickel oxide: An LSDA+U study. *Phys. Rev. B*, 57:1505–1509, 1998.

[46] Karel-Alexander N. Duerloo, Mitchell T. Ong, and Evan J. Reed. Intrinsic piezoelectricity in two-dimensional materials. *J. Phys. Chem. Lett.*, 3(19):2871–2876, 2012.

[47] Keenan E. Dungey, M. David Curtis, and James E. Penner-Hahn. Structural characterization and thermal stability of MoS_2 intercalation compounds. *Chem. Mater.*, 10:2152–2161, 1998.

[48] Goki Eda, Takeshi Fujita, Hisato Yamaguchi, Damien Voiry, Mingwei Chen, and Manish Chhowalla. Coherent atomic and electronic heterostructures of single-layer MoS_2. *ACS Nano*, 6:7311–7317, 2012.

[49] Matthias Ernzerhof and Gustavo E. Scuseria. Assessment of the Perdew–Burke–Ernzerhof exchange-correlation functional. *J. Chem. Phys.*, 110(11):5029–5036, 1999.

[50] C. Faber, P. Boulanger, C. Attaccalite, E. Cannuccia, I. Duchemin, T. Deutsch, and X. Blase. Exploring approximations to the *GW* self-energy ionic gradients. *Phys. Rev. B*, 91(15), 2015.

[51] Xiaofeng Fan, C.-H. Chang, W. T. Zheng, Jer-Lai Kuo, and David J. Singh. The electronic properties of single-layer and multilayer mos_2 under high pressure. *J. Phys. Chem. C*, 119(19):10189–10196, 2015.

[52] Xiaofeng Fan, David J. Singh, and Weitao Zheng. Valence band splitting on multilayer MoS_2: Mixing of spin–orbit coupling and interlayer coupling. *J. Phys. Chem. Lett.*, 7(12):2175–2181, 2016.

[53] Xiaofeng Fan, W.T. Zheng, Jer-Lai Kuo, David J. Singh, C.Q. Sun, and W. Zhu. Modulation of electronic properties from stacking orders and spin-orbit coupling for 3R-type MoS_2. *Sci. Rep.*, 6:24140, 2016.

[54] Zongjian Fan, Qi-Feng Liang, Y. B. Chen, Shu-Hua Yao, and Jian Zhou. Transition between strong and weak topological insulator in $ZrTe_5$ and $HfTe_5$. *Sci. Rep.*, 7(12):45667, 2017.

[55] Yuqiang Fang, Xiaozong Hu, Wei Zhao, Jie Pan, Dong Wang, Kejun Bu, Yuanlv Mao, Shufen Chu, Pan Liu, Tianyou Zhai, and Fuqiang Huang. Structural determination and nonlinear optical properties of new 1T‴-type MoS_2 compound. *J. Am. Chem. Soc.*, 141:790–793, 2019.

[56] Yuqiang Fang, Jie Pan, Jianqiao He, Ruichun Luo, Dong Wang, Xiangli Che, Kejun Bu, Wei Zhao, Pan Liu, Gang Mu, Hui Zhang, Tianquan Lin, and Fuqiang Huang. Structure re-determination and superconductivity observation of bulk 1T MoS_2. *Angew. Chem. Int. Ed.*, 57:1232 –1235, 2018.

[57] J. L. Feldman. Elastic constants of 2H-MoS_2 and 2H-$NbSe_2$ extracted from measured dispersion curves and linear compressibilities. *J. Phys. Chem. Solids*, 37(12):1141–1144, 1976.

[58] Tianli Feng, Xuewang Wu, Xiaolong Yang, Peipei Wang, Liyuan Zhang, Xu Du, Xiaojia Wang, and Sokrates T. Pantelides. Thermal conductivity of $HfTe_5$: A critical revisit. *Adv. Funct. Mater.*, 30(5):1907286, 2020.

[59] Apurva Gaikwad, Song Sun, Peipei Wang, Liyuan Zhang, Jennifer Cano, Xi Dai, and Xu Du. Strain-tuned topological phase transition and unconventional zeeman effect in $ZrTe_5$ microcrystals. *Commun. Mater.*, 3:94, 2022.

[60] Deepak Thrithamarassery Gangadharan and Dongling Ma. Searching for stability at lower dimensions: current trends and future prospects of layered perovskite solar cells. *Energy Environ. Sci.*, 12:2860–2889, 2019.

[61] Yunye Gao, Mingyuan Gao, and Yuerui Lu. Two-dimensional multiferroics. *Nanoscale*, 13:19324–19340, 2021.

[62] Yanfeng Ge, Wenhui Wan, Yulu Ren, and Yong Liu. Large thermoelectric power factor of high-mobility transition-metal dichalcogenides with 1T″ phase. *Phys. Rev. Res.*, 2:013134, 2020.

[63] Xiumei Geng, Yucong Jiao, Yang Han, Alolika Mukhopadhyay, Lei Yang, and Hongli Zhu. Freestanding metallic 1T MoS_2 with dual ion diffusion paths as high rate anode for sodium-ion batteries. *Adv. Funct. Mater.*, 27:1702998, 2017.

[64] Mladen Georgiev, Lubomir Mihailov, and Jai Singh. Self-assembly of broadband white-light emitters. *Pure and Appl. Chem.*, 67:447–456, 1995.

[65] Pouyan Ghaemi, Roger S. K. Mong, and J. E. Moore. In-plane transport and enhanced thermoelectric performance in thin films of the topological insulators Bi_2Te_3 and Bi_2Se_3. *Phys. Rev. Lett.*, 105:166603, 2010.

[66] Hannah Giang, Omair Adil, and Ian I. Suni. Electrodeposition of Ni-doped MoS_2 thin films. *J. Electrochem. Soc.*, 167(8):082512, 2020.

[67] P Giannozzi, O Andreussi, T Brumme, O Bunau, M Buongiorno Nardelli, M Calandra, R Car, C Cavazzoni, D Ceresoli, M Cococcioni, N Colonna,

I Carnimeo, A Dal Corso, S de Gironcoli, P Delugas, R A DiStasio, A Ferretti, A Floris, G Fratesi, G Fugallo, R Gebauer, et al. Advanced capabilities for materials modelling with Quantum ESPRESSO. *J. Phys.: Condens. Matter*, 29:465901, 2017.

[68] Paolo Giannozzi, Stefano Baroni, Nila Bonini, Matteo Calandra, Roberto Car, Carlo Cavazzoni, Davide Ceresoli, Guido L Chiarotti, Matteo Cococcioni, Ismaila Dabo, Andrea Dal Corso, Stefano de Gironcoli, Stefano Fabris, Guido Fratesi, Ralph Gebauer, et al. QUANTUM ESPRESSO: a modular and open-source software project for quantum simulations of materials. *J. Phys.: Condens. Matter*, 21(39), 2009.

[69] F. Giustino. Materials modelling using density functional theory: properties and predictions. *Oxford University Press*, 2014.

[70] Dominik Gresch, Gabriel Autès, Oleg V. Yazyev, Matthias Troyer, David Vanderbilt, B. Andrei Bernevig, and Alexey A. Soluyanov. Z2pack: Numerical implementation of hybrid wannier centers for identifying topological materials. *Phys. Rev. B*, 95:075146, 2017.

[71] Stefan Grimme. Semiempirical GGA-type density functional constructed with a long-range dispersion correction. *J. Comput. Chem.*, 27:1787–1799, 2006.

[72] Enrique Guerrero, Rijan Karkee, and David A. Strubbe. Phase stability and Raman/IR signatures of Ni–doped MoS_2 from DFT studies. *J. Phys. Chem. C*, 125:13401–13412, 2021.

[73] Enrique Guerrero and David A. Strubbe. Atomistic mechanisms of sliding in few-layer and bulk doped MoS_2. *arXiv:2209.15629*, 2022. https://doi.org/10.48550/arXiv.2209.15629.

[74] Xiaowei Guo, Erhong Song, Wei Zhao, Shumao Xu, Wenli Zhao, Yongjiu Lei, Yuqiang Fang, Jianjun Liu, and Fuqiang Huang. Charge self-regulation in 1T‴-MoS_2 structure with rich S vacancies for enhanced hydrogen evolution activity. *Nat. Commun.*, 13:5954, 2022.

[75] Zhiying Guo, Xingyu Hao, Juncai Dong, Haijing Li, Yu Gong, Dongliang Yang, Jiangwen Liao, Shengqi Chu, Yanchun Li, Xiaodong Li, and Dongliang Chen. Prediction of topological nontrivial semimetals and pressure-induced lifshitz transition in 1T′-MoS_2 layered bulk polytypes. *Nanoscale*, 12:22710–22717, 2020.

[76] R. Gómez-Balderas, J. M. Martínez-Magadán, R. Santamaria, and C. Amador. Promotional effect of Co or Ni impurity in the catalytic activity of MoS_2: An electronic structure study. *Int. J. Quantum Chem.*, 80:406–415, 2000.

[77] Mikko Hakala, Rasmus Kronberg, and Kari Laasonen. Hydrogen adsorption on doped MoS_2 nanostructures. *Sci. Rep.*, 7:15243, 2017.

[78] Hamida Hallil, Weifan Cai, Kang Zhang, Peng Yu, Sheng Liu, Ran Xu, Chao Zhu, Qihua Xiong, Zheng Liu, and Qing Zhang. Strong piezoelectricity in 3R-MoS_2 flakes. *Adv. Electron. Mater.*, 8(7):2101131, 2022.

[79] D. R. Hamann. Optimized norm-conserving Vanderbilt pseudopotentials. *Phys. Rev. B*, 88:085117, 2013.

[80] Yu Hao, Ya Tong Wang, Li Chun Xu, Zhi Yang, Rui Ping Liu, and Xiu Yan Li. 1T-MoS_2 monolayer doped with isolated Ni atoms as highly active hydrogen evolution catalysts: A density functional study. *Appl. Surf. Sci.*, 469:292 – 297, 2019.

[81] Lars Hedin. New method for calculating the one-particle green's function with application to the electron-gas problem. *Phys. Rev. series I*, 139:796–823, 1965.

[82] Ganesh Shridhar Hegde and A. N. Prabhu. A review on doped/composite bismuth chalcogenide compounds for thermoelectric device applications: Various synthesis techniques and challenges. *J. Electron. Mater.*, 51:2014–2042, 2022.

[83] Joy Heising and Mercouri G. Kanatzidis. Exfoliated and restacked MoS_2 and WS_2: Ionic or neutral species? encapsulation and ordering of hard electropositive cations. *J. Am. Chem. Soc.*, 121:11720–11732, 1999.

[84] P. Hohenberg and W. Kohn. Inhomogeneous electron gas. *Phys. Rev.*, 136:B864, 1964.

[85] Ting Hu, Rui Li, and Jinming Dong. A new (2×1) dimerized structure of monolayer 1T-molybdenum disulfide, studied from first principles calculations. *J. Chem. Phys.*, 139:174702, 2013.

[86] H. H. Huang, Xiaofeng Fan, David J. Singh, and W. T. Zheng. First principles study on 2H–1T′ transition in MoS_2 with copper. *Phys. Chem. Chem. Phys.*, 20:26986–26994, 2018.

[87] Ke-Jing Huang, Lan Wang, Yu-Jie Liu, Hai-Bo Wang, Yan-Ming Liu, and Ling-Ling Wang. Synthesis of polyaniline/2-dimensional graphene analog MoS_2 composites for high-performance supercapacitor. *Electrochim. Acta*, 109:587–594, 2013.

[88] Mark S. Hybertsen and Steven G. Louie. Electron correlation in semiconductors and insulators: Band gaps and quasiparticle energies. *Phys. Rev. B*, 34:5390–5413, 1986.

[89] Roberto Improta, Fabrizio Santoro, and Lluís Blancafort. Quantum Mechanical Studies on the Photophysics and the Photochemistry of Nucleic Acids and Nucleobases. *Chem. Rev.*, 116(6):3540–3593, 2016.

[90] Sohrab Ismail-Beigi and Steven G. Louie. Excited-State Forces within a First-Principles Green's Function Formalism. *Phys. Rev. Lett.*, 90(7):4, 2003.

[91] Sohrab Ismail-Beigi and Steven G. Louie. Self-Trapped Excitons in Silicon Dioxide: Mechanism and Properties. *Phys. Rev. Lett.*, 95(15):156401, 2005.

[92] Viktoria V. Ivanovskaya, Alberto Zobelli, Alexandre Gloter, Nathalie Brun, Virginie Serin, and Christian Colliex. Ab initio study of bilateral doping within the MoS_2-NbS_2 system. *Phys. Rev. B*, 78:134104, 2008.

[93] Fujio Izumi and Koichi Momma. Three-dimensional visualization in powder diffraction. In *Appl. Cryst. XX*, volume 130 of *Solid State Phenomena*, pages 15–20. Trans Tech Publications Ltd, 2007.

[94] E.S. Jatirian-Foltidesa, J.J. Escobedo-Alatorrea, P.A. Marquez-Aguilar, H. Hardhienatab, K. Hingerlc, and A. Alejo-Molinaa. About the calculation of the second-order susceptibility $\chi^{(2)}$ tensorial elements for crystals using group theory. *Rev. Mex. Fis. E*, 62:5–13, 2016.

[95] Gwangsik Jeong, Chan Hun Kim, Young Gul Hur, Geun-Ho Han, Seong Ho Lee, and Kwan-Young Lee. Ni-doped MoS_2 nanoparticles prepared via core–shell nanoclusters and catalytic activity for upgrading heavy oil. *Energy Fuels*, 32:9263–9270, 2018.

[96] Kang Jia, Chuan-Lu Yang, Mei-Shan Wang, and Xiao-Guang Ma. High thermoelectric figure of merit and thermopower of $HfTe_5$ at room temperature. *J. Phys.: Condens. Matter*, 32(34):345501, 2020.

[97] Xingxing Jiang, Zhengwei Xu, Yueshao Zheng, Jiang Zeng, Ke-Qiu Chen, and Yexin Feng. A first-principles study of exciton self-trapping and electric polarization in one-dimensional organic lead halide perovskites. *Phys. Chem. Chem. Phys.*, 24:17323–17328, 2022.

[98] T.E. Jones, W.W. Fuller, T.J. Wieting, and F. Levy. Thermoelectric power of $HfTe_5$ and $ZrTe_5$. *Solid State Commun.*, 42(11):793–798, 1982.

[99] Mikkel Jørgensen, Kion Norrman, Suren A Gevorgyan, Thomas Tromholt, Birgitta Andreasen, and Frederik C Krebs. Stability of Polymer Solar Cells. *Adv. Mat.*, 24(5):580–612, 2012.

[100] Yang Jun-Feng, Parakash Braham, and Fang Qian-Feng. Tribological properties of transition metal di-chalcogenide based lubricant coatings. *Front. Mater. Sci.*, 6:116–127, 2012.

[101] Kristen Kaasbjerg, Kristian S. Thygesen, and Karsten W. Jacobsen. Phonon-limited mobility in n-type single-layer MoS_2 from first principles. *Phys. Rev. B*, 85:115317, 2012.

[102] M. Kan, J. Y. Wang, X. W. Li, S. H. Zhang, Y. W. Li, Y. Kawazoe, Q. Sun, and P. Jena. Structures and phase transition of a MoS_2 monolayer. *J. Phys. Chem. C*, 118:1515–1522, 2014.

[103] Rijan Karkee, Enrique Guerrero, and David A. Strubbe. Enhanced interlayer interactions in Ni-doped MoS_2, and structural and electronic signatures of doping site. *Phys. Rev. Materials*, 5:074006, 2021.

[104] Rijan Karkee and David A. Strubbe. Panoply of Ni-doping-induced reconstructions, electronic phases, and ferroelectricity in 1T-MoS_2. *arXiv:2107.07541*, 2023.

[105] H. S. Khare and D. L. Burris. The effects of environmental water and oxygen on the temperature-dependent friction of sputtered molybdenum disulfide. *Tribology Lett.*, 52:485–493, 2013.

[106] Charles Kittel. *Introduction to solid state physics*. Wiley, 1953.

[107] Hannu-Pekka Komsa and Arkady V. Krasheninnikov. Native defects in bulk and monolayer MoS_2 from first principles. *Phys. Rev. B*, 91(12):125304, 2015.

[108] Satoru Konabe and Takahiro Yamamoto. Piezoelectric coefficients of bulk 3R transition metal dichalcogenides. *Jpn. J. Appl. Phys.*, 56:098002, 2017.

[109] Neha Kondekar, Matthew G. Boebinger, Mengkun Tian, Mohammad Hamza Kirmani, and Matthew T. McDowell. The effect of nickel on MoS_2 growth revealed with *in situ* transmission electron microscopy. *ACS Nano*, 13:7117–7126, 2019.

[110] O. Krause, F. Müller, S. Birkmann, A. Böhm, M. Ebert, U. Grözinger, Th. Henning, R. Hofferbert, A. Huber, D. Lemke, R.-R. Rohloff, S. Scheithauer, et al. High-precision cryogenic wheel mechanisms of the JWST/MIRI instrument: performance of the flight models. *SPIE*, 7739:421 – 432, 2010.

[111] Partha Kumbhakar, Jitha S. Jayan, Athira Sreedevi Madhavikutty, P.R. Sreeram, Appukuttan Saritha, Taichi Ito, and Chandra Sekhar Tiwary. Prospective applications of two-dimensional materials beyond laboratory frontiers: A review. *iScience*, 26(5):106671, 2023.

[112] Michele Lazzeri and Francesco Mauri. First-principles calculation of vibrational Raman spectra in large systems: Signature of small rings in crystalline SiO_2. *Phys. Rev. Lett*, 90(3):036401, 2003.

[113] Sujin Lee, Rijan Karkee, Azza Ben-Akacha, Derek Luong, JS Winfred, Xinsong Lin, David A Strubbe, and Biwu Ma. One-dimensional organic metal halide nanoribbons with dual emission. *Chem. Commun.*, 59:3711–3714, 2023.

[114] Dominik Lembke and Andras Kis. Breakdown of high-performance monolayer MoS_2 transistors. *ACS Nano*, 6:10070–10075, 2012.

[115] Xia Leng, Fan Jin, Min Wei, and Yuchen Ma. GW method and Bethe-Salpeter equation for calculating electronic excitations. *WIREs Comput. Mol. Sci.*, 6(5):532–550, 2016.

[116] Linn Leppert, Tonatiuh Rangel, and Jeffrey B. Neaton. Towards predictive band gaps for halide perovskites: Lessons from one-shot and eigenvalue self-consistent GW. *Phys. Rev. Mater.*, 3:103803, 2019.

[117] G. Levita, A. Cavaleiro, E. Molinari, T. Polcar, and M. C. Righi. Sliding properties of MoS_2 layers: Load and interlayer orientation effects. *J. Phys. Chem. C*, 118:13809–13816, 2014.

[118] Jian Li, Xiuxun Han, Jiajia Li, Yun Zhao, and Changzeng Fan. Structural, electronic and optical properties of famatinite and enargite Cu_3SbS_4 under pressure: A theoretical investigation. *phys. stat. sol. (b)*, 254(5):1600608, 2017.

[119] Yafei Li, Zhen Zhou, Shengbai Zhang, and Zhongfang Chen. MoS_2 nanoribbons: High stability and unusual electronic and magnetic properties. *J. Am. Chem. Soc.*, 130:16739–16744, 2008.

[120] Zhenglu Li, Gabriel Antonius, Meng Wu, Felipe H. da Jornada, and Steven G. Louie. Electron-Phonon Coupling from Ab Initio Linear-Response Theory within the G W Method: Correlation-Enhanced Interactions and Superconductivity in $Ba_{1-x}K_xBiO_3$. *Phys. Rev. Lett.*, 122(18):186402, 2019.

[121] Charles M. Lieber and Y. Kim. Characterization of the structural, electronic and tribological properties of metal dichalcogenides by scanning probe microscopies. *Thin Solid Films*, 206:355–359, 1991.

[122] Chun Lin, Masayuki Ochi, Ryo Noguchi, Kenta Kuroda, Masahito Sakoda, Atsushi Nomura, Masakatsu Tsubota, Peng Zhang, Cedric Bareille, Kifu Kurokawa, Yosuke Arai, et al. Visualization of the strain-induced topological phase transition in a quasi-one-dimensional superconductor $TaSe_3$. *Nat. Mater.*, 20:1093–1099, 2021.

[123] Yu-Chuan Lin, Riccardo Torsi, Rehan Younas, Christopher L. Hinkle, Albert F. Rigosi, Heather M. Hill, Kunyan Zhang, Shengxi Huang, Christopher E. Shuck, et al. Recent advances in 2D material theory, synthesis, properties, and applications. *ACS Nano*, 17(11):9694–9747, 2023.

[124] Zhong Lin, Bruno R Carvalho, Ethan Kahn, Ruitao Lv, Rahul Rao, Humberto Terrones, Marcos A Pimenta, and Mauricio Terrones. Defect engineering of two-dimensional transition metal dichalcogenides. *2D Mater.*, 3:022002, 2016.

[125] Jeffrey R. Lince. Effective application of solid lubricants in spacecraft mechanisms. *Lubricants*, 8:74, 2020.

[126] Alexey Lipatov, Pradeep Chaudhary, Zhao Guan, Haidong Lu, Gang Li, Olivier Crégut, Kokou Dodzi Dorkenoo, Roger Proksch, Salia Cherifi-Hertel, Ding-Fu Shao, Evgeny Y. Tsymbal, Jorge Íñiguez, Alexander Sinitskii, and Alexei Gruverman. Direct observation of ferroelectricity in two-dimensional MoS_2. *npj 2D Mater. Appl.*, 6:18, 2022.

[127] Guoliang Liu, Alex W. Robertson, Molly Meng-Jung Li, Winson C. H. Kuo, Matthew T. Darby, Mohamad H. Muhieddine, Yung-Chang Lin, Kazu Suenaga, Michail Stamatakis, Jamie H. Warner, and Shik Chi Edman Tsang. Mos_2 monolayer catalyst doped with isolated Co atoms for the hydrodeoxygenation reaction. *Nat. Chem.*, 9:810–816, 2017.

[128] Lina Liu, Juanxia Wu, Liyuan Wu, Meng Ye, Xiaozhi Liu, Qian Wang, Siyao Hou, Pengfei Lu, Lifei Sun, Jingying Zheng, Lei Xing, Lin Gu, Xiangwei Jiang, Liming Xie, and Liying Jiao. Phase-selective synthesis of 1T′ MoS_2 monolayers and heterophase bilayers. *Nat. Mater.*, 17:1108–1114, 2018.

[129] S. Liu, M. X. Wang, C. Chen, X. Xu, J. Jiang, L. X. Yang, H. F. Yang, Y. Y. Lv, J. Zhou, Y. B. Chen, S. H. Yao, M. H. Lu, Y. F. Chen, C. Felser, B. H. Yan, Z. K. Liu, and Y. L. Chen. Experimental observation of conductive edge states in weak topological insulator candidate $HfTe_5$. *APL Mater.*, 6(12):121111, 2018.

[130] Yudong Liu, Erlin Tresna Nurlianti Wahyudin, Jr-Hau He, and Junyi Zhai. Piezotronics and piezo-phototronics in two-dimensional materials. *MRS Bull.*, 43:959–964, 2018.

[131] Oriol Lopez-Sanchez, Dominik Lembke, Metin Kayci, Aleksandra Radenovic, and Andras Kis. Ultrasensitive photodetectors based on monolayer MoS_2. *Nat. Nanotech.*, 8:497–501, 2013.

[132] C. M. Lueng, H. L. W. Chan, C. Surya, and C. L. Choy. Piezoelectric coefficient of aluminum nitride and gallium nitride. *J. Appl. Phys.*, 88(9):5360–5363, 2000.

[133] Jiajun Luo, Xiaoming Wang, Shunran Li, Jing Liu, Yueming Guo, Guangda Niu, Li Yao, Yuhao Fu, Liang Gao, Qingshun Dong, Chunyi Zhao, Meiying Leng, Fusheng Ma, Wenxi Liang, Liduo Wang, et al. Efficient and stable emission of warm-white light from lead-free halide double perovskites. *Nature*, 563:541–545, 2018.

[134] Ruichun Luo, Min Luo, Ziqian Wang, Pan Liu, Shuangxi Song, Xiaodong Wanga, and Mingwei Chen. The atomic origin of nickel-doping-induced catalytic enhancement in MoS_2 for electrochemical hydrogen production. *Nanoscale*, 11:7123, 2019.

[135] Antonio Luque and Antonio Martí. A metallic intermediate band high efficiency solar cell. *Prog. Photovolt: Res. Appl.*, 9:73–86, 2001.

[136] Antonio Luque, Antonio Martí, and Colin Stanley. Understanding intermediate-band solar cells. *Nat. Photonics*, 6:146–152, 2012.

[137] Jan Luxa, Lucie Spejchalová, Ivo Jakubec, and Zdeněk Sofer. MoS_2 stacking matters: 3R polytype significantly outperforms 2H MoS_2 for the hydrogen evolution reaction. *Nanoscale*, 13:19391–19398, 2021.

[138] Hou-Yi Lyu, Zhen Zhang, Jing-Yang You, Qing-Bo Yan, and Gang Su. Two-dimensional intercalating multiferroics with strong magnetoelectric coupling. *J. Phys. Chem. Lett.*, 13(49):11405–11412, 2022.

[139] Per-Olov Löwdin. On the non-orthogonality problem connected with the use of atomic wave functions in the theory of molecules and crystals. *J. Chem. Phys.*, 18:365, 1950.

[140] Chunqing Ma, Dong Shen, Bin Huang, Xiaocui Li, Wen-Cheng Chen, Ming-Fai Lo, Pengfei Wang, Michael Hon-Wah Lam, Yang Lu, Biwu Ma, and Chun-Sing Lee. High performance low-dimensional perovskite solar cells based on a one dimensional lead iodide perovskite. *J. Mater. Chem. A*, 7:8811, 2019.

[141] Dongwei Ma, Weiwei Ju, Tingxian Li, Xiwei Zhang, Chaozheng He, Benyuan Ma, Zhansheng Lu, and Zongxian Yang. The adsorption of CO and NO on the MoS_2 monolayer doped with Au, Pt, Pd, or Ni: A first-principles study. *Appl. Surf. Sci.*, 383:98 – 105, 2016.

[142] Xiaoyan Ma, Jinquan Li, Changhua An, Juan Feng, Yuhua Chi, Junxue Liu, Jun Zhang, and Yugang Sun. Ultrathin Co(Ni)-doped MoS_2 nanosheets as catalytic promoters enabling efficient solar hydrogen production. *Nano Res.*, 9:2284–2293, 2016.

[143] Georg K.H. Madsen, Jesús Carrete, and Matthieu J. Verstraete. BoltzTraP2, a program for interpolating band structures and calculating semi-classical transport coefficients. *Comp. Phys. Commun.*, 231:140–145, 2018.

[144] Kin Fai Mak, Changgu Lee, James Hone, Jie Shan, and Tony F. Heinz. Atomically thin MoS_2: A new direct-gap semiconductor. *Phys. Rev. Lett.*, 105:136805, 2010.

[145] Kin Fai Mak and Jie Shan. Photonics and optoelectronics of 2D semiconductor transition metal dichalcogenides. *Nat. Photonic*, 10:216–226, 2016.

[146] G. Makov and M. C. Payne. Periodic boundary conditions in ab initio calculations. *Phys. Rev. B*, 51:4014–4022, 1995.

[147] Jun Mao, Zihang Liu, Jiawei Zhou, Hangtian Zhu, Qian Zhang, Gang Chen, and Zhifeng Ren. Advances in thermoelectrics. *Adv. in Phys.*, 67(2):69–147, 2018.

[148] Jun Mao, Yong Wang, Zhilong Zheng, and Dehui Deng. The rise of two-dimensional MoS_2 for catalysis. *Front. Phys.*, 13:138118, 2018.

[149] Luke M. McClintock, Long Yuan, Ziyi Song, Michael T. Pettes, Dmitry Yarotski, Rijan Karkee, David A. Strubbe, Liang Z. Tan, Azza Ben-Akacha, Biwu Ma, Yunshu Shi, Valentin Taufour, and Dong Yu. Surface effects on anisotropic photoluminescence in one-dimensional organic metal halide hybrids. *Small Struct.*, 4:2200378, 2023.

[150] L. W. McKeehan. The crystal structure of iron-nickel alloys. *Phys. Rev.*, 21:402, 1923.

[151] H. Mine, A. Kobayashi, T. Nakamura, T. Inoue, S. Pakdel, D. Marian, E. Gonzalez-Marin, S. Maruyama, S. Katsumoto, A. Fortunelli, J. J. Palacios, and J. Haruyama. Laser-beam-patterned topological insulating states on thin semiconducting MoS_2. *Phys. Rev. Lett.*, 123:146803, 2019.

[152] Dario Mosconi, Paul Till, Laura Calvillo, Tomasz Kosmala, Denis Garoli, Doriana Debellis, Alessandro Martucci, Stefano Agnoli, and Gaetano Granozzi. Effect of Ni doping on the MoS_2 structure and its hydrogen evolution activity in acid and alkaline electrolytes. *Surfaces*, 2:531–545, 2019.

[153] Arash A. Mostofi, Jonathan R. Yates, Young-Su Lee, Ivo Souza, David Vanderbilt, and Nicola Marzari. wannier90: A tool for obtaining maximally-localised wannier functions. *Comput. Phys. Commun.*, 178(9):685 – 699, 2008.

[154] Félix Mouhat and François-Xavier Coudert. Necessary and sufficient elastic stability conditions in various crystal systems. *Phys. Rev. B*, 90:224104, 2014.

[155] Nicolas Mounet, Marco Gibertini, Philippe Schwaller, Davide Campi, Andrius Merkys, Antimo Marrazzo, Thibault Sohier, Ivano Eligio Castelli, Andrea Cepellotti, Giovanni Pizzi, and Nicola Marzari. Two-dimensional materials from high-throughput computational exfoliation of experimentally known compounds. *Nat. Nanotech.*, 13:246–252, 2018.

[156] Hui-Ying Mu, Yi-Tong Yao, Jie-Ru Li, Guo-Cai Liu, Chao He, Ying-Jie Sun, Guang Yang, Xing-Tao An, Yongzhe Zhang, and Jian-Jun Liu. Valley polarization and valleyresistance in a monolayer transition metal dichalcogenide superlattice. *J. Phys. Chem. Lett.*, 11(10):3882–3888, 2020.

[157] J. Nordlander, M. Campanini, M. D. Rossell, R. Erni, Q. N. Meier, A. Cano, N. A. Spaldin, M. Fiebig, and M. Trassin. The ultrathin limit of improper ferroelectricity. *Nat. Commun.*, 10:5591, 2019.

[158] Giovanni Onida, Lucia Reining, and Angel Rubio. Electronic excitations: density-functional versus many-body Green's-function approaches. *Rev. Mod. Phys.*, 74(2):601–659, 2002.

[159] Banabir Pal, Anjali Singh, Sharada G., Pratibha Mahale, Abhinav Kumar, S. Thirupathaiah, H. Sezen, M. Amati, Luca Gregoratti, Umesh V. Waghmare, and D. D. Sarma. Chemically exfoliated MoS_2 layers: Spectroscopic evidence for the semiconducting nature of the dominant trigonal metastable phase. *Phys. Rev. B*, 96:195426, 2017.

[160] Ioanna Pallikara, Prakriti Kayastha, Jonathan M Skelton, and Lucy D Whalley. The physical significance of imaginary phonon modes in crystals. *Electron. Struct.*, 4(3):033002, 2022.

[161] Diego Pasquier and Oleg V. Yazyev. Unified picture of lattice instabilities in metallic transition metal dichalcogenides. *Phys. Rev. B*, 100:201103, 2019.

[162] Lars Pastewka and Mark O. Robbins. Contact between rough surfaces and a criterion for macroscopic adhesion. *Proc. Nat. Acad. Sci.*, 111:3298–3303, 2014.

[163] H. Peelaers and C. G. Van de Walle. Elastic constants and pressure-induced effects in MoS_2. *J. Phys. Chem. C*, 118:12073–12076, 2014.

[164] John P. Perdew, Kieron Burke, and Matthias Ernzerhof. Generalized gradient approximation made simple. *Phys. Rev. Lett.*, 77:3865–3868, 1996.

[165] John P. Perdew and Yue Wang. Accurate and simple analytic representation of the electron–gas correlation energy. *J. Phys. Chem. C*, 45:13244, 1992.

[166] Michael Thompson Pettes, Jesse Maassen, Insun Jo, Mark S. Lundstrom, and Li Shi. Effects of surface band bending and scattering on thermoelectric transport in suspended bismuth telluride nanoplates. *Nano Letters*, 13(11):5316–5322, 2013.

[167] Frederic Peyskens, Chitraleema Chakraborty, Muhammad Muneeb, Dries Van Thourhout, and Dirk Englund. Integration of single photon emitters in 2D layered materials with a silicon nitride photonic chip. *Nat. Commun.*, 10:4435, 2019.

[168] Michele Pizzochero and Oleg V. Yazyev. Point defects in the 1T′ and 2H phases of single-layer MoS_2: A comparative first-principles study. *Phys. Rev. B*, 96:245402, 2017.

[169] V. Podzorov, M. E. Gershenson, Ch. Kloc, R. Zeis, and E. Bucher. High-mobility field-effect transistors based on transition metal dichalcogenides. *App. Phys. Lett.*, 84(17):3301–3303, 2004.

[170] L. E Pope, T. R. Jervis, and M. Nastasi. Effects of laser processing and doping on the lubrication and chemical properties of thin MoS_2 films. *Surf. Coat. Technol.*, 42:217 – 225, 1990.

[171] Xiaofeng Qian, Junwei Liu, Liang Fu, and Ju Li. Quantum spin Hall effect in two-dimensional transition metal dichalcogenides. *Science*, 346:1344–1347, 2014.

[172] Li Na Quan, Mingjian Yuan, Riccardo Comin, Oleksandr Voznyy, Eric M. Beauregard, Sjoerd Hoogland, Andrei Buin, Ahmad R. Kirmani, Kui Zhao, Aram Amassian, Dong Ha Kim, and Edward H. Sargen. Ligand-stabilized reduced-dimensionality perovskites. *J. Am. Chem. Soc.*, 138:2649–2655, 2016.

[173] B. Radisavljevic, A. Radenovic, J. Brivio, V. Giacometti, and A. Kis. Single-layer MoS_2 transistors. *Nat. Nanotech.*, 6:147–150, 2011.

[174] N. M. Renevier, V. C. Fox, D. G. Teer, and J. Hampshire. Coating characteristics and tribological properties of sputter-deposited MoS_2/metal composite coatings deposited by closed field unbalanced magnetron sputter ion plating. *Surf. Coat. Technol.*, 127:24–37, 2012.

[175] Raffaele Resta. Macroscopic polarization in crystalline dielectrics: the geometric phase approach. *Rev. Mod. Phys.*, 66:899–915, 1994.

[176] Michael Rohlfing and Steven G. Louie. Electron-hole excitations and optical spectra from first principles. *Phys. Rev. B*, 62(8):4927–4944, 2000.

[177] Robert H. Savage. Graphite lubrication. *J. Appl. Phys.*, 19:1, 1948.

[178] Martin Schlipf and Francois Gygi. Optimization algorithm for the generation of ONCV pseudopotentials. *Comput. Phys. Commun.*, 196:36–44, 2015.

[179] Schlüter, M. A pseudopotential approach to the electronic structure of iii-iv layer-compounds. *J. Phys. Colloques*, 33(C3):C3–273–C3–276, 1972.

[180] Bruno Schuler, Diana Y. Qiu, Sivan Refaely-Abramson, Christoph Kastl, Christopher T. Chen, Sara Barja, Roland J. Koch, D. Frank Ogletree, Shaul Aloni, Adam M. Schwartzberg, Jeffrey B. Neaton, Steven G. Louie, and Alexander Weber-Bargioni. Large spin-orbit splitting of deep in-gap defect states of engineered sulfur vacancies in monolayer WS_2. *Phys. Rev. Lett.*, 123:076801, 2019.

[181] Klaus J. Schulz, Nadine M. Piatak, and John F. Papp. Niobium and tantalum, chap. M of Schulz, K.J., DeYoung, J.H., Jr., Seal, R.R., II, and Bradley, D.C., eds., Critical mineral resources of the United States—Economic and environmental geology and prospects for future supply. *U.S. Geological Survey Professional Paper 1802*, page M1–M34, 2017. https://doi.org/10.3133/pp1802M.

[182] T. Sekine, Julien C., I. Samaras, M. Jouanne, and M. Balkanski. Vibrational modifications on lithium intercalation in MoS_2. *Mat. Sci. Eng., B*, 3:153–158, 1989.

[183] Roey Shaviv, Edgar F. Westrum, Helmer Fjellvåg, and Arne Kjekshus. $Zrte_5$ and $hfte_5$: The heat capacity and derived thermophysical properties from 6 to 350 K. *J. Solid State Chem.*, 81(1):103–111, 1989.

[184] Natalya Sheremetyeva, Drake Niedzielski, Damien Tristant, Liangbo Liang, Lauren E. Kerstetter, Suzanne E. Mohney, and Vincent Meunier. Low-frequency Raman signature of Ag-intercalated few-layer MoS_2. *2D Mater.*, 8(2):025031, 2021.

[185] Sharmila N. Shirodkar and Umesh V. Waghmare. Emergence of ferroelectricity at a metal-semiconductor transition in a $1T$ monolayer of MoS_2. *Phys. Rev. Lett.*, 112:157601, 2014.

[186] Patrick H.-L. Sit, Roberto Car, Morrel H. Cohen, and Annabella Selloni. Simple, unambiguous theoretical approach to oxidation state determination via first-principles calculations. *Inorg. Chem.*, 50:10259–10267, 2011.

[187] Amit Sitt, Leeor Kronik, Sohrab Ismail-Beigi, and James R. Chelikowsky. Excited-state forces within time-dependent density-functional theory: A frequency-domain approach. *Phys. Rev. A*, 76(5):1–4, 2007.

[188] Maria S. Sokolikova and Cecilia Mattevi. Direct synthesis of metastable phases of 2D transition metal dichalcogenides. *Chem. Soc. Rev.*, 49:3952, 2020.

[189] Alexey A. Soluyanov and David Vanderbilt. Computing topological invariants without inversion symmetry. *Phys. Rev. B*, 83:235401, 2011.

[190] K.S. Song and Richard T. Williams. *Self-Trapped Excitons*. Springer, Berlin, Heidelberg, 1996.

[191] Seunghyun Song, Dong Hoon Keum, Suyeon Cho, David Perello, Yunseok Kim, and Young Hee Lee. Room temperature semiconductor-metal transition of $MoTe_2$ thin films engineered by strain. *Nano Lett.*, 16:188–193, 2016.

[192] Andrea Splendiani, Liang Sun, Yuanbo Zhang, Tianshu Li, Jonghwan Kim, Chi-Yung Chim, Giulia Galli, and Feng Wang. Emerging photoluminescence in monolayer MoS_2. *Nano Lett.*, 10:1271–1275, 2010.

[193] H. T. Stokes and D. M. Hatch. Program for identifying the space group symmetry of a crystal. *J. Appl. Cryst.*, 38:237–238, 2005.

[194] Jyah Strachan, Anthony F. Masters, and Thomas Maschmeyer. 3R-MoS_2 in review: History, status, and outlook. *ACS Appl. Ener. Mater.*, 4(8):7405–7418, 2021.

[195] David Strubbe. *Optical and Transport Properties of Organic Molecules: Methods and Applications*. PhD thesis, 2012.

[196] David A. Strubbe, Eric C. Johlin, Timothy R. Kirkpatrick, Tonio Buonassisi, and Jeffrey C. Grossman. Stress effects on the Raman spectrum of an amorphous material: Theory and experiment on *a*-Si:H. *Phys. Rev. B*, 92:241202, 2015.

[197] B.C. Stupp. Synergistic effects of metals co-sputtered with MoS_2. *Thin Solid Films*, 84:256–257, 1981.

[198] Joonki Suh, Teck Leong Tan, Weijie Zhao, Joonsuk Park, Der-Yuh Lin, Tae-Eon Park, Jonghwan Kim, Chenhao Jin, Nihit Saigal, Sandip Ghosh, Zicong Marvin Wong, et al. Reconfiguring crystal and electronic structures of MoS_2 by substitutional doping. *Nat. Commun.*, 9:199, 2018.

[199] Fengrui Sui, Min Jin, Yuanyuan Zhang, Ruijuan Qi, Yu-Ning Wu, Rong Huang, Fangyu Yue, and Junhao Chu. Sliding ferroelectricity in van der Waals layered γ-InSe semiconductor. *Nat. Commun.*, 14:36, 2023.

[200] Kuntal Talit and David A. Strubbe. Stress effects on vibrational spectra of a cubic hybrid perovskite: A probe of local strain. *J. Phys. Chem. C*, 124(50):27287–27299, 2020.

[201] Nicolas Tancogne-Dejean, Micael J. T. Oliveira, Xavier Andrade, Heiko Appel, Carlos H. Borca, Guillaume Le Breton, Florian Buchholz, Alberto Castro, et al. Octopus, a computational framework for exploring light-driven phenomena and quantum dynamics in extended and finite systems. *Journ. Chem. Phys.*, 152(12):124119, 2020.

[202] Dai-Ming Tang, Dmitry G. Kvashnin, Sina Najmaei, Yoshio Bando, Koji Kimoto, Pekka Koskinen, Pulickel M. Ajayan, Boris I. Yakobson, Pavel B. Sorokin, Jun Lou, and Dmitri Golberg. Nanomechanical cleavage of molybdenum disulphide atomic layers. *Nat. Commun.*, 4:3631, 2014.

[203] Junhui Tang, Yanling Chen, Samantha R. McCuskey, Lidong Chen, Guillermo C. Bazan, and Ziqi Liang. Recent advances in n-type thermoelectric nanocomposites. *Adv. Electron. Mater.*, 5(11):1800943, 2019.

[204] Peizhe Tang, Quan Zhou, Gang Xu, and Shou-Cheng Zhang. Dirac fermions in an antiferromagnetic semimetal. *Nat. Phys.*, 12:1100–1104, 2016.

[205] H. Tanino, W. W. Rühle, and K. Takahashi. Time-resolved photoluminescence study of excitonic relaxation in one-dimensional systems. *Phys. Rev. B*, 38:12716, 1988.

[206] Aleksander A. Tedstone, David J. Lewis, and Paul O'Brien. Synthesis, properties, and applications of transition metal-doped layered transition metal dichalcogenides. *Chem. Mater.*, 28:1965–1974, 2016.

[207] D. G. Teer. New solid lubricant coatings. *Wear*, 251:1068–1074, 2001.

[208] John C. Thomas, Wei Chen, Yihuang Xiong, Bradford A. Barker, Junze Zhou, Weiru Chen, Antonio Rossi, Nolan Kelly, Zhuohang Yu, Da Zhou, Shalini Kumari, Edward S. Barnard, Joshua A. Robinson, Mauricio Terrones, Adam Schwartzberg, D. Frank Ogletree, et al. A substitutional quantum defect in WS_2 discovered by high-throughput computational screening and fabricated by site-selective STM manipulation. *arXiv:2309.08032*, 2023. https://doi.org/10.48550/arXiv.2309.08032.

[209] A Togo and I Tanaka. First principles phonon calculations in materials science. *Scr. Mater.*, 108:1–5, 2015.

[210] Hsinhan Tsai, Wanyi Nie, Jean-Christophe Blancon, Constantinos C. Stoumpos, Reza Asadpour, Boris Harutyunyan, Amanda J. Neukirch, Rafael Verduzco, Jared J. Crochet, Sergei Tretiak, Laurent Pedesseau, et al. High-efficiency two-dimensional ruddlesden–popper perovskite solar cells. *Nature*, 536:312–316, 2016.

[211] Mohammad R. Vazirisereshk, Ashlie Martini, David A. Strubbe, and Mehmet Z. Baykara. Solid lubrication with MoS_2: A review. *Lubricants*, 7:57, 2019.

[212] A. Vellore, S. Romero Garcia, D. Johnson, and A. Martini. Ni-doped MoS_2 dry film lubricant life. *Adv. Mater. Interfaces*, 7:2001109, 2020.

[213] Pablo Villar Arribi, Jian-Xin Zhu, Timo Schumann, Susanne Stemmer, Anton A. Burkov, and Olle Heinonen. Topological surface states in strained dirac semimetal thin films. *Phys. Rev. B*, 102:155141, 2020.

[214] Steven A. Vitale, Daniel Nezich, Joseph O. Varghese, Philip Kim, Nuh Gedik, Pablo Jarillo-Herrero, Di Xiao, and Mordechai Rothschild. Valleytronics: Opportunities, challenges, and paths forward. *Small*, 14(38):1801483, 2018.

[215] Dian Wang, Matthew Wright, Naveen Kumar Elumalai, and Ashraf Uddin. Stability of perovskite solar cells. *Sol. Ener. Mater. Sol. Cells*, 147:255–275, 2016.

[216] Guowei Wang, Guikai Zhang, Xiaoxing Ke, Xiangyu Chen, Xu Chen, Yueshuai Wang, Guoyu Huang, Juncai Dong, Shengqi Chu, and Manling Sui. Direct synthesis of stable 1T-MoS_2 doped with Ni single atoms for water splitting in alkaline media. *Small*, 18(16):2107238, 2022.

[217] Roger Clark Wells. Relative abundance of nickel in the Earth's crust. *U.S. Dept. of the Interior Professional Paper 205-A*, pages 1–21, 1943. https://pubs.usgs.gov/pp/0205a/report.pdf.

[218] Astrid Weston, Yichao Zou, Vladimir Enaldiev, Alex Summerfield, Nicholas Clark, Viktor Zólyomi, Abigail Graham, Celal Yelgel, Samuel Magorrian, Mingwei Zhou, Johanna Zultak, David Hopkinson, et al. Atomic reconstruction in twisted bilayers of transition metal dichalcogenides. *Nat. Nanotechnol.*, 15:592–597, 2020.

[219] R. T. Williams and K. S. Song. The self-trapped exciton. *J. Phys. Chem. Solids*, 51:679–716, 1990.

[220] Guanhong Wu, Chenkun Zhou, Wenmei Ming, Dan Han, Shiyou Chen, Dong Yang, Tiglet Besara, Jennifer Neu, Theo Siegrist, Mao-Hua Du, Biwu Ma, and Angang Dong. A one-dimensional organic lead chloride hybrid with excitation-dependent broadband emissions. *ACS Energy Lett.*, 3:1443–1449, 2018.

[221] Maokun Wu, Xiaolong Yao, Yuan Hao, Hong Dong, Yahui Cheng, Hui Liu, Feng Lu, Weichao Wang, Kyeongjae Cho, and Wei-Hua Wang. Electronic structures, magnetic properties and band alignments of 3d transition metal atoms doped monolayer MoS_2. *Phys. Lett. A*, 382:111–115, 2018.

[222] Di Xiao, Gui-Bin Liu, Wanxiang Feng, Xiaodong Xu, and Wang Yao. Coupled spin and valley physics in monolayers of MoS_2 and other group-VI dichalcogenides. *Phys. Rev. Lett.*, 108:196802, 2012.

[223] Junfeng Xie, Jiajia Zhang, Shuang Li, Fabian Grote, Xiaodong Zhang, Hao Zhang, Ruoxing Wang, Yong Lei, Bicai Pan, and Yi Xie. Controllable disorder engineering in oxygen-incorporated MoS_2 ultrathin nanosheets for efficient hydrogen evolution. *J. Am. Chem. Soc.*, 135:17881–17888, 2013.

[224] Alireza Yaghoubi, Ramesh Singh, and Patrice Melinon. Predicting the primitive form of rhombohedral silicon carbide (9R-SiC): A pathway toward polytypic heterojunctions. *Cryst. Growth Des.*, 18(11):7059–7064, 2018.

[225] Shuang Yang, Yun Wang, Porun Liu, Yi-Bing Cheng, Hui Jun Zhao, and Hua Gui Ya. Functionalization of perovskite thin films with moisture-tolerant molecules. *Nat. Energy*, 1:15016, 2016.

[226] Yi Yang, Fei Gao, Shiwu Gao, and Su-Huai Wei. Origin of the stability of two-dimensional perovskites: a first-principles study. *J. Mater. Chem. A*, 6:14949–14955, 2018.

[227] Wang Yao, Di Xiao, and Qian Niu. Valley-dependent optoelectronics from inversion symmetry breaking. *Phys. Rev. B*, 77:235406, 2008.

[228] Sajad Yazdani and Michael Thompson Pettes. Nanoscale self-assembly of thermoelectric materials: a review of chemistry-based approaches. *Nanotechnology*, 29(43):432001, 2018.

[229] Sadegh Imani Yengejeh, William Wen, and Yun Wang. Mechanical properties of lateral transition metal dichalcogenide heterostructures. *Front. Phys.*, 16:13502, 2021.

[230] Jinran Yu, Xixi Yang, and Qijun Sun. Piezo/tribotronics toward smart flexible sensors. *Adv. Intel. Syst.*, 2(7):1900175, 2020.

[231] K. M. Yu, W. Walukiewicz, J. Wu, W. Shan, J. W. Beeman, M. A. Scarpulla, O. D. Dubon, and P. Becla. Diluted II-VI oxide semiconductors with multiple band gaps. *Phys. Rev. Lett.*, 91:246403, 2003.

[232] Jiao-Nan Yuan, Yan Cheng, Xiu-Qing Zhang, Xiang-Rong Chen, and Ling-Cang Cai. First-principles study of electronic and elastic properties of hexagonal layered crystal mos_2 under pressure. *ZNA*, 70(7):529–537, 2015.

[233] Zhao Yuan, Chenkun Zhou, Yu Tian, Yu Shu, Joshua Messier, Jamie C Wang, Lambertus J Van De Burgt, Konstantinos Kountouriotis, Yan Xin, Ethan Holt, et al. One-dimensional organic lead halide perovskites with efficient bluish white-light emission. *Nat. commun.*, 8(1):1–7, 2017.

[234] Zhao Yuan, Chenkun Zhou, Yu Tian, Yu Shu, Joshua Messier, Jamie C. Wang, Lambertus J. van de Burgt, Konstantinos Kountouriotis, Yan Xin, Ethan Holt, Kirk Schanze, Ronald Clark, Theo Siegrist, and Biwu Ma. One-dimensional organic lead halide perovskites with efficient bluish white-light emission. *Nat. Commun.*, 8:14051, 2017.

[235] Qi Hao Zhang, Xiang Yang Huang, Sheng Qiang Bai, Xun Shi, Ctirad Uher, and Li Dong Chen. Thermoelectric devices for power generation: Recent progress and future challenges. *Adv. Eng. Mater.*, 18(2):194–213, 2016.

[236] Qin Zhang, Zuo Shanling, Chen Ping, and Pan Caofeng. Piezotronics in two-dimensional materials. *InfoMat*, 3(9):987–1007, 2021.

[237] Wei Zhang, Changchun Chai, Qingyang Fan, Yanxing Song, and Yintang Yang. Direct and quasi-direct band gap silicon allotropes with low energy and strong absorption in the visible for photovoltaic applications. *Res. Phys.*, 18:103271, 2020.

[238] Xiaohang Zhang, Stephan von Molnár, Zachary Fisk, and Peng Xiong. Spin-dependent electronic states of the ferromagnetic semimetal EuB_6. *Phys. Rev. Lett.*, 100:167001, 2008.

[239] Yong Zhang. Applications of Huang–Rhys theory in semiconductor optical spectroscopy. *J. Semicond.*, 40:091102, 2019.

[240] B. Zhao, L. L. Liu, G. D. Cheng, T. Li, N. Qi, Z. Q. Chen, and Z. Tang. Interaction of O_2 with monolayer MoS_2: Effect of doping and hydrogenation. *Mater. Des.*, 383:1 – 8, 2017.

[241] Chuanyu Zhao, Chuanhong Jin, Jianlan Wu, and Wei Ji. Magnetism in molybdenum disulphide monolayer with sulfur substituted by 3d transition metals. *J. Appl. Phys.*, 120:144305, 2016.

[242] Wei Zhao, Jie Pan, Yuqiang Fang, Xiangli Che, Dong Wang, Kejun Bu, and Fuqiang Huang. Metastable MoS_2: Crystal structure, electronic band structure, synthetic approach and intriguing physical properties. *Chem. Eur. J.*, 24:15942–15954, 2018.

[243] W. X. Zhou and A. Ariando. Review on ferroelectric/polar metals. *Jpn. J. Appl. Phys.*, 59(SI):SI0802, 2020.

[244] Yupeng Zhu, Xiao Liang, Jun Qin, Longjiang Deng, and Lei Bi. Strain tunable magnetic properties of 3d transition-metal ion doped monolayer MoS_2: A first-principles study. *Int. J. Quantum Chem.*, 8:055917, 2018.

[245] Houlong Zhuang. Department of Mechanical and Aerospace Engineering, Arizona State University, Tempe, AZ. *personal communication*, 2022.

[246] Houlong L. Zhuang, Michelle D. Johannes, Arunima K. Singh, and Richard G. Hennig. Doping-controlled phase transitions in single-layer MoS_2. *Phys. Rev. B*, 96:165305, 2017.